UNIVERSITÀ DEGLI STUDI DI TRIESTE

UNIVERSITÀ DEGLI STUDI DI TRIESTE

XXXIV CICLO DEL DOTTORATO DI RICERCA IN

NANOTECNOLOGIE

Nanostructured Multilayer Ceramic Coatings For Wood Cutting Tools

Settore scientifico-disciplinare: **ING-IND/22**

DOTTORANDO / A

MARCO BELTRAMI

COORDINATORE

PROF. ALBERTO MORGANTE

SUPERVISORE DI TESI

PROF. ORFEO SBAIZERO

CO-SUPERVISORE DI TESI

DR. SIMONE DAL ZILIO

ANNO ACCADEMICO 2020/2021

A mia madre

Abstract

Lo sviluppo di questo dottorato di ricerca è stato supportato e finanziato dal progetto europeo Interreg ITA-SLO NANOREGION. La missione del progetto NANOREGION consiste nel costituire un consorzio tra università ed enti di ricerca locali atti a fornire una piattaforma scientifica di supporto alle imprese del territorio comprensivo delle regioni dell'Italia nord-orientale e la Slovenia. In tali regioni, l'impatto economico-sociale dell'industria del legno è rilevante. È noto che nella manifattura di materiali legnosi la necessità di una frequente sostituzione degli utensili da lavorazione, necessaria a garantire gli standard di qualità del prodotto finito, ha un forte impatto sull'economia del processo di lavorazione. Gli utensili da taglio sono generalmente protetti con rivestimenti a film sottile costituiti da materiali duri e refrattari per aumentarne la durabilità, riducendo la frequenza di sostituzione e quindi aumentando la produttività delle aziende. Tuttavia, a causa della natura del legno come materiale da lavorazione e dei rigorosi requisiti tecnici specifici della lavorazione del legno, il rapporto costi/benefici del processo di rivestimento degli utensili si è finora dimostrato non sufficiente a giustificare i costi addizionali legati al processo di rivestimento. Questo risulta in una minore penetrazione nel mercato degli utensili rivestiti rispetto a quanto accade invece nell'industria metalmeccanica. Un'eccezione, seppure in misura limitata, è rappresentata dai rivestimenti a base di cromo, come il nitruro di cromo (CrN), che forniscono la massima protezione contro l'usura dovuta a processi di corrosione. Questi, infatti, sono riconosciuti come una delle principali cause di usura nella lavorazione del legno, favorendo la successiva usura abrasiva dei fragili prodotti d'ossidazione operata da inclusioni di minerali duri presenti all'interno di materiali a base legnosa, soprattutto prodotti secondari già sottoposti a lavorazioni precedenti. Tuttavia, a causa della relativamente bassa durezza, il CrN fornisce di per sé una scarsa resistenza all'usura abrasiva. Una possibile soluzione consiste nel sostituire rivestimenti monostrato di CrN con rivestimenti multistrato. Ricerche e applicazioni pratiche approfondite hanno dimostrato che la progettazione di rivestimenti multistrato offre numerosi vantaggi rispetto ai rivestimenti a strato singolo, soprattutto se lo spessore degli strati costitutivi è ridotto al regime nanometrico. Tuttavia, la ricerca per lo sviluppo di rivestimenti multistrato mirati a rispondere ai severi requisiti dell'industria del legno è molto limitata. Pertanto, lo scopo di questo progetto di ricerca era di effettuare preliminari studi sulle proprietà protettive

dei sistemi di rivestimento PVD multistrato a base di CrN accoppiato con nitruri di indurimento. L'abbinamento di proprietà anticorrosive e migliori caratteristiche meccaniche potrebbero rendere tali sistemi di rivestimento dei potenziali candidati per il rivestimento di utensili da taglio del legno. I nitruri di Tungsteno e molibdeno (WN e MoN, rispettivamente) sono stati scelti in quanto già applicati per la realizzazione di sistemi multistrato con altri nitruri, e anche per fornire uno studio comparato su due sistemi che raramente vengono studiati in parallelo nelle stesse condizioni sperimentali. L'obiettivo fondamentale dell'aggiunta di questi materiali aggiuntivi è fornire al CrN una migliore durezza meccanica mantenendo o migliorando l'elevata resistenza alla corrosione, e la letteratura pregressa suggerisce ottime potenzialità di questi materiali come nitruri indurenti.

Nel Capitolo 1, si chiariscono le motivazioni del progetto, fornendo prima una breve introduzione circa l'importanza dell'industria del legno nell'economia dell'Unione Europea e dell'Italia come caso particolare, e successivamente viene chiarito l'impatto dell'usura degli utensili da taglio sulla catena di lavorazione del legno. Quindi, viene presentata un'introduzione alle principali classi di materiali e rivestimenti per utensili da taglio, con un focus sui vantaggi derivanti dalle architetture multistrato. Il Capitolo 2 introduce i concetti fondamentali alla base delle tecniche sperimentali che sono state utilizzate direttamente durante lo sviluppo della ricerca e che hanno fornito risultati significativi. Il Capitolo 3 apre di fatto la sezione sperimentale. Questa parte dell'attività di ricerca si è concentrata sullo studio dell'impatto dei parametri del processo di deposizione mediante DC Magnetron Sputtering sulle proprietà chimiche, topografiche e strutturali di sistemi di rivestimento monostrato di CrN, MoN e WN. In ogni sezione del capitolo, i risultati sono presentati e discussi parzialmente. Il capitolo 4 riguarda i risultati pubblicati di studi condotti sui rivestimenti multistrato nanostrutturati (detti nano-laminati) basati sul sistema CrN/WN depositati su wafer di silicio. Questa ricerca ha comportato un'indagine sull'impatto dei progetti nanostrutturati sulla conformità dei rivestimenti e sulle caratteristiche strutturali/microstrutturali come lo sviluppo della rugosità interfacciale lungo la struttura multistrato. Viene fornito un metodo analitico per la discriminazione dei contributi individuali allo sviluppo delle asperità interfacciali. Nel Capitolo 5, è stata affrontata la relazione tra architettura e proprietà di sistemi nano-laminati basati su unità ripetitive CrN/WN e CrN/MoN depositate su substrati di acciaio

per utensili. In particolare, è stata studiata la variazione delle proprietà strutturali, meccaniche ed elettrochimiche in base allo spessore dei singoli strati costituenti. Infine, il Capitolo 6 fornisce una sintesi della discussione dei risultati più rilevanti dei risultati ottenuti nei Capitoli 4-5, chiarendo i limiti dei risultati ottenuti e stabilendo i punti di partenza per possibili sviluppi futuri.

Abstract

The research activity of this PhD thesis is grounded is founded by the European Interreg ITA-SLO NANOREGION project. The mission of NANOREGION was to provide scientific support to local enterprises in the region comprehending North-eastern Italy and Slovenia. In such regions the impact of the wood industry on local economics is relevant. It is well known that the impact of tool replacement has a strong impact on the economics of the wood-working process to maintain the manufacturing standards required to obtain high-quality products. Cutting tools are usually coated with hard, refractory thin film coatings to increase their service life and hence increase manufacturing productivity. Nonetheless, owing to the nature of the wood as a workpiece and the strict technical requirements specific to wood-machining, the cost-to-benefits ratio of tools coating has so far proved not enough to allow the same market penetration of coated tools that is instead recorded in the metal-working industry. An exception to some extent is represented by Chromium-based coatings such as CrN, which provide the highest protection against corrosive wear, which in turn is recognized as of the main causes of wear in wood-machining, as it favours the subsequent abrasive wear of the brittle oxidation products mediated by hard mineral inclusions within the wood-based materials. Nonetheless, CrN alone is known to provide poor resistance to abrasive wear, due to its relatively low hardness. A large amount of research has demonstrated that the design of multilayer coatings offers several advantages over single-layer coatings, especially if the thickness of the constituent layers is reduced to the nanometric regime. Nonetheless, the research investigating the development of multilayer coatings specifically targeting the strict requirements of the wood industry is very limited. Hence, this research process aimed to investigate the preliminary protective properties of multilayer PVD coating systems based on oxidation-protective CrN coupled with hardening nitrides as potential candidate coatings for wood-cutting tools. WN and MoN were chosen due to reported

literature on the successful coupling of such coatings with other nitrides such as TiN or ZrN and CrN, and because of the limited number of scientific and systematic comparative investigations on these systems. The fundamental aim of the addition of these additional materials is to provide CrN with improved mechanical hardness while retaining or improving high corrosion resistance. The manuscript is organized as follows.

In Chapter 1, project motivations are first enlightened by a brief introduction to the importance of the wood industry in the economy of the European Union and Italy as a particular case and the impact of cutting tools-wear on the wood-working chain is elucidated. Then, an introduction to the main classes of cutting tools materials and coatings is presented, with a focus on the benefits arising from multilayer architectures.

Chapter 2 introduces the basic concepts behind the experimental techniques that have been directly used throughout the development of the research and that have provided meaningful results.

Chapter 3 officially opens the experimental section. This part of the research activity has focused on the investigation of the impact of deposition process parameters on the structural, chemical, and topographical features of single-layer coatings of CrN, MoN and WN. Results and discussions are provided at the end of each subsection.

Chapter 4 deals with published results on nanostructured multilayer coatings (nanolaminates) based on the CrN/WN system deposited onto silicon wafers. This research involved an investigation of the impact of nanostructured designs on coatings' conformity and structural/microstructural features such as the development of interfacial roughness across the stack. An analytical method for the discrimination of individual contributions to the development of interfacial asperities is provided.

In Chapter 5, the structure-to-property relation of nanolaminate systems based on CrN/WN and CrN/MoN repetitive units deposited on tool-steel substrates has been tackled concerning the structural, mechanical, and electrochemical properties. In particular, the dependence of such properties on the nanostructured design has been addressed.

Finally, Chapter 6 provides a summary of the most relevant results and discussion of the results obtained in chapters 4-5 and states the starting points for future developments.

SUMMARY

1 PROJECT OVERVIEW AND BACKGROUND

1.1 INTRODUCTION TO THE FIELD OF CUTTING TOOLS TECHNOLOGIES

1.1.1 THE WOOD-INDUSTRY

Wood has always been an important material for construction and furniture production [1]. As a building material, wood offers a series of interesting properties, such as exceptional self-support length, electrical insulation, thermal stability at normal outdoor temperatures, sound absorption, renewability, biodegradability, and aesthetical fascination. Besides, during the last very few decades, the industrial interest in wood has been boosted by ecological concern and consequently enhanced attention towards environmentally friendly materials [2]. Wood and wood-based composite materials such as particle-boards or laminates are being machined in large and increasing volumes in many countries for building construction and decorative purposes [3]. The EU's wood-based industries cover a range of downstream activities, including woodworking industries, large parts of the furniture industry and construction. Before the Covid-pandemic explosion, almost 400k enterprises were active in wood-based industries across the EU, representing almost 20% of the total manufacturing enterprises across the EU, mostly small and medium-sized enterprises (source www.eurostat.com). The turnover of the wood industry in the European Union at the beginning of the decade exceeded 120 billion euros, with a total amount of wood processed in the EU of nearly 5×10^{8} m^3 [4]. The wood-based industries employed over 3 million people across the EU in 2018, more than 10 % of the total manufacturing industries. Of these, there were more than 900 000 persons employed within both the manufacture of wood and wood products and the manufacture of furniture, about 3% of the manufacturing total. The Italian furniture tradition is grounded in the Renaissance period, which exploded in the Republique of Florence and then diffused in Rome and the big cities in the north, primarily Milan and Venice. Then, the development of industrialized cities during the industrial revolutions in the 17th and 19th century favored the modern uneven distribution of the wood industry in Italy, with the regions of Lombardia, Veneto and Friuli-Venezia Giulia covering about two-thirds of the total number of enterprises and turnover. Nowadays Italy is the second

and sixth exporter of wood-based finished products across the EU and globally, respectively, with most of the exportations and revenue being related to the furniture [5] (see **Figure 1** and **Table 1**).

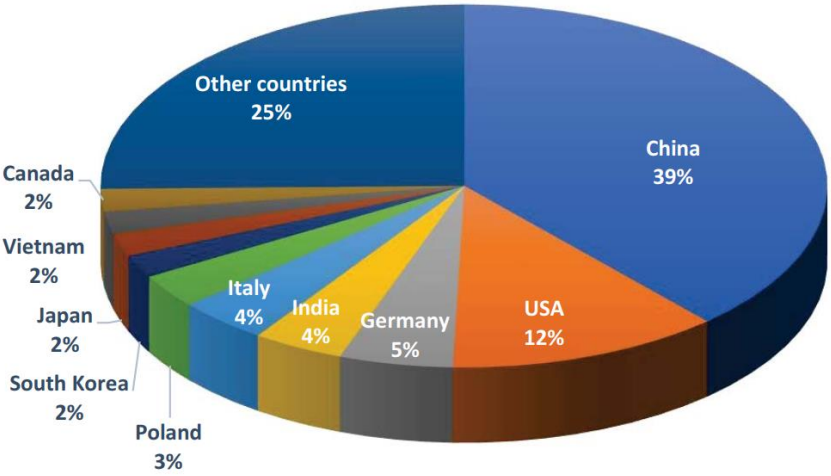

***Figure 1**: Worldwide share of furniture production (from*[6]*)*

The popularity of Italian furniture lies in the fact that the Italian furniture industry is recognized at the forefront for what regards product design, aesthetics, and craftsmanship quality. More than 50% of the furniture produced in Italy is exported, with some of the major market scenarios for Italian furniture including France, Germany, the United States, and Canada.

***Table 1**: The numbers of the wood industry in the European Union and Italy (source Eurostat, 2020)*

	WOOD INDUSTRY EUROPE (€)	WOOD INDUSTRY ITALY (€)	FURNITURE INDUSTRY EUROPE (€)	FURNITURE INDUSTRY ITALY (€)
ENTERPRISES	> 170 K	≤ 75 K	≤ 130 K	> 18K
EMPLOYEES	≤ 1 M	≤ 170 K	≤ 1 M	≤ 130K
TURNOVER	> 130 B	≤ 14 B	> 96 B	≥ 23 B

1.1.2 CUTTING TOOLS IN THE MANUFACTURING INDUSTRY

Cutting tools are commonly used, not only in industrial applications but also in our everyday life. Generally speaking, a cutting tool is an instrument through which some excess material is removed from the workpiece body through machining processes including, but not limited to, drilling, milling, and turning [7]. These processes aim to provide the workpiece with a new shape and geometry, which results in novel functional or aesthetical characteristics [8]. Industrial tools are employed in the processing of metals, alloys, and wood-based materials in many industries, such as construction, energy, power generation, automotive, aerospace and military. By 2022, the global market size of cutting tools is estimated at around 25 billion US dollars and following the post-Covid-19 industrial reprise, it is foreseen that by the end of 2030, the worldwide market size of cutting tools will reach 31-35 billion dollars, with an annual-growth exceeding 6% (data source report from *www.marketwatch.com*).

Because of the severe processing conditions faced during machining processes, cutting tools are subjected to severe wear phenomena, consisting of the progressive loss of their geometrical, structural, and mechanical features. Wear is a result of complicated physical, chemical, and thermomechanical phenomena and is not uniquely defined. In fact, a variety of wear modalities have been identified, whose relative importance depends on both the tool and the workpiece materials involved in a machining process [9]–[15]. Because of wear, tools must be replaced to maintain the desired characteristics in the final product. Typical immediate effects of machining with worn tools are a loss of surface finishing in the workpiece [13] and the increase of cutting forces and power consumption [16]–[18]. Practically, the impact of tool wear and replacement is the loss of line productivity due to downtimes, and hence the increased cost-per-part. In modern manufacturing industries, especially in those involved in the production of high-performance components such as the automotive, military or aerospace industries, the total cost associated with machining tools represents a significant percentage, up to 15-20%, of the total manufacturing costs [19]. This is primarily due to the reduction in the production rate, owning to the downtime for parts replacement, and to a minor extent to the cost-per-part associated with the cutting tools themselves [19], [20]. Simultaneously, there is a steady increase in the commercial request for manufactured products owning to

the fast economic development of countries like China and India in the last decades (www.weforum.org). Therefore, there is a constant need to increase the active time and performance of manufacturing processes to meet these requirements. From a technological perspective, this is pursued by following two parallel directions, involving the materials selection and processing methods for cutting tools materials and the development of coating technologies for increased wear protection.

1.1.3 CUTTING TOOL MATERIALS

There are many parameters able to affect the cutting performance of cutting tools, such as cutting speed, feed rate, depth of cut, lubrication regimen, tool geometry, and when it is the case, the properties of the coating system used [21]. Therefore, the effectiveness of cutting tools relies on a series of specific properties [7], [22]. First, to achieve successful machining, cutting tools must be mechanically harder than the material to be machined. But hardness is not the only property of relevance, as soft materials such as wood-based materials are not necessarily easy to cut [8]. Of primary importance are also thermal properties such as high-temperature stability and thermal shock resistance, chemical inertness, high fracture toughness and low deformability, and high wear resistance [22]. In modern manufacturing industries, three classes of materials are used to produce cutting tools [23]: high-speed steel (HSS)[24], cemented carbides (also called hard metals) [20], [25]–[27] and, more recently, ceramic cutting tools [2], [22], [28]–[31]. Super hard coatings such as polycrystalline Cubic Boron Nitride (p-CBN) and Diamond are also commercialized, but due to their high costs only cover a limited share of the market [32], therefore these will not be discussed further.

1.1.3.1 HIGH-SPEED STEELS (HSS) TOOLS

High-speed steels are the oldest of the three classes of materials currently employed for the manufacture of cutting tools. HSS can be used to machine metal and alloy workpieces at a higher processing speed than other kinds of tool steels [33]. While there exist several classes of HSS [7], [24], they have in common the fact of being martensitic steels with high carbon contents, up to nearly 2%wt. and a variable but usually high amount (4-10%wt.) of hard carbide -forming elements such as Chromium (Cr), Vanadium

(V), Tungsten (W), and Molybdenum (Mo) [34]–[36]. The purpose of such carbide-forming elements is to provide high volume fractions of carbides (see **Figure 2** for an example) yielding relatively high mechanical hardness up to about 900 HV [37], sufficient to machine common metals and soft alloys, and improved wear resistance [38]. HSS is the cheapest among all modern cutting tool materials classes, generally overwhelmed by cemented carbide tools, but still covers nearly 20% of the total worldwide market share [32], [39].

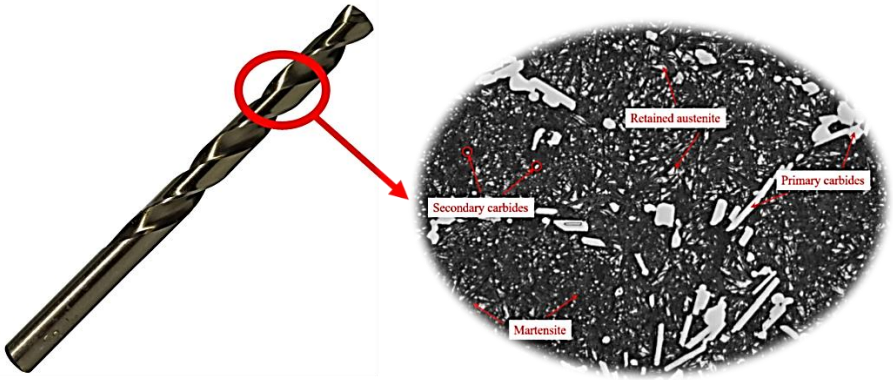

***Figure 2**: An M42 HSS drill tool with a typical microstructure of the same type of HSS steel shown by SEM micrograph. In the micrograph, steel phases and carbide formations are indicated (SEM micrograph from* [40]*)*

1.1.3.2 CEMENTED CARBIDE TOOLS

The first cemented carbide composed of Tungsten carbide and cobalt (WC-Co) was introduced into the global market by the German company *Friedrich Krupp* under the suggestive commercial name of WIDIA, an acronym for the German words "WIe DIAmant", meaning "like diamond" [26]. Due to their outstanding mechanical thermo-mechanical properties, cemented carbides' popularity rapidly grew to such a point to substitute HSS steels in many applications, especially in machining very hard alloys. Cemented carbides consist of sintered compounds in which a metal binder, usually Co but also Ni or Fe [41]–[45], consisting 5-15% of the total material weight, embeds micron and sub-micro sized Tungsten carbide grains (95-85%wt.)[46]. Depending on the relevant amount of soft binder and hard carbide phases, as well as on the microstructure [26], cemented carbide tools exist in several grades (**Figure 3**) offering a wide range of hardness and toughness flexibility [25]. At the cost of higher manufacturing and selling prices, in general, cemented carbide tools offer improved machining capabilities than

HSS tools, in terms of increased hardness (from 800 HV up to 2000 HV depending on composition, grade and microstructure) [26], [46], cutting speed (up to a few hundreds of m min^{-1} for softer Al-alloys and down to a few tens of m min^{-1} for harder Ti-alloys, versus the low cutting speed of a few tens of m min^{-1} for HSS), wear resistance, superior chemical stability and high-temperature mechanical properties [7], [25]. The great performance-to-cost ratio of cemented carbide tools has permitted such tools to cover up to nearly 80% of the total cutting tools market worldwide [21], [32].

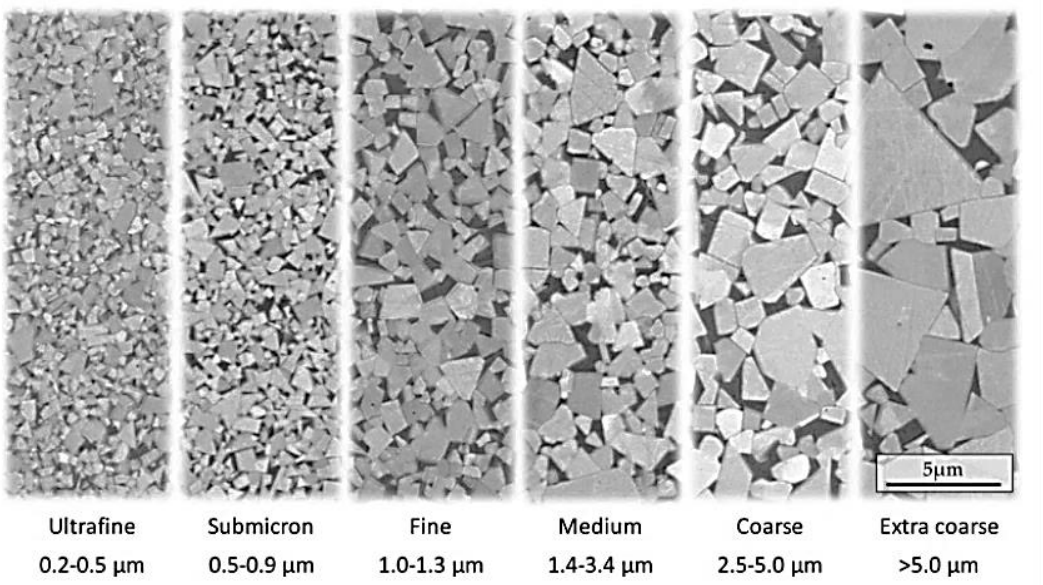

***Figure 3**: Classification of WC-Co cemented carbides based on the size of carbide grains. Image from* [26]*, property of Sandvik Coromant R&D.*

1.1.3.3 CERAMIC TOOLS

Cobalt and Tungsten, the main elements constituting cemented carbide tools, fall within the category of Critical Resource Materials (CRM), which are those rare metals whose extraction and provisions constitute an ethical, health and economical concern [20], [47]. This, along with their massive usage for tool forming, has stimulated the research of alternate materials with suitable properties to substitute, whenever possible, the usage of cemented carbides. This has led to the development of ceramic cutting tools. The main characteristics of ceramic materials are outstanding chemical inertness, retention of very high hardness at high cutting temperatures and superior thermal resistance. For these reasons, ceramic tools have found applications principally in processing very hard materials such as cast irons and superalloys [32]. The two main classes of ceramics are

silicon nitride (Si_3N_4) [48]–[51] and Aluminium Oxide (Al_2O_3) [28], [49], [52]. Ceramic tools based on Al_2O_3 are the most chemically inert and hard ceramic materials. Usually, about 10% of ZrO_2 is added to improve the toughness of the otherwise very brittle Al_2O_3 [53]. In other cases, Al_2O_3 is enriched with nanoparticles or whiskers of carbides or nitrides such as SiC, TiC or TiN for improved abrasion and thermal shock resistance [22], [54], [55]. Ceramic cutting tools based on Silicon Nitride include pure Si_3N_4 tools and SiAlON, a ceramic alloy consisting of an amorphous Si_3N_4 matrix embedding grain of hard Al_2O_3 [22], [32], [56]. SIALON cutting tools (**Figure 4**) provide a combination of the properties of Si_3N_4 and Al_2O_3. In comparison with Al_2O_3-based composite tools, Si_3N_4-based tools have superior fracture toughness, crack resistance and thermal shock resistance [22], [31], [32]. This last property makes them very useful in high-speed intermittent cutting operations, where intense thermal cycles impart severe thermal stresses on the tool. Si_3N_4-based tools retain hot hardness at temperatures higher than those suitable for cemented carbides, and are tougher than Al_2O_3-based ceramics, resulting in more reliable and all-purpose cutting tool materials [22], [32]. Nowadays, the market share of ceramic tools is about 8-10% of the total cutting tools sold worldwide [32], [57].

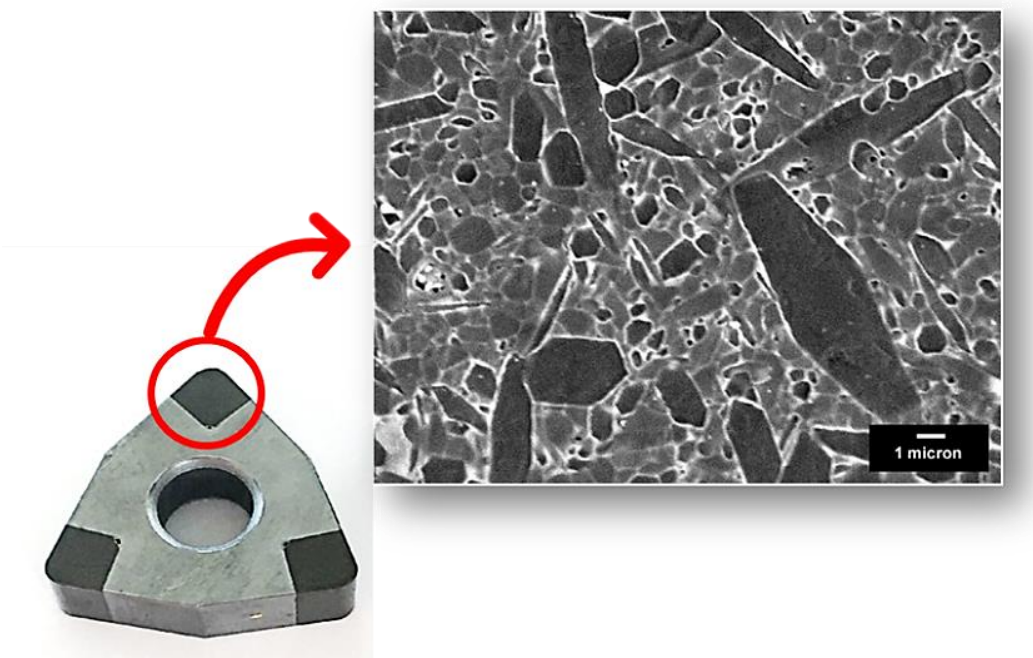

***Figure 4**: Left, a turning tool with SIALON inserts. Right, SEM micrograph of the microstructure of SIALON tool following the preferential chemical etching of Al_2O_3 (readapted from (*[56]*)*

1.1.4 HARD COATINGS FOR CUTTING TOOLS

As a general trend, the request for high-performance tools increases constantly in the attempt to pursue increased productivity and sustainability of machining processes. Such demands include the use of minimum quantity lubrication and conversion towards dry-machining driven by ethical and health concerns, but also the use of higher cutting speeds [57]. Because of the combination of these factors, cutting temperatures are expected to increase, and this can significantly impact the service time of cutting tools. An increase in tools lifetime is nonetheless needed to improve productivity and product quality, while also decreasing the usage of lubricants due to health and environmental concerns [58]–[60]. This goal can be partly achieved by optimizing tool geometries and machining parameters, or by tailoring the intrinsic properties of the tool material for the specific applications. Unfortunately, the design of cutting tools materials can be only slightly modified to meet the complex array of necessary and often competing properties. For instance, the tool has to be both ductile to prevent fracture and hard to decrease tool wear [61]. A way to bypass such limitation consists in covering the tools cutting surfaces with hard and refractory coatings materials. Hard coatings are thin films a few microns thick that are deposited on tool substrates through chemical vapour deposition (CVD) or physical vapour deposition (PVD) techniques [62]–[65]. CVD films are produced by pumping gas-phase precursors in the desired proportions inside the deposition chamber. The precursor molecules are made to react at the substrate site by thermal or plasma-aided activation. The reaction process occurs at a substrate temperature range from 300 up to 900 ◦C, depending on the precursors and the specific CVD apparatus (thermal or plasma-enhanced). CVD coatings are characterized by high adhesion and structural homogeneity, but the use of relatively high process temperature restricts the coupling of materials due to the different thermal responses and expansion coefficients. PVD consists of different methods, such as evaporation, cathodic evaporation (also called arc-plating) sputtering techniques and molecular beam epitaxy (MBE). Among these methods, DC (direct current) magnetron sputtering is the most used technique for cutting tools coatings. In PVD deposition materials are deposited in form of films by evaporating, under different conditions, a source solid material which is then recondensed on the substrate to form the

coating. PVD processes typically operate at lower temperatures than CVD processes (usually under 500 ◦C), allow the deposition of thinner coatings and higher versatility for the deposited materials [21].

The focus on coatings development is on providing the tool with additional wear protection against abrasion and high-temperature oxidation/corrosion. Besides, high fracture toughness is required to withstand the high thermo-mechanical loads in typical cutting processes. In the attempt to pursue these goals, a large variety of coatings materials have been studied, developed and commercialized since the introduction of the first CVD coating, TiC, and PVD coating, TiN, in 1969 and 1980, respectively [57]. Of these, the most commercially diffused are PVD coatings such as CrN [66]–[70], TiAlN [71]–[74] and CrAlN [69], [75]–[78] and also CVD ceramic coatings such as TiCN [79]–[82], Al_2O_3 [69] and Diamond-like-Carbon (DLC) coatings[83]–[87]. TiAlN is currently acknowledged as the gold standard among general-purpose coating materials, thanks to its high-temperature hardness and oxidation resistance [75], [88]–[90]. Nonetheless, Cr-based coatings such as CrN and CrAlN are preferred on Ti-based coatings in applications where oxidation and corrosion constitute the primary source of tools wear [91]. Among binary coatings, CrN is the reference material for corrosion protection. Due to such good protective properties as well as to its fabrication ease and the lower amount of source material against multi-component nitrides, CrN is one of the very few materials which have been proposed as coatings for tools targeting the manufacturing processing of wood-based materials. Nonetheless, due to its relatively low mechanical properties, especially a relatively low hardness of about 18-20 GPa, CrN is susceptible to abrasive wear. A strategy to compensate for this issue consists in coupling CrN with other, harder materials in multilayer coatings architectures.

1.1.5 MULTILAYER AND NANOSTRUCTURED COATINGS

Despite being effective in providing cutting tools with longer service times, it was soon realized that the improvement possibilities offered by monolithic coatings were soon destined to be exhausted. Besides, an individual material can hardly meet the complex ensemble of required properties, as these are often mutually exclusive, as previously mentioned. Covalent, extremely hard, and inert Al_2O_3, DLC and CBN coatings, for

instance, suffer from low fracture toughness, which is important in preventing crack propagation within the coatings. On the contrary, tough materials such as ZrN usually suffer from lower hardness and chemical inertness. The spectrum of properties of protective coatings can be much improved if more complex coatings designs are employed (**Figure 5**). These include bilayer, multilayer, gradient, composite and nanolayered (or nanolaminate) coatings [21], [61]. In particular, multilayered and nanolaminate coatings have attracted much attention due to the possibility to disentangle opposing materials properties among the constituents of the coating, providing a synergistic improvement of the overall protective characteristics [92].

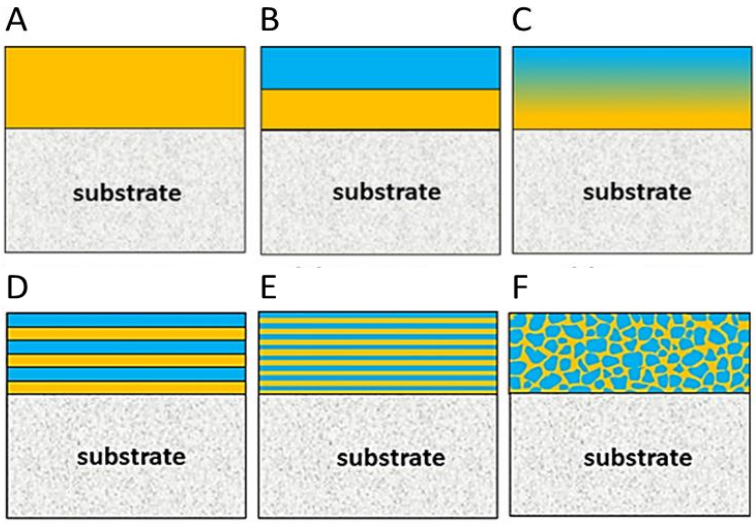

Figure 5*: Architecture designs of cutting tools coatings: A) Monolithic, (B) Bilayer, (C) Gradient, (D) Multilayer, (E) Nanolaminate and (F) Composite. Image readapted from* [61].

In the literature, the effectiveness of many multilayer and nanolaminate coatings is widely reported and reviewed [57], [93]–[101]. In general, the design of multilayer coatings follows some fundamental criteria [102], [103]. First, adjoined materials should be chemically, structurally, and thermo-mechanically compatible. It is paramount that the adhesion among the coating's constituents and between coating and substrate is sufficiently good enough to withstand the severe thermomechanical stresses during the machining processes. This requires a good interdiffusion at the interfaces among the various materials, and the compliance of each layer to the structural alterations of the neighboring layers following thermal expansion and mechanical deformations. If these requirements are not fulfilled, interlayer detachment can occur at some point across the

multilayer structure, with the consequent delamination of the coating. It is commonly accepted that the multilayer architectures help prevent the longitudinal propagation of cracks from the surface, where they originate, down to the substrate through interfacial crack-deflection mechanisms [79], [97], [104]–[107]. It is argued that the occurrence of anisotropies in the stress fields deriving from the multilayer architecture impedes the propagations of cracks and dislocations across the interfaces. This results in the retardation of the coating failure, with defects extending laterally across the coating interfaces, preserving the underlying tool material (**Figure 6**).

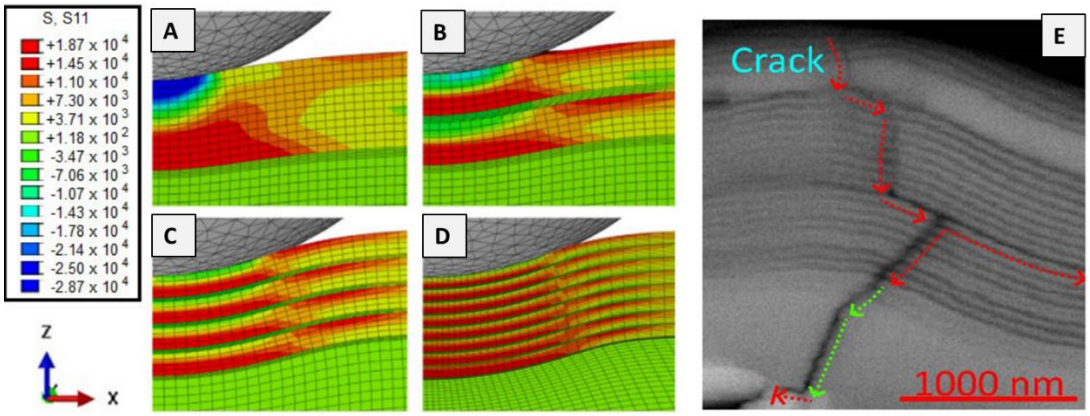

***Figure 6**: From A to D, simulation of the stress distribution across multilayer coatings with differently thick constituent layers, with compressive stresses increasing in the blue direction and tensile stresses in the red direction (from* [79]*); in (E), the TEM cross-sectional observation of cracks retardation through interface deflection (from* [107]*)*

For enhanced toughness, hard ceramics coatings have been coupled to metallic single- and multilayers in duplex multilayer systems [79], [95]. The higher coating density and better endurance to mechanical deformation and crack propagation have recently been reported as crucial factors for the production of super hard multilayer coatings, starting from materials with lower specific hardness values [108]–[111]. Another major benefit arising from the multilayer architecture is enhanced corrosion resistance. This is mainly attributed to two factors. First, the possibility to include a corrosion-resistant material usually containing Cr or Al to form passivating Cr_2O_3 and Al_2O_3 layers [78], [112], [113]. Second, multilayer coatings are usually denser, more compact, and finer grained than monolithic coatings. Besides, the abrupt composition gradients at the interfaces provide higher resistance to the diffusion of electrochemically active species across the numerous interfaces, this slowing down the electrochemical conversion and dissolution of metallic species into the surrounding environment [114]–[117].

1.2 MACHINING OF WOOD-BASED MATERIALS

1.2.1 WOOD: A TROUBLESOME WORK-MATERIAL

In Countries with a solid history of crafting wood-based products of value, the quality of finished products is paramount to keep the high-quality standards. This requires a high machining precision of workpieces. Unfortunately, and somewhat counterintuitively, machining wood-based materials (an example of which is illustrated in **Figure 7**) is not a simple task. Wood-based materials present a very harsh cutting environment. The inclusion of hard mineral particles [15], [118] and acidic extractives [3], [119] results in high abrasive and corrosive wear rates for both HSS and cemented carbide tools, resulting in tools lifetimes of a few tens of minutes depending on the cutting conditions [120]. The high structural and mechanical anisotropy of wood [1], [121], [122] has strongly limited the use of brittle ceramic tools, due to the abrupt and inhomogeneous variations of mechanical and chemical conditions encountered while cutting through the cellular structure of wood-based materials [1], [121], [123], [124]. Also, localized high temperatures of a few hundred degrees are developed at the cutting interface [125]. Besides, due to its porous and hydrophilic nature, wood cannot be cooled by refrigerant fluids and is usually dry-cut [126].

***Figure 7**: Wood drilling with a cemented carbide tool.*

1.2.2 WEAR SOURCES IN WOOD-CUTTING

The main wear mechanism in wood machining are abrasive and corrosive/erosive wear [18], [127]. Abrasive wear is particularly important when machining secondary wood-based products coming from recycled wood or wood-based compounds. In such materials, residual metallic or mineral hard particles heterogeneously distributed across the workpiece volume can impart severe mechanical damage to the cutting tool. Corrosive wear is due to both intrinsic and extrinsic organic constituents [3], [119], [128]–[130]. Intrinsic constituents include natural acids such as tannic acid or acid-precursor molecules such as tannins [119]. Extrinsic substances are organic binders, glues and additives which derive from previous material processes [129]. The formation of brittle oxidation products facilitates the removal of tool material by mechanical action, leading to facile erosion of the tool surface [127]. Also, the different levels of moisture determine the stiffness of the wood-based material, therefore influencing the mechanical response and stress exertion on the cutting tool [122]. The effect of the simultaneous abrasive-corrosive wear is particularly dramatic in wood machining. It affects both cemented carbides and HSS tools. Industrially, wood cutting tools are mostly constituted of cemented carbide tools, as HSS suffer from severe abrasive erosion in presence of hard mineral particles. The erosion of cemented carbide tools starts with the galvanic corrosion of the metal binder, which results in a progressively lower binding of the hard carbides, which are more easily detached from the tool [131]–[133]. The substitution of Co binder with Ni and Ni Cr biner somewhat reduces the corrosion rate but also results in lower wettability of the WC grains [133]. Along with optimizing the chemical composition and microstructure of cemented carbide tools, CVD or PVD hard and refractory thin-film coatings have been used to mitigate wear phenomena and improving the cutting performances. That said, besides materials properties, machining conditions for wood-cutting pose very strict requirements such as very high working speed [134] and use of extremely sharp tool edges [18], [135]. The requirement of sharp tool edges poses severe limitations on the protection of cutting tools utilizing coatings. The reason for this requirement lies in the fibrous and elastic nature of wood. If the cutting edge is rounded at edge curvature radii of just a few tens of microns, the tool starts tearing and misplacing wood fibers rather than cutting through them. This enhances the elastic recovery of the wood which results in the enhancement

of power consumption and tool deterioration which ultimately requires the substitution of the tools [14], [136].

1.2.3 COATINGS FOR WEAR MITIGATION IN WOOD MACHINING: STATE OF ART

The cutting of wood and wood-based materials is a complex process, owning to the characteristics of wood, including anisotropy in density and mechanical resistance, the inclusion of hard mineral particles, variable moisture contents and the inclusion of extractives. Further complications include the use of high cutting speeds (tens to a few hundred m s^{-1}) and the need for very sharp cutting edges and sharp cutting angles. In wood-machining, cemented carbide cutting tools have overwhelmed High-Speed Steel tools, as the latter easily get worn out, resulting in quick deterioration of productivity, increased energy expenses, and a lower quality of the processed pieces. As of 2022, a limited number of research works report on the possible feasibility of ceramic tools in wood-machining [2], [28], [52].

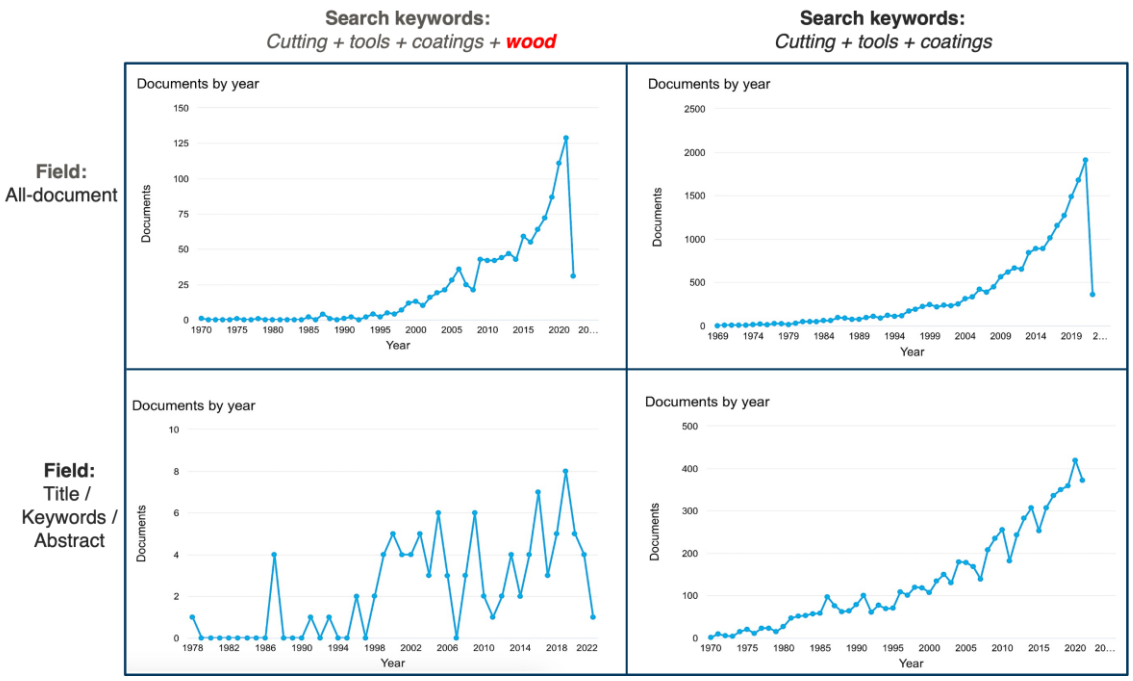

***Figure 8**: Scopus-based search results differences between the annual total research work on cutting tools and coatings and the limited output of research specifically targeting the machining of wood-based materials.*

The application of coated tools has been much delayed in the wood-working industry if compared to the metal-working industry [109]. Due to the very harsh cutting environment [123], [127], [137] and the strict machining technical requirements [124], [135], the cost-to-benefit ratio is still insufficient to compensate for the additional costs associated with the coating process (personal information).

Chromium nitride-based coatings represent an exception to some extent and therefore have been investigated as tools coatings in machining different types of woods [130], [135], [138]–[142]. The orientation towards CrN and Cr-based coatings for wood machining is due to the low material cost and a generally good combination of hardness, high-temperature oxidation resistance and corrosion resistance. Besides, several research works regarding the development of Cr-based multilayer coatings for wood machining have been reported [104], [118], [124], [138], [143].

Nonetheless, the volume of research works targeting specifically the problems of wood-machining is very limited, especially compared to the output of research papers and patents in the metal-working industry (**Figure 8**).

2 EXPERIMENTAL METHODS

2.1 PRELIMINARY CONSIDERATIONS

The purpose of this chapter is to provide an overview of the experimental techniques used in the development of the present research work. In each section, the basic concepts regarding the specific technique and its use in coatings characterization are summarized. The chapter is organized as follows. It opens with an introduction to the Magnetron Sputtering deposition technique, which is the PVD method used to make all the coatings samples used in this research work. Next, an introduction to structural characterization with X-Ray Diffraction is provided, followed by an introduction to Scanning Electron Microscopy, with brief descriptions of the main imaging modes, the factors affecting the image resolution and the implementation of Focused ion Beam tools for depth imaging. A shorter introduction to Atomic Force Microscopy and X-Ray Photoelectron spectroscopy is then presented. The last two sections deal with indentation and electrochemical methods of linear polarization and impedance spectroscopy, which have been used to characterize the mechanical and electrochemical properties of multilayer coating systems. The description of relevant processes and techniques is limited to such an extent to show how the samples are fabricated and treated, and the analytical procedures followed to gather and/or analyze the data.

2.2 COATINGS DEPOSITION VIA DC MAGNETRON SPUTTERING

2.2.1 INTRODUCTION TO THE SPUTTERING PROCESS

Among the Physical Vapor Deposition (PVD) techniques, plasma sputtering is probably the most known and widely used, both in academia and in multiple industrial fields. Its success is primarily due to its high versatility in terms of available source materials and to the high coatings' quality in terms of conformity, density and low defect density compared to other methods such as evaporation, arc plating or laser ablation. It is used to deposit functional coatings for many applications, including but not limited to biomedical, decorative, and anti-wear coatings.

A typical sputtering apparatus basically consists of a source material and a deposition substrate, respectively working as the cathode and anode of a discharge unit, a vacuum chamber connected to a series of vacuum pumps and a gas injection system used to inject both sputtering gases (commonly Ar, less commonly Kr or Xe) and reactive gases such as Oxygen, Nitrogen, or acetylene. Sputtering is a plasma-based technique, whose working principle is depicted in **Figure 9**. By applying an electromagnetic field between the cathode and the anode, the low-pressure (typically 10^{-4} – 10^{-3} millibar) gas is ionized, thus creating a plasma. Positive ions are then accelerated towards the cathode (also called the target) from which atomized particles are mechanically ejected along with secondary electrons. The ejected particles are then deposited on the anodic surface and form the film, while secondary electrons mainly serve to sustain the plasma [144].

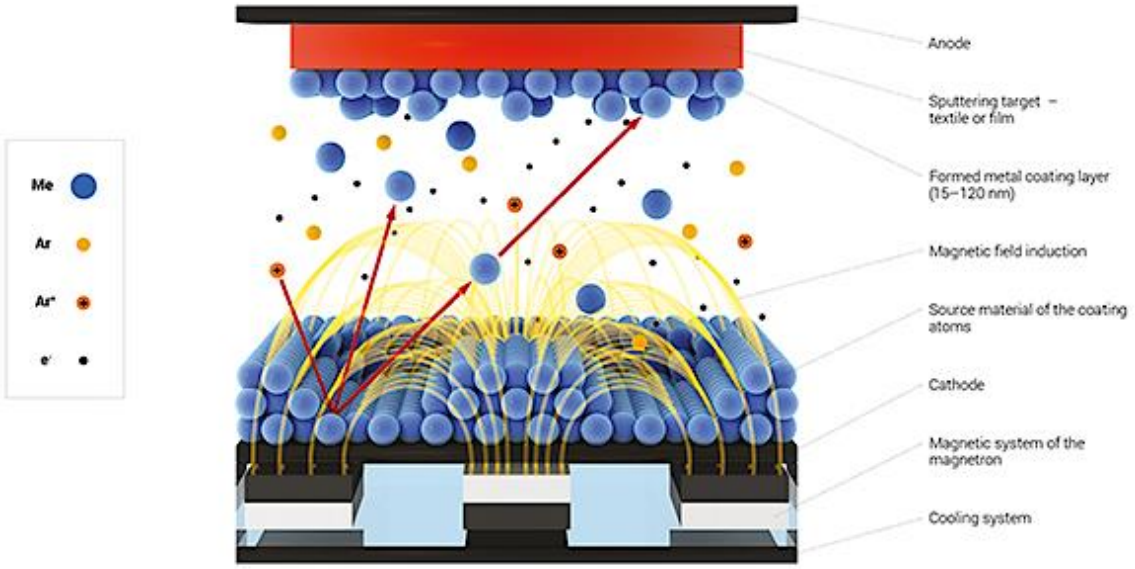

***Figure 9**: Schematics of a magnetron sputtering system (image from www.visual-science.com)*

The deposition occurs in non-equilibrium conditions, meaning that the properties of the deposited coatings are kinetically and not thermodynamically determined [145]–[147]. The kinetic control of the sputtering processes is actuated by tailoring many process parameters such as the substrate-to-target distance, the input target power density (TPD, the input power divided by the target active surface), the working pressure (WP) as well as the substrate temperature and bias.

2.2.2 SPUTTERING MODES

Conventional sputtering systems produced after the 70ies include a permanent magnetic system called magnetron [148]. The purpose of the magnetron is to generate a magnetic field parallel to the target surface which can confine the secondary electrons within the plasma in the vicinity of the target surface [148]. This allows a remarkable increase in the density of ions in the proximity of the target and a consequent enhancement of the sputtering rate without the need of using high gas pressures. This permits to reach suitable deposition rates while keeping the chamber pressure up to two orders of magnitude lower than in older sputtering systems. The configuration of the magnetic systems permits some further classification. If the magnets are symmetrically balanced, the magnetic field is confined in the proximity (5-6 cm) of the target surface. This system configuration, called Balanced Magnetron Sputtering (**Figure 10-A)**, is the oldest configuration of modern sputtering systems and the one with poorer performances in terms of plasma density and ion flux to the substrate. If the magnets are not symmetrically balanced, some of the magnetic field lines can extend further toward the substrate. This is called Unbalanced Magnetron Sputtering and is usually adopted to increase the ion flux to the substrate, improving film density and deposition rate (**Figure 10-B**).

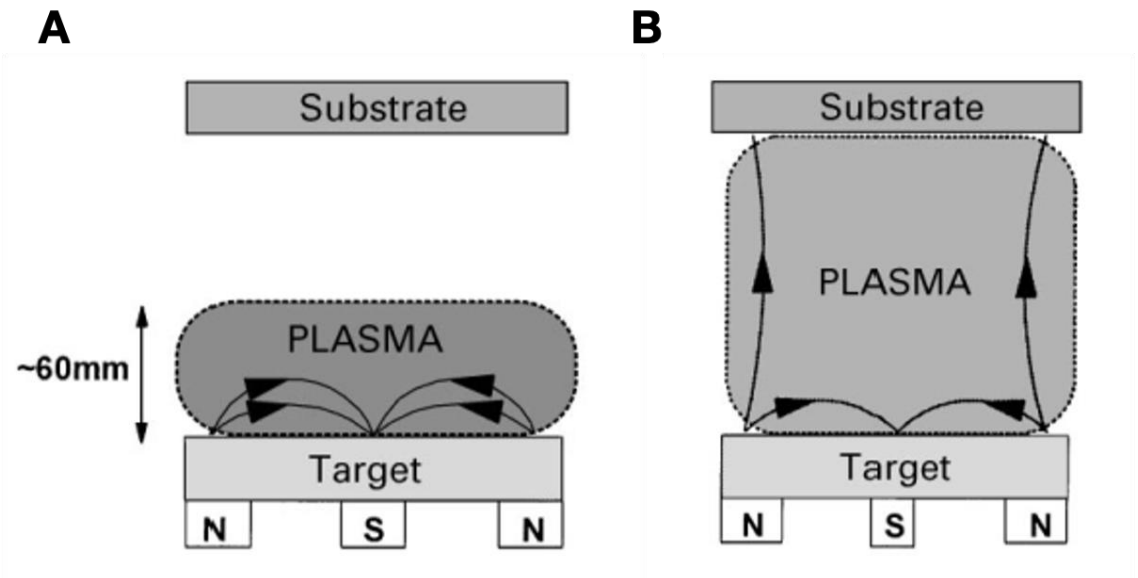

Figure 10*: A) Closed-field magnetron Sputtering and B) Open-field unbalanced Magnetron Sputtering (from* [148]*)*

Originally, sputtering systems were run in DC or RF (at 13.65 MHz) mode. The former was originally used to deposit metals [149], which did not suffer from charging issues due to the interaction with the positive ions. RF sputtering was introduced to sputter insulating target materials.

With DC Sputtering, insulating targets tend to charge over time. This is detrimental for two reasons, target charging and arcing [150]. The problem of target charging lies in a dramatic decrease in the sputtering rate because of the establishment of a counter-acting electric field that extinguishes the target sheath and prevents further sputtering events. Secondly, and most importantly, charge accumulation leads to the generation of cathodic arc discharges, and collective and abrupt emissions of electrons from the target surface which can ruin the target material and even damage the chamber system[151]. The problems concerning arc discharges and the low deposition rate are also very common in reactive sputtering of metal targets [152]. In such a process, a reactive gas is introduced into the chamber along with the sputtering gas. When the plasma is ignited, such gas molecules are activated and react with the particles ejected from the target surface to deposit compounds such as oxides, nitrides, and carbides. During the process, the surface of the target can be progressively covered with insulating layers, a process called *target poisoning*. These insulated areas can accumulate charge from the input power source and lead to arc discharges.

RF sputtering was used to deposit coatings from insulating targets. It typically uses lower input powers and has an effective sputtering time which is one-half of the total time (RF), as the positive ions are attracted towards the target in the negative branch while the positive branch of the RF input wave is sed to neutralize the positive charges with the plasma electrons. The resulting low deposition rate and high machinery cost limited its diffusion, especially outside academia, where reactive sputtering using metallic targets has been preferred over using compound targets in RF mode [148]. In the mid of the 90ies, a novel sputtering mode called High-Power Impulse Magnetron Sputtering (HiPIMS) emerged as an alternative to RF sputtering and has shown major improvements also concerning DC Magnetron Sputtering in terms of coatings properties and process control [153]–[155]. In HiPIMS a pulsed high TPD input of many hundreds of W cm^{-2} with a frequency usually between 20 and 100 kHz is used in place of conventional DC powering, which uses TPD of at most a few tens of W cm^{-2} to prevent target overheating

[154]. The high TPD promotes the ionization of gas species, forming extremely dense plasma with very high-energy ions and electrons. Besides, the extremely high power and short pulses prevent the poisoning of the target surface in reactive sputtering processes. During the off time, a low inverse polarization is applied to the target to neutralize the positive charge delivered by argon ions. This prevents target charging and the consequences of arcing. For the development of this research, a conventional close-field DC Magnetron Sputtering system was used, therefore no further insights into more recent advances in HiPIMS technologies are provided.

2.2.3 DEPOSITION RATE IN DC-MS

The properties of sputtered coatings depend strongly on the energetics f the process involved. In DC Magnetron Sputtering (DCMS), the deposition rate R is proportional to the target erosion rate Φ is defined as the amount of material that is deposited on the substrate per time unit. It depends on the flux of ions to the target, the target current J_T and the ability of such ions to eject particles from the target, a quantity which is called the gas ion sputtering yield Y_{Ar+}. Therefore the erosion rate Φ is approximately [153]:

$$\Phi \cong J_T * Y_{Ar+} \qquad (2\text{-}1)$$

The sputtering yield increases with the Ar ion energy E_{Ar+} following a power law $Y_{Ar+} \propto (E_{Ar+})^m$, with m<1. The ion energy in turn is proportional to the electrostatic field established by the voltage drop V_T between the cathode and the plasma within the region called target sheath [144], [150] so that $E_{Ar+} = q * e * V_T$ with e the elementary charge and q an integer number indicating the oxidation state of the impinging ion). Therefore, the dependence of the deposition rate R on the plasma characteristics can be approximated as:

$$R \propto \Phi \cong J_{Ar+} * Y_{Ar+} \approx J_{Ar+} * (qeV_T)^m \qquad (2\text{-}2)$$

The basic process parameter used to modulate the deposition rate is therefore the input power density, which determines the magnitude of V_T [156], [157]. Another contribution

defining the sputtering deposition rate comes from the chamber pressure. In general, a lower pressure implies lower flight-collisions and lower recombination rates, which ultimately result in an enhanced deposition rate [158].

2.2.4 PROCESS FACTORS AFFECTING THE PROPERTIES OF SPUTTERED COATINGS

Many fundamental and functional properties of sputtered coatings are inherently related to the energetics of the deposition process. This involves many aspects of the sputtering process, from the relative mass of the sputtering gas to the target material [158], the deposition rate and the input of energy employing substrate heating and external substrate bias.

2.2.4.1 RELATIVE GAS-TO-TARGET ATOMIC MASSES

The relative masses of sputtering ions and target atoms determine the efficiency of energy transfer from the ion to the atom [158]. In general, the larger the mass difference, the lower the energy transfer efficiency. This affects the energy retained by the sputtered particle during its travel towards the substrate. Besides, due to the lower penetration in heavy elements, sputtered particles from heavier elements are primarily ejected from the very target surface, thus suffering lower collisions with other targets atoms and hence escaping the surface with higher energy [150].

2.2.4.2 SUBSTATE BIAS

In sputtering processes with a negatively biased substrate, the energy delivered to the growing surface is largely constituted by the kinetic energy of impinging positive ions accelerated through the substrate sheath and the flux of reflected neutrals [159], [160] and only marginally on the target power density [161]. In general, biasing the substrate results in a higher adhesion and density of the coatings and impacts the crystallographic growth by favouring low-surface energy directions [162]–[164]. Besides, substrate bias has a strong impact on the mechanical properties of the coatings, due to higher compression imparted by the high energy bombarding ions [163], [165].

2.2.4.3 SUBSTRATE TEMPERATURE

Heating the substrate serves to provide the impinging atoms (adatoms) with additional energy to promote adatom mobility on the growing surface [149], [166], [167]. This also affects the microstructure of the coating, as the higher temperature can unbalance the nucleation-to-growth rate favoring the nucleation phase or the desorption of lighter elements with local structural readjustments, resulting in finer-grained coatings with lower crystallinity [168].

2.3 STRUCTURAL ANALYSIS VIA X-RAY DIFFRACTION (XRD)

2.3.1 A BRIEF INTRODUCTION TO X-RAY DIFFRACTION

Solid state materials, both elemental and compounds, can be arranged into amorphous, polycrystalline, and single-crystalline structures (**Figure 11**). Amorphous materials are isotropic, as constituent atoms do not arrange themselves ordinately. In polycrystalline materials, isotropy is interrupted as a short-to-medium range order, i.e., over distances from a few tens of nanometers up to a few micrometers, is established. Each portion of the material with some spatial coherency is called a crystal grain, whose shape and growth direction vary for each crystal. In single-crystal materials long-range order is established within the whole volume of the material. Such materials show the lowest isotropy as many properties depend strongly on the crystal orientation.

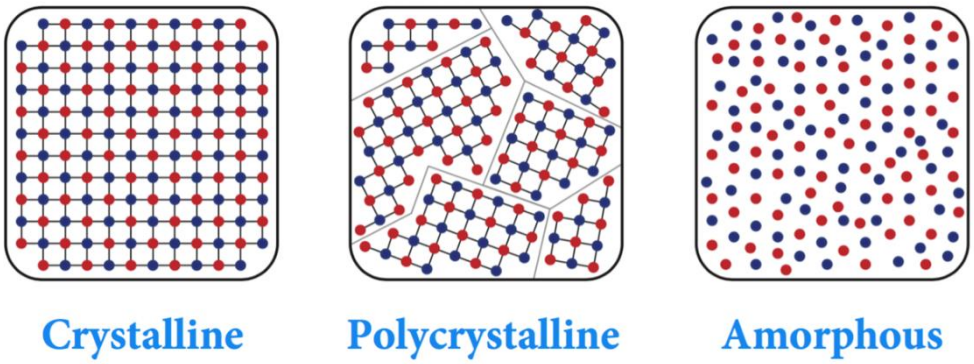

***Figure 11**: Schematic representation of crystalline, polycrystalline, and amorphous materials. In polycrystalline materials, grey lines represent grain boundaries.*

Since its first discoveries at the beginning of the 20th century, thanks to the research activities of Laue and Bragg [169]–[173], X-Ray Diffraction (XRD) has rapidly become

the most important and widespread technique used to characterize the structure of solid materials in many fields of research at both academic and industrial level [174]. Although the main field of application involves metals, steels and alloys [175]–[178], XRD is nowadays commonly employed to study other classes of materials such as ceramics [179], polymers [180] and biological macromolecules [181]. In XRD, a diffraction pattern is generated through the interaction of a monochromatized X-Ray beam with the crystal lattice. The interaction of X-Rays with crystalline solid materials occurs as the x-ray wavelength is comparable with the distances among atoms in a crystal, typically 1-10 Å [182]. In metallurgy and coating technologies, XRD is one of the most important characterization tools, as many properties of these materials are correlated to their crystal structure and the size of the crystal grains. XRD's most known application resides in the phase identification of materials. Qualitative phase identification is achieved by comparing the experimental plot of the diffraction intensity against the diffraction angle with databased data from known structures. Here, each peak is identified through an indexing procedure attributing three numbers known as Miller indexes. Following the indexing, by applying the Bragg law to individual peaks one can derive the lattice plane spacing and lattice parameters [175], [183]. For sake of completion, quantitative phase identification is performed by using an analytical procedure known as Rietveld refinement [184]–[186], which will be no further addressed here. Another common way an XRD diffractogram is used consists of analyzing the peak shape and position in the diffractogram to estimate the size of the crystallite which generates that peak, using Scherrer analysis [187]–[191] and the lattice parameter of the crystal, using Bragg analysis. Finally, another use of XRD, which is particularly useful in the field of coatings is the measurement of the residual stresses [192]. In this chapter, the basic concepts behind the specific use of XRD in the present work will be briefly introduced and the analytical tools used to treat the XRD data will be shown and explained.

2.3.2 CRYSTAL STRUCTURES

The abstract collection of points upon which a physical crystal is built is called a *lattice*. The smallest, repeating unit of a crystal is called a unit cell, which contains all the symmetry properties of the lattice [193]. A crystal is virtually generated by the pure translation of the atoms constituting the unit cell. All possible three-dimensional

arrangements of points in a lattice can be represented by 14 lattices grouped into 7 crystal systems (**Figure 12**) based on the relative length and orientation of the axes which determine the symmetry properties such as translation, reflection and inversion [169], [193], [194]. Most metals and ionic solids crystallize in the cubic system, that is, the systems with the higher symmetry, while metal compounds such as oxides, dichalcogenides, nitrides and carbides tend to crystallize in less isotropic structures such as hexagonal, tetragonal, and monoclinic, reflecting the anisotropic chemical bonds between the constituent elements [195].

Lattice System	Point Group	Primitive	Base-Centered	Body-Centered	Face-Centered
Triclinic	$\bar{1}$	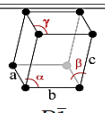 $P\bar{1}$			
Monoclinic	$2/m$	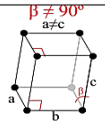 $P2/m$	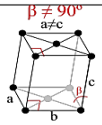 $C2/m$		
Orthorhombic	mmm	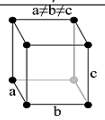 $Pmmm$	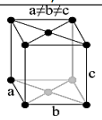 $Cmmm$	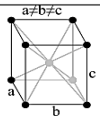 $Immm$	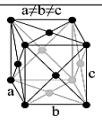 $Fmmm$
Tetragonal	$4/mmm$	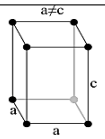 $P4/mmm$		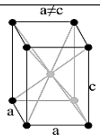 $I4/mmm$	
Rhombohedral	$\bar{3}m$	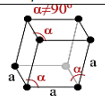 $R\bar{3}m$			
Hexagonal	$6/mmm$	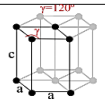 $P6/mmm$			
Cubic	$m\bar{3}m$	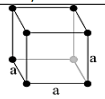 $Pm\bar{3}m$		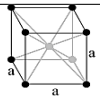 $Im\bar{3}m$	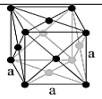 $Fm\bar{3}m$

***Figure 12**: The fourteen crystal lattices are classified according to their lattice system and space group (from* [194]*)*

The crystal phase a material crystallizes into depends on a series of intrinsic factors such as the nature and proportion of the constituent elements, as well as on external factors such as the pressure, the temperature and the speed and mechanisms by which the solid

is produced [195]–[198]. Many properties of materials are correlated to the crystal structure. For instance, depending on the crystallographic directions to which loads are applied to, resistance to plastic deformation or fracture toughness may vary because of the different atomic densities along particular planes and directions [199], [200].

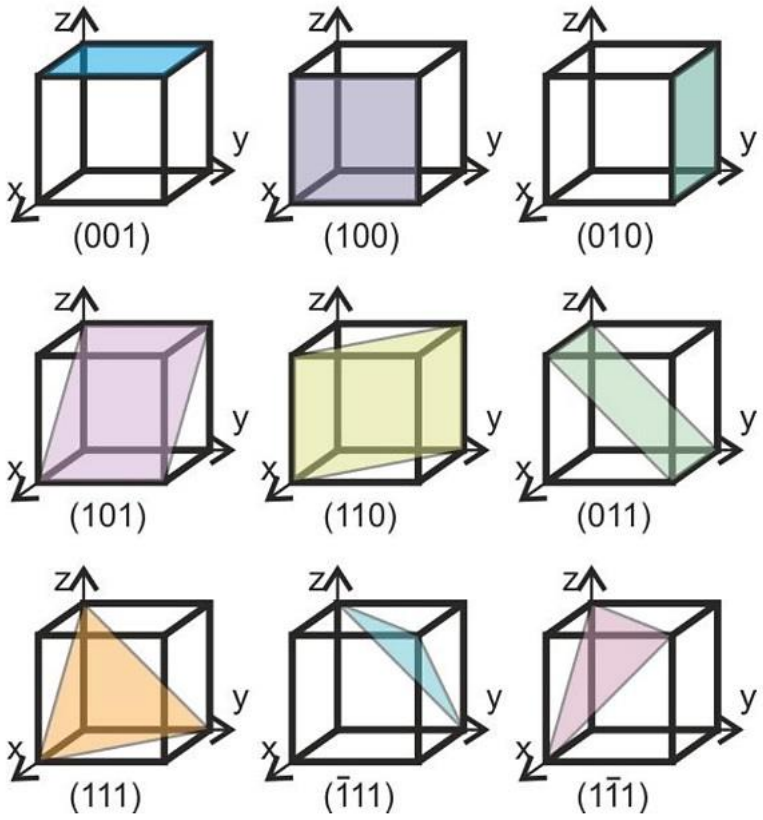

***Figure 13**: Some Crystallographic planes in the unit cell of cubic lattice and the corresponding Miller indices (from* [201]

Each plane in a unit cell is uniquely defined by three numbers, known as Miller indexes, generally represented as the {h, k, l} numbers. The physical interpretation of such indices for a cubic system is straightforward. The cubic unit cell is defined in the real three-dimensional space by three orthogonal axes of coordinates, x, y, and z. The values of {h, k, l} correspond to the reciprocal of the intercept value of the plane with the x, y and z axes of the cell, respectively. Some examples of typical lattice plains for the cubic system are depicted in **Figure 13**. For sake of completion, it is worth mentioning that the set of basis vectors identifying the unit cell, and hence the graphical interpretation of the Miller indices, is more complex for the other crystal systems. More unknown parameters

originating from the lower symmetry need to be addressed and the {h, k, l}values are not directly related to the intercepts on the x, y, and z axes, which is strictly valid only for the cubic symmetry [173], [188].

2.3.3 XRD FUNDAMENTALS: BRAGG LAW AND GENERATION OF A DIFFRACTION PATTERN

Diffraction is a phenomenon consisting in the splitting and deviation of the direction of propagation of a light beam interacting with a grid of apertures (slits) of size comparable with the beam's wavelength, whose extrema act as scattering centers. In a crystal, the grid is represented by the periodic arrangement of atoms, whose relative distance is of a few angstroms and hence can diffract X-Ray radiation [169], [173], [182]. In X-Ray diffraction, the scattering centers are the electron orbiting around the nuclei of localized atoms. The formal description of the criteria that determine the occurrence of a diffraction event from the interaction of an impinging X-Ray beam with material is due to Laue, but a more intuitive description was provided by Bragg in 1912 [170]–[173]. When X-Rays impinge on a crystalline sample each atom acts as a scattering center, and X-Rays are scattered in all directions with constructive or destructive interference leading to diffraction [185]. A diffraction peak occurs only for X-Rays interacting constructively. This requires a long-range three-dimensional array of ordered atoms; therefore, only polycrystalline and crystalline materials can originate diffraction patterns. When a crystal with crystallographic planes identified by generic {h, k, l}Miller indexes and separated by an interplane distance d_{hkl}, interacts with X-Rays of wavelength λ impinging with an angle θ with respect to the sample surface, the condition for constructive interference is that the difference in the optical path is an integer number of wavelengths of the impinging x-ray (**Figure 14**). This condition is expressed by the Bragg law [182], [183]:

$$n\lambda = 2d * sin\vartheta$$

(2-3)

Bragg law imposes a relationship between the angle of incidence of the x-ray beam and the interplanar distance which will originate coherent scattering for a given wavelength. The most common XRD measurements are performed in the so-called Bragg-Brentano (BB) configuration (**Figure 15**). Detailed description of BB configuration and recent

developments are present in the literature [182], [183], [202], [203]. In BB, the sample is scanned by tilting the sample in a predetermined range at a given scan rate. Simultaneously, the detector of the reflected (or diffracted) X-Rays is moved at double speed to the detector [183]. Therefore, BB is also commonly known as scan. The diffraction intensity is recorded as a function of the value, i.e., the angle between the incident and the collected X-Ray beam. By scanning the diffraction angle, a diffraction pattern is generated.

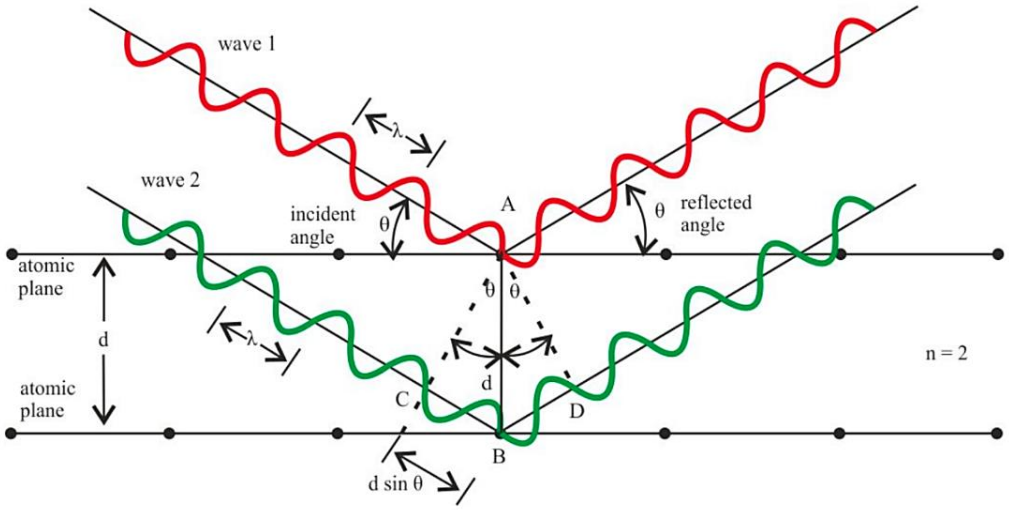

***Figure 14**: Schematic representation of the Bragg condition for the coherent scattering from two adjacent planes of the same {h, k, l} family. The difference in optical path corresponds to the segment CBD (from* [201]*)*

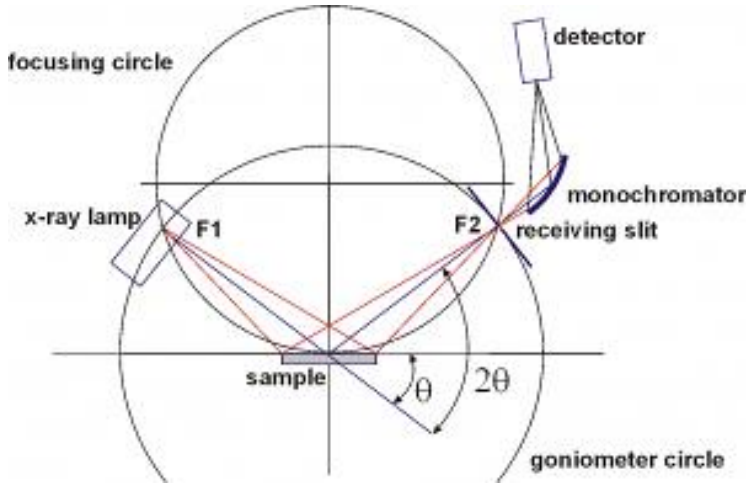

***Figure 15**: Bragg-Brentano configuration. X-Ray lamp, receiving slit and sample surface are kept on the tangent plane of the focusing circle, whose radius increases for lower theta values. X-ray source and*

receiving slid move along a goniometer circle of fixed radius. At low angle, the focusing circle is large and this implies loss of angular resolution which reduces the quality of diffraction peaks (from [202]*)*

The plot of the detected X-Ray intensity versus the corresponding 2θ value originates a pattern called diffractogram, lime the one shown in **Figure 16**. The shape of the pattern, i.e., the peaks position, is primarily related to the crystallographic properties (e.g., system and structure) of the specimen. The identification of the proper crystal structure and the proper attribution of a certain set of {hkl} numbers to each peak is called pattern indexation and constitutes the first step for further analyses. Pattern indexation is performed by comparing experimental data with existing databases, such as the Powder Diffraction File (PDF) database from the International Centre for Diffraction Data (ICDD), or by software-driven simulations from crystallographic data [204]. The specific features of a diffractogram, e.g., number of peaks, their shape and relative intensity, depend on several factors:

- The shape of a diffractogram depends on the crystal structure, therefore materials with the same crystal structure will result in an XRD pattern of similar shape [173], [185]. Nonetheless, the exact angular position depends on the interplane distances in the crystal samples, according to Bragg law. In each material, the interatomic distances are different as they are correlated to the size of the constituent atoms [205]. Also, identical materials subjected to different uniform compressive/tensile stress states will have modified interatomic distances [206].

- In BB configuration, only diffraction contributions from the crystal planes which are parallel to the sample surface are collected. Hence, to express all the possible diffraction peaks, test materials should be powdered. In solid-state materials, both bulk and coatings, the occurrence of texturing, namely some preferential growth direction during the crystallization process, can change the powder diffraction pattern by altering the nominal peaks proportions, even annihilating some contributions [207].

- The intensity of each peak is related to the atomic species, i.e. the number of electrons it includes, and the position within the unit cell [182], [185]. The higher the electron density of an element, i.e., its atomic number, the higher the scattering

efficiency and the intensity of the diffracted beam. Also, texturing can have a strong impact on the relative intensity of diffraction peaks.

- The peak shape is related to the crystal size, parasitic signals from contaminants or non-monochromatized X-Ray source, non-uniform stress state, presence of structural defects and instrumental error [173], [185], [202], [204], [206].

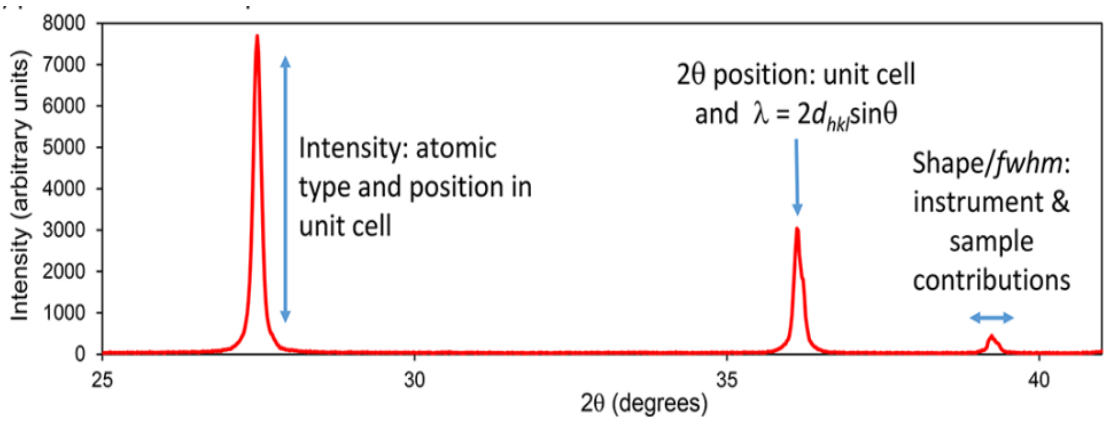

***Figure 16**: Example of a diffractogram obtained by a BB measurement. Relevant factors impacting the pattern features are pointed out (from* [185] *)*

2.3.4 SCHERRER ANALYSIS FOR CRYSTALLITE SIZE DETERMINATION

From the angular position and the width of diffraction peaks, it is possible to estimate the size of the crystallites from which that peak originated. The first correlations between the shape of diffraction peaks and the size of the crystal portions originating those signals, i.e. the crystallites, are due to Paul Scherrer, who in 1918 found out that a collimated monochromatic x-ray beam interacting with a mass of random crystals, gave diffraction patterns whose breadth broadened by downscaling the particles size [187]. Similarly, the width of the diffraction peaks in a diffractogram is inversely proportional to the crystallite size in polycrystalline materials [188]. Such relation is expressed by the Scherrer formula:

$$D_{hkl} = K * \frac{\lambda}{FWHM_{hkl} * \cos\theta_{hkl}} \qquad (2\text{-}4)$$

Where D_{hkl} is the crystallite size, λ is the x-ray wavelength, $FWHM_{hkl}$ is the full width at half maximum (in radians) of the reference diffraction peak, θ_{hkl} is the incidence angle

in radians (or equivalently one half of the diffraction angle for that peak, as shown in **Figure 17**) and K is a constant whose value depends on the shape of the crystallite. In general, a value of 0.9 is adopted for K if no knowledge of the exact crystallite shape is available [190], [191].

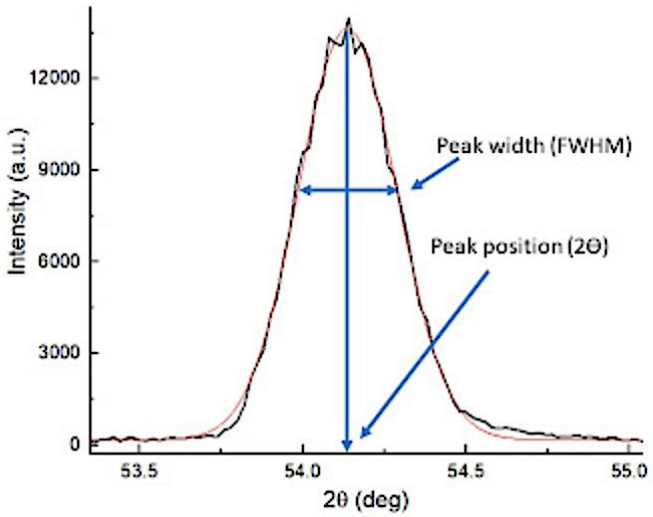

***Figure 17**: Visualization of the parameters used in the Scherrer equation. The red profile is the fit (usually a Voigt function) to the experimental data, from which the peak position and width can effectively be determined.*

The assumptions upon which this formula is derived are that each atom acts as an independent scatterer and that the scattered radiations do not interact with other atoms in the material [208]. Besides, the formula is appliable only for crystallite sizes below about 200 nm, as peak broadening for large crystals becomes too small and multiple scattering phenomena occur, which are not considered in the Scherrer description [190], [208]. Despite this, if the specimen is polycrystalline with small crystallite sizes (< 100-200 nm), which is the case, for instance, for PVD thin film coatings, Scherrer approximation provides an adequate description and **Equation *(2-4)*** can be employed.

2.3.5 RESIDUAL STRESS MEASUREMENT

Another way XRD is widely employed to characterize bulk and coating materials is the determination of the residual stress. Residual stress is the stress present in a component in the absence of an external load or force. It can originate from any process involved in the production line of the piece, such as solidification processes, phase transformations,

heat treatments, cold working, plasma or ionic bombardment, cooling and so on [209], [210]. Residual stress can be tensile or compressive, depending on the mechanisms which generated it. Tensile stresses have often a thermal origin. In bulk metallurgical pieces which solidify from the liquid phase, tensile stresses arise because of the different cooling rates between the interior portion and the exterior which in turn is directly exposed to the cooling agents. In coatings technologies, tensile stresses are a major concern as they can facilitate the initialization and propagation of cracks. On the contrary, residual compressive stresses can be beneficial, as they provide an additional stress field that thermal stresses or applied shear forces must overcome for cracks to be initiated [209].
Residual stresses can be measured at the macro and micro scale by several methods [211], [212], including non-destructive techniques such as XRD [212]–[215] and interferometric approaches [216], [217] and destructive techniques such as core-ring and FIB-based methods [210], [218]–[222]. In residual stress measurement via x-ray diffraction, the strain in the crystal lattice is measured, and the residual stress producing the strain is calculated from it, assuming a linear elastic distortion of the crystal lattice [212]. The strain ε along a specific crystallographic direction associated with corresponding values $\{h, k, l\}$ is defined as the relative difference between the specimen interplanar spacing d_{hkl} and its reference stress-free value d^0_{hkl} [214]:

$$\varepsilon = \frac{d_{hkl} - d^0_{hkl}}{d^0_{hkl}} \qquad (2\text{-}5)$$

When a material is strained by tensile or compressive forces, elongations and contractions are produced within the crystal lattice, respectively. These will alter the appearance of the corresponding diffraction pattern, according to the connection between the diffraction peak angle and interplanar spacing of the {h, k, l} lattice planes carried by the Bragg law.

The traditional XRD method to measure residual stresses is called the $sin^2(\psi)$ (the sin-square method) [212]. In such a method, the diffraction peak occurring at a certain Bragg angle θ is scanned for multiple orientations of the specimen relative to the normal N of the sample surface (**Figure 18**). By changing the relative orientation between the incident X-Ray beam and the sample surface normal (i.e., by tuning ψ), crystallites with the same

crystallographic planes that are differently oriented with respect to the sample surface will match the condition for Bragg diffraction. The sign and magnitude of the residual stress in the specimen can be obtained by monitoring the change in the 2θ value where the Bragg peak occurs as a function of the tilt angle ψ.

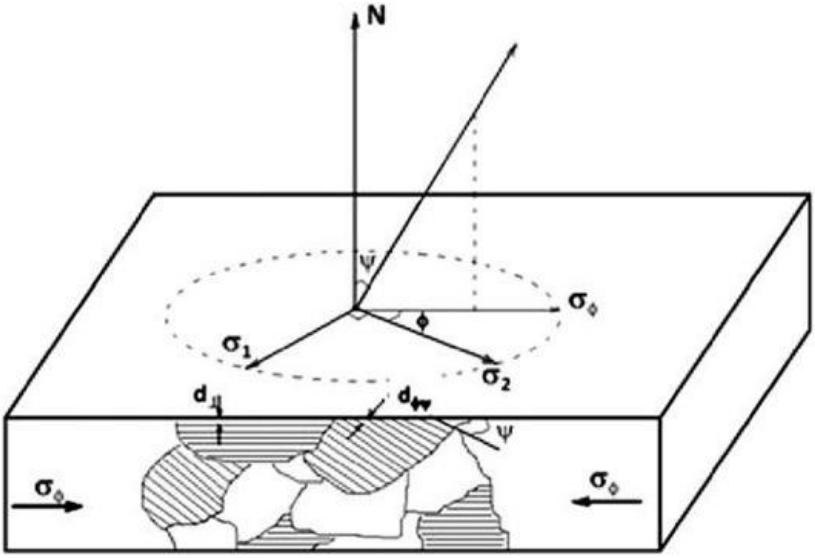

***Figure 18**: Schematic representation of the diffraction relevant angles, crystal planes orientation and biaxial stress components used in the $sin^2(\psi)$ method (from* [223]*)*

In the application of this method to thin films and surfaces, usually, a condition of plane stress with a biaxial stress tensor is assumed with no stress component along the coating's thickness direction [214], [215]. The fundamental equation relating the crystallographic spacing to the tilt angle and the internal stress σ_φ is [212], [215]:

$$\sigma_\varphi = [\frac{E}{1+v}]_{hkl} * \frac{\partial \varepsilon_{hkl,\varphi}}{\partial sin^2\psi}$$

(2-6)

Where φ is the in-plane angle of rotation, the elastic strain coefficient $[\frac{E}{1+v}]_{hkl}$ is defined by using direction-specific values for the Young Modulus *E* and Poisson ratio *v* and $\varepsilon_{hkl,\varphi}$ is defined according to Equation (2-5). If the hypothesis of equiaxial stress is made, so that $\sigma_1 = \sigma_2$ in **Figure 18**, the dependance of the residual stress on the rotation angle φ in **Equation (2-6)** can be neglected [214], [223], [224].

The $sin^2\psi$ method, like other XRD-based methods for residual stress evaluation, has many advantages. It is non-destructive, reliable, and easy to interpret [212]. The fundamental value of such a method is establishing a linear relationship between the strain and the $sin^2\psi$, with the residual stress. The stress can be obtained from the slope of the linear regression of the measured strain as a function of $sin^2\psi$, once the elastic strain coefficient $[\frac{E}{1+\nu}]_{hkl}$ is known by external procedures or approximated to the bulk values [224], keeping in mind that some error in the stress estimation is introduced in the latter case [212], [214].

Nonetheless, some limitations can impair its usefulness in real practice [212], [223], [225]. First, as previously mentioned, the test material must be polycrystalline with a sufficiently small grain size. Fortunately, in the case of PVD coatings with thicknesses of a few microns, this is the case as crystallites usually well below 100 nm are obtained [226], [227]. Also, the sample surface should be perfectly flat to avoid the convolution of multiple crystallites for a given tilt angle.

The most important limitation of the present technique arises when the specimen material is textured, meaning that the crystal growth proceeds in preferential directions [228]. As a matter of fact, texturing can limit the number of ψ values where the investigated (h, k, l)-peak is intense enough to permit an accurate determination of the strain. Moreover, textured materials might present an additional drawback. The $sin^2(\psi)$ method is more sensitive to shifts in 2θ values for higher diffraction angle [212], [225]. With textured materials, only a small subgroup of diffraction peaks is detected. Hence, if no high angle signals are detected, the linear dependence of stress upon the $sin^2\psi$ might not hold and the usefulness of the method can be therefore compromised [225]. As a matter of fact, PVD coatings are usually textured, owning to the non-equilibrium conditions determined by ion bombardment, plasma composition, fast cooling rates and substrate effects [62], [145], [229]–[231]. In such cases, the availability of multiple, high angle peaks is limited. Nonetheless, it has been reported that signals {hkl} with h=k=l or with h=h and k=l=0 coming from cubic lattices have intensities which are independent on texture and can reliably be used for the determination of the residual stresses [225].

2.4 FOCUSED ION BEAM ASSISTED SCANNING ELECTRON MICROSCOPY

2.4.1 A BRIEF INTRODUCTION TO ELECTRON MICROSCOPY

The history of electron microscopy started in the early decades of the 20th century, with the two fundamental discoveries consisting in the quantum mechanical description of electrons from Louis De Broglie and the observations of Hans Busch about the analogy between the effect of magnetic fields on electron and that of glass lenses on the light [232], [233]. Nowadays, electron microscopy is probably the most widely employed characterization technique in materials science, with applications spanning from inorganic and organic materials science [234], [235], failure analysis [236], [237], historical heritage [238], soft-matter chemistry and medical-biological studies [239]–[241]. Two distinct classes of electron microscopy techniques have been developed, namely Scanning Electron Microscopy (SEM) and Transmission Electron Microscopy (TEM), with combined technologies implemented in Scanning Transmission Electron Microscopy (STEM) machinery [232], [242], [243]. The first TEM was built by Ernst Ruska in 1933 [233], [244] and was recognized as an invaluable breakthrough in materials science. Due to the high energy of beam electrons, the associated wavelength allows for spatial resolution orders of magnitude lower than optical microscopes. Theoretical resolution limits on the order of the picometer are available for keV accelerated electrons, with practically viable resolution on the order of a few nm down to less than 1 Å in modern systems [245]. TEM is nowadays one of the most complete and insightful characterization tools, despite its working principle requiring careful and demanding sample preparation and the high-quality information provided comes along with very high machinery costs [246], [247]. The development of SEM was delayed due to the lack of the outmatched spatial resolution of the TEM and was only in the 50ies and 60ies with the development of more efficient signal detection and processing tools that the SEM gained its place in many fields of scientific research [232], [243]. The practical resolution limit is due to instrumental factors and the mechanisms of interaction between the beam and the specimen.

In this section, a brief introduction of the SEM working principle, the main limits to image resolution and the basic concepts of electron image production are provided. Along with

SEM basics, the implementation of a microanalytical tool known as Energy Dispersive X-Ray Spectroscopy (EDXS) and the Focused Ion Beam (FIB) milling are addressed.

2.4.2 THE SCANNING ELECTRON MICROSCOPE

In a typical Scanning Electron Microscope, a fine probe of electrons with energies typically of a few to a few tens of keV is focused on a specimen and raster-scanned along a pattern of parallel lines by a coil deflection system.

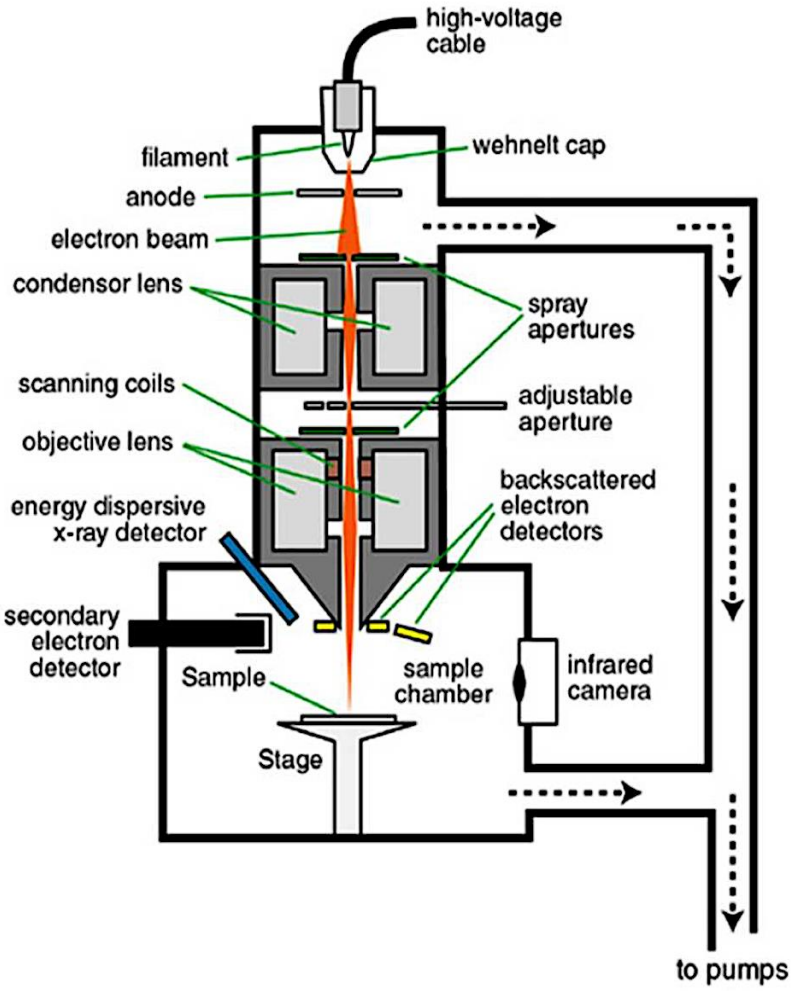

***Figure 19**: Scheme of a hot cathode SEM apparatus. One-to-three condenser lenses can be mounted in real machinery to increase the collimation of the electron beam. The aperture at the entrance of the objective lens serves to reduce aberrations of the entering beam by reducing its divergence angle. The role of the objective lenses is to provide the final demagnification of the beam and focus the beam onto the sample.*

The electron beam is usually generated by Tungsten tips which emit electrons by thermoionic effect or by field emission extraction for the so-called FE-SEM. The beam

size is then progressively reduced by a series of electromagnetic lenses known as *condenser lenses* and a final *objective lens* which provides the final demagnification of the electron beam and focuses the beam onto the specimen (see **Figure 19** and **Figure 20**). The electron source, the electron beam column and the specimen chamber are vacuum pumped at about 10^{-7}-10^{-8} millibar to avoid collision of electrons with atmospheric particles and the consequent loss of energy and path coherency [243].

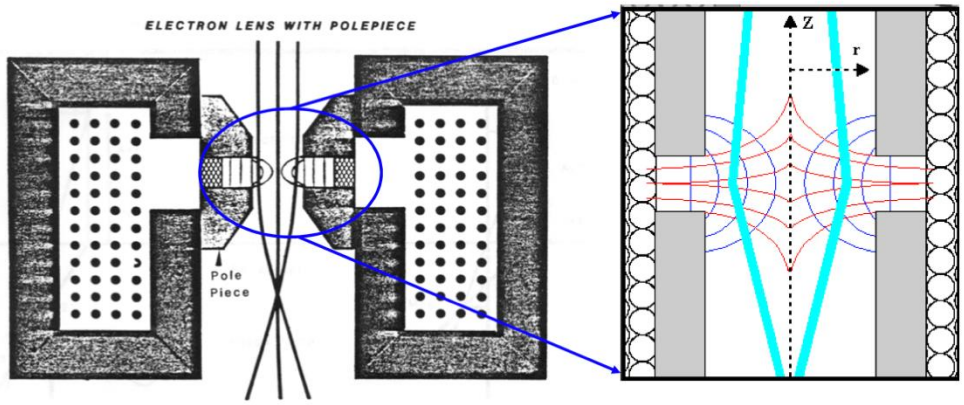

***Figure 20**: Representation of an electromagnetic lens deflection of an electron beam passing through it. In the right part of the image, Z identifies the optical axis while r is the optical axis distance from the polepiece.*

Even top-end high-resolution SEM cannot achieve the atomic resolution achievable by high-resolution TEM. The reason can be easily understood by considering the interaction phenomena occurring between electrons and the specimen.

In Transmission Electron Microscopes, a very thin electron probe with high energy (200-300 keV) is transmitted through a thin (<200 nm) specimen, providing a contrast image based on the different energy loss at each point of the specimen [244]. SEM instead, is generally used to image the surface of bulk materials by using relatively low-energy electrons (30 – 100 keV). A wealth of information can be obtained from the abundance of different signals originating from the impact of the incident electrons with the specimen, which in general terms can be either collected to form an image or to analyze the sample surface. [232]. A visual representation of all the outcoming signals from an electron imaging process is shown in **Figure 21,** while the atomic-level interactions for each process are sketched in **Figure 22**. As the beam electrons enter the specimen, they interact with the electrical field exerted by the surrounding atoms. Such interaction can deflect the beam electrons through elastic and inelastic scattering events, causing them to

spread out laterally from the incidence spot. From these interactions, several output signals are generated, which constitute the wealth of information provided by the electron microscopy. Both elastic and inelastic scattering increase with heavier atoms/ denser materials and decrease by increasing the beam energy, although with different functional dependencies [243], [248]. Because of these interactions, a certain "*interaction volume*" of material is involved, the size of which depends on multiple specimen and beam factors and can extend as deep as a few microns below the specimen surface. Despite the beam spot size at the specimen is usually around 10 nm in modern SEM [243] and down to 1-2 nm in TEM [249], the output signals used for imaging and analytical purposes are collected from the whole interaction volume, with the inevitable loss of spatial resolution [232], [243]. The size of the interaction volumes has an opposite trend to the scattering probability, in the sense that all the factors contributing to higher scattering events (higher specimen atomic weight, lower beam energy) will limit the propagation of electrons within the material, thus confining the interaction volume closer to the surface [243]. An approximate estimate of the penetration depth in a solid is given by the following formula by Kanaya and Okayama [246], [248]:

$$R_{K-O} = 27.6 * \left(\frac{A}{Z^{0.89}\rho}\right) E_0^{1.67} \qquad (2\text{-}7)$$

Where A is the atomic weight, Z is the atomic mass, ρ is the density and E_0 is the electron beam energy. For compound materials, such relation can be used by employing weighted average values instead of elemental ones.

In TEM, the very thin specimen offers an interaction volume that is much more restricted than in SEM (see ref. [246], chapter 1, page 9). For this reason, higher energy electrons can be used, with much better resolution than in SEM. Despite this, SEM has found incredible success and is much more diffused than TEM. This can be explained by considering that the lower resolution achievable with SEM is counterbalanced by the much easier flexibility, sample preparation procedures and much lower machinery costs than TEM. Besides, an atomic resolution is not necessary for many applications where important features occur at the micro or nanometric levels, well within the reach of

commercial SEM. In what follows, the main output signals from an SEM characterization are described (see ref. [243], Chapter 3, pages 61-94).

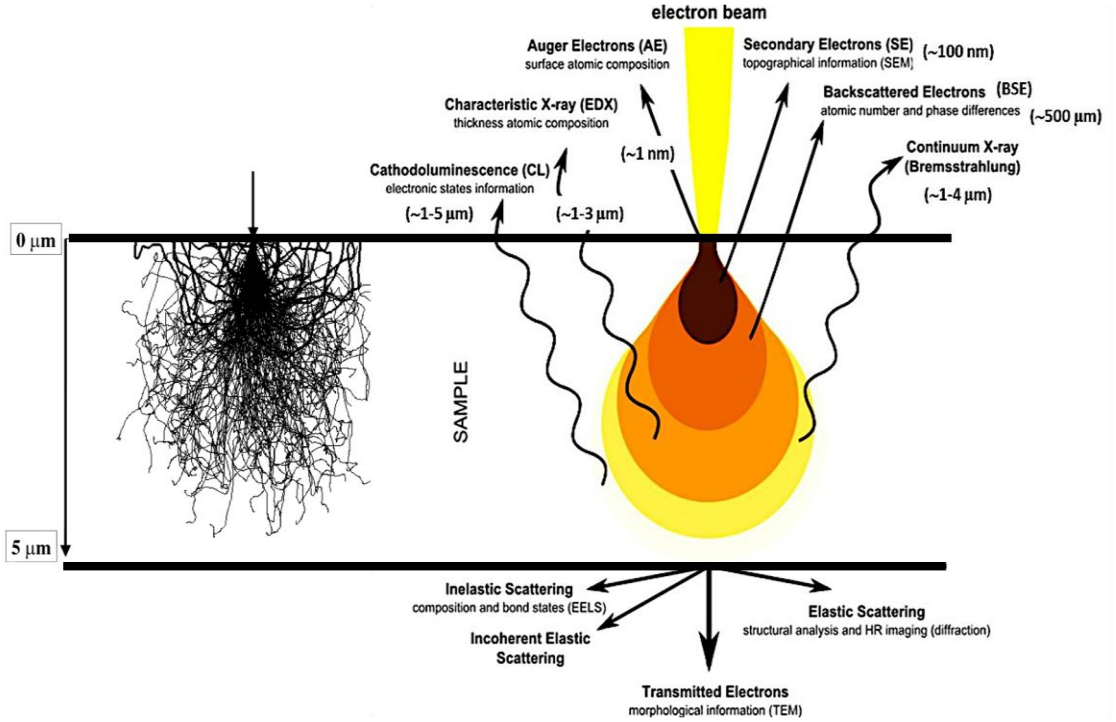

***Figure 21**: Left, Monte Carlo simulations of electron trajectories at 20 keV, with a focused spot size of 1 nm* [243]. *Right, visual representation of the output signals deriving from the electron-specimen interaction. The specific use and the corresponding depth of each signal is also reported. For transmitted signal to be analyzed, the specimen thickness should not exceed 100-200 nm.*

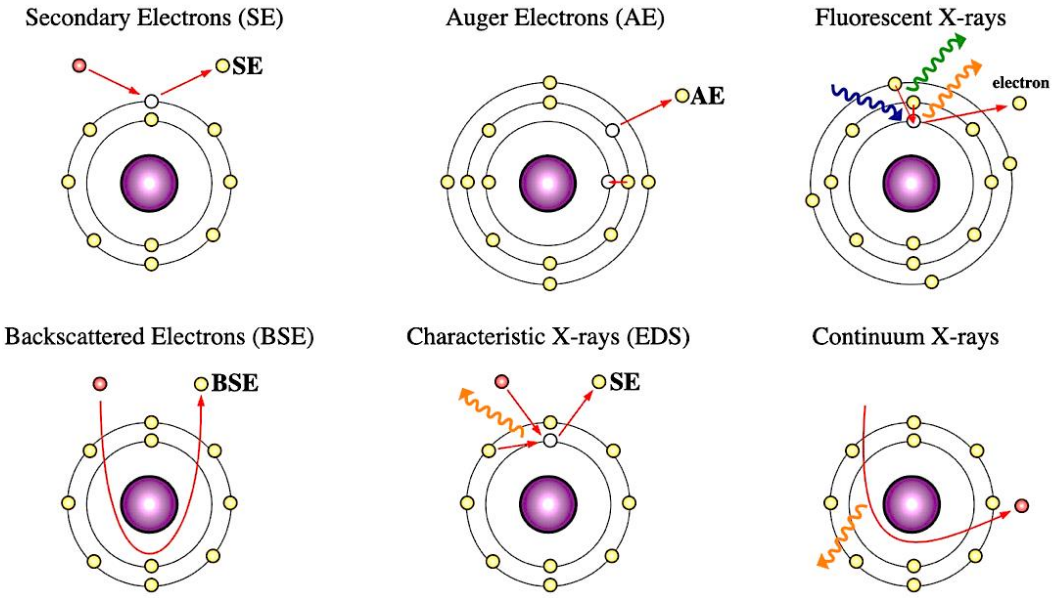

***Figure 22**: Schematic origin at atomic level of the several output signals originating from the interaction of primary beam electrons with the specimen*

2.4.3 IMAGING WITH SEM

The basic signal for SEM imaging is constituted by two types of electrons:

- *Backscattered Electrons* (BSE): electrons coming from the beam and reflected after the interaction with the specimen.
- *Secondary Electrons* (SE): electrons emitted from the specimen after the interaction with the impinging beam.

In what follows, the main features of BSE and SE are discussed. Besides BSE and SE, other important output signal is the emission of characteristic X-Rays, which are used to accomplish a compositional analysis of the investigated sample area. This analytical tool takes the name of Energy Dispersive X-Ray Spectroscopy (EDXS) and will be discussed in the chapter regarding the use of X-Rays for chemical characterization purposes.

2.4.3.1 BACKSCATTERED ELECTRONS

Backscattered electrons are beam electrons which undergo enough scattering events that their travel direction is ultimately reverted, causing them to exit the specimen surface. Being electrons originating after many scattering events, they come from a relatively long range beneath the specimen surface, usually a few hundreds of nanometers depending on the beam energy [243]. Depending on their origin, BSE are distinguished into several subcategories [243]. The larger part of BSE is composed of electrons directly reflected from the surface, are termed BSE-1, and have kinetic energy virtually identical to the beam electrons. BSE-2 electrons are those BSE that are ejected from the sample surface after multiple collisions, with an energy spectrum spanning all energy values up to the primary beam energy. Finally, BSE-3 electrons are those electrons scattered from the chamber after being ejected from the sample surface. BSE electrons are primarily used to convey what is known as “Atomic Mass-Contrast” or “Z-contrast” imaging, thanks to the monotonic dependence of the backscattering efficiency from the second power of the atomic number Z of the target material [250] (**Figure 23**). When a BSE image is acquired from a flat specimen surface, changes in composition can be observed as differences in image contrast. The backscattering efficiency increases by tilting the specimen with

respect to the incident beam (ref. [246], chapter 2, pages 18-25) and decreases with increasing beam energy [250].

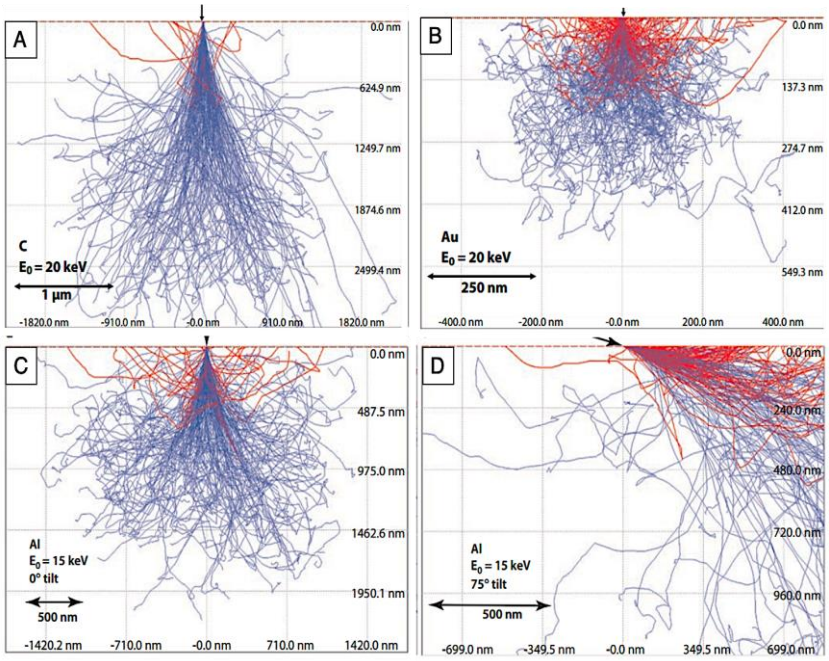

***Figure 23**: Monte Carlo simulations of electron trajectories as a function of the atomic mass of the target element (A, B) and tilt angle (C, D). Electron beam energy, target element and tilt angle are reported. Red trajectories identify the fraction of backscattered electrons (taken from* [246]*)*

2.4.3.2 SECONDARY ELECTRONS

Secondary electrons (SE) are created after inelastic scattering events between the beam and backscattered electrons with the atoms of the specimen, which eject weakly bound electrons with energies below 20 eV (ref. [246], chapter 3, pages 30-37). Secondary electrons can be generated within the whole interaction volume, following cascade processes [251], [252]. Nonetheless, due to the very low kinetic energy, only SE coming less than 10 nm beneath the surface can escape the specimen surface and reach the detector without being reabsorbed by the specimen [251], as the specific escape depth is a function of beam energy and target material. Depending on their ejection site, secondary electrons are distinguished into subcategories [243], [253]. SE-1 are SE ejected from the parent atoms by the primary beam, SE-2 are ejected from the interaction with backscattered electrons, and SE-3 are ejected by the chamber surface via interaction with BSE-3 electrons. The yield of secondary electrons increases by decreasing the beam energy [251], because of the higher rate of energy loss and lower beam energy penetration

at lower energies. The yield of SE depends non-monotonically on the atomic number, hence their direct use in Z-contrast is less convenient. Their main use is based on their very low kinetic energy and short mean-free path [251], resulting In an enhanced surface sensitivity to gather topographical contrast. Nonetheless, an important proportion (close to 30%) of secondary electrons comes from the interactions of backscattering electrons with the specimen (SE-2) [243], [252], [254], and their number thus depends on the atomic number of the specimen material. Hence, some Z-contrast and hence compositional information is indirectly available also with SE [252].

2.4.3.3 DETECTORS FOR ELECTRON SIGNALS

Each type of electron, as well as any other output signal, has a specific detector. The differences between the collection of BSE and SE lie in the very different energy distribution of BSE and SE [243]. In general, the discrimination between BSE and SE electrons is achieved by biasing the detector receiving surface: positive bias will attract both high energy BSE and low energy SE, while negatively biased detectors will reject low energy SE and hence increase their sensitivity to BSE [243]. The first SE detectors were scintillation detectors known as conventional Everhart-Thornley (ET) detectors. Such detectors, still used, are placed laterally to the specimen and probe. To increase the amount of SE collected and reduce the amount of BSE, in-lens detectors have been developed. In-lens detectors are placed inside the beam column and arranged rotationally symmetric around the optical axis for efficient collection of Secondary electrons of type SE-1 and SE-2 [253], [255]. In the absence of dedicated BSE detectors, in-lens detectors provide a way to collect signals with a higher intensity and Z-contrast than out-of-lens ET detectors for secondary electrons, especially at low working distances. BSE detectors were originally similar to ET detectors, with the selectiveness to BSE imposed by negatively biasing the detector surface relative to the specimen[256]. BSE carry various information, and such information depends on the direction of emission, which for BSE can be very spread out from the emission point [256]. ET detectors are very directional, thus unsuitable to gather all the information provided by BSE. For this, solid state detectors (SSD) were developed which are composed of separated solid state grids or annular semiconducting detectors whose directional components can be merged or discriminated for high information detail [257].

2.4.4 OPTICAL FACTORS AFFECTING THE RESOLUTION LIMIT

The theoretical spatial resolution of 200-300 keV electrons used in common TEM should allow reaching resolutions on the order of the picometer, according to the De Broglie equation [243]. Further increasing the electron energy to achieve higher resolution is not feasible, as an electron with such high electron energies would deteriorate most of the specimens [244]. As for SEM, electron energies higher than a few tens of keV would interact with such large specimens' volumes to irremediably impair the spatial resolution. A safer approach to improve the spatial resolution of electron microscopes involves the development of more performing electromagnetic systems for the collimation and focusing of the electron beam. It is known since the early stages of electron microscopy history that the main issue for achieving atomic resolution with electron microscopes was the inevitable loss of focusing capability because of lens aberrations [232], [258], [259].

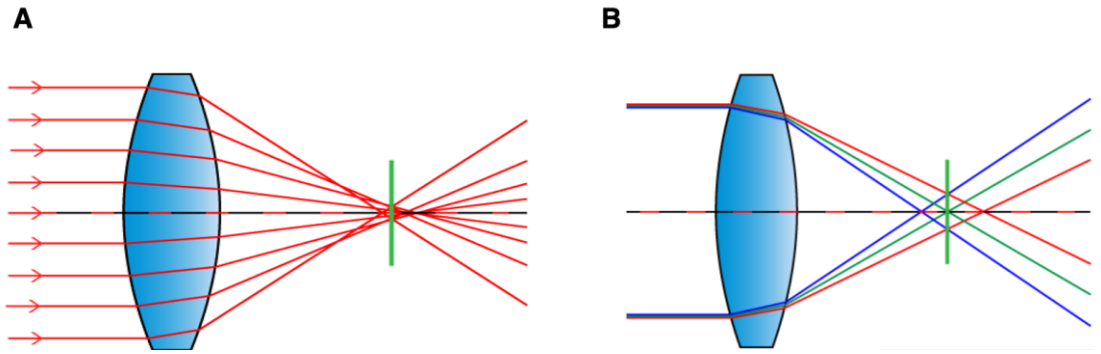

***Figure 24**: Defocusing induced by (A) spherical and (B) chromatic aberration. The defocusing is due to the different focusing strength between peripheral and inner beam components with spherical aberrations. Chromatic aberrations cause defocusing due to different deflection of beam components with different energies. The outcome of either or both the effects is the impossibility of finding a unique focal spot, but rather a focusing plane that minimizes the effects of aberrations, here represented by the green plane perpendicular to the optical axis.*

Spherical and chromatic aberrations (**Figure 24**) limit the resolution d of conventional electron microscopes to a real value which is about $d = 100*\lambda$, with λ being the electron wavelength [244], [260]. Despite modern electron microscopes are equipped with effective aberration correction systems [258], [259], [261], [262], aberrations cannot be completely removed and some resolution-limiting focal spread is always present.

2.4.4.1 SPHERICAL ABERRATIONS

Spherical aberrations are due to a non-uniform focus spot for the electrons passing through the lens, as a function of their distance from the beam axis and constitute a fundamental cause of resolution limits in both TEM and SEM [260], [262], [263]. Within the focusing system of an electron microscope, the focal plane of the electron beam is adjusted by tuning the deflecting magnetic fields of the condenser lenses, with apertures and electron beam energy being kept constant. In the absence of spherical aberrations, all the portions of the electron beam would be focused on the same spot on the focal plane. Unfortunately, for spherical lenses, due to the so-called "Scherzer Theorem", the unavoidable non-uniform distribution of the lens potential always make outer electrons to be more strongly focused than inner ones [244]. Because of this effect the focal plane is not uniquely defined for all the electrons of the beam, but it depends on the distance of the electron from the optical axis, with peripheral and paraxial electrons having shorter and longer focal distance, respectively (**Figure 24-A)**. This means that in place of a well-defined focal spot, a condition of minimum focal spread must be achieved. In this optimized condition, a focal disc is defined on the focal plane, whose diameter depends on the initial width of the electron beam. In principle, the problem of spherical aberrations could be reduced by using narrower beam size, achievable by using higher beam energies and smaller apertures. Unfortunately, this conflicts with the concurrent need to maintain sufficiently intense electron currents to keep the signal-to-noise ratio high enough to acquire sufficiently bright images, which prevents excessive beam demagnification [232]. Besides, diffraction effects due to the wave nature of electrons may be enhanced if too narrow apertures are used [259], which would further impair the image quality. Therefore, further corrections for spherical aberrations involve the implementation of multipole electromagnetic correctors and mirrors in the electron-beam path. This permits to reach of a resolution in the sub-Angstrom regime for TEM and below 1 nm for high-resolution SEM without losing signal brightness [258], [261].

2.4.4.2 CHROMATIC ABERRATIONS

Chromatic aberrations originate because of the non-perfect monochromaticity of the electron beam [249]. Charged particles travelling in an electromagnetic field perceive a deflecting force that depends on their velocity, according to the Lorenz force [264]. As an electron beam consists of electrons with a certain distribution of velocities around the

nominal one [244], each electron is subjected to a slightly different deflecting force according to its velocity. This results in correspondingly different deflection angles, leading to focal spots falling at different distances from the lens (**Figure 24-B)**. As for the spherical aberrations, this implies the impossibility to define a unique focal spot and the need to find a focal distance where the effects of chromatic aberrations are minimized. Chromatic aberrations are more important at low electron energies, so they constitute a major concern for SEM, which usually operate at energy as low as 1-5 keV [263]. Chromatic aberrations can be reduced using monochromators [241], which confine the energy spread of the incident electron beam down to 0.1 eV, and energy filters remove the inelastically scattered electrons. This, coupled with the multiple corrections for spherical aberrations, allows spatial resolution below 0.1 nm for high resolution (HR) TEM and less than 1 nm for HR-SEM [249], [260], [263].

2.4.4.3 ASTIGMATISM

In real SEMs the magnetic fields created in the electron gun and used to collimate and focus the electron beam are never perfectly symmetric, due to inevitable imperfections in the electromagnetic lenses which result in asymmetric magnetic fields in the electron gun [246]. By slightly defocusing the image in either overfocused or under focused conditions, it can be noticed that the image is not only blurred but also distorted, to an extent that depends on the degree of asymmetry of the magnetic fields in the gun. Such phenomenon is called astigmatism and consists of an asymmetrical focus strength of the beam towards a certain direction. If not properly corrected, even at the best focal distance, an image blurring will occur in addition to that provided by aberrations (**Figure 25**). Astigmatism must be corrected by tuning the current of the electromagnetic lenses in such a way as to compensate for this asymmetry as much as possible.

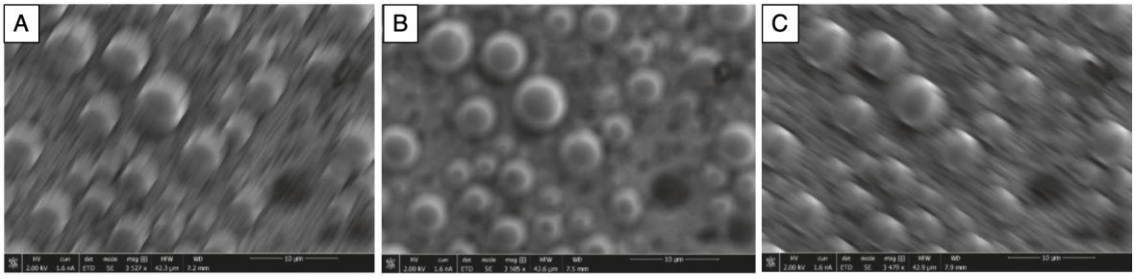

***Figure 25**: Example of imaging with an astigmatic beam in case of (A)under-focused, (B) focused, and (C) overfocused image (readapted from ref.* [246]*, chapter 5, page 74)*

2.4.4.4 IMAGE QUALITY OPTIMIZATION

In electron microscopy, the wealth of information that can be obtained comes at a price. The high number of optical and physical parameters involved in electron microscopy make the definition of the optimal operative conditions a fluid concept.

Besides optical limitations, other factors may impair the ultimate resolution achievable by an SEM. For instance, the use of smaller apertures can be pursued to reduce the interaction volume. This is particularly suitable if the targeted specimen area includes details with high compositional or topographical contrast. Nevertheless, the electron beam cannot be indefinitely restricted by the apertures, as it implies progressively low beam currents and consequently a poor signal-to-noise ratio. For low contrast specimens, such as flat surfaces of compositionally homogeneous materials, the use of low current results in poorly defined images. In such cases, using larger apertures yields higher received signals, but at the cost of lower spatial resolution and reduced depth of field, the span of vertical points at which defocusing does not yield image blurring (see ref. [246], chapter 5). Besides, the accelerating voltage of the electron beam must be tuned accordingly to the specimen. Higher beam energy results in narrower beams but also implies larger interaction volumes, so a trade-off must be found by also cutting the beam current through the choice of suitable apertures. Besides, as predicted by the Kanaya-Okayama equation (Equation *(2-7)*), for given beam energy the final beam penetration decreases with denser and heavy elements, which adds another parameter to account for in defining the optimal imaging conditions. Finally, as will be discussed in the next chapter, the beam energy defines the number of spectral lines which can be revealed in the microanalysis of samples via Energy loss x-ray spectroscopy. Thus, the proper configuration depends on the instrument and the specimen properties, and not a single choice of parameters can be defined a priori.

2.4.5 FOCUSED ION BEAM-ASSISTED SEM

The use of Focused Ion Beams (FIB) in the field of electron microscopy for the preparation of site-specific samples and imaging has become a very common practice in micro-nano fabrication [265], coatings technologies [83], [266], [267], porous materials in battery technologies [268], failure analysis [269], [270], TEM sample preparation [271]

and even in biological sciences [272] especially thanks to the increasing implementation of Cryo-electron tomography for in-situ imaging of biological structures in near-native state [273]. Preparation of cross-section through ion milling for depth imaging of micro-nano structured specimens and thin film coatings materials is the most common use of the focused ion beam tools, although there are uses for imaging with secondary electrons produced by the ion beam (see ref. [246], chapter 30, pages 518-526). The bombardment of target materials with energetic ions is an inevitably destructive process, which alters the surface of the target material. When an energetic ion beam bombards the surface of solid material, the interaction of the ion beam with nuclei and electrons of the target material's atoms produces several different physical phenomena, such as sputtering, sample heating, secondary electron production, ion implantation and amorphization of the target material [246], [265], [274], [275].

The typical set-up and operative principle of a FIB is depicted in **Figure 26** and described in ref. [271]. Commercial FIB systems usually employ a Ga liquid metal ion source (LMIS) for ion production, thanks to the longer stability of Ga sources to other low melting point metal sources such as In or Sn. Despite this, alternative ion sources are currently being developed for improved performance and minor ion implantation, a major concern, especially in the semiconductor industry where the typically high implantation of Ga ions and the consequential alteration of the crystallographic and compositional properties can impair the electronic properties of microelectronic devices [276]–[278].

In Ga-LMIS, a reservoir of gallium is put in contact with a sharp Tungsten needle, so that Ga wets the needle down to the needle tip (**Figure 27**). A high extraction potential is applied between the Tungsten and an extraction electrode. In response to the strong extraction potential (usually 10-50 keV), Ga forms a sharp cone at the edge of the needle, called the Taylor cone, with an apex radius of a few nanometers.

Field ionization leads to the extraction of Ga ions and hence an ion beam is generated.

The beam current, which ultimately depends on the milling rate and the extent of damage delivered to the target material, is tuned from a few tens of pA to several nA by selecting the size of the aperture placed between the condenser and objective lenses (see **Errore. L'origine riferimento non è stata trovata.**). The aperture's diameter determines the size of the beam, which is passed forward towards the specimen, which can be as narrow as a

few nanometers for small apertures (pA currents) up to hundreds of nanometers for large apertures (nA currents).

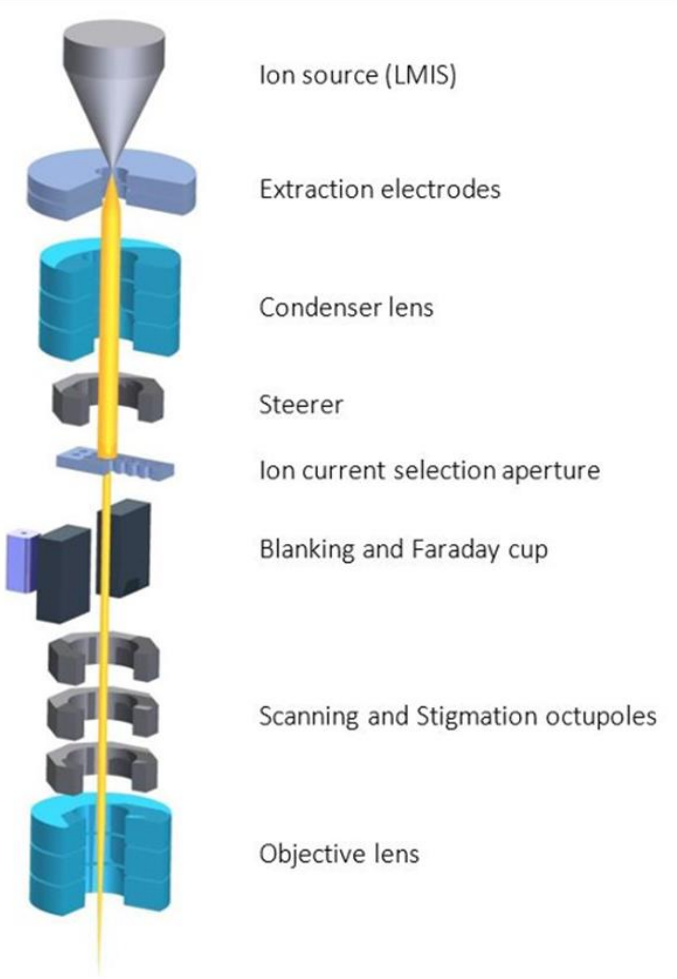

***Figure 26**: Schematic representation of a liquid metal ion source (LMIS) FIB Gun architecture*

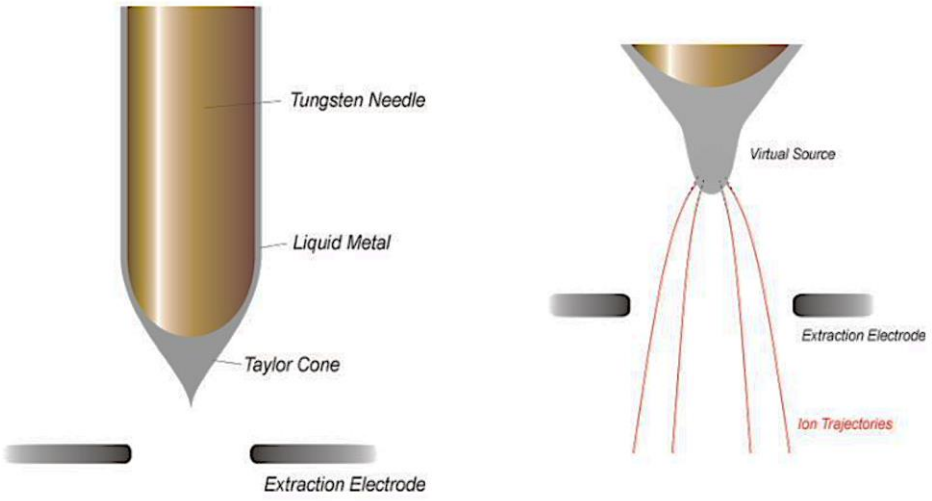

***Figure 27**: Extraction process of Ga+ ion beam. The "Virtual source" corresponds to the point where Ga ions are extracted under the effect of the extraction potential, where a tip-effect enhancement is established at the apex of the Taylor cone.*

Instruments simultaneously equipped with an SEM and a FIB tool are commonly known as Dual-Beams or Crossbeams. FIB/SEM platforms employ the FIB to process the specimen by ion bombardment with an ionic beam, and the SEM for imaging and/or analyzing the treated site with all the modalities offered by the electron-specimen interaction. In dual-beam platforms, the electron and ion beams are independently collimated and focused onto the specimen to perform imaging and milling respectively, but they point to the specimen from different beam orientations (see **Figure 28**). Conveniently, the FIB and SEM imaging planes coincide in a single point (the eucentric point) for fast and easy milling-imaging protocols [246]. To achieve this, the beam relative angle and the optimum height of the sample holder must be carefully tuned when installing the machinery. If this is not the case, when switching between the two probes, the target area position must be corrected.

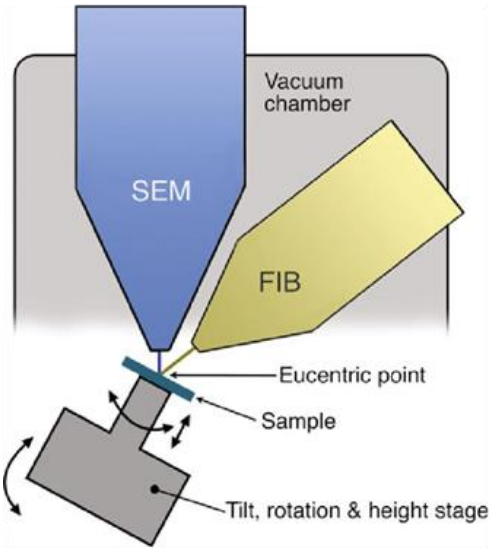

***Figure 28**: Sketch of a typical dual-beam configuration*

2.5 CHEMICAL MICROANALYSIS VIA EDXS AND XPS

2.5.1 EXPLOITING THE CHARACTERISTIC ENERGY OF ELECTRONS

In the first section of this chapter, it has been shown the use of X-Rays to investigate the structural features of solid materials, thanks to the elastic interactions between X-Rays and crystalline specimens. X-Rays can be also used to obtain compositional information on materials, exploiting the quantum nature of electronic energy levels. Each electron within a solid is immersed in an electrostatic field due to the attractive forces with the positively charged protons within the nucleus and the repulsive forces imposed by the surrounding electrons. The chemical environment of each atom within a solid, or in other words the nature of its neighboring atoms, affects the distribution of electrons around the reference atom, thus modifying the electrostatic field perceived by the electrons on that atom. The result of these electrostatic interactions is that for each equivalent atomic species, meaning all the atoms of the same element and in the same chemical environment, each electron is bound to its parent atom by characteristic energy. Such energy spans from a few eV for loosely bound valence electrons to several hundred eV for strongly bound core electrons. The elemental specificity of such energies is exploited in two techniques known as Energy-Dispersive -X-Ray Spectroscopy (EDXS) and X-Ray Photoelectron Spectroscopy (XPS). Both these techniques will be briefly introduced in this section, with emphasis on the relative advantages and limitations.

2.5.1.1 ELECTRONIC TRANSITIONS

According to IUPAC notation, the electronic levels involved in electronic transitions of core-level electrons are identified by letters and numbers [279], as shown in **Table 2**:

***Table 2**: IUPAC notation for electronic states in spectroscopy*

Shell	Electronic State	Shell	Electronic State	Shell	Electronic State	Shell	Electronic State
K	$1s$	L_1	$2s$	M_1	$3s$	N_1	$4s$
		L_2	$2p_{1/2}$	M_2	$3p_{1/2}$	N_2	$4p_{1/2}$
		L_3	$2p_{3/2}$	M_3	$3p_{3/2}$	N_3	$4p_{3/2}$
				M_4	$3d_{3/2}$	N_4	$4d_{3/2}$
				M_5	$2d_{5/2}$	N_5	$4d_{5/2}$
						N_6	$4f_{5/2}$
						N_7	$4f_{7/2}$

The first quantum number identifies the electronic shell and is indicated by capital letters so that n = 1,2,3 correspond to shells K, L, and N respectively. A numeric subscript to the shell letter refers to the specific electronic state in that shell, inclusive of the orbital type (*s*, *p*, *d* or *f*) and spin-orbit coupling J = l +/- s, with l and s being the second quantum number and spin number respectively. Numeric subscripts are ordered from 1 to 2l+1 in ascending order of the corresponding level energy. The transition is denoted by first indicating the state from where the electron relaxes, followed by the vacant state. Therefore, an X-ray transition indicated as L_2-M_1 means originate from a 2p electron with spin-orbit ½ relaxing into a 3s electronic state. Sometimes, the alphanumeric code for the ejected electron is omitted, so that only the notation for the state of the relaxing electron is reported. The lower energy required to eject an electron from a material is defined as K-edge. For a transition to be physically viable, selection rules apply. In brief, these rules require that in an electronic transition with photonic emission the total spin must be conserved and that the shell of the two electronic states involved differs by at least 1 so that K-L_2 or L_2-M_3 transition can occur but not an L-L, nor a K-L_1 or L_1-M_1 transitions. Electronic Transitions are often still represented in the traditional but archaic Siegbahn notation [246]. In this notation, the transition is identified by the capital letter of the initial state, a Greek letter, and a numerical subscript. The Greek letter identifies the shell of the final state, with usually alpha being the highest and beta the lowest, respectively. The number subscript indicates the electronic level of the final state, with a lower number for the higher energy state (lower transition energy). A comparison of electronic transitions definition between IUPAC and Siegbahn notation is reported in **Table 3**:

***Table 3**: IUPAC and Siegbahn notation for the electronic transitions*

Initial Level	Final Level	Siegbahn notation	IUPAC notation
K (1s 1/2)	L_3 (2p 3/2)	K α 1	K-L_3
	L_2 (2p 1/2)	K α 2	K-L_2
	M_3 (3p 3/2)	K β 1	K-M_3
	M_2 (3p ½)	K β 3	K-M_2
L_3 (2p3/2)	M_5 (3d 3/2)	L α 1	L_3-M_5
	M_4 (3d 3/2)	L α 2	L_3-M_4
L_2 (2p ½)	M_4 (3d 3/2)	L β 1	L_2-M_4
M_5 (3d 5/2)	N_7 (4f 7/2)	M α 1	M_5-N_7

2.5.2 ENERGY DISPERSIVE X-RAY SPECTROSCOPY

2.5.2.1 FUNDAMENTAL ASPECTS

As described in the previous chapter, by bombarding a solid material with an electron beam of sufficiently high energy to overcome the material's electron binding energies, electrons from the target material are ejected from their parent atoms and escape the material. Doing so, emitted electrons leave behind an empty electronic state. When the ejected electrons come from tightly bound core levels, such a condition is highly energetically unstable. Therefore, electrons from outer electronic states within the material tend to relax in the empty core level to minimize the overall energy of the excited system. One of the ways this relaxation process can develop involves the emission of characteristic X-Rays, with an energy equal to the energy difference between the electronic levels involved in the relaxation process [246]. Such X-Rays can travel through the specimen and eventually reach a dedicated EDX semiconductor detector based on a p-n junction diode and placed within the SEM (or TEM) chamber, inducing electronic valence-conduction transitions in the semiconductor material [247]. The so-formed conduction electrons are then drawn away through a potential difference, and the current is converted into an X-Ray counting signal as a function of incident X-Ray energy by the detector's electronics [247]. Superimposed on the characteristic X-Rays, EDX spectra show a background signal originating from what is called Bremsstrahlung radiation. This signal originates from the repulsive field that the beam electron experiences from the electronic cloud in the target material. This repulsion deflects and decelerates the beam electrons, which consequentially lose energy in the form of a continuum of X-ray radiation spanning energies from about 100 eV up to the electron beam energy. Such noise is usually not high compared to characteristic X-Rays. Nonetheless, its intensity increases for high Z elements, especially at low energies [246], and can hinder or even make impossible the identification and quantification of signals belonging to light elements.

2.5.2.2 LIMITATIONS OF EDX

One major limitation of EDX involves the poor sensitivity for light elements. This deals with the fact that the number of electrons generated by the detector, and hence the photon counts reproduced by the detector) is proportional to the energy and intensity of the

incident X-Rays. Light elements generate much less intense and less energetic X-Rays than heavier elements, therefore lower X-Ray photon counts are collected from light elements than from heavy elements. Besides, the relatively intense background signal from heavy elements could hide the characteristic X-Rays produced by light elements. This is the main reason for which light elements such as Carbon, Nitrogen and Oxygen are inefficiently detected if present in small amounts and/or in presence of heavy elements (see for example the low-energy portion of the spectra in **Figure 29**). Another important limitation of EDX consists in the poor energetic resolution. Normally, EDX semiconductor detectors have energetic resolutions of about 100 eV, owning to the process by which the signal is received and processed. Such resolution is enough to discriminate most of the spectral lines of different elements, so it does not constitute a concern for qualitative analysis. Nevertheless, it can be a problem for quantitative analysis if the main peaks of a given signal overlap (such as the Si Kα and W Mα lines in **Figure 29**). The poor energetic resolution also allows only the quantification, in the best case, of the total relative amount of the elements making up the specimen, but EDX is completely blind to fine energetics discrepancies between atoms of the same element in a different oxidation state or coordination, where the energy differences are on the order of a few eV down to a few tens of milli eV.

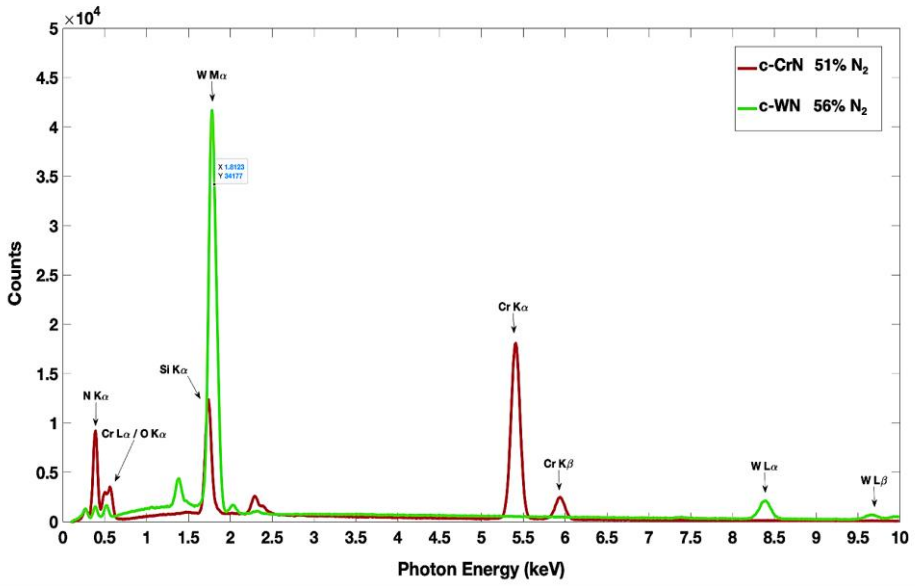

***Figure 29**: EDX spectra collected for two distinct samples consisting of CrN and WN coatings 1 micron thick. The Nitrogen percentage in the two materials was quantified as 49% for CrN and 55% for WN. From the spectra, it is possible to observe the overlap at 1.75 keV of Si ka (red curve) and W Ma lines (green curve). Also, the masking of light element signals due to the presence of Tungsten is higher than in the presence of Chromium (see Nitrogen and Oxygen lines at 0.3-0.5 keV).*

2.5.3 X-RAY PHOTOELECTRON SPECTROSCOPY

2.5.3.1 FUNDAMENTAL ASPECTS

X-ray photoelectron spectroscopy (XPS), also known as electron spectroscopy for chemical analysis (ESCA), represents the most widely used electron spectroscopy method for investigating the elemental composition and/or speciation of any solid substrate and surfaces [280]. The physical phenomenon behind XPS is the emission of electrons from surfaces irradiated by electromagnetic radiation of suitable energy. This effect was first discovered by Hertz at the end of the 19th century and later physically formalized by Einstein in 1905, who was accordingly awarded the Nobel prize in physics in 1921 [281]. Nonetheless, the bulk of the work to develop the XPS technique we know today was due to Kai Siegbahn, in the 1950s and 1960s [282], with the first XPS machinery only introduced in the early 1970ies, driven by a strong industrial interest [283]. Nowadays, XPS is probably the most used method for qualitative and quantitative elemental characterization materials on the nanometer-depth scale in both academia and industry [284]. A schematic representation of the photoemission process and of the energy levels involved is reported in **Figure 30-A** and **Figure 30-B**, respectively. Photoelectric emission takes place only if the energy transferred from the incident radiation exceeds the minimum energy required to extract an electron from its bound state [246], [285], the excess energy being carried by the photoelectron in the form of kinetic energy. Thus, knowing the incident X-Ray radiation energy, $h\nu$, the binding energy of electrons E_b can be calculated by subtracting the measured kinetic energy from the incident X-ray energy. The only small correction to this simple statement is that the work function of the instrument φ must be considered. Hence, the correct formula correlating these quantities is [280], [282]:

$$E_b = h\nu - E_K - \varphi \qquad (2\text{-}8)$$

A more detailed discussion on the physical meaning of the binding energy calculated in XPS analysis, taking into account the so-called “final state” assumption, can be found in ref. [285]–[287], but it is beyond the scope of this introduction and will be no further treated. The kinetic energy is the quantity measured in XPS experiments, and it is a function of the binding energy, which is discrete and element and environment specific

[280]. This specificity permits the unique identification of elements and their chemical environment and constitutes the most important feature of XPS.

Qualitative XPS measurements are based on **Equation (2-8)**. By confronting the binding energy of a spectral line with databases, the chemical species originating the signal can be accurately identified. The correct identification, though, requires accurate energy scale calibration to compensate for any shift introduced by the measurement procedure. This is done by first recording the energy lines of inert metals such as Au 4f lines or by using the C 1s peak of adventitious carbon, always present because of air exposure [285]. The latter is also used for compensating charging of insulating samples under photoemission.

Once the photoelectron has been emitted, the system will tend to relax in two possible ways (**Figure 30-A**). One is a radiative fluorescence process in which x-rays are emitted by direct decay of an outer electron into the core level left vacant from the photoelectron. This effect is of little use in XPS. Another relaxation pathway involves first a radiative decay of an electron into the electron hole, followed by the reabsorption of the emitted radiation from another outer electron of lower energy, which is then emitted. This auxiliary photoemission process is called Auger emission. Auger Electron Spectroscopy (AES) is an important spectroscopic tool in XPS, helping the identification of elements in the specimen, but will not be developed further in this introduction.

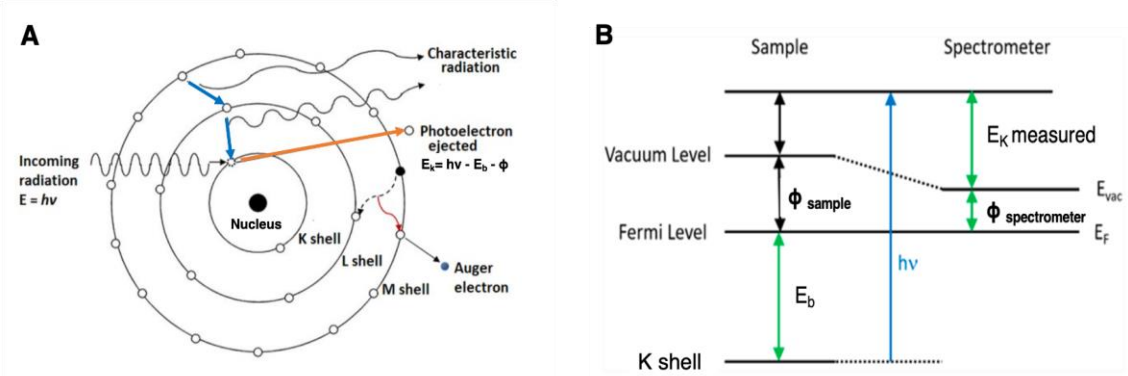

***Figure 30**: A) Atomistic representation of the photoemission process with the possible relaxation pathways; (B) Energy diagram for the definition of the binding energy. The use of the spectrometer work function derives from the fact that the kinetic energy of the photoelectrons is calculated by the spectrometer's detector, which has its energetic references (readapted from* [282] *)*

The popularity of XPS for the chemical characterization of materials in both academy and industry stems from the following possibilities:

- High surface sensitivity enables the collection of useful signals from 1-10 nm beneath the specimen surface.
- High spectral resolution enables the identification and quantifications of elements in a different chemical environment.
- High sensitivity, elements in a small fraction as less than 0.1-1% being detectable, the exact value depending on several factors like the noise generated by each element [288].

The high surface sensitivity is due to the electron mean free path in solid materials being less than 10 nm, the exact value depending on the kinetic energy and the material's density. Despite X-Rays can penetrate microns beneath the specimen surface and produce photo-emitted electrons, the particles produced deeper than their statistical mean free path will lose their energy through interactions with the solid[289]. Hence, even if they can escape the specimen, their kinetic energy has lost any connection with the binding energy and contributes to the noise signal [289]. The spectral resolution depends on several factors, such as the x-ray source used, the photoemission width, and the energy analyzer. Of these, the energy spread of the x-ray source is the most fundamental factor and depends on the kind of x-ray radiation.

2.5.3.2 X-RAY SOURCES FOR XPS

X-ray sources can be classified into standard, and synchrotron sources. Synchrotron sources offer several benefits over standard sources [284]. First, the higher brilliance of synchrotron radiation permits an enhanced monochromatizating of the radiation over standard sources, while maintaining the received signal high enough for fast material characterization with a high signal-to-noise ratio. Also, the availability of a continuum of X-Ray energies allows to optimize the energy of the probe X-Ray radiation to maximize the sensitivity of transitions of each specific sample material. In contrast, standard sources produce X-Ray radiation of specific energy by bombarding a target with high-energy electrons in an X-Ray tube. Following this bombardment, electrons in the target are

ejected and a relaxation process leads to the production of characteristic X-rays. By applying energy filters, the most intense emission line can be selected and conveyed towards the sample for the photoemission process. Despite the evident benefits of synchrotron-based sources over conventional sources, the latter are much more diffused than the formers, due to the limited availability of synchrotron facilities.

Two characteristics of X-Ray radiations are very important in XPS, namely the peak energy and the energy spread. The peak energy defines the maximum energy that can be provided to the sample, so the maximum binding energy that can be overcome or, in other words, the most tightly bound electron in the specimen which can be ejected. The energy spread is the distribution of X-Ray energy around the peak energy and must be the smallest as possible as it defines the spectral resolution. The applications of quartz diffractive monochromators can greatly reduce the energy spread, at the cost of higher machinery costs, lower x-ray fluxes, and longer scan times. Al and Mg sources, whose characteristics are reported in **Table 4**, present the best combination of peak energy and energy spread, and are therefore the most used.

Table 4: Some standard X-ray sources with the main specifications in comparison. The colour code goes from optimum (green) to medium (yellow) to worst (red)

Anode	Z	Emission line	Peak Energy (eV)	Energy Spread (eV)	Energy Spread (eV) Monochromatized)
Y	39	Y-M ζ	132.3	0.47	
Mg	12	Mg- K α	1253.6	0.7	0.15-0.25
Al	13	Al - K α	1486.6	0.85	0.2-0.3
Ag	47	Ag-L α	2984	2.6	0.92

2.5.3.3 THE HEMISPHERICAL ENERGY ANALYZER

Another factor contributing to the excellent energy resolution of XPS is the employment of hemispherical electron energy analyzers (HEEA) for the selective collection of the incoming photoelectrons [280], [285]. HEEA, whose sketch is shown at the left-most part of **Figure 31**, consists of two concentric hemispheric electrodes that, by applying an electric field, bend the trajectories of the electrons entering a narrow slit at one end so that their final radii depend on their kinetic energy. When X-rays impinge on a surface, photoelectrons of all energies up to the incoming X-ray radiation will be ejected in all

directions. Of these, only those ejected at the acceptance angle of the spectrometer will be analyzed. To improve the energy resolution, all accepted electrons are retarded before they enter the HEEA as they pass through a column where they are decelerated from the initial kinetic energy E_K^0 to final kinetic energy using an electric potential, so that:

$$E_K^{in} = E_K^0 - eV_{dec} \tag{2-9}$$

At the same time, the HEEA electrode potentials are set in such a way that only electrons entering the hemispherical analyzer with a certain kinetic energy, called the "pass energy", will be focused onto the detector at the other end of the spectrometer. The decelerating field at the entrance column is gradually tuned to provide a different decrease in kinetic energy so that photoelectrons arriving with different kinetic energies will match the pass energy and will reach the detector at the exit of the HEEA. The value of the pass energy is usually set between 5 and 150 eV. The larger the value, the poorer the energy resolution and the higher the signal intensity, and vice versa. At the exit of the HEEA, a multichannel detector collects electrons in specific positions, which allows counting passing electrons as a function of their kinetic energy. Energy analyzers do not have the same sensitivity for all energies and this results in differences in peak intensities which do not merely depend on the relative elemental abundancy [290]. This nonuniformity is considered by the transfer energy function of the analyzer, which must be empirically determined for accurate quantitative characterization purposes.

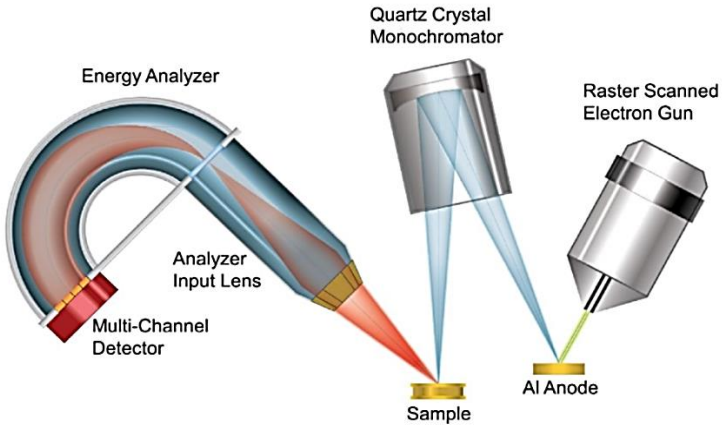

***Figure 31**: Representation of the fundamental elements of an XPS setup, including the electron gun, the monochromator system and the hemispherical energy analyzer connected to the multichannel detector for precise spectral separation.*

2.5.3.4 SPECTRAL INTERPRETATION AND THE CHEMICAL SHIFT

Spectral lines for photoelectrons are conventionally reported in the form "$X\ nl_j$", where X denotes the element, n and l refer to the first and second quantum number respectively and j is the spin-orbit coupling, given by $J = l + s$, with l being the second quantum number ($l = 0 \ldots n-1$) and s the spin number ($s = \pm 1/2$) [284], [285].

With exception of lines coming from s states (l=0), all other spectral lines have a form of doublets (**Table 5**). The origin of the doublet is due to the two different values of total angular momentum arising from spin-orbit coupling, namely $J_1 = l - s$ and $J_2 = l + s$. The ratio between the areas of the two peaks of a doublet is theoretically by the degeneracy of the two spin-orbit states, which is given by the 2J+1 values, from -J to +J increasing by integer steps [285]. In practice, the actual ratio can deviate from the prediction, depending on the chemical environment of the parent element. Doublet peaks correspond to electronic states of different binding energies; hence they are separated by an energy gap, whose magnitude depends on the element and its chemical state.

***Table 5**: XPS spectral lines and the associated spin-orbit number, degeneracy, and doublet intensity ratio.*

Shell	Line "nl $_J$"	J = l ± s	Degeneracy (2J+1)	Peak ratio (J_2:J_1)
s	ns $_{1/2}$	0 +1/2 = 1/2	2	ND
p	np $_{3/2}$	1+ 1/2 = 3/2	4	2:1
	np $_{1/2}$	1 - 1/2 = 1/2	2	
d	nd $_{5/2}$	2 + 1/2= 5/2	6	3:2
	nd $_{3/2}$	2 - 1/2 = 3/2	4	
f	nf $_{7/2}$	3 + 1/2 = 7/2	8	4:3
	nf $_{5/2}$	3 - 1/2 = 5/2	6	

The fundamental point is that each element has a specific set of associated core-level peaks that allow unambiguous identification of the element, while the precise binding energy at which peaks are located depends on the chemical environment for that element. The blue or red shift of peak lines is called a *chemical shift*. The chemical shift of an XPS spectral line is caused by changes in the electron binding energies [291]. These changes may depend on the oxidation state of the element from which the photoelectron is extracted, on the proximity of elements with different electronegativity or, to a minor extent, on a different coordination state. Both cause impact on the effective electrostatic

attraction of the electron to their parent atoms, end hence on their binding energy. In most cases, a blue shift is encountered, meaning a shift towards higher binding energies due to the chemical, electrostatic or physical bonding with electronegative species such as oxygen, Nitrogen, and halogens elements. These atoms exert an attractive force on the valence electrons of most metals, resulting in a displacement of such electrons and hence in an enhancement of the net electrostatic attraction of core electrons to the nuclei, which ultimately is reflected into higher electron binding energy (**Figure 32**).

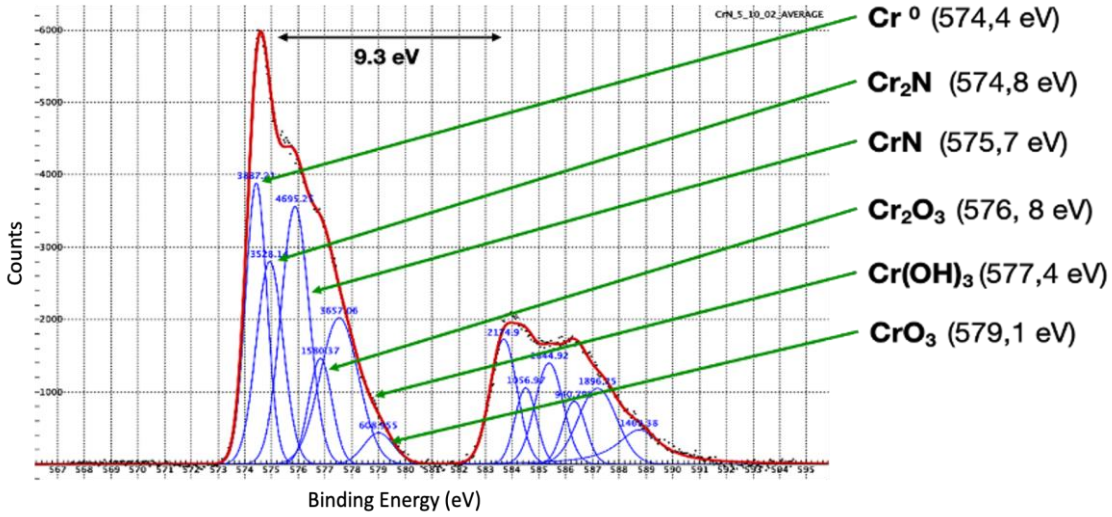

***Figure 32**: XPS spectrum of the 2p lines of a Chromium Nitride (CrN) film. The experimental points are represented by black dots, the blue curves are individual fitting components, and the red curve is the total fit to the experimental data. Each contribution is shown on the right with the corresponding binding energy* [67]. *In general, by increasing the electronegativity of the chemical environment the energy of the Cr 2p electron shifts towards higher binding energies.*

2.5.3.5 QUANTITATIVE ANALYSIS WITH XPS

A major advantage of XPS consists in its ability to provide quantitative information on the chemical composition of the specimens. For the quantitative analysis (QA) to be accurate and reliable, several factors should be considered. These include knowledge of the characteristics of the instrumental apparatus in use, such as the analyzer calibration status, the sensitivity factors and the geometry of the x-ray source-sample-detector system, the level of accuracy needed, prior knowledge of the sample and proper treatment and interpretation of experimental data [285], [287], [290], [292]. The instrumental characteristics are usually known and very important if one needs to compare measurements from different XPS setups. If a single machine is used, then the only relevant requirements for materials identification are the X-ray source used and the

sensitivity factors of the analyzer [290]. The knowledge of the sample is necessary to estimate the spectral range of interest and the possible occurrence of phenomena like multiple peaks due to different oxidation states, peak contributions due to scattering losses [290], shake-up and shake-op features [293] peak asymmetries due to charge build-up [292]. The treatment of the experimental data can be non-trivial. It is important to properly subtract the background by using a proper model, usually linear, Shirley or Tougaard [285], but in any case, some error can be introduced, the relevance of it depending on the requested degree of accuracy. It is quite common to have the necessity of quantifying chemical species whose relevant x-ray peaks are overlapping. The most common case involves the separation of spectral lines originating from the same element in different oxidation states, which usually differ in fractions to a few eV and are not efficiently resolved, especially if traditional and non-monochromatized X-Ray sources are used (see for example **Figure 32**).

Quantitative XPS data are usually reported as atomic percentages. If the sample is homogeneous and single phase, which is an assumption non necessarily corresponding to the real case, and no reference of pure substances is available [287], one can use the following procedure to estimate the elemental composition of the specimen:

1. Select the most intense peak for each element detected from survey spectra which is attributed to the sample (exclude any external contaminants)
2. Fit the experimental data of each peak with proper background removal
3. Determine the area of the background-corrected peak giving the peak intensity I_i
4. Divide each peak Intensity by its sensitivity factor, S_i
5. Calculate the relative abundance of a given peak (element) as [285], [290]:

$$X_i(\%) = 100 * \frac{\frac{I_i}{S_i}}{\sum_{j=1}^{n} \frac{I_j}{S_j}} \qquad (2\text{-}10)$$

The XPS sensitivity Factors, S_i, are empirically derived factors (from compounds of known composition), specific for each core-level peak, by which peak intensity is normalized to provide an atomic concentration. A common approximation for S_i is to

substitute this with the product of the photoemission cross-section of the incident x-ray for each relevant electronic state, σ_i, by the inelastic mean free path (IMFP) λ_i [294], [295] [285], [290] . The photoionization cross-section, also known as the Scofield factor, represents the probability that a photon of given energy provokes the photoionization of a target electron in each orbital. Scofield factors have been calculated and tabulated for all elements using Al and Mg X-Ray sources [286], [296]. The IMFP is defined as the mean distance travelled by a charged particle between consecutive inelastic collisions within the medium [297], which depends mainly on the photoelectron energy and, for energies above 50 eV is almost independent of the material it passes through, according to the so-called "Universal Curve" [298], whose values are tabulated. Both cross-sections and IMFP are tabulated in databases for given X-Ray energies and materials' density [287], [290]. A further improvement is accomplished by adding the experimentally calculated value of the instrumental energy transfer efficiency at each peak line, to include the different instrumental sensitivity to electrons of different energies [285]. By this approximation, $S_i \approx T(hv) * \sigma_i * \lambda_i$.

2.6 SURFACE TOPOGRAPHY VIA ATOMIC FORCE MICROSCOPY

2.6.1 A TOOL TO PROBE INTERATOMIC FORCES

Atomic Force Microscopy (AFM) is a type of Scanning Probe Microscopy (SPM) invented in 1986 by Binnig et al. [299]. A few years earlier, in 1982 Scanning Tunneling Microscope (STM) was proved to be able to provide atomic resolution images on conductive samples by exploiting the exceptional sensitivity of the tunnelling current on the tip-sample distance [300]. Already in 1987, atomic resolution imaging was accomplished also with AFM [301], with the remarkable advantage of being a kind of SPM suitable to investigate both conductive and insulating samples, while providing true topographical images, where STM was mapping a combined outcome of topography and local density of states of specimens [300], [302], unless the local work function is constant [300]. Nowadays, AFM is used to investigate the surface topographical features of any kind of materials, such as metals [303], [304], ceramics [305] and hard coatings[306], soft materials [307], composites [308] and even biological systems [309], [310].

The idea behind the AFM consists in approaching a tip, located at the end of a microfabricated cantilever, either very close to (within a few angstroms) or "touching" the specimen's surface, measuring the interaction forces between tip and specimen by means of the bending of the cantilever [311] and translating such measured forces into a topographic image of the specimen. The total force acting on a tip due to the tip-sample interaction is made up of two distinct components, namely long-range attractive forces due to van der Waals, which prevail over distances of a few nanometers, and short range repulsive forces arising from charge overlap and Pauli exclusion principle at distances of typically less than 5 Å [311].

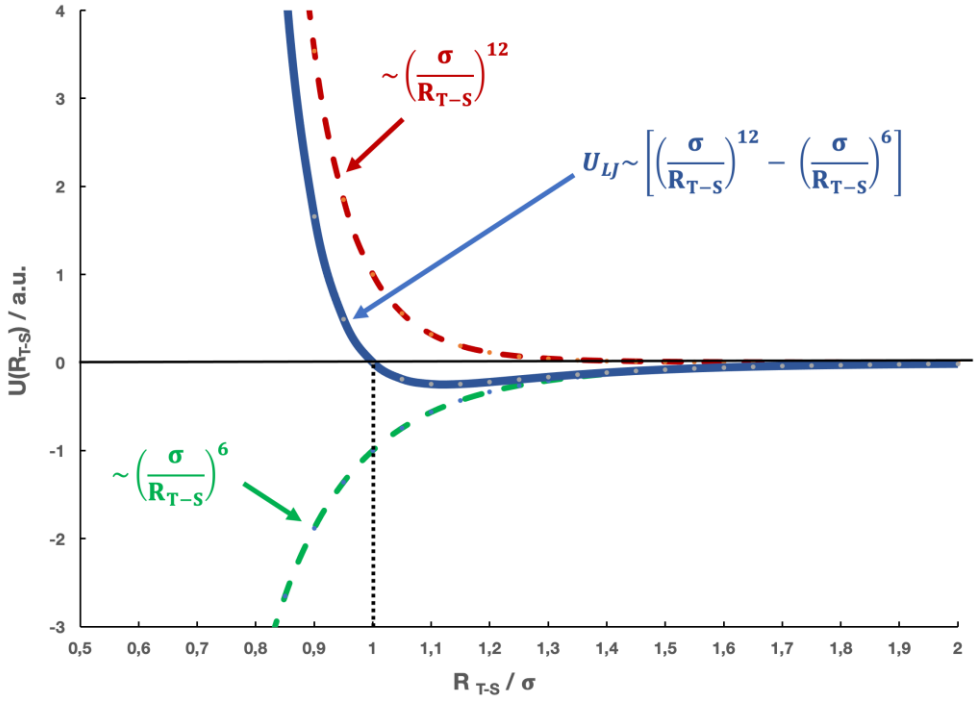

***Figure 33**: Representation of the typical trend of tip-sample potential energy as a function of tip-sample distance. Attractive and repulsive contributions are highlighted. Tip-sample distance is reported relative to the distance σ where the potential energy changes sign.*

The general cumulative behavior of attractive and repulsive forces as a function of tip-sample distance can be depicted by the well-known Leynard-Jones (LJ) potential curve represented in **Figure 33** and given by the following expression:

$$U(r_{ij}) = k\varepsilon * \left[\left(\frac{\sigma}{r_{ij}}\right)^{n} - \left(\frac{\sigma}{r_{ij}}\right)^{m}\right] \qquad (2\text{-}11)$$

Where n and m are selected positive integers where n > m (in LJ potential n=12 and m=6), k is a constant calculated from n and m, r_{ij} is the distance between particles, σ the interparticle distance where the potential changes its sign. The gradient of the potential with the distance between particles gives the average interparticle interaction force.
In general, both attractive and repulsive contributions act simultaneously, but the average predominant contribution depends on the tip-specimen distance. As will be briefly discussed in the following sections, several ways to correlate the measured tip-sample forces to variations in topographic features have been developed, each one with its own advantages and limitations.

2.6.2 AFM SYSTEM SET-UP

Typically, AFM systems are constituted by the elements and descripted in **Table 6** and represented in **Figure 34.**

***Table 6**: Elements of a typical AFM set-up*

Element	Description
PROBE:	A sharp tip typically made of silicon, silicon nitride or diamond mounted at the end of a microfabricated cantilever made of silicon or sapphire, sometimes back coated with Au or Al.
OPTICAL DETECTION SYSTEM	A laser is focused onto the back of the cantilever from which it is reflected and directed by a mirror system onto a 4-quadrants PSD to detect vertical and lateral displacement of the cantilever
FEEDBACK SYSTEM	Some physical parameters whose variation from a predetermined set-point as a function of the tip-sample interaction is recorded by the PSD and transmitted to instruct the piezo movement
SAMPLE-TIP ADJUSTMENT TOOL	A piezoelectric actuator which translates the feedback signal into a x-y-z motions of the cantilever- specimen relative to follow the specimen profile and to raster scan the specimen surface. It can be attached at the cantilever unit or beneath the specimen.
COMPUTER UNIT	The feedback loop is controlled automatically by a software unit. Scanning parameters and feedback set-point can be adjusted by the user while the scanned surface is live shown on the screen.

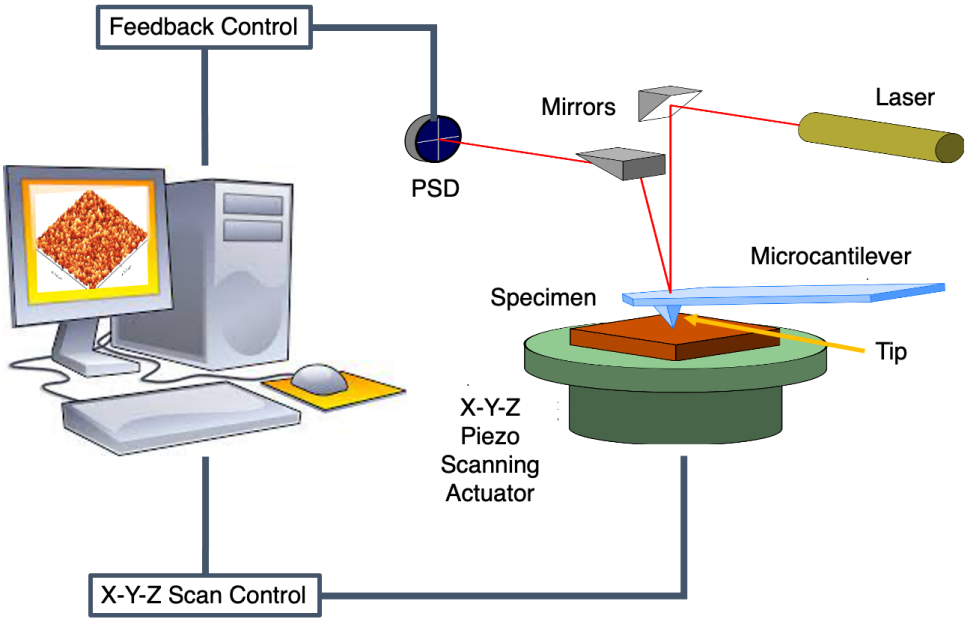

***Figure 34**: Schematic representation of the elements constituting an AFM imaging system*

2.6.3 AFM IMAGING MODES

Since its invention, AFM imaging has evolved in such a way to exploit the attractive or repulsive force regimes to gather information on the specimen's surface.

2.6.3.1 CONTACT AFM

The first AFM imaging modality was the static or contact mode (C-AFM). In this mode, the probe is approached to the specimen until a contact is established, and the image is performed by raster scanning a predetermined specimen surface area by moving the sample through the piezoelectric actuator. Commonly, C-AFM works in constant force or deflection feedback mode, in which the cantilever deflection is set by the user and constitutes the feedback parameter. The deflection was originally measured by a back-placed STM, later substituted with an optical system involving a focused laser beam and a position-sensitive photodiode detector (PSPDD), ensuring a series of advantages over STM deflection modes [312]. The piezo-driven sample adjustments imposed by the feedback to restore the set-point cantilever deflection in response to the surface profile are used to reconstruct the surface topography[301]. The main risk with C-AFM is to damage both the tip, especially with rough samples surfaces [311], [313] or the specimen itself, particularly if it is of biological or soft materials [313].

2.6.3.2 NON-CONTACT AFM

Non-contact AFM (NC-AFM) was introduced just a year later than contact AFM [314]. The AFM tip is kept at distances on the order of the nm from the sample, in an effective attractive regime. The cantilever is vibrated at a frequency close to its natural frequency, defined as $\omega_0 = c\sqrt{k/m}$, with k being the elastic constant of the cantilever and m its effective mass, at a given amplitude, which is a function of its natural frequency. By approaching the sample, the attractive forces arising between tip and sample modify the effective force acting on the cantilever, which translates into a change in its frequency and amplitude. The amplitude variation as a function of the tip-sample distance is recorded by a laser-PSSD system and used as a feedback parameter [314]. The image is therefore built based on the sample displacement necessary to restore the set-point amplitude of the cantilever. The main benefit of NC-AFM imaging is the minimized damage of both tip and samples compared to C-AFM. Nonetheless, due to the relatively long distance between tip and sample as well as the long range of van der Waals forces, the convolution effect reduces the maximum lateral resolution achievable [315]–[318]. Due to the different distance ranges, attractive forces are delocalized on several atomic distances, while repulsive forces are localized at the atomic level. This implies that with AFM, a true atomic resolution requires working in a pure repulsive regime, i.e., in contact mode. Such modality has the major drawback of exposing the sample and, more importantly, the tip, to be damaged by sudden vertical drops or surface asperities[311]

2.6.3.3 TAPPING-MODE AFM

An imaging modality lying between the contact and the non-contact mode, known as dynamic or semi-contact or tapping mode AFM (TM-AFM) [319], [320] was developed to retain a high lateral resolution and at the same time minimize the risk of tip or sample damage thanks to the application of small, intermittent vertical contact [313], [320]. Analogously to NC-AFM, in TM-AFM the cantilever is sinusoidally driven at a frequency close to its natural frequency (experimentally determined) and put into oscillation. The cantilever's vibration amplitude constitutes the feedback parameter used to build the image, its value depending on the interaction between the tip and the sample.

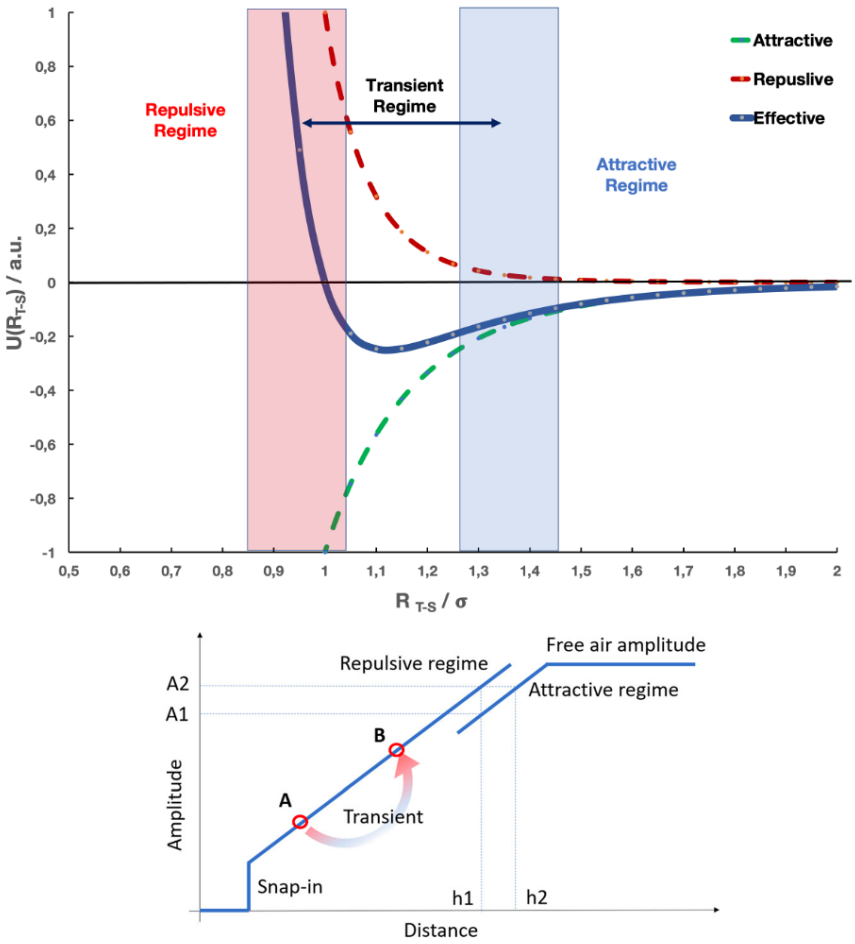

***Figure 35**: A) Interaction regimes as a function of the tip-sample distance and (B) oscillation amplitude modifications in the different interaction regimes during a TM-AFM cycle defined by points A and B. Beyond the attractive regime, the cantilever frequency is independent of sample-tip distance and oscillates at its natural frequency. By approaching the sample, the amplitude is reduced by the attractive interactions. Once in contact, a sudden drop of amplitude (snap-in) is observed due to the repulsive forces impeding the cantilever approach (readapted from* [320])

Unlike NC-AF, during the approaching semi-cycle of its oscillation, the tip gets in contact with the specimen. Hence, tapping mode AFM works in a transient force regime (**Figure 35**) between attractive forces (used in C-AFM) and repulsive forces (used in NC-AFM mode). AFM is nowadays the most general-purpose imaging mode with AFM. Usually, it is used to derive topographical information and phase contrast information, based on the elastic response of the specimen which can anticipate (stiff materials) or retard (compliant materials) the oscillation of the cantilever [321]. A mechanistic description of the transient behavior of TM-AFM describing the non-linear relationship of the oscillation amplitude with tip-sample distance and the possible image artifacts originating from this is provided in ref. [320].

2.7 MECHANICAL CHARACTERIZATION VIA NANOINDENTATION

2.7.1 A BRIEF INTRODUCTION TO INDENTATION METHODS

The mechanical properties of materials play a fundamental role when components are subjected to high external forces. The most relevant mechanical properties for a system consisting of a coating and a substrate material are microhardness, elastic modulus, and coating-to-substrate adhesion. The hardness and elastic modulus are of primary interest for coatings technology, as they are intimately linked to the wear resistance of a coating. The hardness has long been considered the main property affecting the wear resistance of coatings. Nonetheless, it is now accepted that hardness alone is not a good predictor of the tribological behavior of protective coatings. Rather, some reciprocal relationship between hardness and elasticity constitutes a much more effective indicator. The main ones are the H/E and H^3/E^2 ratios, which are correlated with the elastic strain to break and with the resistance to plastic deformation, respectively [322]–[324]. The Modulus of elasticity is defined as the ratio between the applied load and the elastic (i.e., reversible) deformation that the load produces on the specimen. Brittle materials such as ceramics are characterized by high elasticity, on the order of hundreds of GPa. In general, stiffer materials having high elastic modulus are also characterized by high hardness values. Hardness is defined as the resistance of a material to localized plastic deformation [325]. Hardness and modulus of elasticity are measured by a class of techniques comprehensively acknowledged as Indentation tests. In general terms, an indentation test consists of the application of a load to a probe, which usually is a diamond tip, which is then pressed onto the surface of a material with a certain loading rate, i.e., the velocity at which the mechanical load exerted by the tip to the specimen, is increased. Depending on the peak load, i.e., the maximum applied load, and on the intrinsic properties of the test material, the tip will penetrate inside the latter until a certain depth. Based on the penetration depth reached, hardness tests are subdivided into macro-indentation tests, micro-indentation tests, and nano-indentation tests [325].

The first classification of materials concerning their abrasion resistance can be attributed to Friedrich Mohs, which introduced the Mohs scale in 1812, it was not until the 1850ies that the first indentation machinery and methods were introduced, prompted by the industrial revolution [326]. Since then, a large variety of hardness-measuring techniques

commonly known as indentation tests have been established to routinely assess the quality of products in the new aeronautic, automotive, and machine tool industries [325]. The industrial impact of indentation tests received another huge boost during World War I, World War II, and all through the Cold War era, where macro-indentation and later micro-indentation tests had a big role in controlling the quality of war machines, guns, and aerospace machinery.

The first scientific basis of tribology and indentation was established by the pioneering work of Tabor, mathematically and physically describing the indentation process [327]. Comprehensive descriptions of the main methods and the basic equation through which the mechanical properties are measured are provided in the literature [325], [328]. Here, only the two methods employed for the development of the research work will be introduced in the following paragraphs, namely the Vickers and Rockwell-C tests.

2.7.1.1 VICKERS HARDNESS TEST

In Vickers hardness tests, a square pyramid-shaped diamond tip is impressed into the test materials under loads of about 10 to 1000 N (**Figure 36**). The hardness is defined as the ratio between indenter load L and the actual surface area of the impression, A_c.

$$HV = \frac{L}{A_c} = \frac{2L}{d^2} * \sin\frac{136°}{2} = 1.8544\frac{L}{d^2} \ [\frac{kgf}{mm^2}] \tag{2-12}$$

Where L is measured in kgf and *d*, in millimeters, is the length of the diagonal measured from corner to corner of the residual impression on the specimen surface with the aid of a microscope.

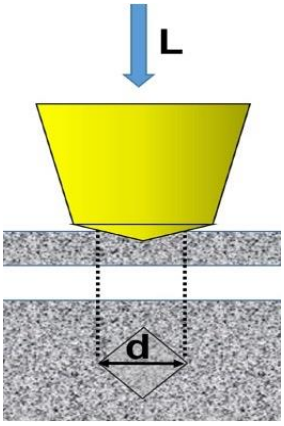

***Figure 36**: A sketch of a Vickers hardness test*

2.7.1.2 ROCKWELL HARDNESS TEST

In Rockwell hardness tests, the hardness is determined through a two-step routine consisting of a low-load penetration (pre-load step) and a high-load penetration (**Figure 37**). The use of a pre-load has the advantage to remove errors in the measurement of the penetration depth arising from surface imperfections. It sets the "zero" depth value for the indentation measurement. Usually, the preload is 10 N, while standard main loads are 60, 100 or 150 N. Rockwell hardness is defined as:

$$HR = N - 500 * h \tag{2-13}$$

Where h is the penetration depth under the main load, and N is a value depending on the indenter's shape and equal to 100 for sphere-conical indenters and 130 for ball indenters. Hardness values are directly read from dials implemented in Rockwell Indenters [327]. Depending on the pre-load, main load, and the indenter shape and size, several Rockwell tests have been standardized. Each method is identified by a letter. For example, the three major Rockwell tests using sphere-conical indenters with 120°C aperture and curvature radii of about 200 nm are reported in **Table 7**.

***Table 7**: Rockwell tests using a sphere-conical indenter*

Scale	Name	Indenter	Load (kgf)
A	HRA	Sphere-conical diamond, 120°	60
C	HRC	Sphere-conical diamond, 120°	150
D	HRD	Sphere-conical diamond, 120°	100

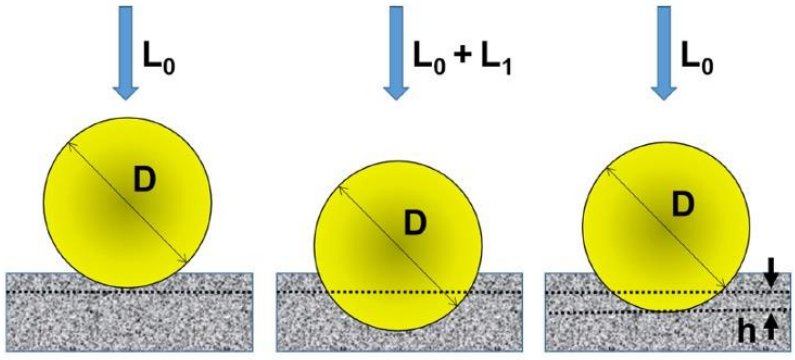

***Figure 37**: Sketch of a Rockwell test. The tip shape is spherical or sphere-conical. L_0 represents the pre-load and L1 the main Load, where h is the penetration difference occurring after the application of L_1.*

Rockwell-C test is also used for a qualitative evaluation of coatings' adhesion on the substrate, a method known as the Daimler-Benz test [329]–[331]. Depending on the contour features of the residual indentation mark, coatings are ranked into one of the six or four categories defined by the DIN 4856 or ISO 26433 standards, respectively [331] . The DIN 4856 categories are sketched in **Figure 38**. The adhesion is not a property of the coating alone, but rather a property of the coating-substrate system[332]. When the adhesion between a coating and the substrate is good, the shear forces imposed by the indentation will be dissipated within the coating in the form of cracks, a phenomenon known as cohesive failure [329]. In the case of low adhesion, the coating-substrate interface constitutes the weaker point of the system. In such condition, if the indentation load exceed some critical value, adhesive failure occurs and coatings delaminate [333].

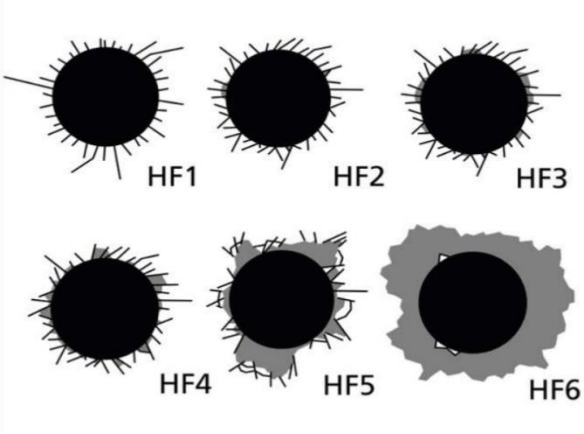

***Figure 38**: Classification of the indentation imprint from a Rockwell-C test according to the DIN 4856 Standard protocol.*

2.7.2 FROM MACRO- TO NANO-INDENTATION

Before the advent of micro- and nanotechnologies, indentation tests were uniquely used to test the bulk properties of massive materials. Such tests used indentation loads as high as a few hundreds of Newtons and impressed areas a few millimeters-wide and hundreds of micrometers deep. The most diffused techniques were, in decreasing order of applied load, Brinell, Rockwell and Vickers tests, employing spherical, spherical, or sphere-conical and squared-pyramid shaped tips respectively. Micro-indentation emerged when thin film-based technologies arose in the second half of the 20th century. Conceptually analogous to macro-indentation tests, the main difference resides in the load range applied

to the test materials. With micro-indentation, the load is lowered down to less than 2 N, with penetration depth as low as a few hundreds of nanometers and indentation areas of the order of micrometers [325], [327], [334]. The most common techniques are Vickers and Knoop indentations, both employing square-pyramid-shaped tips but with different apex angles. The localized and small-scale features of micro-indentation tests are much more sensitive to vibrational noise, hence sophisticated microelectronics is employed to control the vertical displacement and applied loads with vertical resolutions of fractions of nanometer and force resolutions of fractions of millinewton. The application of indentation testing to the nanometer regime has been widely explored in the last decades. This was promoted by the increasing interest in low-dimensionality materials such as 2D materials such as graphene and dichalcogenides and protective thin-film coatings. Atomic Force Microscopy (AFM) is usually employed in the former case thanks to its ability to perform nanoindentations with indentation loads in the micro to pico-newton regimes with practically atomic resolution in the load direction and on the in-plane direction [335]–[337]. On the contrary, the AFM technique is still unsuitable to perform hardness evaluation on hard materials, although several reports exist on the AFM-based measurement of hardness on soft metals [338] and stiffness values of hard materials [69], [304]. So, the measurement of hardness and elastic modulus of thin and hard materials is nowadays performed by nanoindentation tests employing diamond tips with standardized conical or pyramidal shapes as shown in **Table 8**.

***Table 8**: tips used in Vickers Indentation and the corresponding area functions (readapted from* [339]*)*

Indenter	Tip Shape	Area Function
Berkovich	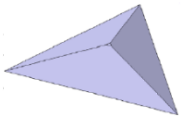	$24.68*\mathbf{h_c}^2 + 0.562*\mathbf{h_c} + 0.00322$
Vickers	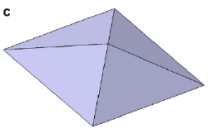	$24.56*\mathbf{h_c}^2 + 0.599*\mathbf{h_c} + 0.00322$
Conical	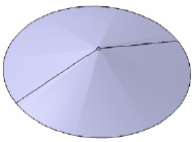	$24.50*\mathbf{h_c}^2 + 0.559*\mathbf{h_c} + 0.00032$

Conceptually, the working principle of nano-indenters is analogous to conventional indenters or micro-indenters, in the sense that a diamond tip is pressed onto the test materials (**Figure 39**) and hardness and young modulus are extracted by knowledge of the impression area, the maximum applied load and the unloading stiffness.

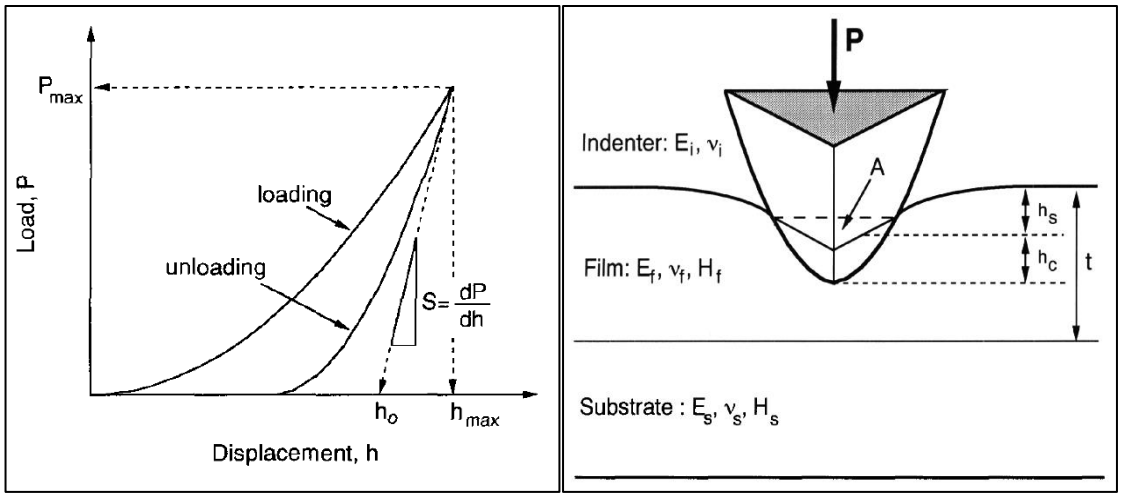

***Figure 39**: a) typical loading-unloading curve of an indentation experiment with typical quantities. b) Sketch of an indenter penetration into a coating material. Here, $h_{max}= h_s + h_c$. Reproduced from* [340].

The difference is that in macro and first micro indentation routines, the measurement protocol involves the sequence of tip indentation followed by a microscopy-based measurement of the indentation mark and post-measurement analysis of the unloading curve for the calculation of the Elastic modulus. Instead, in nanoindentation tests, the tip displacement and applied load are continuously monitored during the whole loading-unloading curve with high precision using advanced microelectronics controls [341]. The impression area is derived by applying surface area functions [342] that, for a given tip shape, provide a value for the impression area A as a function of the penetration depth h. Such a method was introduced by Oliver and Pharr in the early 90ies and is known as the Constant Stiffness Measurement (CSM) or Oliver-Pharr method [342], [343]. CSM provided a significant improvement in nanoindentation testing accuracy, especially when probing thin film coatings [340]–[342], [344]. CSM consists of the measurement of the contact stiffness during the whole loading-unloading curve, rather than solely at the onset of the unloading step, as done in conventional instrumental indentation testing (IIT) methods. This is also a major improvement in testing soft materials such as polymers, for

which the unloading curve is strongly nonlinear and conventional IIT approaches would yield deeply inaccurate results [341]. CSM is accomplished by superimposing a small, sinusoidal signal over a DC signal driving the vertical motion of the indenter [341], [343], [344]. The motion of the indenter can be modelled by a harmonic oscillator driven at a certain frequency, whose oscillation amplitude would be modulated at the same frequency as the driving AC but lagging by a certain phase angle [341], [342], [345]. The frequency-dependent displacement of the indenter and the phase angle between the displacement and the driving AC are continuously analyzed as a function of depth [341], [343], [344] by a lock-in amplifier. Once the dynamic contact stiffness S is determined, it is possible to determine the contact depth h_c [344]:

$$h_c = h_{max} - \varepsilon \frac{P_{max}}{S}$$

(2-14)

Where (**Figure 39)** P_{max} is the peak load, h_{max} is the penetration depth at peak load, S is the contact stiffness and ε is a tip-specific constant close to 0.7-0-75 [343], [346]. Then, using the tip shape specific area functions $A(h_c)$ reported in Table 8, the contact area can be calculated [339]. For perfectly sharp tips only the first term of each function is considered, while the other terms are corrections taking into account deviations from the ideal case, e.g. tip blunting [347]. Eventually, the calculated contact area is used to calculate the hardness and the reduced elastic modulus of the test materials according to the following equations [340], [341]:

$$H = \frac{P_{max}}{A}$$

(2-15)

$$E_r = \frac{\sqrt{\pi}}{2} \frac{S}{\sqrt{A}}$$

(2-16)

$$\frac{1}{E_r} = \frac{(1 - v_f^2)}{E_f} + \frac{(1 - v_i^2)}{E_i}$$

(2-17)

Where P_{max} is the peak load, A is the impression area, S is the unloading contact stiffness, h is the penetration depth, E_r is the reduced Elastic modulus in which v_f and E_f are the Poisson Ratio and Elastic Modulus of the thin-film coating material and v_i and E_i are the Elastic modulus and Poisson ratio of the indenter (for a diamond tip E_i= 1141 GPa e v_i= 0.07 [343], [344]).

2.7.3 RULE OF THUMBS FOR RELIABLE NANOINDENTATION TESTS

To have reliable measurements from Vickers indentation tests on thin films coatings the following three operative rules must be respected [348]:

1. The **"***10% Rule***"**, or Bückel Rule, for indentation depth
2. The **"***5% Rule***"**, or Surface Roughness rule
3. The **"***1 Degree Rule***"** for surface tilt and alignment

The "10% Rule" is specific for coatings testing and tells that when the microhardness and the Elastic modulus of a thin-film coating are to be measured, the maximum penetration depth must not exceed 10% of the coatings' thickness, so that the size of the contact impression is kept small and measurements are substrate-independent [340], [342], [349]. If the diamond tip of the indenter penetrates too deeply inside the coating, the forces exerted by the indenter might reach the underlying substrate, whose mechanical response, e.g., hardness, elasticity, plastic flow, will then influence the measured quantities.

The "5% Rule" imposes that the surface roughness of the specimen should not exceed 5% of the penetration depth [350]. This is because while measuring the mechanical properties of a specimen via CSM methods, an accurate estimation of the geometrical shape of contact area A is required. As the projected area of impression, A(fc), is calculated as a function of the penetration depth hc, a rough surface will introduce errors in the determination of hc, and consequently in A(fc) [351]. Eventually, this would result in inaccurate mechanical probing of the specimen and in a large scattering of measure values [348]. The "1 Degree Rule" says that the surface of the sample must not be misaligned more than 1 degree with respect to the direction of tip penetration When a

surface under testing is not orthogonally aligned to the tip direction of movement, the true contact area at a certain contact depth h_c diverges from what should be expected for a given indenter shape penetrating normally to the specimen surface, i.e. from the value calculated using the contact-area Function $A(h_c)$. Eventually, this results in an inaccurate estimation of the mechanical properties of the sample.

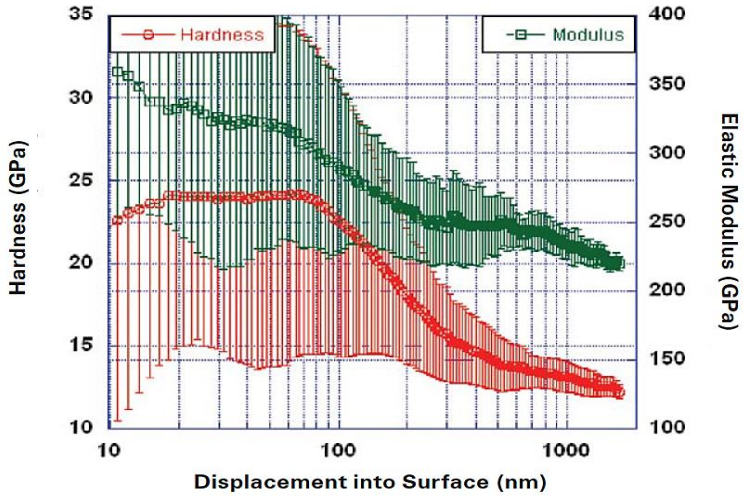

Figure 40: Dependence of hardness and elastic modulus of a 1 μm-thick TiN coating onto a tool steel substrate. The scattering of values is correlated to the influence of surface roughness (from [348]*).*

2.8 CORROSION TESTS

2.8.1 A BRIEF INTRODUCTION TO CORROSION

Although the electrochemical basis for corrosion was disclosed only between the end of the 19th century and the first half of the 20th century with the seminal works of Tafel [352], Stern and Geary [353], Butler and Volmer, the problem of metal corrosion has been known for millennia, with the first written observation attributed to Plato, during the 4th century before Christ. The term corrosion from the Latin etymology means something like " to eat into", or "to eat away", referring to the visual observation of debris formation and material removal on corroded surfaces [354]. Corrosion of metals and metallic-based materials is a highly undesirable process since it leads to a gradual loss of functionality of corroding components [355]. In the field of cutting tools protection, corrosion is

recognized to significantly contribute to the wear processes of steel and Tungsten carbide blades. Tool steels usually have a low amount of Chromium [24], [33] around 4% wt., which makes them prone to oxidation [356]–[358]. The wear of hard metal tools is promoted by the preferential dissolution of the metal binder phase and the subsequent loosening of the Tungsten carbide micro-grains embedded in the metallic matrix by the effect of external mechanical loads [3], [137], [359]. PVD hard coatings deposited on tool materials have been shown to increase the corrosion resistance of such materials [97], [112], [267]. Nonetheless, the practically unavoidable occurrence of surface defects such as pinholes and cracks can expose the underlying tool material[360], [361], leading to localized corrosion wear and coatings failure [362]. The most common technique used to investigate corrosion properties of tool material and coatings is Potentiodynamic polarization, from which important quantities like the corrosion current density and the corrosion rate can be determined. Another technique, Electrochemical Impedance Spectroscopy, has emerged as an important complementary tool able to provide deeper insights into the mechanisms of corrosion processes.

2.8.2 POTENTIODYNAMIC POLARIZATION

Corrosion is an electrochemical redox process during which a material works as the anode of an electrochemical cell and as such is gradually dissolved into the surrounding environment by the effect of charge exchange in form of ions and electrons [363]. Without any external interference, the charge exchange reaches an equilibrium condition in which both the anodic and cathodic reactions occur and a steady state corrosion potential E_{eq} is established [364]. At E_{eq}, albeit no net current can be measured, the metal is continuously corroded. Perturbing such a system by applying an external potential is referred to as polarization and results in a net current density flowing through the metal-electrolyte interface due to the enhancement of one of the two semi-reactions and suppression of the other [365]. Potentiodynamic tests are polarization tests. As such, they are “destructive tests” in the sense that once the material has been polarized, its surface properties are generally different from those of the pristine material [366]. Despite this, Potentiodynamic polarization is a valuable technique to easily and quickly determine important information such as the polarization resistance, the corrosion current and the corrosion rate of a material in the electrolytic system of choice. The corrosion kinetics is

described by the well-known Butler-Volmer (BV) equation, which describes changes in the electrical currents caused by an external power source [367], [368]:

$$J = J_{corr} * \left(e^{\frac{nF*\alpha_A*\eta}{RT}} - e^{-\frac{nF*\alpha_C*\eta}{RT}} \right) = J_0 * (e^{\frac{\eta}{\beta_A}} - e^{-\frac{\eta}{\beta_C}})$$

(2-18)

Where J and J_{corr} correspond respectively to the measured current density (uA/cm^2), flowing through the electrode-electrolyte interface at a certain potential E and to the corrosion current density (uA/cm^2), e.g. the exchange current flowing at equilibrium conditions; F is the Faraday's constant equal to 96500 C/mol(e-), n is the number of electrons involved in the redox process, T is the temperature in Kelvin, R is the universal gas constant, $\eta = E - Eeq$ is the overpotential, i.e. the polarization potential difference (in Volt) between the applied external potential E and the equilibrium potential E_{eq}, while α_A and α_C (or equivalently ß$_A$ and ß$_C$) are the so-called anodic and cathodic dimensionless transfer coefficients, whose accurate interpretation is still open to debate [369], [370], but in general are related to the strength of the dependence of the current to the overpotential and to the symmetry of the reduction and oxidation processes at the specimen surface [369]–[371]. For a perfectly symmetric redox potential, $\alpha_A = \alpha_C = 0.5$.

As represented in **Figure 41**, the Butler-Volmer equation (**Equation (2-18)**) is the algebraic sum of two components, describing the whole redox process [365]. The first term gives the anodic current, whose magnitude increases with increasing positive overpotential (i.e., with applied potential more positive than the equilibrium potential). The second term gives the cathodic current, whose magnitude increases by applying potentials more negative than the equilibrium potential, i.e., with more negative overpotential. When the applied polarization potential is large so that the overpotential is strongly shifted in the anodic or cathodic direction, the contribution from the opposite mechanisms is negligible and **Equation (2-18)** reduces to the Tafel Equation [352], [353], [372], [373]:

$$\eta = \mathrm{a} + b * \log(J)$$

(2-19)

With $a = \frac{RT}{\alpha F}\log_{10}(J_{corr}) = \beta * \log_{10}(J_{corr})$ and $b = \frac{RT}{\alpha F} = \beta$. Here, α and β can be either α_A and β_A or α_C and β_C, respectively, depending on the sing of η.

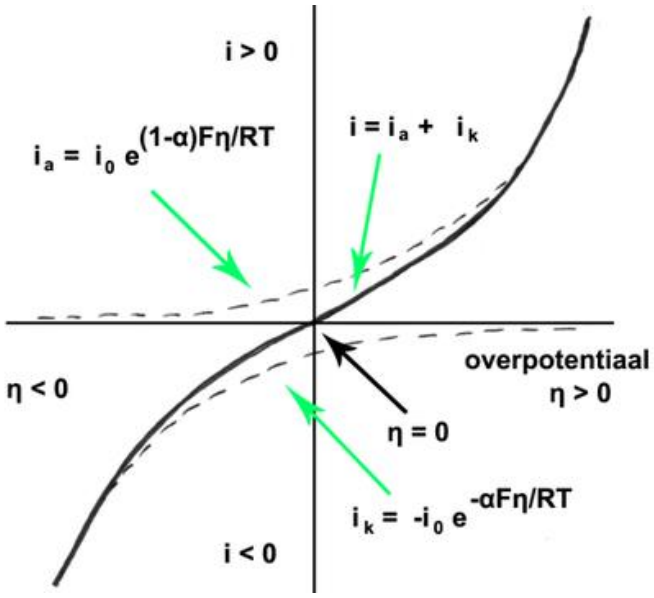

***Figure 41**: Representation of the Butler-Volmer description of the polarization current versus overpotential. The anodic and cathodic contributions are also reported in the corresponding overpotential regime (image from the web)*

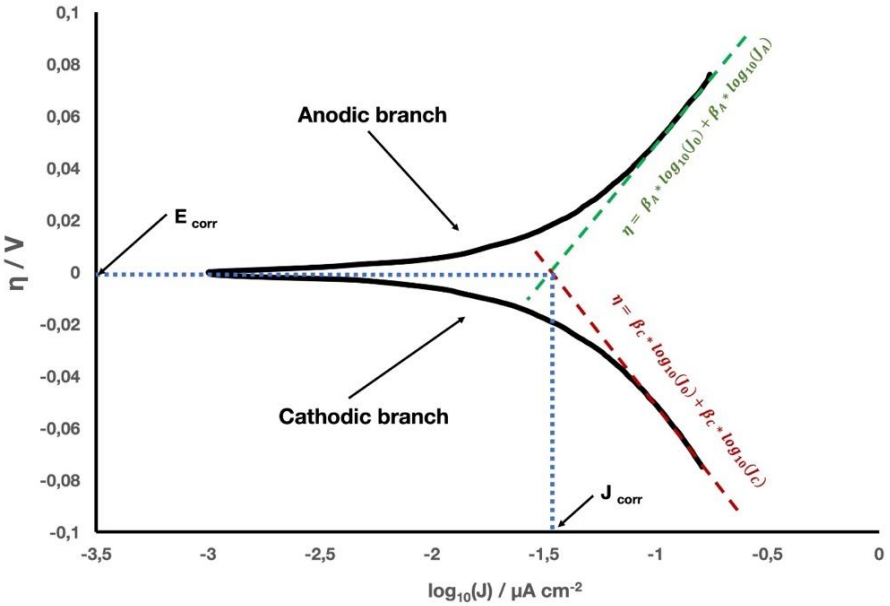

***Figure 42**: Potentiodynamic polarization curve of current density J versus overpotential. Tafel curves are represented superimposed to the experimental data along with the corresponding equations. Here, subscripts A and C refer to the Anodic and Cathodic processes, respectively.*

Using the Tafel equation, from a plot of log(J) vs η like the one shown in **Figure 42**, it is possible to obtain α from the so-called Tafel-Slope, while J_{corr} is derived from the extrapolation to zero overpotential [373]. Alternatively, one can use the Stern-Geary equation to calculate J_{corr} [353], [374] :

$$J_{corr} = \frac{\beta_A \beta_C}{2.3 * R_p * (\beta_A + \beta_C)}$$

(2-20)

Where R_p is the polarization resistance and β_A and β_C are the transfer coefficients defined earlier. R_p is obtained from the J vs E curve (**Figure 43-A**) in the vicinity of the corrosion potential (**Figure 43-B**), where a linear relationship dE/dJ can be established [372].

Materials can be ranked with respect to their corrosion resistance by simply comparing the relative corrosion current values calculated in each system. Nonetheless, it is useful to correlate an electrochemical property such as the corrosion current to some valuable information giving a more practical idea of the effect of corrosion on materials deterioration kinetics. Knowledge of the corrosion current permits estimating the amount of material that is corroding per time unit, i.e., the corrosion rate, in a specific environment. The corrosion rate is mathematically defined as [366]:

$$C_R = J_{corr} * \frac{K * PM}{n * \rho}$$

(2-21)

Where K is a constant that determines the units of C_R, PM is the molecular weight of the test material, n is the number of exchanged electrons and ρ ($\frac{g}{cm^3}$) is the material's density. The ratio PM/n is often called equivalent weight ($\frac{g}{mol}$). Potentiodynamic polarization (PP) is nowadays still the most common tool to investigate the corrosion properties of materials. From such measurements, it is possible to derive information on the corrosion rate in a determined environment as well as identify the potential regimes at which chemical reactions occur in the cathodic or anodic region. The main limit of PP is that it does not provide any insight on the mechanisms by which corrosion occurs, nor the theoretical description based on the BV model can interpret the current to voltage

relationship at high overpotentials, where mass transport through the electrolyte becomes an important factor. In the next section, another electrochemical technique is introduced, the Electrochemical Impedance Spectroscopy, which takes advantage of a small, time-varying potential applied to the electrode to extract more detailed information on the physical mechanisms occurring during the corrosion process of the specimen.

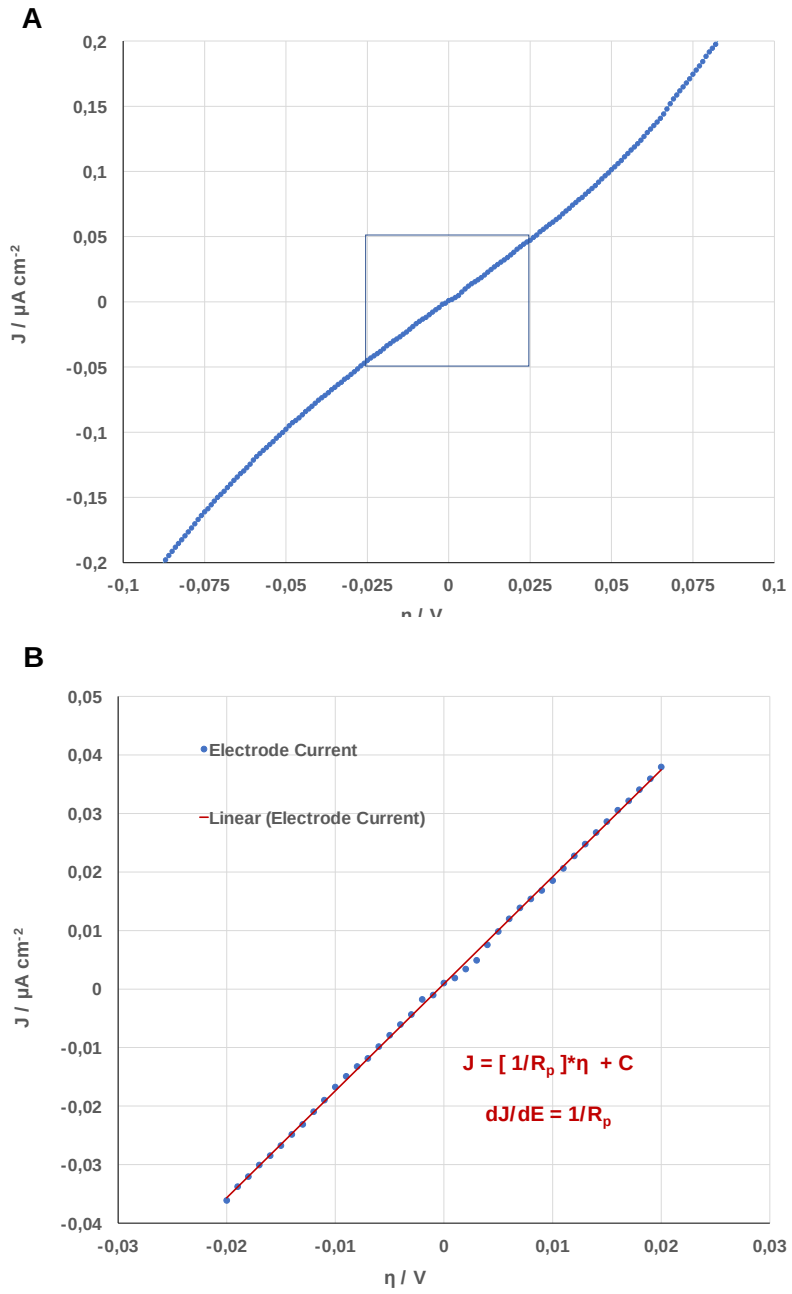

***Figure 43**: (A) Plot of electrode current J versus overpotential η data from a typical Potentiodynamic experiment and (B) focus on the highlighted area in (A) with a linear fit showing the ohmic relation between overpotential and electron current in the vicinity ($\pm$ 20 mV) of the corrosion potential.*

2.8.3 ELECTROCHEMICAL IMPEDANCE SPECTROSCOPY (EIS)

Conventional electrochemical techniques such as Potentiodynamic Polarization (PP) or cyclic voltammetry (CV) are commonly used to characterize the corrosion properties of materials and the occurrence of phenomena like passivation or trans-passivation[375]. Nonetheless, they lack a full description of the complex phenomenological processes occurring at the electrified electrode interface. Such limitation can be overcome by employing a relatively new technique known as Electrochemical Impedance Spectroscopy (EIS). EIS has emerged in the last few decades as a powerful tool in fields such as the corrosion of structural material [376], metals [377], [378] and thin films [115], [379]–[382], in the conversion efficiency of membranes in proton-exchange [383] and microbial fuel cells [384], [385] . The method involves the application of a small sinusoidal signal (voltage or current) to the working electrode and the measurement of the system response (current or voltage) in terms of amplitude and phase, from which the system complex impedance is obtained as [386], [387]:

$$Z(\omega, \varphi) = \frac{V_{AC,in}(\omega,\ \varphi)}{I_{AC,out}(\omega,\ \varphi + \Delta\,\varphi)}$$

(2-22)

The critical prerequisite of EIS analysis is that the system is electrochemically stable [388], and that the perturbation is small so that the perturbation is linear and the response will be of the same frequency as the input signal with no harmonics generation [389]. As represented in **Figure 44**, the origin of the complex impedance is due to the formation of electrical double layers at the interface between electrodes and the electrolyte [363], [388], [390]. An ideal electrical double layer can be depicted as a capacitor of capacitance C, whose impedance is:

$$Z_C(\omega) = \frac{1}{i\omega C}$$

(2-23)

In contrast, charge transfer processes can be modelled by real resistors which are independent of the perturbation frequency:

$$Z_R(\omega) = R$$

(2-24)

At low frequency, mass transport through the double layer becomes the rate-limiting step in the electrochemical process. Mass transport through EDL can be included in the description by introducing a frequency-dependent quantity called Warburg Impedance (see *Figure 44*), defined as [391], [392]:

$$W(\omega) = \frac{\frac{K_f}{\sqrt{D_O}} + \frac{K_b}{\sqrt{D_R}}}{\sqrt{2\omega}} = \frac{\lambda}{\sqrt{2\omega}} \qquad (2\text{-}25)$$

With K_f and K_b being the forward and backward reaction rate for the reduction reaction O + $ne^- \leftrightarrow$ R, and with D_O and D_R being the diffusion coefficients of the oxide and reduced species.

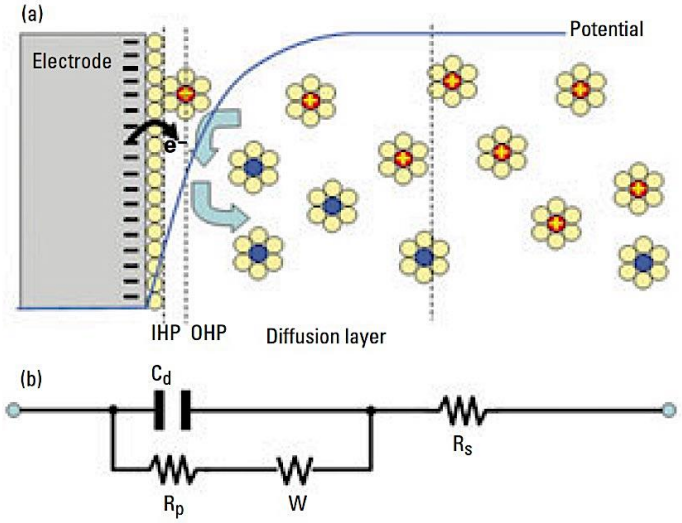

***Figure 44**: Representation of a negatively polarized surface in an electrolyte and the corresponding equivalent circuit used to model the physical system. In the ECM, Cd is the double-layer capacitance, delimited by the Inner and Outer Helmholtz Planes (IHP and OHP respectively) and placed in parallel to a polarization, i.e., charge transfer, resistance, and a Warburg resistance representing diffusion resistance through the diffusion layer. The parallel system is put in series to a resistor Rs simulating the electrolyte resistance (from* [393]*)*

As shown in **Figure 45**, the current response is then correlated to the frequency of the input signal and experiences a phase shift with respect to the latter whose magnitude depends on the mechanisms involved in the charge transfer process [387]. The most useful feature of EIS is the possibility to discriminate among the various mechanisms contributing to the overall electrochemical impedance. This is done by taking advantage of the different timescale and relaxation times of the different phenomena involved in the

process [387], [394], by probing the electrode-electrolyte system using a spectrum of discrete frequencies [388]. The output current signal is processed and decomposed into a real and imaginary part by a Frequency Response Analyzer (FRA), and from this, an imaginary and real part of the impedance will be calculated [393] (**Figure 46**).

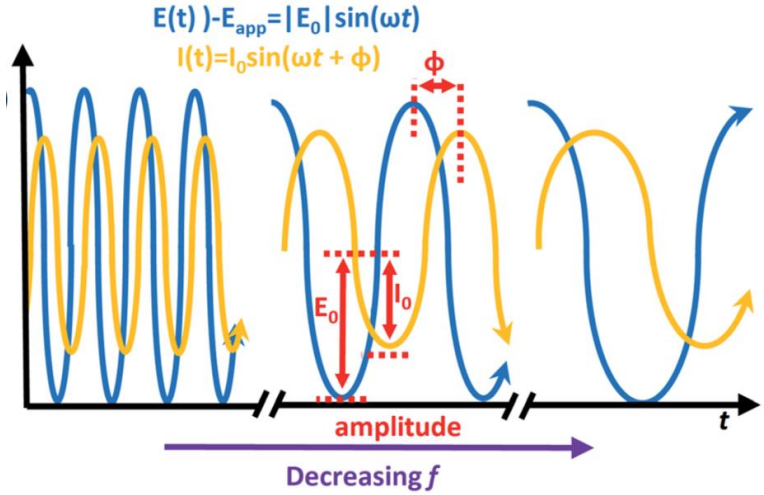

***Figure 45**: Representation of the phase shift between an input voltage and a capacitively delayed current response at different frequency regimes (from* [387]*)*

2.8.3.1 EQUIVALENT CIRCUIT MODELS (ECM)

All physical and chemical processes involved in the charge transfer at the electrode surface during an EIS experiment can be modelled by AC circuit elements [393]. By combining such elements in such a way to model the phenomena occurring in the electrochemical system, equivalent circuits models (ECMs) can be built, like the one shown in Figure 44. By fitting the experimental data with ECMs, a quantitative description of the electrochemical system can be achieved. The ECM model has the purpose of simulating the functional dependence of the impedance on the input frequency. For example, the global impedance of the equivalent circuit in **Figure 44** is [393]:

$$Z_{ECM}(\omega) = R_s + \frac{R_{tot}}{1+\omega^2 R_{tot}^2 C^2} - i * \frac{\omega R_{tot}^2 C}{1+\omega^2 R_{tot}^2 C^2} = Z'(\omega) + iZ''(\omega) \quad (2\text{-}26)$$

Where Rs is th4e electrolyte resistance, C is the double-layer capacitance, and $R_{tot}=R_p+W$ is the sum of the charge-transfer (Rp) and Warburg (W) resistances, respectively.

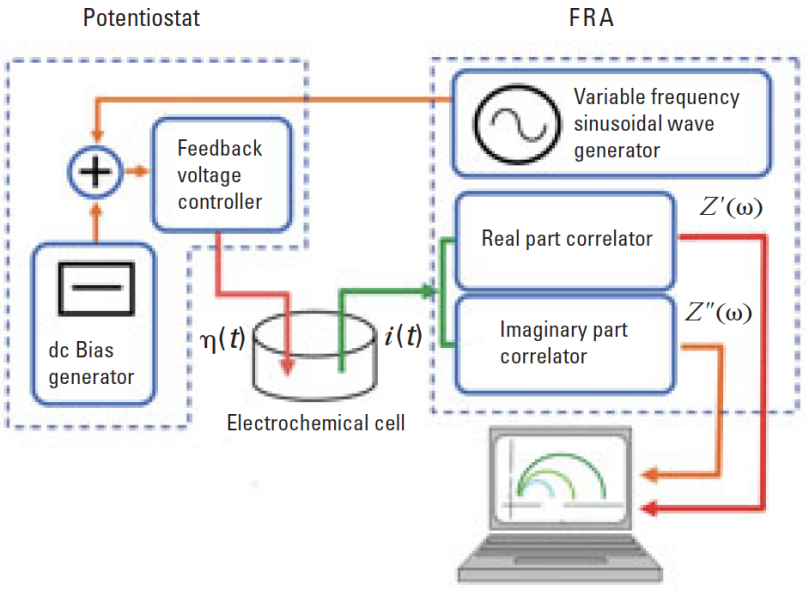

***Figure 46**: Scheme of an EIS experimental set-up and of the Frequency Response Analyzer (From* [393]*)*

The model represented is one of the simplest, but it already provides a lot of information on the described electrochemical system. Focusing on the use of EIS in the electrochemical characterization of ceramic thin film coatings, different ECMs have been proposed by [395]–[398]. Because of the presence of surface imperfections, roughness, porosities, and contaminations, electrical double layers rarely behave as pure capacitors. To account for these deviations from ideality, the EDL capacitance is usually substituted with a circuit element known as Constant Phase Elements (CPE) [399], [400]. CPEs owe their name to the fact that they carry a constant (negative) phase shift in the electrical response which is different from 0 (pure resistor) or -90° (pure capacitor), and are their impedance Z_{CPE} is defined as:

$$Z_{CPE} = \frac{1}{(i\omega)^{\alpha}C} \qquad (2\text{-}27)$$

Where α has values ranging between 0 (pure resistor) and 1 (pure capacitor).

2.8.3.2 EIS DATA REPRESENTATION: BODE AND NYQUIST PLOTS

Data are represented in EIS in two different ways, the so-called Nyquist plot and Bode plots (**Figure 47**), providing useful and complementary insights on the electrochemical system, which are well described in [387] and that will be here briefly summarized. Nyquist plots are plots of $Z^{"}(\omega)$ versus $Z'(\omega)$, where each data point is taken at a given frequency of the input AC signal. Their shape is strongly correlated to the physical contributions to the electrochemical impedance. Electrical double layers can be modelled by the so-called Randles circuit [387], [393], [401], like the one shown in **Figure 44**.

The Nyquist plot of such a system is a semicircle, whose radius is correlated to the interface resistance to charge transfer (**Figure 47**-A). The semicircular shape arises from the modulation of the capacitive and resistive contributions as a function of the input frequency [387]. At high frequency, diffusion contribution is trivial and only the electron transfer resistance affects the response. By decreasing the input frequency, the capacitive contribution to the impedance becomes more relevant *(***2-26**). The frequency where Z'' reaches its maximum can be used to calculate the time constant τ of the electron transfer process, defined as $\omega_{Max} = \frac{1}{\tau} = 1/(R_{cy} * C_{dl})$. At lower frequencies Z'' diminishes again as the main impedance factor becomes the diffusion of material towards the electrode. In this region a linear Z'' vs Z' relationship is often encountered, with an angle of about 45° against the plot axes. This implies the establishment of a mass-transport regime in which the Warburg impedance dominates the impedance response. The circular shape and linear relationship of the Warburg regime can be altered in real systems, for instance owing to passivation or the formation of pores with the onset of galvanic corrosion in coated systems and /or the formation and accumulation of corrosion products [115], [402], [403].

Bode plots are plots of either Impedance amplitude or Phase Angle versus the input frequency. Impedance Bode Plot is the plot of the Impedance modulus $Z(\omega) = \sqrt{Z'^2 + Z''^2}$ against the input frequency (**Figure 47-B**, upper panel). From these plots, two main features are of interest: the magnitude of the impedance at low frequencies and the slope of the curve at middle frequencies.

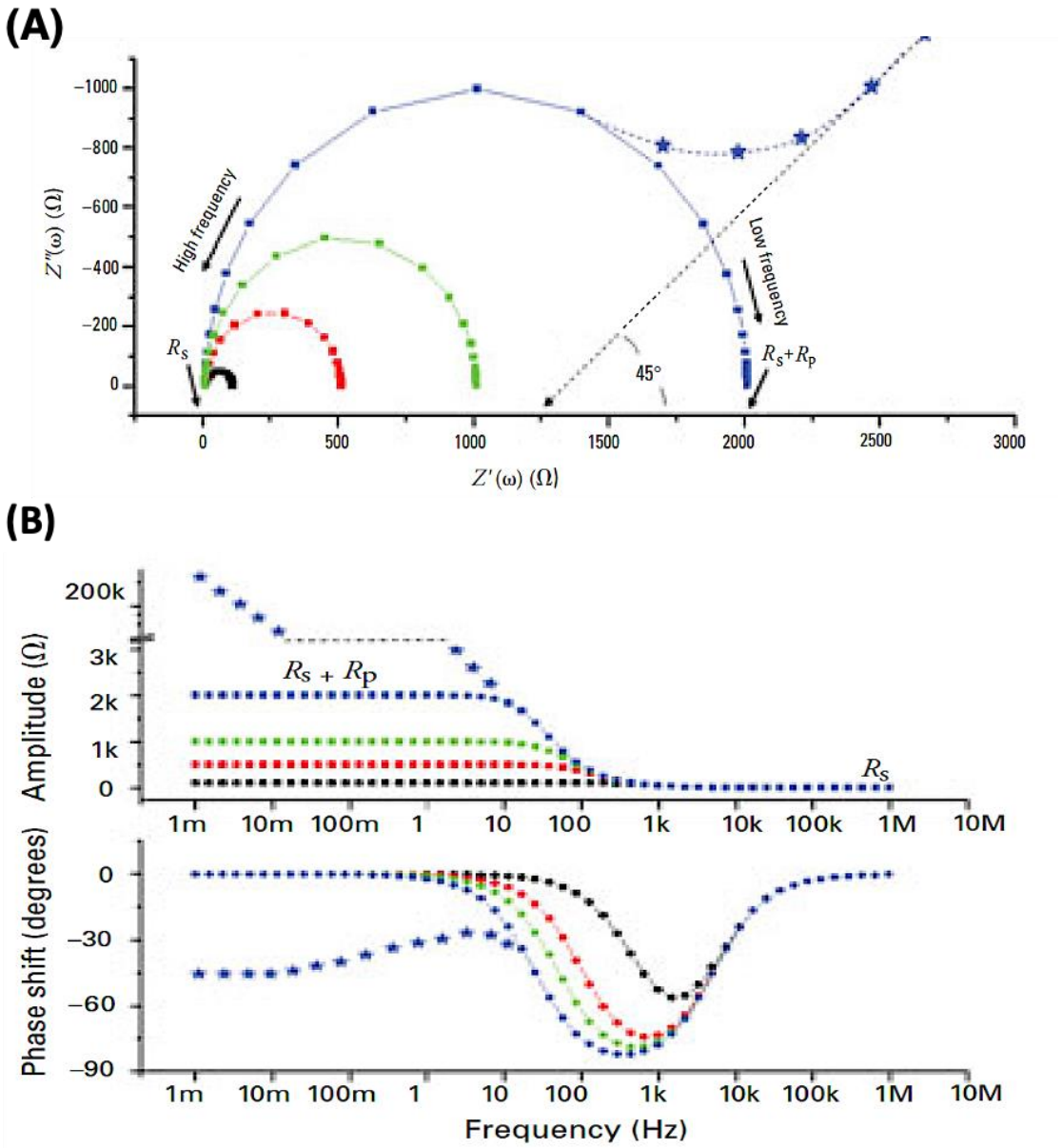

***Figure 47**: A) Nyquist and B) Bode plots simulations. Nyquist plots are built from higher frequencies at the left to low frequencies at the right. In panel A), the linear part at low frequencies at 45° is due to Warburg's impedance contribution, which also accounts for the rise of the impedance amplitude and the approach of the phase shift to -45° in panel B). Images were taken from* [393]

In general, the higher the impedance the higher the resistance of the system to electron flow, i.e., its insulating properties. Phase Angle Bode Plot is a plot of the phase shift $\varphi = arctan(\frac{Z''}{Z'})$ [404] between input and output signal against the input frequency (**Figure 47-B**, lower panel). It can be used to discern between purely resistive (no phase shift) to purely capacitive (-90° phase-shift) regimes, or to identify the occurrence of leaking phenomena, for phase shifts between 0 and 90 in the low-frequency regime.

2.8.4 LIMITATIONS

Like any other technique, EIS also has its limitations. First, EIS assumes the test system to be stable. Nonetheless, the frequency sweep takes time, especially in the low-frequency regime. If the system is electrochemically unstable, the test might be altered during the acquisition of the data [393], [401]. The second critical point regards the accuracy of the physical interpretation of the data, as different models depicting different physical processes can fit equally well in an experimental data set but not necessarily provide the real physical description of the processes involved [384], [387], [389]. For this, prior knowledge of the material and the complementing use of other techniques such as electron microscopy are necessary to choose the proper model. Because of the difficult interpretation of the physical quantities obtainable from ECMs fitting, the use of EIS for the present research project was limited to a qualitative comparison of coatings as a function of their multilayer architecture and composition. Such comparison can be achieved by directly comparing Nyquist and Bode plots from different specimens. Despite providing a limited wealth of information, a qualitative interpretation of EIS data can be done with a higher degree of accuracy than for quantitative analysis.

3 SINGLE LAYERS ANALYSIS

3.1 CHOICE OF MATERIALS: CrN, MoN and WN

The design of effective multilayer systems must start with a proper selection of the constituent materials and the optimization of relevant process parameters influencing the final properties of the coatings. Chromium Nitride (CrN) was chosen as the base material because it is one of the very few nitride-based coatings studied for wood-cutting applications [79], [124], [135], [138], [139], [141], [405], principally owning the superior resistance of CrN-based coatings towards high temperature corrosion and oxidation [91], [113], [115], [406]–[409]. The relatively low microhardness of CrN coatings, usually lower than 20 GPa [69], [99], [139], [410], [411], make it susceptible to abrasive wear [141]. The main feature of the coupling material was therefore a higher mechanical hardness to compensate for the relatively low hardness of CrN. In this regard, Tungsten Nitride (WN) is particularly interesting for its high hardness. Past research have shown WN coatings deposited by sputtering techniques to express hardness values consistently well above 30 GPa ([412]–[414]), an increase of about 50% over typical values for CrN [66], [95], [99], [213], [415], [416]. Molybdenum Nitride (MoN) has a good combination of high hardness values between 24-34 GPa for the cubic phases [417]–[419] and good corrosion resistance [420]. Such materials have been extensively studied as single-layer systems by many authors [147], [414], [428], [429], [419], [421]–[427] but only a limited number of reports on the fabrication and characterization of multilayer coatings based on CrN coupled with WN [59], [430]–[432] and MoN [96], [110], [405], [433] are available. Besides, a unique systematic comparison of mechanical structural and electrochemical properties of multilayer CrN/MoN and CrN/WN coatings was not found in the literature, with only a few studies directly comparing the properties of CrN, MoN and WN single-layer coatings [425], [434]. This observation is important, as comparing results obtained with different types of machinery and operational conditions is somewhat difficult, as also demonstrated by the usually large spread of property values among different works. Therefore, the first goal was to determine the optimum process conditions to produce single-layer coatings of CrN, MoN and WN with stable and controllable fundamental

properties. Target power density and chamber pressure were initially tuned to achieve a suitable deposition rate. The deposition rate was calculated by measuring the thickness of the coatings from FIB-cut cross sections produced in our dual-beam system. Then, the effects of reactive gas mixture and substrate bias on crystallographic, topographical, and compositional properties of coatings were investigated using XRD, AFM and EDX/XPS studies respectively.

3.2 MATERIALS AND METHODS

The substrate temperature calibration tests were performed by inserting a 1 mm-thick type-K thermocouple inside the substrate holder, 1 mm below the holder surface. This thermocouple served to read the approximated actual substrate temperature. Another thermocouple was placed beneath the substrate holder and in between the two heating lamps to control the heating ramp and provide a feedback signal to the heating system. Single layer coatings of CrN, MoN and WN were deposited on mirror-polished Si (100) substrates of approximately 1.5 cm*1.5 cm via reactive DC magnetron sputtering using disc-shaped, 6 inches metal targets of Cr (99.995%), Mo (99.95%) and W (99.95%). The substrate bias was applied by means of an external DC supply. In all cases, the base pressure was lower than $1*10^{-5}$ mbar. Before each deposition, targets were pre-sputtered for 5 minutes at 500W in a pure argon atmosphere at a working pressure of $4*10^{-3}$ mbar. After the pre-sputtering, substrates were etched for 10 minutes in an Ar and O_2 atmosphere with an Ar:O_2 flux ratio (in sccm) of 4:1 to remove residual contaminants on the substrate surface and to facilitate the adhesion of the coatings. The FIB-cut cross-sections were produced in a ZEISS Gemini dual-beam machinery equipped with a FE-SEM and a Gallium-based FIB (Carl Zeiss, Oberkochen, Germany) by delimiting a rectangular area of 7 µm * 3 µm using a milling current of 100 pA and a scanning time of 10 minutes for a single processing layer. The thickness of the coating was then calculated by using the built-in measuring tools provided by the ZEISS SmartSEM software (see **Figure 49** for an example). X-Ray diffraction data were collected using a powder-diffractometer Bruker-AXS Siemens D5005 (Bruker, Billerica, Massachusetts, USA) mounting a monochromatized Cu radiation source and a 2-mm convergence slid. XRD theta-2theta scans were run in a conventional Bragg-Brentano arrangement, with 2θ

values ranging between 20 and 50 degrees at steps of 0.05 degrees and an acquisition time of 10 s per point. Scherrer analysis was used for the determination of the crystallite's apparent size in nanolaminates. Any additional contributions to the width of the diffraction peaks besides the crystallite size, such as instrumental effects and micro-strain, were not considered. AFM measurements were run in semi-contact mode on an Asylum Research MFP3D AFM probe (Oxford Instruments, Abingdon, England) using diamond-like carbon (DLC) non-contact NSG01 tips with a nominal tip-curvature radius of 2 nm (NT-MDT®, NT-MDT LLC, Moscow -Zelenograd, Russia). For each sample, five 5-µm-square surface areas were imaged, from which average and standard deviation data were calculated through Gwydion™ software.

3.3 RESULTS

3.3.1 DETERMINATION OF THE SUBSTRATE TEMPERATURE

PVD processes require deposition temperatures several hundreds of degrees lower than those required by CVD techniques [65], [435]. This is particularly beneficial for the deposition of single and multilayer coatings based on refractory materials such as carbides and nitrides, and consist in one of the main benefits delivered by PVD deposition techniques [436]. Differences in the thermal expansion coefficients among the different coating materials and the substrates can impart severe tensile thermal stresses to the coating, which is detrimental to the mechanical stability [437], [438]. Nonetheless, substrate temperatures of a few hundred degrees are known to provide adatoms with additional energy, promoting diffusive processes on the surface and improving adhesion and uniformity as well as impacting the structural and compositional properties of the coatings [149], [159], [167]. In our case, though, the substrate temperature modulation was limited by the instrumental apparatus in use. In our system, the substrate heating was furnished by hot-filament lamps (250W) placed beneath the substrate holder at roughly 2 cm from the bottom side of the rotating plate, hence about 5 cm beneath the actual substrate placed on a 3-cm-tall stage to reach the target-to-substrate distance of 8 cm. Therefore, during the process, the heating is provided by irradiation from the lamp under a vacuum. This poses strong limitations on the actual temperatures which could be

reached, demonstrated by a preliminary temperature calibration correlating the set-point temperature with the temperature recorded inside the substrate holder approximating the actual temperature of the Si substrates used (**Figure 48**).

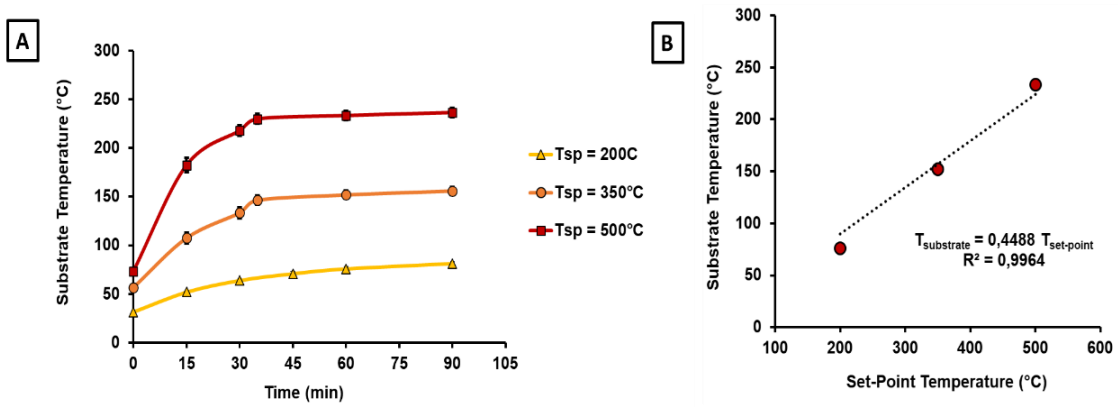

***Figure 48**: A) Substrate temperature calibration as a function of the equilibration time calculated from the end of the heating stage (50°/min) and B) linear relation between the substrate and the set point temperature, calculated at an equilibration time of 60 minutes.*

The maximum substrate temperature reached using the maximum set-point (480°C) was just 230°C with the samples placed on the lifted stage holder. This temperature range corresponds to the lower limit of recommended PVD substrate temperatures lying between 200 and 400 °C. Accordingly, the maximum possible substrate temperature was applied in all subsequent investigations.

Besides the external heating, during continuous sputtering processes a major source of heating comes from the ion flux and plasma exposure. In a separate experiment (data not shown) it was observed that during continuous CrN deposition at 500W, $3*10^{-3}$ mbar and applying an external bias of -40V, the approximate substrate temperature could reach about 300°C without any external heating, and up to nearly 450°C with the additional heating from the lamps set at maximum power, against the 230 °C reached without plasma ignition.

Nonetheless, during the intermittent deposition route employed for the deposition of the multilayer systems, dead times of about 90 seconds were necessary to relocate the substrate beneath the appropriate target. Hence, for multilayer coatings deposition the plasma heating was believed to be ineffective and was therefore neglected.

3.3.2 DETERMINATION OF THE DEPOSITION RATE

Determining the deposition rate of each constituent material forming a multilayer architecture is fundamental to control the characteristic dimensions of the coatings such as the individual layer thickness and total coating thickness. The target power density (TPD) and working pressure (WP) have a major impact on the deposition rate of sputtered coatings. In general, a higher deposition rate can be achieved by either increasing the TPD or decreasing the WP. Increasing the TPD increases the number of collisional events between Ar ions and the target surface while a lower working pressure reduces the number of collisions in the space between the target and the growing surface [161]. With reactive sputtering, also the relative amounts of Argon and Nitrogen impact the deposition rate. In this context, larger rates are achievable with low reactive gas fractions. This can be due to two reasons. First, the mass-driven different sputtering efficiencies of Ar and N_2 and secondly the transition from metallic to the reactive sputtering mode by increasing the relative content of reactive N_2 [439], [440]. In the next sections of this chapter, the relationship between deposition rates and working pressure (WP), target power density (TPD) and reactive gas mixture composition are shown.

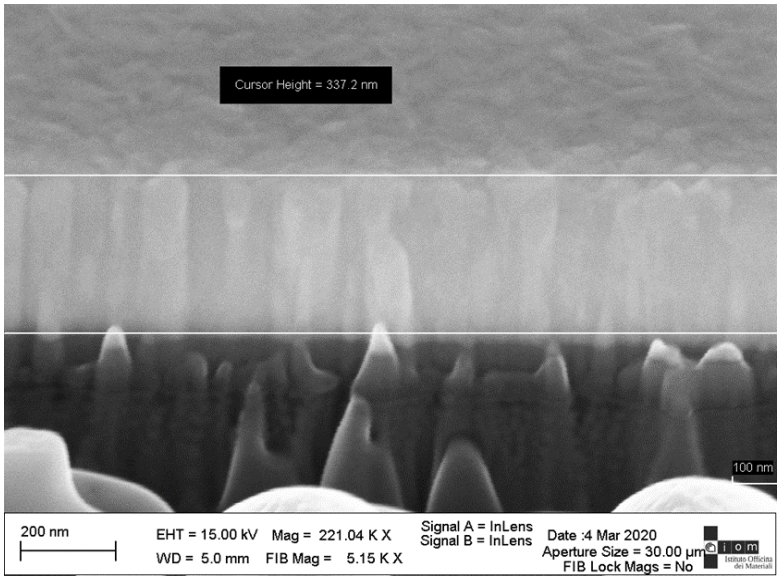

***Figure 49**: Example of a FIB cut cross-section used to determine the deposition rate with predetermined deposition conditions. The deposition rate is calculated as the ratio between the measured thickness and the deposition time.*

3.3.2.1 EFFECT OF PROCESS GAS COMPOSITION

A first investigation regarded the effect of reactive gas composition on the deposition rate. This was pursued by varying the relative fluxes of Nitrogen and Argon in the sputtering chamber, with all others deposition parameters unchanged. Results are summarized in **Figure 50**. In all cases, the rate of deposition decreases monotonically with increasing Nitrogen amounts. The effect is more pronounced for CrN than for MoN and WN, which in turn show similar trends and absolute values. The difference can be explained by considering the different chemical affinities of Chromium, Molybdenum and Tungsten to Nitrogen [434]. The formation energies at room temperature of CrN, MoN and WN are respectively -118 kJ/mol, -70 kJ/mol and -72 kJ/mol [425]. The deposition rates of MoN and WN are lower than that of CrN. This is mostly due to the lower target power (reported in the figure legend) and because of the lower sputtering yield of Mo and W targets relatively to the Cr target, owing to the larger difference in atomic weight between Mo and W with Ar ions rather than between Cr and Ar.

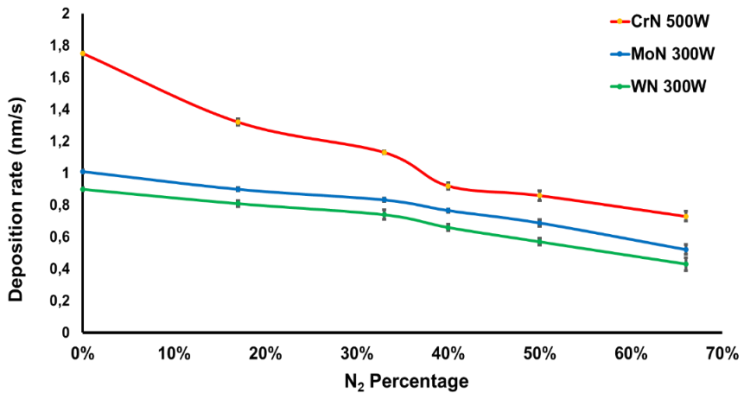

***Figure 50**: Deposition rate as a function of the reactive gas mixture for the three single-layer materials. N_2 percentages refer to the flux percentages of Nitrogen on the total gas fluxed in, consisting of Argon and Nitrogen.*

Before proceeding, it is useful to make some clarifications on the data reported in **Figure 50**. The first analysis was about the identification of the best reactive gas mixture composition to achieve well-crystallized coatings. To achieve that, some first deposition processes were run by tuning the reactive gas mixture while using an arbitrarily chosen target power input of 300W and a working pressure of $2*10^{-3}$ millibars. First XRD studies suggested that an $N_2/(Ar+N_2)$ ratio of 0.66, 0.5 and 0.4 was required to deposit well-crystallized CrN, MoN and WN, respectively (see **Figure 53**, **Figure 54** and **Figure 55**

in the next section for comparison). Both WN and MoN processes yielded a deposition rate of about 0.7 nm/s at their corresponding process gas compositions. In the case of CrN, this choice yielded a relatively low deposition rate of about 0.5 nm/s, probably due to the high N_2 fraction. Hence, in the case of CrN, it was decided to increase the target power to 500 W to achieve a deposition rate closer to those of WN and MoN. The investigation was then repeated for CrN with the high-power settings. **Figure 50** shows the data for this second set of measurements, with the input power settings that have been selected for all the following studies.

3.3.2.2 EFFECT OF THE WORKING PRESSURE

The working pressure (WP) has a strong impact on the deposition rate and on the energy of deposited particles [161]. A higher working pressure results in a reduction of the deposition rate and particles energy due to the larger scattering of particles through in-flight collisional events [160], [441]. The WP influence on deposition rate was investigated using CrN as test material (**Figure 51**), with the TPD set at 2.75 $W*cm^{-2}$ and a Nitrogen-to-Argon ratio of 66%, within the regime of formation of cubic CrN according to the literature [425]. The effective working pressure could be varied between about $1*10^{-2}$ and $1*10^{-4}$ millibar. At lower pressures, instabilities in the plasma arose which made the sputtering process unreliable. At pressures between $1*10^{-3}$ and $3*10^{-2}$ millibars, the deposition rate showed a minor dependence on the pressure, with values ranging between 0.8 and 0.7 nm/s. For lower pressures, the deposition rate increases more strongly.

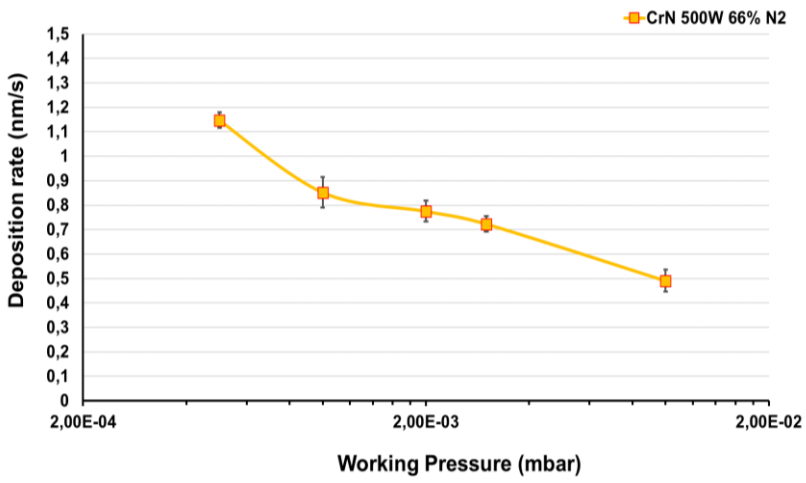

***Figure 51**: Dependence of the deposition rate of CrN on the working pressure. Other deposition parameters were arbitrarily chosen and fixed.*

The mild variation of deposition rate in the nearby of such pressure value allows making minor adjustments during each specific process without significantly impacting the amount of material deposited. An arbitrary pressure value of $3*10^{-3}$ millibars was set, corresponding to a deposition rate of 0.73 nm/s for CrN. The WP for the MoN and WN was also set at $3*10^{-3}$ mbar for further depositions. In both cases, the opposite contributions of lower TPD (1.65 vs 2.75 Wcm^{-2}) and lower N_2 percentage (50% and 40% for MoN and WN vs 66% for CrN) resulted in similar deposition rates of 0.69 and 0.71 nm/s for MoN and WN respectively.

3.3.2.3 EFFECT OF THE INPUT TARGET POWER DENSITY

In sputtering processes, the amount of material that can be deposited onto the substrate per time unit is related to the sputtering rate at the target. Ar ions within the plasma are accelerated towards the target by the potential drop between the plasma (positive pole) and the target (negative pole). Increasing the TPD increases the voltage drop at the target sheath, which enhances the kinetic energy of bombarding Ar ions towards the target and the ionization efficiency of Ar atoms by the electrons within the plasma. Therefore, the neat contribution of an increased TPD is to increase the number of collisional events at the target surface, which directly affect the deposition rate while only slightly affecting the energy of the sputtered particles [161].

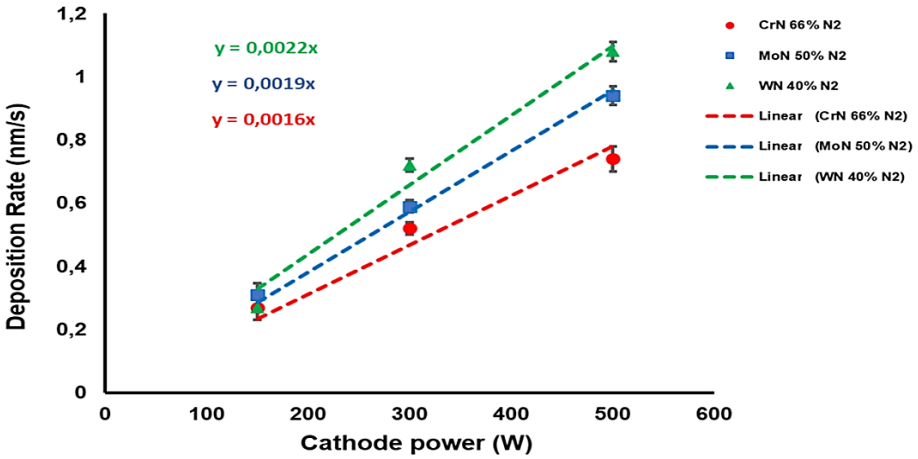

***Figure 52**: Deposition rate against target input power for the three single-layer coating systems. Linear fits are reported by imposing the intercept at 0 nm/s for an input power of 0W.*

All other factors being fixed, the functional dependence of the deposition rate on the input power is usually linear [156], [442]. In his work, three target input power values were tested (**Figure 52**), namely a low-power setting of 150W, a medium power of 300W and a high-power setting of 500W corresponding to a TPD of 0.82, 1.65 and 2.75 W cm-2, respectively. The reactive gas mixture consisted of 66%, 50% and 40% Nitrogen in the CrN, MoN and WN respectively. In all three cases, the relationship is substantially linear in the input cathodic power regime of interest, as expected. WN and MoN coatings deposited at 500W showed a tendency to recover a distinctive metallic character, as was observed by XRD analyses. It is argued that this is due to the faster deposition of metallic particles which was not adequately bound by activated Nitrogen species in the plasma. For this reason, for WN and MoN, it was chosen to keep the medium power of 300W. In the case of CrN, such a problem did not occur, partly because of the higher affinity of CrN to Nitrogen binding, and partly because of the larger N_2 concentration in the reactive gas mixture which provided enough Nitrogen for the formation of the Chromium-Nitrogen compound.

3.3.3 EFFECT OF REACTIVE GAS MIXTURE ON THE STRUCTURAL PROPERTIES OF SPUTTERED COATINGS

3.3.3.1 IMPACT ON CRYSTALLIZATION

The structural phase of solid materials depends on multiple thermodynamical and kinetical factors. The composition of the coating is one of the most important process parameters determining the resulting structural characteristics, and it is operatively determined by tuning the relative amounts of process and reactive gas proportion during the reactive sputtering process. The influence of Nitrogen content on the crystallographic properties of CrN, MoN and WN coatings is shown in **Figure 53**, **Figure 54** and **Figure 55** respectively. In all cases, 300 nm-thick coatings were deposited on a Si (100) wafer with 50 nm of Cr interlayer to increase coatings adhesion. The coatings thickness was predicted from a preliminary determination of the deposition rate for each reactive gas mixture composition via SEM imaging on FIB-cut cross-sections such as that shown in **Figure 49**. A substrate bias of -40V was applied to improve the coatings' adhesion and density, the magnitude being chosen based on the typical values used in the literature.

CrN gradually forms with increasing N_2 content. For N_2 flux ratios lower than 40%, poor crystallization is observed. On the contrary, with N_2 flux ratios higher than 40% clear crystallization in the cubic CrN phase (PDF #11-65) can be observed. The highest nitride-related signals are observed for N_2 flux percentage of 66%, after which the signal-to-noise ratio is reduced again slightly. MoN grows in very poorly crystallized films for N_2 flux percentages lower than 40%. The N_2 amount yielding the highest crystal quality lies between 40% and 50%, where a clear cubic $\gamma - Mo_2N$ phase (PDF #25-1366) is formed. At higher N_2 fluxes, the further incorporation of Nitrogen inside the growing films results in the onset of hexagonal $\delta -$ MoN phase formation (PDF #25-1367) at the expense of the cubic phase. Finally, the impact of N_2 flux on the crystallization of WN shows two distinct regimes (Figure 55). The formation of the cubic β-W_2N phase (PDF #25-1257) takes place in an N_2 flux percentage range between 16 and 40%, with a retention of the metallic character up to 33% N_2. This can be due to the low thermodynamic affinity of Tungsten to Nitrogen [443] and also to the possible expulsion of N interstitials from the growing film due to the high impact energy of heavy W atoms during film growth [157], [444]. At 40% N_2, a well-crystallized cubic WN is formed. Then, an abrupt phase shift to the hexagonal δ-WN phase (PDF #25-1256) is observed with 50% N_2.

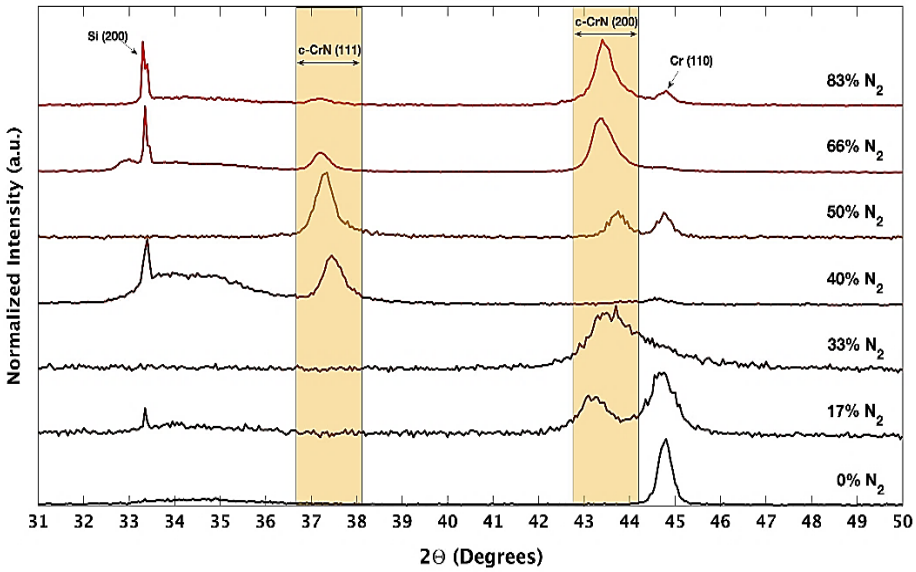

***Figure 53**: XRD plot of single-layer Cr_xN_y coatings as a function of Nitrogen amount in the reactive gas mixture. The angular positions of (111) and (200) peaks relative to the cubic nitride phase are highlighted.*

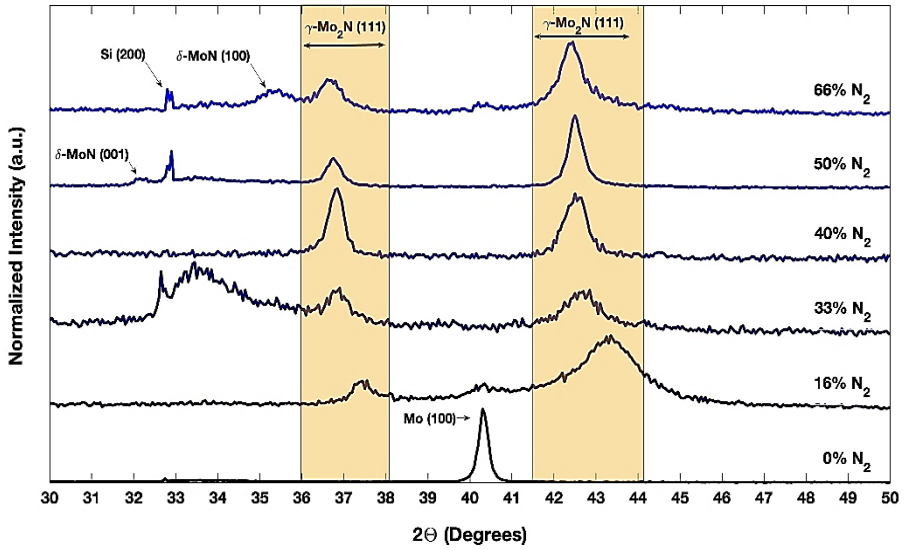

***Figure 54**: XRD plot of single-layer Mo_xN_y coatings as a function of Nitrogen amount in the reactive gas mixture Angular positions of (111) and (200) peaks relative to the cubic nitride phase are highlighted.*

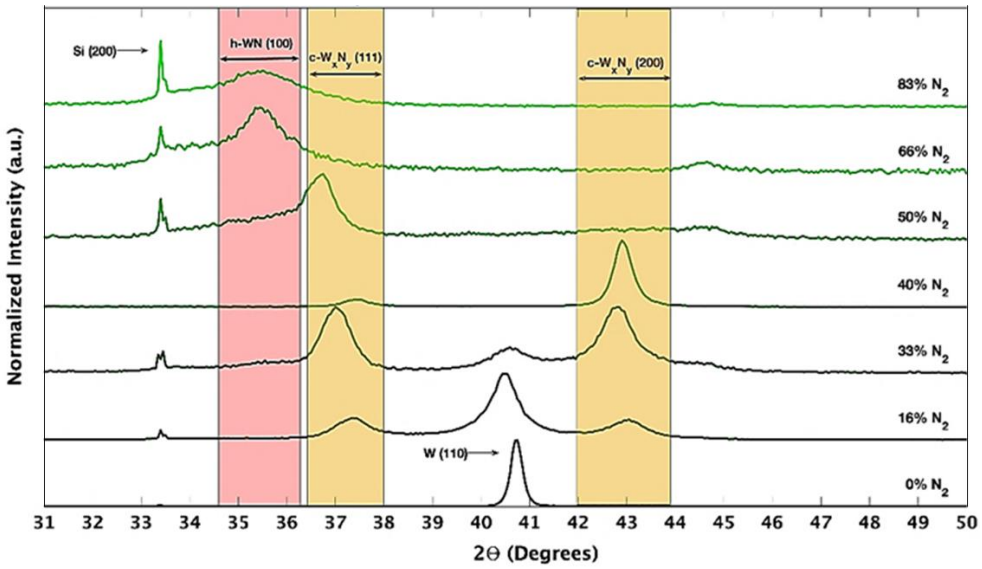

***Figure 55**: XRD plot of single-layer W_xN_y coatings as a function of Nitrogen amount in the reactive gas mixture Angular positions of the (111), (200) and (100) peaks corresponding to the cubic (yellow background) and hexagonal (red background) l nitride phases are highlighted.*

3.3.3.2 IMPACT ON INTERPLANAR DISTANCES AND GRAIN SIZE

The trends of the d-spacing of <200> planes, calculated by applying the Bragg law on the <200> peak signals, and the evolution of the apparent crystallite size estimated by using the Scherrer equation are reported for the three transition metal nitrides as a function of the N_2 flux during the sputtering process in **Figure 56** and **Figure 57**, respectively.

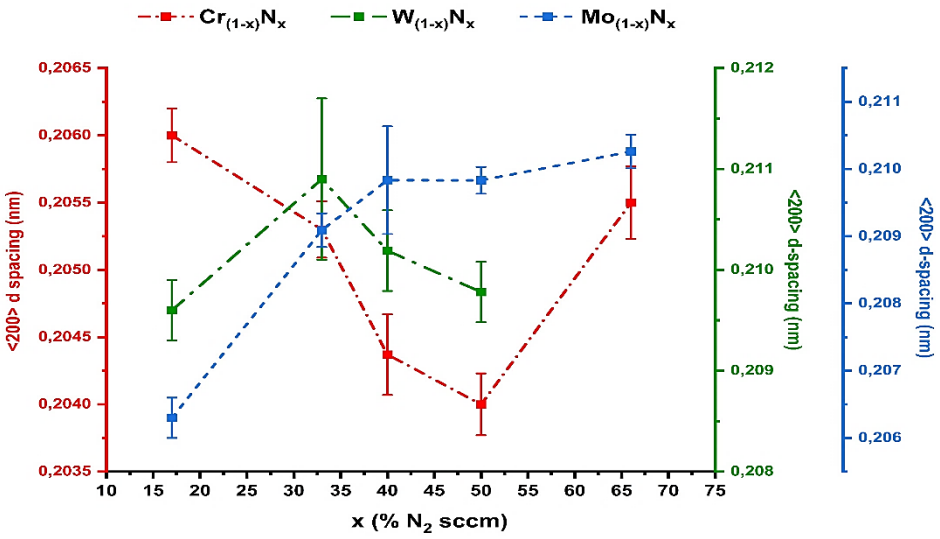

***Figure 56**: Calculated d-spacing values for the <200> peak positions. Data for WN at 66% N_2 are missing because no c-WN <200> peak was observed at that composition. Incidentally, the unit cell size can be derived by simply multiplying by a factor of two the <200>-d spacing value.*

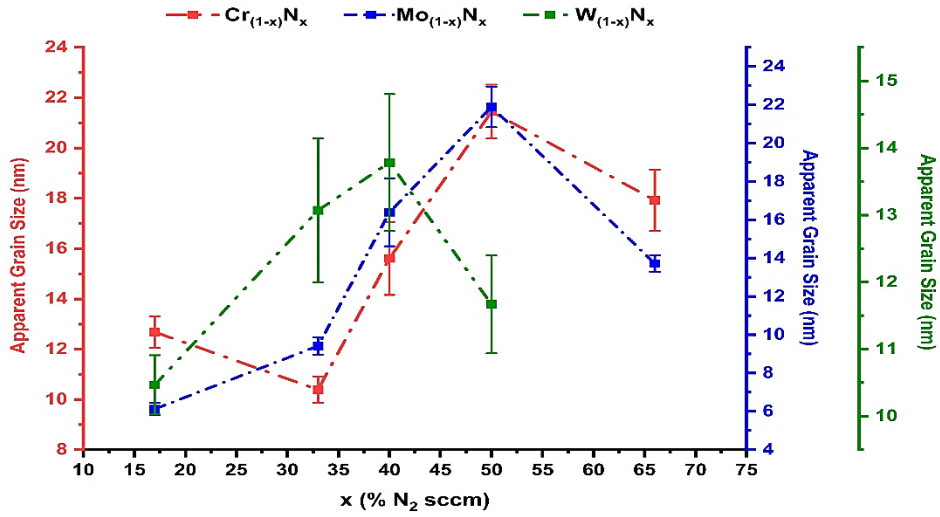

***Figure 57**: Apparent crystallite size as a function of Nitrogen flux percentage. In all systems, grain size increases up to a certain Nitrogen flux and then is rapidly reduced. Data for the WN series at 66% N_2 are missing as no <200> peak was observed for this configuration.*

The <200> spacing of CrN shows a non-monotone trend, with a first decrease of <200> interplanar distance with increasing Nitrogen flux percentages between 16% and 50% and a subsequent increase at higher Nitrogen fractions. At 16% N_2, metallic Cr is partly amorphized whilst a fine-grained cubic CrN starts to be visible. At higher N_2 fraction, only cubic CrN is observed, with a better crystalline character up to N_2 fractions of 50%.

The crystallographic improvement shown in **Figure 53** can explain the reduction of the interplanar distances in this N_2 flux regime (16-50%), as the higher Nitrogen chemical potential drives the formation of more crystalline material with less Nitrogen entrapped as excess interstitials in previously formed CrN unit cells. The improvement of the crystallization process is confirmed by the increase in the crystallite size up to 50% N_2 fluxes. The following slight reduction of crystallite size and the simultaneous increase in the <200> interplanar distances at 66% N_2 can then be due to the loss of crystalline order driven by an oversaturation of Nitrogen [445]

For the MoN system, the <200> interplanar distance first increases monotonically with increasing Nitrogen fluxes, and then substantially stabilizes for N_2 flux percentages as high as 40 %. From the observation of the XRD profiles in **Figure 54**, this can be explained by considering that MoN starts to crystallize in its cubic phase γ-Mo_2N phase (PDF#25-1366) yet at low Nitrogen proportions, with progressively improved crystalline features up to 50% Nitrogen flux. Hence, it is argued that Nitrogen accumulation within the cubic γ-Mo_2N phase progressively expands the unit cells while more cubic γ-Mo_2N is formed. A further increase in Nitrogen inclusion initializes the nucleation of the hexagonal δ-MoN along with cubic γ-Mo_2N. This results in the stabilization of the lattice expansion of Mo_2N portions and a progressive accumulation of Nitrogen at the grain boundaries, where the hexagonal phase starts to nucleate. These observations are supported by the trend of the crystallite size against the Nitrogen flux. The cubic γ-Mo_2N domain is progressively larger up to 50% N_2, while at 66%, the onset of the δ-MoN phase has the effect of reducing the size of cubic γ-Mo_2N domains. The impact of the N_2 flux on the crystallization of WN shows two distinct regimes (**Figure 55**). The formation of cubic WN occurs only for N_2 fluxes as high as 40%, while at 50% N_2, the amount of cubic WN is practically negligible, with a predominant formation of the hexagonal WN. In this regime, the interplanar distance of <200> planes at first increases (from 16% to 33% N2) and then decreases (from 33% to 50% N_2). The first increase can be attributed to the progressive accumulation of Nitrogen within the metal lattice accompanied by the formation of a more crystallized nitride material. The following decrease, instead, can be attributed to the onset of diffusion of Nitrogen from the cubic WN cells to the grain boundaries, where the hexagonal phase starts to form and then predominates at higher Nitrogen fluxes. This trend is supported by the evolution of the crystallite size, with a first

increase up to N_2 flux percentages of 40% and the following decrease at 50% N_2 due to the preferential formation of hexagonal WN. These findings are in good qualitative agreement with the literature [414], [425], [446], [447].

3.3.4 CHEMICAL CHARACTERIZATION OF SINGLE-LAYER SPUTTERED COATINGS

3.3.4.1 QUANTITATIVE COMPOSITIONAL CHARACTERIZATION VIA EDX

Intuitively, the composition of the deposited coatings depends primarily on the composition of the reactive gas mixture used for the sputtering process. In general, by increasing the amount of reactive gas, it is expected a correspondingly higher amount of its elements within the coatings. Transition Metal Nitrides (TMN) are interstitial compounds in which Nitrogen ions are accommodated within the interstitial sites of a metallic matrix. The upper limit for allowed Nitrogen interstitials depends on the crystal phase. Nonetheless, several causes concur to the final amount of Nitrogen within the coating, such as re-sputtering from heavier impinging species (Ar neutrals and metal particles), preferential thermally activated escape of Nitrogen atoms from the matrix, enhanced penetration depth due to negative applied bias, crystallographic defects, crystallite size and the chemical affinity of the host material with Nitrogen to form the nitride bond. Energy Dispersive X-Ray Spectroscopy (EDXS) provides a useful tool for a bulk estimation of the relative proportions of Nitrogen and the compounding metal, thanks to the high escape depth of characteristic X-Rays. EDX analysis was performed on single-layers samples deposited with Nitrogen flux percentages ranging from 0% up to 66%. The energy of the electron beam was set at 10 keV and the acquisition time was set at 100 seconds. The same magnification (100.000x), the working distance (8 mm), acquisition time (100 s) and processing time (52 us) was maintained in all cases, with a dead time between 15% and 40%. **Figure 58** shows the EDX spectra of CrN, MoN and WN monolithic coatings, with spectral lines reported next to the corresponding peak. The Nitrogen signal is visible for the CrN coating case, but it is strongly reduced for the MoN and WN coatings.

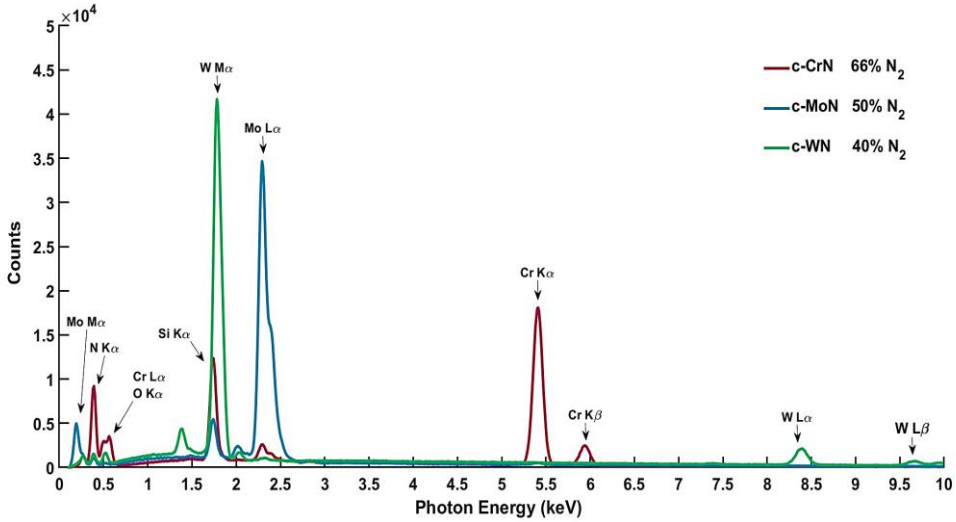

***Figure 58**: EDX spectra of selected CrN, MoN and WN coatings. The characteristic x-ray lines are reported close to the corresponding peak*

The reduction of the N1s signal could be due to a lower content of Nitrogen in MoN and WN as well as on a "shadowing effect" due to the more intense X-Ray emission from heavy Molybdenum and Tungsten atoms hiding the weaker N1s signal. The actual composition of monolithic coatings was assessed by means of quantitative EDX spectroscopy (**Figure 59)**.

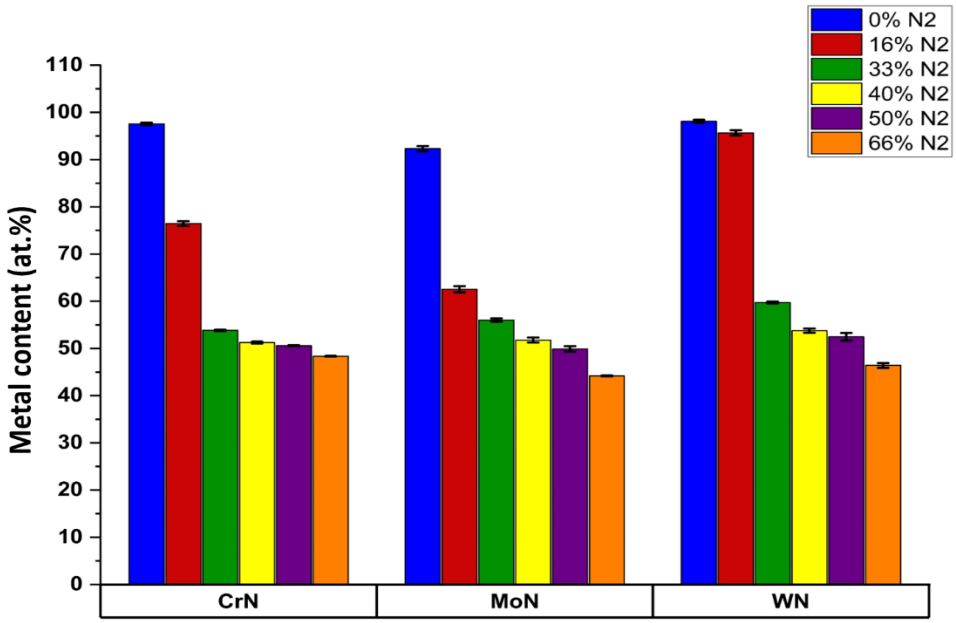

***Figure 59**: Average composition of CrN, MoN and CrN as a function of the N_2 flow fraction during the sputtering process. For each sample, three separated areas of the sample's surface were analyzed.*

Quantitative EDX measurements revealed a Nitrogen content around 50 at.% for all the three coatings (**Table 9**) at the gas composition used for the fabrication of the multilayer systems. This suggests that the differences in the N1s peak intensities among the CrN, MoN and WN coatings are primarily due to the shadowing effect occurring for TMN coatings with high-Z metal constituents. Besides, while CrN is substantially stoichiometric, MoN and WN coatings feature a higher Nitrogen content than what would be expected by the Me_2N (Me= Mo/W) unit formula of the cubic phase in which these coatings are found to crystallize (see **Figure 54** and **Figure 55** and the corresponding discussions therein). This suggests the inclusion of excess interstitials Nitrogen atoms within the Mo_2N and W_2N coatings.

***Table 9**: Composition of CrN, MoN and WN coatings from quantitative EDXS analysis. In the calculation, only the amount of Nitrogen and Chromium were considered.*

Sample	Metal (wt.%)	N (wt.%)	Metal (at.%)	N (at.%)
Cr	99.33 ± 0.2	0.67 ± 0.2	97.57 ± 0.27	2.43 ± 0.27
Mo	98.81 ± 0.1	1.19 ± 0.1	92.32 ± 0.55	7.68 ± 0.55
W	99.85 ± 0,025	0.15 ± 0,025	98.11 ± 0.32	1.89 ± 0,32
CrN - 17% N_2	92.34 ± 0.22	7.66 ± 0.22	76.49 ± 0.35	23.54 ± 0.49
MoN - 17% N_2	91.97 ± 0.21	8.03 ± 0.21	62.56 ± 0.65	37.44 ± 0.65
WN - 17% N_2	99.66 ± 0.05	0.35 ± 0.05	95.67 ± 0.56	4.33 ± 0.56
CrN - 33% N_2	81.23 ± 0.11	18.77 ± 0.11	53.82 ± 0.16	46.18 ± 0.16
MoN - 33% N_2	89.72 ± 0.13	10.38 ± 0.13	56.01 ± 0.35	43.99 ± 0.35
WN - 33% N_2	95.12 ± 0.15	4.88 ± 0.15	59.73 ± 0.79	40.27 ± 0.79
CrN - 40% N_2	79.6 ± 0.14	24.4 ± 0.14	51.23 ± 0.21	48.77 ± 0.21
MoN - 40% N_2	88.03 ± 0.22	11.97 ± 0.21	51.78 ± 0.51	48.22 ± 0.51
WN - 40% N_2	93.64 ± 0.11	6.36 ± 0.11	52.84 ± 0.21	47.16 ± 0.21
CrN - 50% N_2	79.17 ± 0.08	20.83 ± 0.08	50.58 ± 0.12	49.42 ± 0.12
MoN - 50% N_2	87.21 ± 0.26	12.78 ± 0.26	49.89 ± 0.57	50,10 ± 0.57
WN - 50% N_2	93.54 ± 0.05	6.46 ± 0.05	52,46 ± 0.45	47,54 ± 0.45
CrN - 66% N_2	77.66 ± 0.05	22.34 ± 0.05	48.34 ± 0.06	51.65 ± 0.06
MoN - 66% N_2	84.43 ± 0.06	15.57 ± 0.06	44.18 ± 0.12	55.82 ± 0.12
WN - 66% N_2	91.92 ± 0.15	8.09 ± 0.15	46.41 ± 0.51	53.59 ± 0.51

3.3.4.2 QUALITATIVE CHEMICAL STATE DETERMINATION VIA XPS

Determining the chemical state of the coatings' surface can provide more insights into the coating's chemical activity. For instance, it can evidence variations in the affinity towards oxygen or identify species in different oxidation states and their relative occurrence as a function of the gas concentration during the deposition process. The identification of the spectral components of the metal, metal-oxide, and nitrides as well as the 1s peaks corresponding to oxygen and Nitrogen has been done by comparing the experimental data with the reference values found in the NIST database (*https://srdata.nist.gov*).

First, a comparison between the stacked spectra of the most intense metallic core signal and one of the N1s peaks of the corresponding specimen is provided as a function of the Nitrogen fraction used during the sputtering deposition. Then the results of a peak fitting procedure are provided. All samples were measured using an Al source at 1486.6 eV using a pass energy of 50 eV. The number of acquisition iterations is different for different kinds of peaks, as it was determined by need to achieve a reasonable signal-to-noise ratio. In what follows only a qualitative characterization is pursued.

Due to a small energy shift of the order of fractions to a few eV, experimental peaks are usually the result of the convolution of multiple signals. Hence, a peak fitting procedure was performed to distinguish among signals belonging to identical elements in different chemical environments, such as metals, oxides, and nitrides. For the deconvolution, a Doniach-Sunjic fitting function has been used to fit metallic peaks to account for the typical peak asymmetries of metallic samples while for oxide, nitride and non-metallic peaks, a Voigt function for each expected signal was used to fit the experimental data [448]. For fitting p, d and f doublets, a constraint on the relative peak intensity has been adopted to account for the different degeneracies of p, d and f photoelectrons (relative intensities of 2:1, 4:3 and 5:4 in the case of $p_{3/2}/p_{1/2}$, $d_{5/2}/d_{3/2}$ and $f_{7/2}/f_{5/2}$ doublets respectively).

3.3.4.2.1 XPS spectra of Chromium Nitride

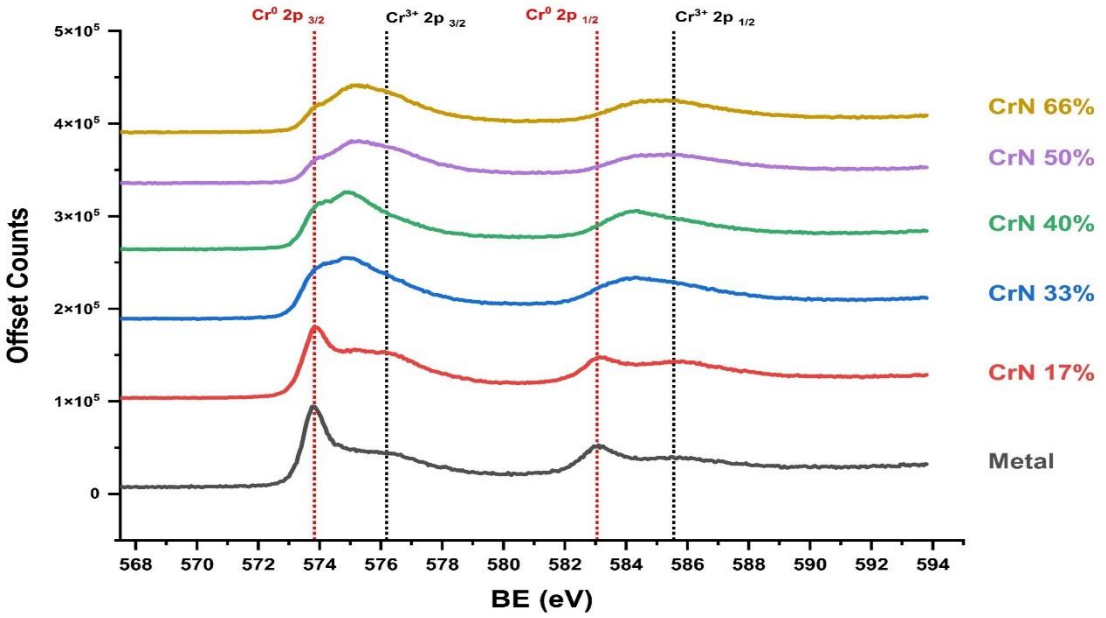

***Figure 60**: XPS spectra of the Cr 2p doublet as a function of the Nitrogen flux. Indicated next to the material unit formula at the corresponding spectrum. The positions of the Chromium and Chromium oxides. Are reported for clarity, with signals placed in between due to the formation of the Cr-N system.*

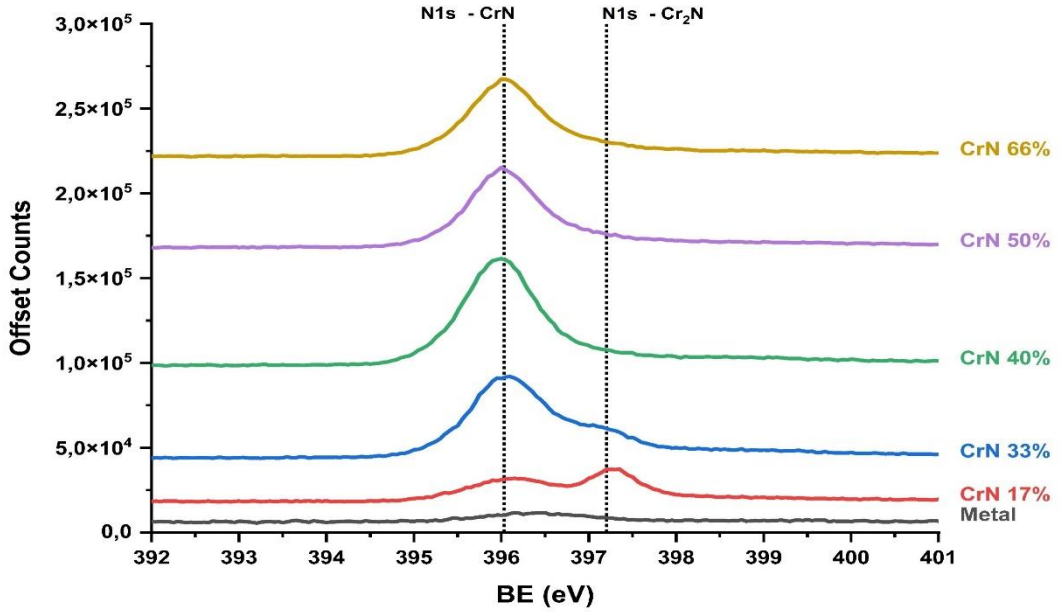

***Figure 61**: XPS spectra of the N1s peak as a function of the Nitrogen flux, indicated next to the material unit formula beside each spectrum. The positions of the Chromium and Chromium oxides. Are reported for clarity, with signals placed in between due to the formation of the Cr-N system.*

***Table 10**: XPS spectral lines for the Cr-N-O system*

Material	Cr 2p 3/2	Cr 2p 1/2	N1s	O1s
Cr	574.8-574.6	583.5	-	-
Cr2N	574.8-575.2	583.3	397.2-397.4	-
CrN	575.6-575.8	584.3	396.4	-
Cr_2O_3	576.6	585.4	-	530-530.6
$Cr(OH)_3$	577.4	-	-	531.2-531.7
CrO_3	580.1	589.2	-	530.6

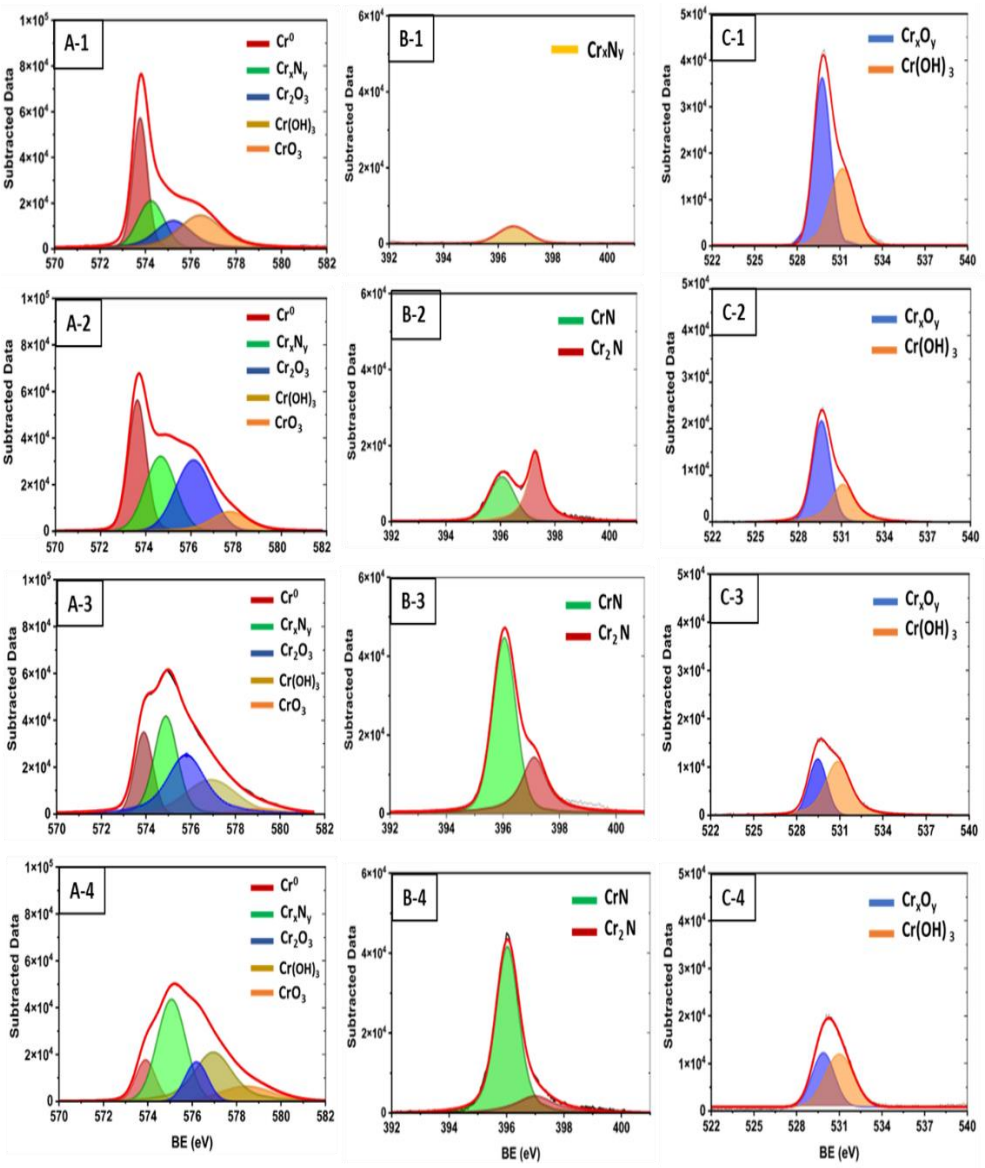

***Figure 62**: Selected fitted XPS spectra of Cr2p $_{3/2}$ (A-vertical series), N1s (B-vertical series) and O1s (C-vertical series) for Cr_xN_y coatings deposited with a Nitrogen flux fraction of 0% (1-horizontal series), 16% (2-horizontal series), 40% (3-horizontal series) and 66% (4-horizontal series).*

3.3.4.2.2 XPS Spectra of Molybdenum Nitride

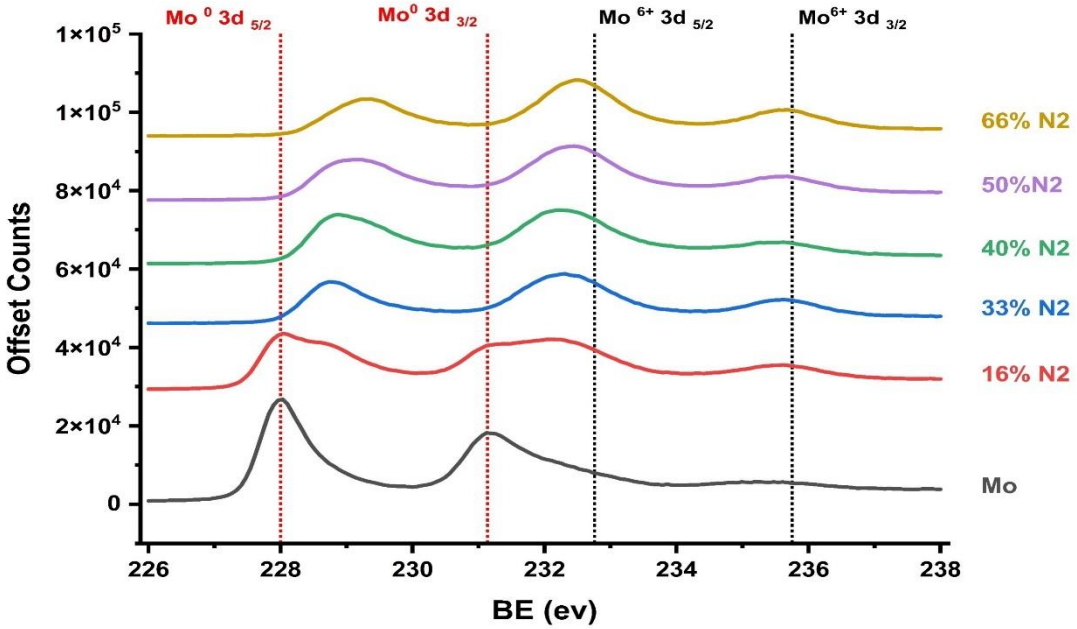

***Figure 63**: Stacked XPS spectra for the Mo 3d signal against the Nitrogen flux percentage. Peaks corresponding to the metallic and oxidized contributions are reported, while signals from the Mo-N system are placed in between the two.*

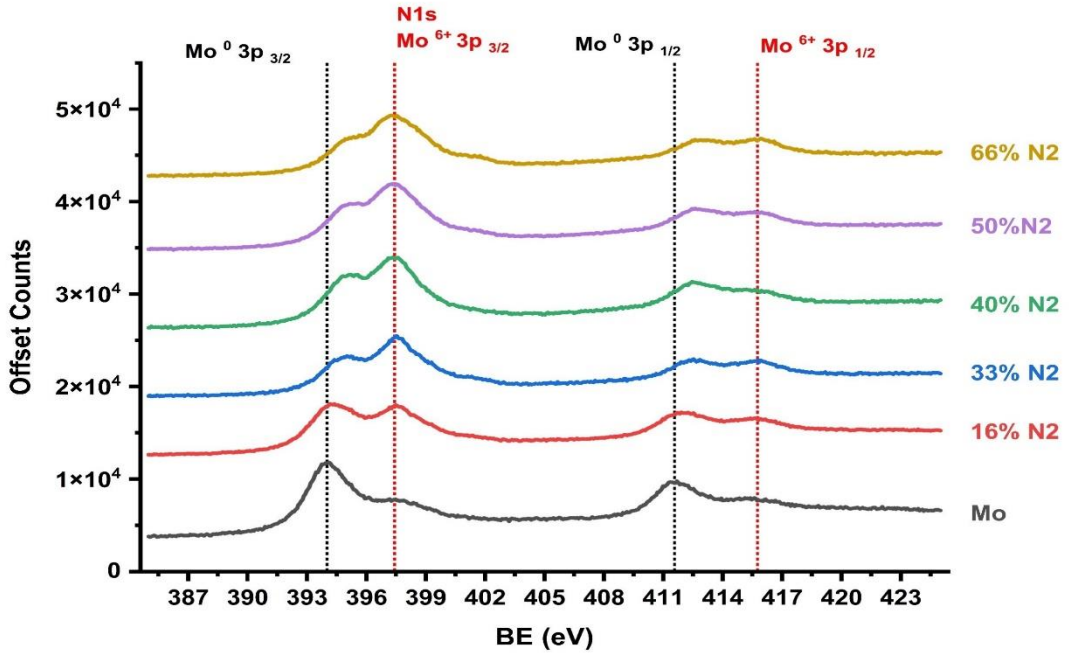

***Figure 64**: XPS spectra for the 3p doublet and the N1s peak as a function of the Nitrogen flux. The identification of the N1s peak is possible thanks to the alteration of the intensity ratio between the 3p $_{3/2}$ and 3p $_{1/2}$ with increasing Nitrogen flux.*

***Table 11**: XPS spectral lines for the Mo-N-O system*

Material	Mo 3d 5/2	Mo 3d 3/2	Mo 3p 3/2	N 1s	O1s
Mo	226.1 - 228.2	229.6 – 231.1	394-396	-	-
MoNx	228.1-229	-	394.6-394.9	397-398	-
MoOx	228.3-233.6	234.2-236.7	396.1-399.5	-	529.8-531.6

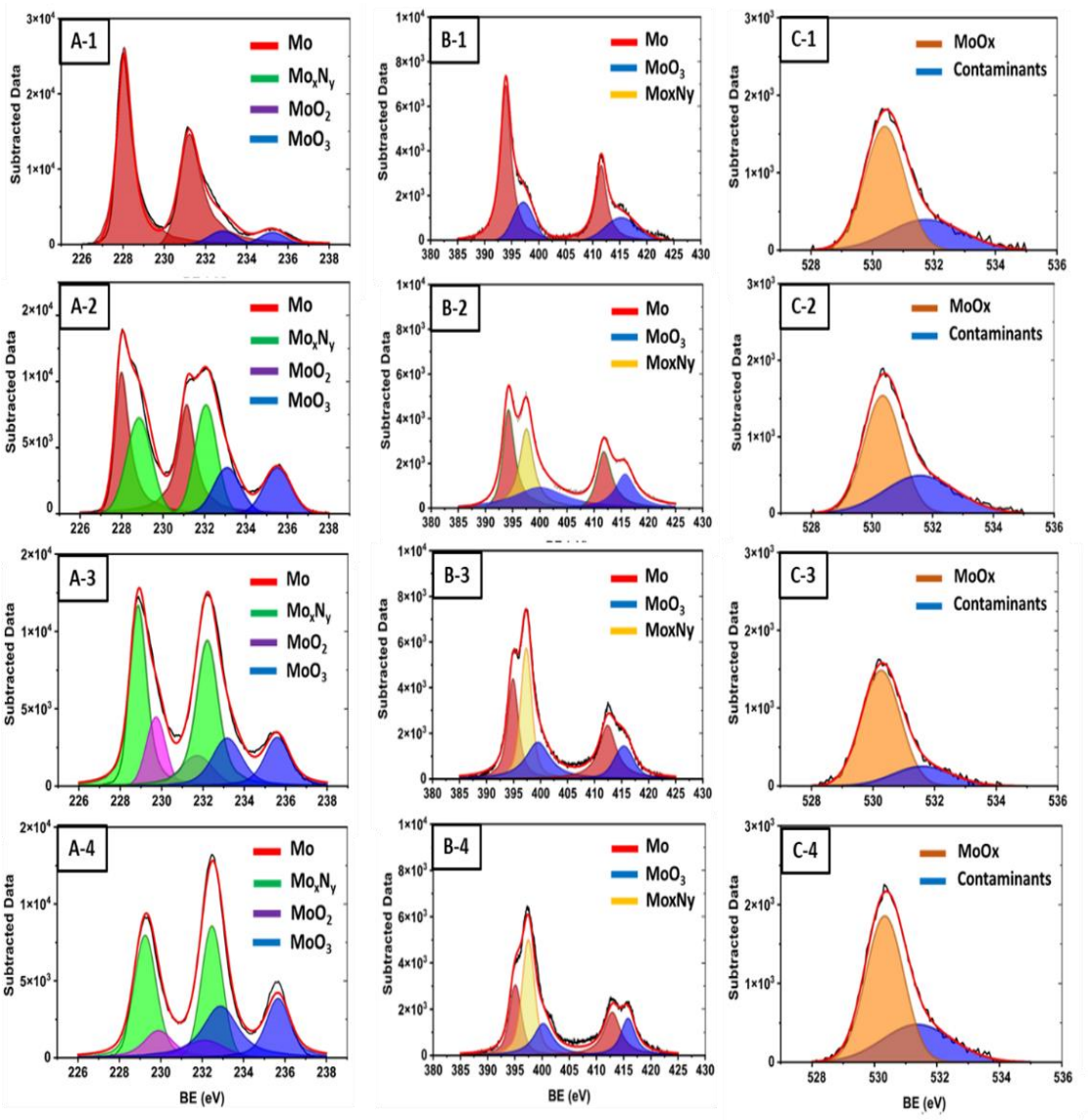

***Figure 65**: XPS fitted profiles for Mo 3d doublet (A – vertical series), Mo3p doublets superimposed to N1s peak (B - vertical series) and O1s peak (C vertical series) for different Nitrogen flux percentages of 0% (1-horizontal series), 16% (2- horizontal series), 40% (3- horizontal series) and 66% (4-horizontal series)*

3.3.4.2.3 XPS spectra of Tungsten Nitride

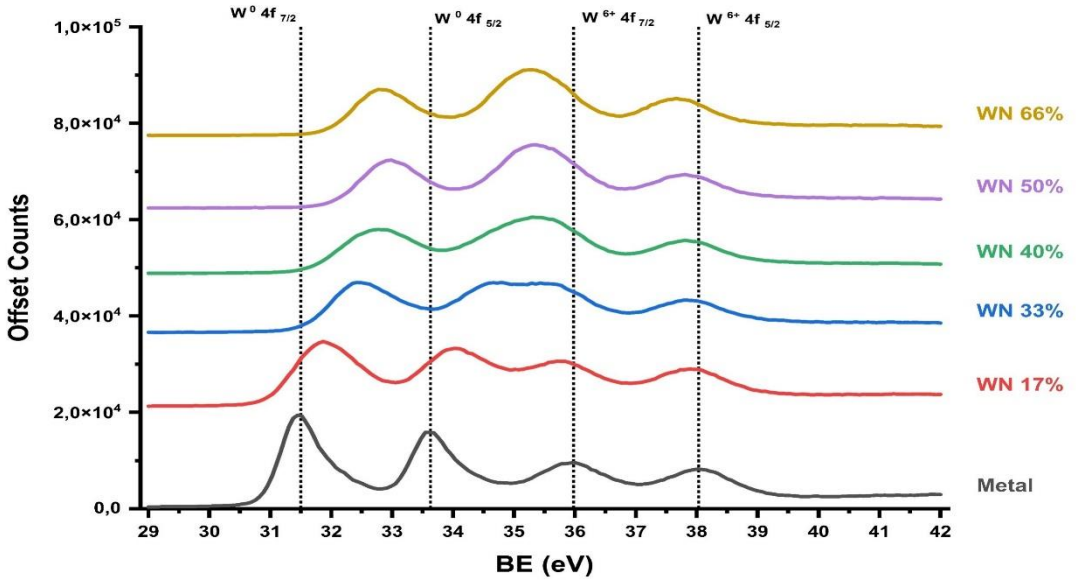

***Figure 66**: Stacked XPS spectra of the W 4f doublet as a function of the Binding Energy (BE). The energy positions of the metallic and oxidized Tungsten 4f lines are reported. Signals for the W-N systems fall within the metal and oxide doublets due to the lower energy shift with respect to oxide species.*

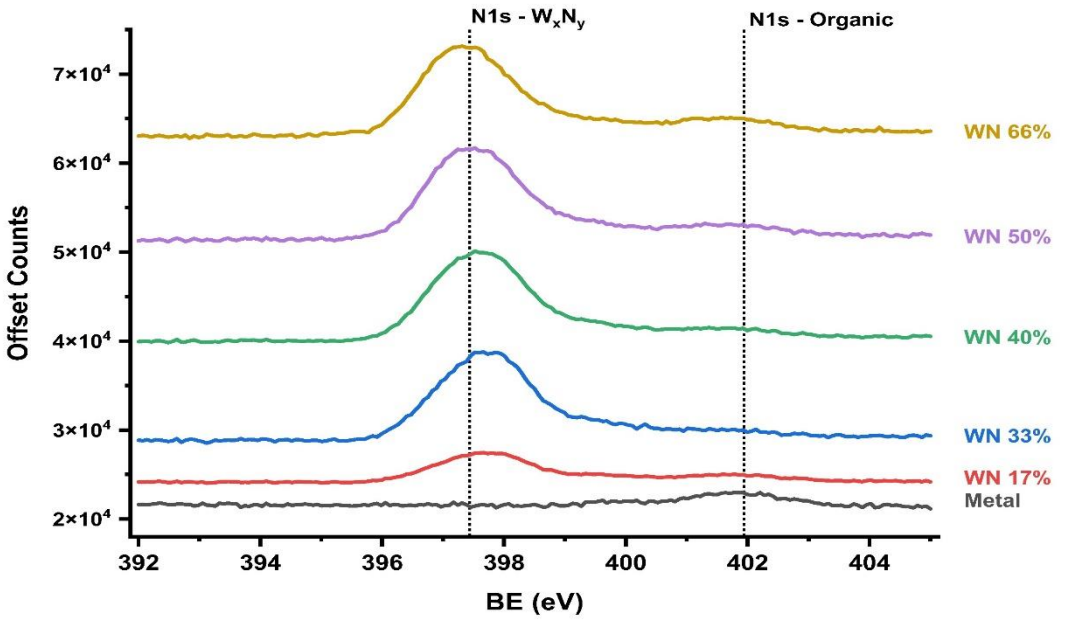

***Figure 67**: Stacked XPS spectra of the N1s lines as a function of the Nitrogen flux. Contributions from the N-W component and contaminants are reported. The energy positions of the metallic and oxidized Tungsten 4f lines are reported. Signals for the W-N systems fall within the metal and oxide doublets due to the lower energy shift with respect to oxide species.*

***Table 12**: XPS spectral lines for the W-N-O system*

Material	W 4f 7/2	W 4f 5/2	N1s	O1s
W	30.9-31.6	33-33.7	-	-
WN_x	32.1-33.0	34.1-35	397.6	-
WO_x	35.4-36.4	37.4-37.9	-	530.5-532.2

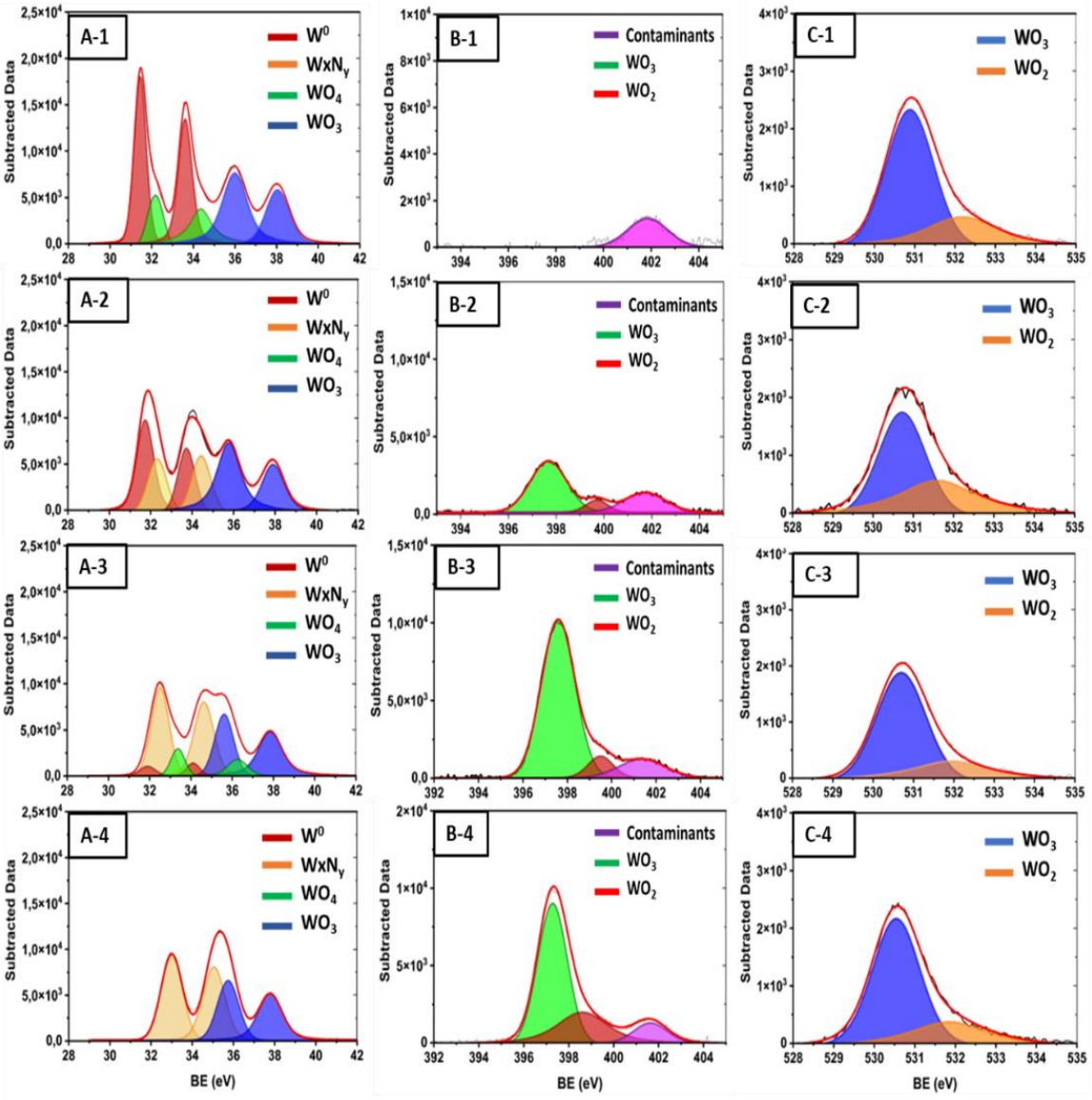

***Figure 68**: Fitted XPS spectra of W 4f (A-vertical series), N1s (B-vertical series) and O1s (C-vertical series) for W_xN_y coatings deposited with a Nitrogen flux fraction of 0% (1-horizontal series), 16% (2-horizontal series), 40% (3-horizontal series) and 66% (4-horizontal series).*

3.3.4.3 COMPOSITIONAL ANALYSIS RESULTS

In **Figure 60** and **Figure 61**, XPS spectra of the Cr 2p doublet and N1s singlet peaks are reported, respectively, f CrN coatings deposited under different reactive gas mixtures. In Figure 62, fitted peaks of the Cr 2p 3/2, N1s and O1s peaks are reported, along with the chemical system associated with each identified component, according to the binding energy values reported in the NIST database and reported in **Table 10**. The Cr 2p signal shows a progressively decreasing Cr^0 contribution for higher Nitrogen percentages, with a progressively more intense nitride contribution from the nitride phase (**Figure 62 A1-A4**). The amount of Cr_xO_y and Cr-OH stays roughly the same independently of the Nitrogen content, albeit their distribution changes. Interestingly, though, the intensity of the O1s signal is sensibly reduced from Nitrogen flux percentages between 0 and 40%, after which no further decrease is observed (**Figure 62 C1-C4**). On the contrary, the intensity of the N1s peak attributed to the Cr-N system increases for percentages of Nitrogen flux up to 40%, after which it stabilizes for higher N_2 fluxes (**Figure 62 B1-B4**). These data are in good agreement with the quantitative EDX results reported in Figure 59. XPS spectra of Mo 3d doublet and N1s singlet are reported in **Figure 63** and **Figure 64**, respectively, while in **Figure 65** fitted peaks of the Mo 3d doublet, N1s singlet and O1s singlet are determined according to the NIST binding energy values reported in **Table 11**. The photoemission signal of metallic Mo decreases only slightly between 0% and 16% of fluxed N_2., while it practically vanishes at 40% of N_2 (**Figure 65 A1-A4**). The N1s signal increases up to 40% N_2 and then stabilizes (**Figure 65 B1-B4**). This suggests a complete nitridation of Mo at N_2 flux percentages of 40%. Contrarily to the case of CrN coatings, no change in the O1s intensity is noticed (**Figure 65 C1-C4**), as confirmed also by the unvaried Mo_xO_y contributions to the Mo 3d doublet signal (**Figure 65 A1-A4**). EDX data in **Figure 59** and **Table 9** suggest a further reduction in Nitrogen content for higher flux percentages of Nitrogen, with Nitrogen atomic percentages increasing from 48 at.% to almost 56 at.% for Nitrogen fluxes of 40% and 66% respectively. This corroborates the hypothesis of additional Nitrogen being incorporated within the nitride matrix as interstitials, with no effect on the Mo 3d binding energy shift. The XPS analysis on W_xN_y coatings reported in **Figure 66**, **Figure 67** and **Figure 68** show a similar trend to that of Mo_xN_y coatings. W 4f doublet signal features significant contributions from the nitride system at N_2 flux percentages higher than 16% and

stabilized above 40% (**Figure 68 A1-A4**). N1s signal appears at 16% of N_2 flux percentage, increases up to 40% and then stabilizes **(Figure 68 B1-B4**). Finally, the O1s signal is practically unaffected by the Nitrogen content in the coating (**Figure 68 C1-C4**). As for the Mo_xN_y system, these findings suggest that above 40% N_2, Tungsten nitridation is complete substantially complete. The small secondary peak visible in **Figure 68 B1-B4** at a binding energy of 399 eV could be attributed to the formation of small fractions of the Nitrogen-rich cubic W_3N_4 phase [449], which are probably hidden in the W 4f doublets region due to overlapping peaks from nitride and oxide contributions (see also **Table 12** for reference NIST data).

3.3.5 EFFECT OF SUBSTRATE BIAS

The purpose of applying an external bias to the substrate is to change the energetics of the deposition process. With a biased substrate, impinging charged particles gain additional kinetic energy which is transferred to the growing surface or substrate and determines the surface mobility and reactivity of the impinging particles, therefore contributing significantly to the development of the growing film. For anti-wear coatings, usually, a negative substrate bias is used to accelerate positive ions across the substrate sheath, principally argon ions, metallic cations and also oxygen and Nitrogen ions [450], [451]. Such particles impart compressive stress on the underlying film following impact, resulting in an enhancement of the compressive stress of the coating.

3.3.5.1 IMPACT ON CRYSTALLIZATION

The XRD plots reported in **Figure 69**, **Figure 70** and **Figure 71** show the dependence of the structural properties of CrN, MoN and WN coatings on the applied negative substrate bias, respectively. The applied bias varied between ground and a maximum value of -150 V in all cases. For values of 130 and 150 V, MoN and mostly WN coatings were not mechanically stable and often delaminated readily upon cooling down at the end of the deposition process. Hence, data for such high negative values are not reported. For each coating, the choice of the reactive gas mixture fell on the one yielding the best crystalline features. Therefore, CrN, MoN and WN were deposited using a reactive gas mixture made up of a Nitrogen fraction of 66%, 50% and 40% respectively. Other deposition parameters are listed in **Table 13**.

***Table 13**: Process parameters for the deposition of nitride coatings*

Sample	T_{sub} (°C)	TPD (W cm^{-2})	V_{plasma} (V)	N2 (% sccm)	I sub (mA @ -50V)
CrN	**200**	**2.75**	**480 ± 5**	**66%**	**430 ± 10**
MoN	**200**	**1.65**	**296 ± 2**	**50%**	**320 ± 15**

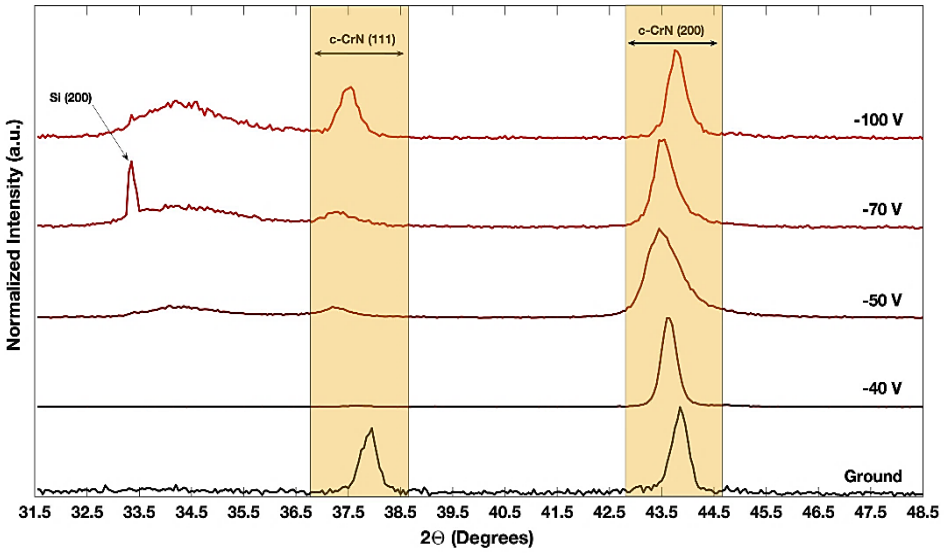

***Figure 69**: Dependence of the crystallographic properties of CrN coatings on the applied substrate bias.*

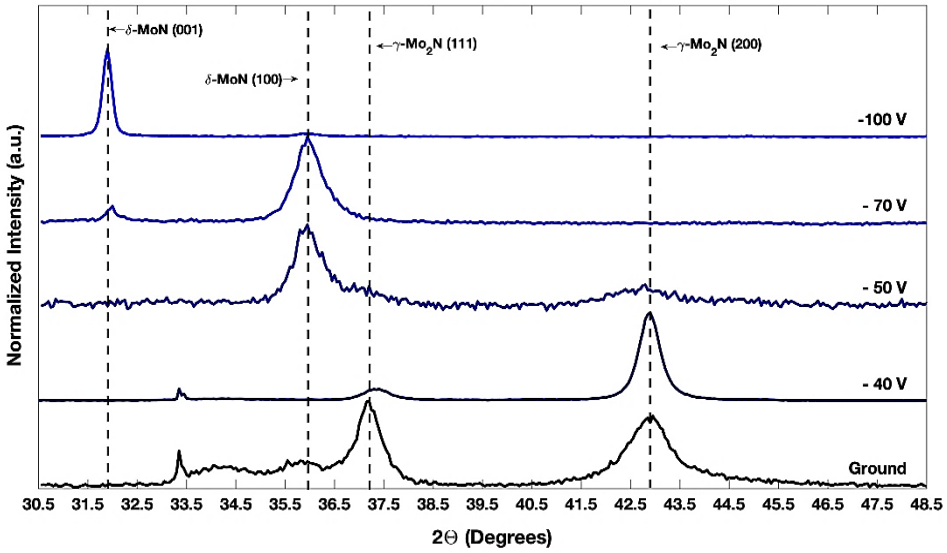

***Figure 70**: Dependence of the crystallographic properties of MoN coatings on the applied substrate bias.*

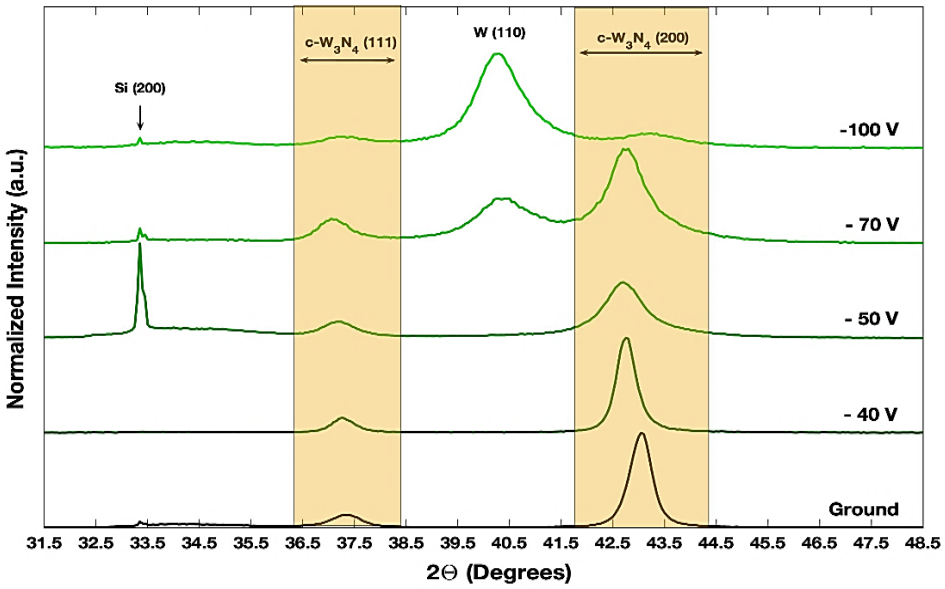

***Figure 71**: Dependence of the crystallographic properties of WN coatings on the applied substrate bias.*

Chromium Nitride retains the cubic structure for all the applied bias values. The preferred growth orientation is predominantly the (200) for negative bias values between -40 and -70 V. For grounded substrates and bias values of -100V, the preferred orientation is still the (200) but relatively intense (111) signal is also present. From the signal-to-noise ratio, it appears that the highest crystallization efficacy is achieved with a bias value of -40V (**Figure 69**). Molybdenum Nitride and Tungsten Nitride resent much more dramatically than Chromium nitride to the applied substrate bias. MoN diffractograms show clear signals of the cubic phase for bias values no larger than -40V (**Figure 70**). By exceeding this threshold value, the onset for the crystallization of the hexagonal phase is reached. The preferred orientation of the hexagonal phase switches from the (100) to the (001) by increasing the applied bias from -50 to -100 V. At this point a very well crystallized and (001) oriented hexagonal $\delta - MoN$ is formed. WN films retain the cubic phase for all the negative bias values. From a negative substrate bias of -50V (**Figure 71**), the reformation of metallic Tungsten at the expense of the nitride phase is observed. The highest crystallographic quality is found for a negative substrate bias of -40V. It is interesting to observe that the effects of increasingly high negative biases on WN and MoN are more dramatic than for CrN. This might be explained considering that Mo and W nitrides at medium-to-high Nitrogen proportions can be formed in more metastable phases, such as the cubic and the hexagonal phases, while for sufficiently high Nitrogen amounts, Cr is

only nitridated in its cubic phase. Variations in the energetics of the growth process can provoke a phase switch, and substrate bias is directly affecting the energetics of film growth. Besides, due to the larger atomic mass, the energy transfer of Mo and W-based particles is higher than that of Cr-based ones. Hence, a stronger energetic contribution to the growth kinetics is provided in the case of MoN and WN, which can explain on a qualitative level the dramatic changes in crystallographic properties of MoN and WN. Besides, in the case of WN, the reformation of metallic W can be due to preferential sputtering of light Nitrogen atoms from the underlying surface because of the bombardment of W ions and neutrals during the process [452]. In the case of CrN, the increased energy transfer changes the texture towards the <200> plane orientation. An increased compressive state of the growing film at larger negative biases can be deduced by the shift of the <200> planes towards a larger Bragg angle. Nonetheless, in the case of CrN, both the phase stability and the limited energy transfer to the growing film owning to the relatively light Cr particles prevent the dramatic atomic restructuring of the material.

3.3.5.2 IMPACT ON INTERPLANAR DISTANCES AND GRAIN SIZE

In Figure 72 and Figure 73, the dependencies of the interplanar spacing and crystallite size calculated from the <200> peak signals using the Bragg and Scherrer formulae are respectively reported as a function of the applied substrate bias. By increasing the substrate negative bias up to -50V, a monotone increase is observed for the interplanar distance between adjacent <200> planes, for all the coatings. A compressive state is expectably imposed by the bombardment of accelerated Ar^+ and Me^+ particles (Me= metal). Nonetheless, the increase in interplanar distances, and hence of the lattice parameter, suggests the concurrence of some different effects. The application of bias poorly affects the composition of coatings [453]. Hence, enhanced Nitrogen retention driven by the higher bias is unlikely. Possible explanations could be the enhanced ion implantation within the coating and the improved mobility of adatoms which overcomes the compressive effect of the bombarding atoms. At higher bias values, the severe impact of bias on the crystallization process observed in **Figure 69**, **Figure 70** and **Figure 71** come along a steady reduction in the lattice spacing (**Figure 72**). A reasonable explanation of this trend inversion is the higher compression imparted by the highly accelerated impinging particles. In the case of MoN (**Figure 70**), the bias has a major

impact on its crystallization, favoring the cubic-to-hexagonal phase transition. Hence, monitoring of the <200> lattice spacing against bias voltages higher than 50V was not possible. For both CrN and WN, the decrease in lattice spacing at high voltages can be due to the relaxation of internal stresses promoted by the reformation of the metallic phase in the case of WN (check **Figure 71**) and loss of microstructural order in the case of CrN (**Figure 69**). The same argumentations can explain the reduction in crystallite size with increasing bias (**Figure 73**). The higher bombardment energy results in phase reformation (WN and MoN) and loss of lattice coherency, leading to the loss of crystallographic order in the coating. For CrN, a crystallite size recovery is observed at bias values exceeding 50 V. This could be since at bias values exceeding -50 V, the substrate current for CrN was substantially saturated (data not shown), suggesting a negligible gain of bombardment ions for increased negative bias. Besides, due to the lower weight of Cr ions to W and Mo, the impact energy of impinging particles is kept relatively low, and the gain in kinetic energy is mostly used by adatoms to migrate on the deposition surface, eventually allowing partial recovery of crystallographic coherency, leading to an increased crystallite size.

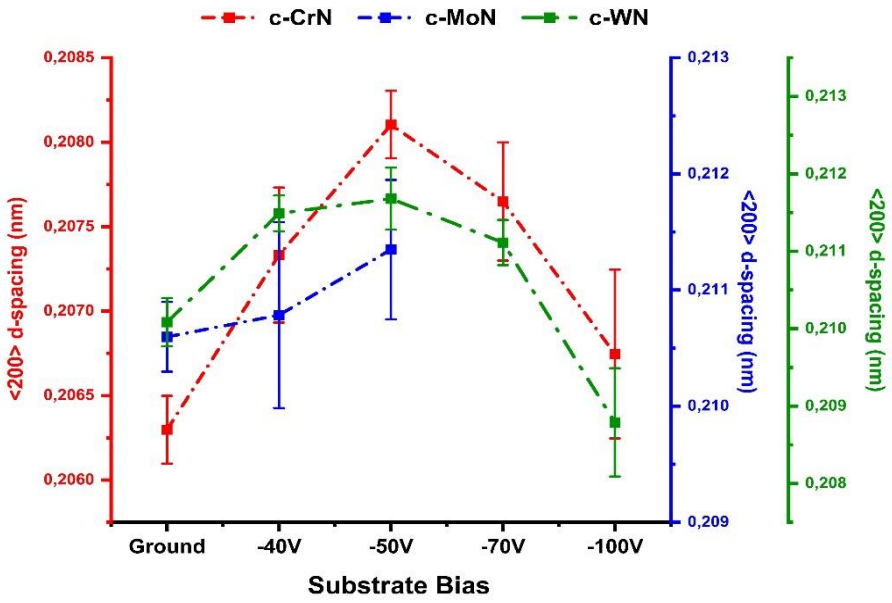

***Figure 72**: Dependence of the interplanar distance of <200> planes against the applied negative substrate bias. For the MoN series, data for substrate bias exceeding -50V was not available due to the absence of the <200> peak signal.*

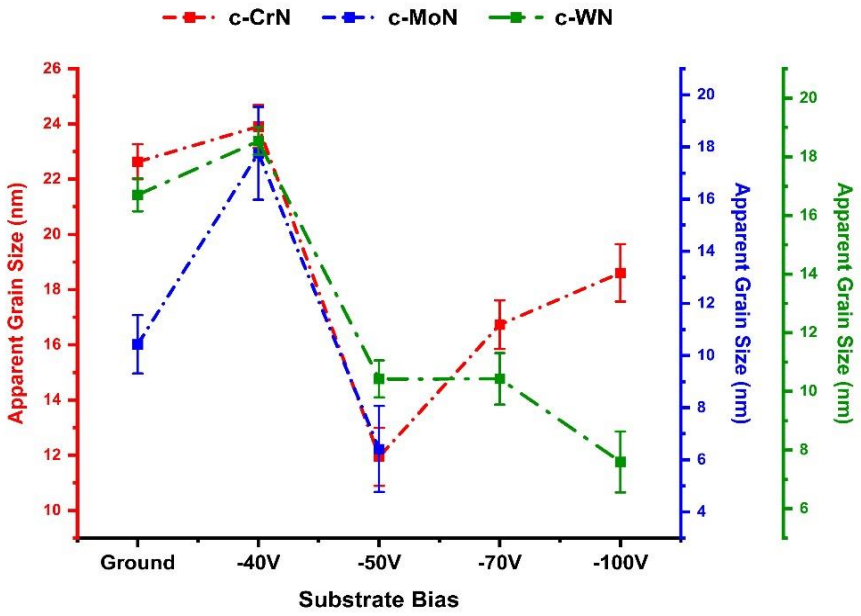

***Figure 73**: Dependence of the apparent crystallite size against the applied negative substrate bias. For the MoN series, data at substrate bias exceeding -50V was not available due to the absence of the <200> peak signal.*

3.3.5.3 IMPACT ON SURFACE ROUGHNESS

The impact of energetic particles on the growing film can level the film's surface [306] . This happens because of the mechanical removal of loosely attached particles and because of the reduced porosity of PVD films grown under intense ion bombardment. The effect of substrate bias on the surface roughness, though, can be more complex. The enhanced stresses imposed on the coatings can eventually lead to stress relaxation through the formation of defects such as cracks formation, buckling and delamination, which ultimately increase the surface irregularity [148]. The effect of increasing substrate bias on surface morphology has been investigated via semi-contact AFM. Example images of each coating type are reported in **Figure 74**. Next to each image, a color scale representing the total surface height excursion is reported. In **Figure 75**, the distributions of the heights of each pixel in the AFM images are plotted for the three coatings against the substrate bias magnitude. As a general trend, an increase in substrate bias results in narrow height profile distribution and substantially affects the coating surface appearance.

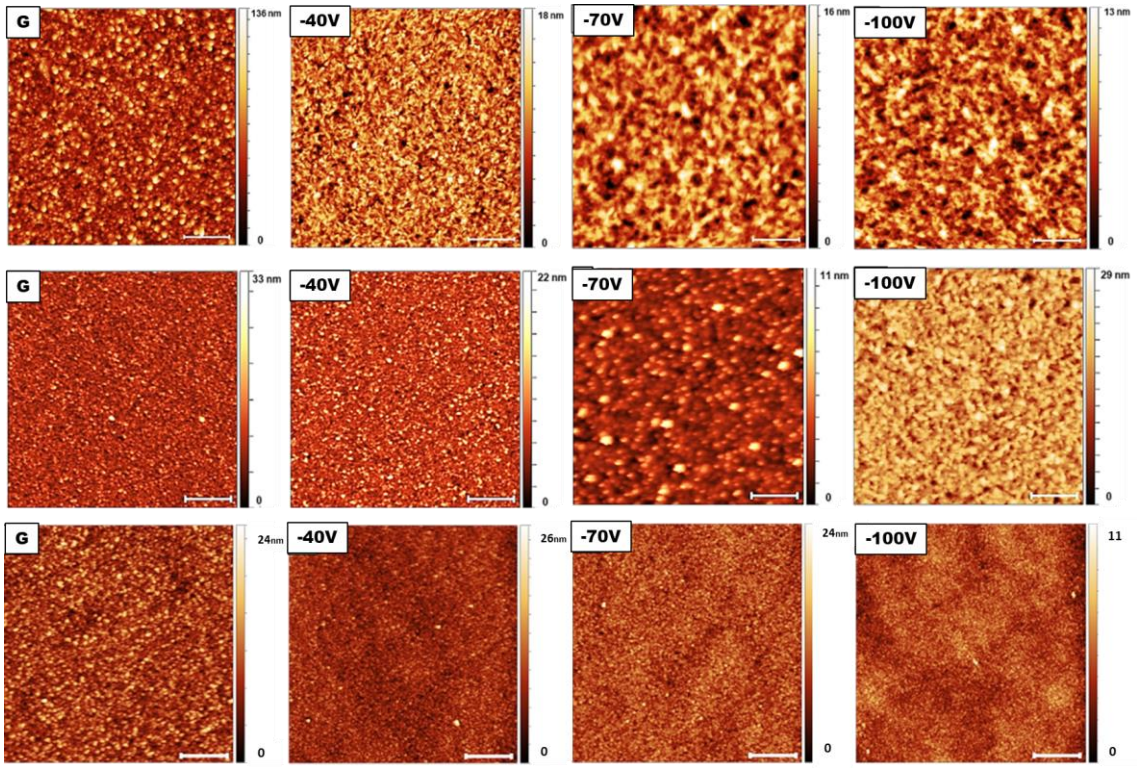

Figure 74*: AFM topographies of 5 um x 5 um surface regions of CrN (top row), MoN (middle row) and WN (bottom row). Bias values are reported in the top-left corner of each image. The bar's length is 1 um.*

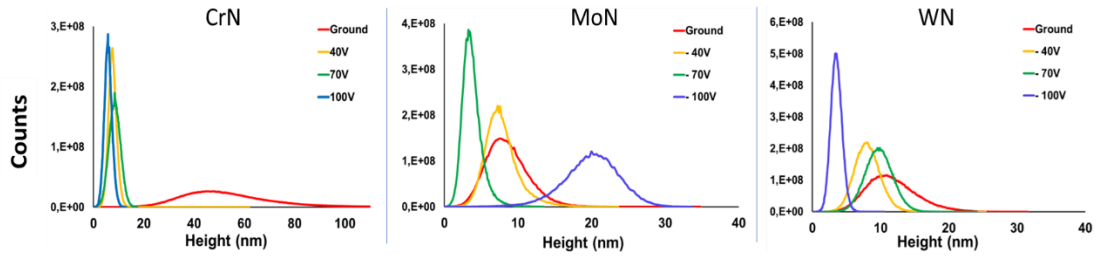

Figure 75: *Distribution of features height for CrN (left panel) MoN (middle panel) and WN (right panel) coatings plotted for different substrate bias values. In general, applying a negative bias as the effect of levelling the coating surface, which results in the shift and narrowing of the height distribution profiles to lower values.*

For CrN (top row in **Figure 74**) the surface of grounded substrates shows a spike-like feature with a very large variation in profile height (**Figure 75,** left panel**)**. Such elevated irregularity is dramatically reduced by about one order of magnitude with negative biases of -40V. Further increasing the substrate bias does not change the asperity range significantly, but the surface appears to be coarser and less finely granulated. In the case of MoN (middle row in **Figure 74)**, no substantial differences in neither surface

appearance and asperity regime are noticed between grounded and -40 V biased samples. Then, with a substrate bias of -70V and -100V, the surface is progressively coarsened (**Figure 75,** middle panel) . By comparing these findings with the XRD data in **Figure 70**, **Figure 72** and **Figure 73**, the surface modification at high bias values can be correlated to the formation of the hexagonal δ-MoN phase and an increase in surface defects induced by the bias-boosted ion bombardment. As for the WN (bottom row in **Figure 74)**, along with a gradual reduction of the surface height distribution with increasing bias magnitude (**Figure 75,** right panel**)**, a progressively finer-grained surface appearance is also observed. This is probably due to the larger levelling effect of heavy W particles and the increased number of Ar neutrals scattered back from the W target surface [157], [166], [167], [439].

3.3.5.4 IMPACT ON COATINGS STABILITY

It is worth mentioning that the high stress imparted by the high energy flux during deposition processes at high bias often resulted in the quick delamination of the coating soon after the end of the deposition process. An example of extensive surface damage of a WN single-layer coating is shown in the SEM image in **Figure 76**.

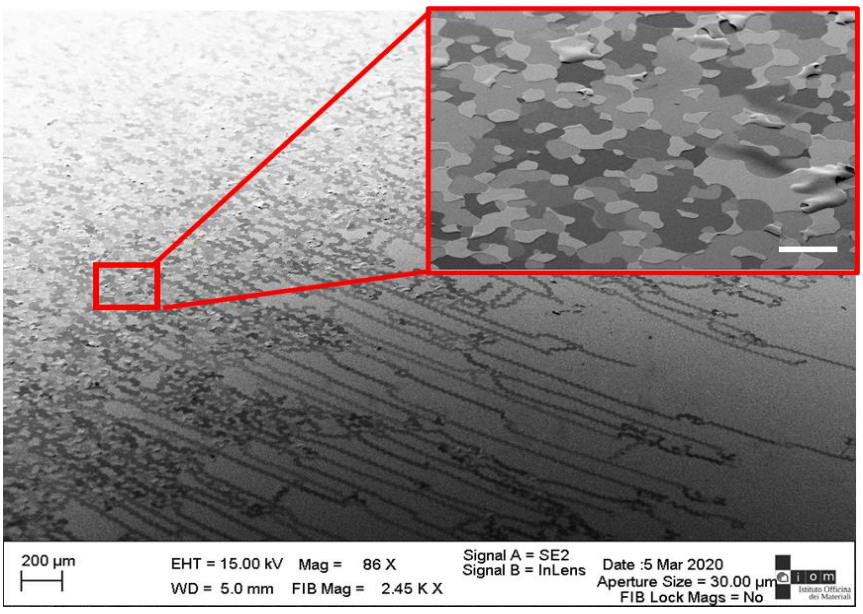

***Figure 76**: SEM image of typical surface defects of WN coating occurring after deposition with the highest bias value of -100V. The inset is a 10x magnification showing the fragmentation of the coating. Gray contrast is due to the different materials exposed, namely Silicon (darker), Chromium adhesive layers (dark grey) and Tungsten nitride (light grey). Insert's scale bar is 50 microns.*

The vertical linear profiles were visible to naked-eye and rapidly propagating. In the most severe cases, complete detachment of the coating from the surface occurred. For WN deposition, such high coatings instability was not observed for negative bias values of -50V or lower. In the case of MoN coatings, a maximum substrate bias of -70 was applicable without the occurrence of similar surface defects. On the contrary, no such issue was encountered for CrN, which exhibited the highest stability.

3.4 DISCUSSION AND CONCLUSIONS

The first part of the research activity was dedicated to the definitions of the proper process conditions for the deposition of CrN, MoN and WN coatings. In all cases, single-layer coatings were deposited for a fixed time of 15 minutes onto a plasma-cleaned Si substrate pre-deposited with a thin (50-70 nm) layer of the Chromium adhesion layer. To promote the adhesion of the coatings on the silicon. The preliminary study on the determination of the deposition rate led to the choice of working pressure of $3*10^{-3}$ mbar and TPD of 2.75 W* cm^{-2} for CrN, and 1.65 W*cm^{-2} for MoN and WN. Then, it has been found that both the composition of the gas mixture used in the reactive sputtering process and the applied substrate bias have a major impact on the crystallization properties of the resulting coatings. To facilitate a good interfacial match between adjacent layers in a multilayer structure, it is preferable that the adjacent constituent materials have similar structures, to reduce the interfacial strain due to lattice distortions. So, the criterion followed to determine the best deposition conditions was to obtain the most closely related crystallographic structures. Well-crystallized cubic phases of CrN, γ-Mo_2N and β-W_2N/W_3N_4 were obtained at Nitrogen flux percentages of 66%, 50% and 40% respectively (**Section 3.3.3**). At such compositions, XPS and EDX investigations (**Section 3.3.4.1** and **3.3.4.2**) confirm that the coatings are strongly nitridated. By comparing the diffraction data with EDX quantitative chemical analysis, we stated that CrN coatings consist of a stoichiometric cubic CrN phase, while MoN has an atomic concentration of Nitrogen of 50%, a 17 at.% excess from the theoretical value. Finally, WN coatings deposited with 40% of Nitrogen flux percentage consist of a non-stoichiometric cubic phase with a Nitrogen atomic fraction of 45.2% at., just in the middle between the predicted values for the pure cubic β-W_2N and c-W_3N_4 phases, respectively

33.3% at. and 57.2at.% Scherrer analysis confirms all the coatings are nanocrystalline, with crystallite sizes around 10-25 nm with medium-to-low bias values (**Figure 73)** and using the structure-optimizing reactive gas mixture (**Figure 57**). A low substrate bias of -40V yields the best crystallographic properties of each coating individually, and it also determines a cubic structure for each material. This also provides a low coatings surface roughness of the order of a few nanometers. In the case of WN, the internal stresses developed because of imparted bias values exceeding 70V resulted in the premature and spontaneous detachment of parts of the coatings from the Chromium-coated silicon substrate. Because of these analyses, for the development of multilayer systems the process conditions summarized in **Table 14** were adopted:

***Table 14**: Process parameters chosen for the making of multilayer coatings*

Material	WP (mbar)	$\%N_2$ (sccm)	TPD (W cm^{-2})	V_{bias} (V)	T_{sub} (°C)	Rate (nm/s)
CrN	3 E-03	66%	2.65	-40	230	0.75
MoN	3 E-03	50%	1.75	-40	230	0.71
WN	3 E-03	40%	1.75	-40	230	0.69

4 MULTILAYERS ANALYSIS PART I: INTERFACE AND SURFACE ROUGHNESS CONTROL IN NANOLAMINATE CrN/WN COATINGS DEPOSITED ON Si <100>

4.1 INTRODUCTION

The topic of this section is based on the paper titled "Surface roughness control in nanolaminate coatings of Chromium and Tungsten nitrides", published in the *Micro and Nano Engineering*" journal (DOI: *https://doi.org/10.1016/j.mne.2022.100107*). The problem of coatings' surface roughness, its sources, and the role of multilayer designs to optimize the coatings surface features are first presented in this section. Then, a thorough description of the original analytical protocol followed to unravel the contributions of the constituent materials is provided and results are eventually discussed in terms of the deposition energetics.

4.1.1 SURFACE ROUGHNESS AND FRICTION IN PVD COATINGS

Surface roughness plays an important role in friction at the tool-workpiece interface. As a matter of fact, frictional heat is generated during machining operations from the dissipation of shear forces between the tool and the workpiece materials, which interlock through their surface asperities [51], [267], [413]. In general, surface asperities originate from surface defects on the substrate, such as scratches produced during mechanical polishing or residual particles due to uncomplete substrate cleaning. Other defects can form during the deposition process itself as a consequence of stress relaxation mechanisms [454], [455]. Finally, disordered microstructural evolution stemming from the crystal growth of misoriented crystallites can contribute to the ultimate development of surface defects [149], [456]. The impact of crystallite size, internal stresses and defects linked to non-conformal growth increases with coating thickness [456]–[458]. As a consequence, roughness builds up by increasing the coating thickness [267], [459], [460]. As tribological coatings must be a few micrometers thick to provide the substrate with sufficient protection, strategies must be adopted to reduce the surface roughness while maintaining a suitable coating volume. A way to improve the control over roughness

development is based on the substitution of monolithic coatings with multilayer coatings. Multilayer coatings are constituted of an alternate stack of different layered materials with individual thicknesses of a few up to a few tens of nanometers. The alternate deposition of different materials can help limit the growth of defects in several ways. The alternation of materials with different mechanical, thermal and crystallographic properties generates periodically changing stress fields which retard the onset of stress-related defects and hinders the propagation of cracks through the coating in respect to monolithic systems [454], [457], [461]. Also, the thickness of the individual layers imposes an upper boundary for crystal growth, thus limiting the microstructural contribution to the development of rough profiles. Notably, the individual contributions of each constituent material to the development of the overall coating's roughness are usually not addressed in the connection between multilayers design and surface roughness. As a matter of fact, the overall surface roughness is usually correlated to the individual layers thickness, where the bilayer repetitive unit is used as the smallest-size parametric unit. Accordingly, little investigation is dedicated to the understanding on how the roughness is developed along the thickness of a multilayer coating [462], and whether it can be rationalized in terms of materials properties, process conditions and design parameters such as the individual layer thickness. It is worth to mention that this aspect is particularly important for multilayer mirror coatings, whose interfacial roughness plays a fundamental role in the multiple interfacial reflections of the impinging radiation and ultimately to the overall reflective efficiency.

4.1.2 UNRAVELLING THE INDIVIDUAL CONSTITUENTS' CONTRIBUTIONS

The challenge of discriminating against layers-specific contributions to the construction of roughness along the coating has been investigated in detail. In this study, a set of nanolaminate coatings consisting in an alternated repetition of cubic Chromium nitride (CrN) and cubic Tungsten nitride (c-WN) layers is fabricated via unbalanced DC magnetron Sputtering. The individual layers thickness range is between 100 and 10 nm. The reduction of surface roughness as a function of individual layers thickness is demonstrated by semi-contact Atomic Force Microscopy (AFM). Scherrer analysis performed on X-Ray Diffraction (XRD) crystallographic signals shows that the reduction

in surface roughness is correlated to a reduction in crystallite size, modulated by the nanolaminate architecture. Conformity and uniformity of multilayer coatings is observed via FIB-SEM cross-section micrographs. The relative contribution of CrN and c-WN layers to the overall roughness development is investigated through a SEM cross-section micrograph-based analysis. The microstructural and topographical features of nanostructured CrN/c-WN multilayer coatings are correlated to the observations from the cross-section analysis and discussed in terms of the energy transfer to the growing surface during each deposition step.

4.2 MATERIALS AND METHODS

The materials and methods used for the AFM and XRD analyses developed for the multilayer coatings investigated in this chapter are the same as those descripted in **Section 3.2**. Here, only the specific methods and materials used for the present investigation are descripted in detail.

4.2.1 COATINGS DEPOSITION

Si (100) substrates were cleaned in a two-step process by an ultrasound bath in ethanol (96% pure) for 5 minutes and RCA-1 solution (H_2O:H_2O_2: NH_4OH at a 3:1:1 ratio in volume) for 10 minutes at 80°C, rinsed in deionized water and blow-dried with a Nitrogen gun. After the wet-cleaning procedure, substrates were placed in the deposition chamber and pre-treated by Argon - Oxygen plasma cleaning (Ar:O2 ratio of 4:1, working pressure $4*10^{-3}$ mbar, RF power of 100W). Monolithic and nanolayered coatings were deposited via balanced DC Magnetron Sputtering in reactive mode. Substrate to target distance was 8 cm. A negative substrate bias of -40V was applied to the substrates by means of an external DC generator and substrates were heated to 200 °C, to ensure a good film adhesion and low porosity. An interlayer of 75 ± 9 nm of metallic Cr was deposited in each process prior than the multilayer coatings to improve the adhesion to the Si substrates. The deposition of nitride coatings was accomplished by a DC Reactive Sputtering procedure using 6-inches target of metallic Cr (99.995%) and W (99.95%) in

a Nitrogen and argon reactive gas mixture. CrN layers were deposited at a N_2 sccm fraction of 66% with a Cr target power density of 2.7 W cm^{-2}, while WN layers were obtained by introducing a gas mixture consisting of a N_2 sccm fraction of 35% with a target power density of 1.6 W cm^{-2}. In both cases, the working pressure was regulated to $3.0 \pm 0.1 * 10^{-3}$ mbar. In such conditions, deposition rates were 0.74 nm/second and 0.72 nm/second for CrN and WN layers respectively, as measured in separate calibration experiments via FIB cross-section imaging on single layers coatings, with the same procedure shown in Section 3.2. In all the samples, the first nitride layer being deposited was CrN and the total coating thickness was controlled to 1.2 ± 0.1 μm to exclude the thickness dependence on coatings roughness.

4.2.2 CROSS-SECTION PREPARATION AND ANALYSIS

FIB cross-sections on CrN/WN nanolaminate samples were fabricated using FIB-SEM Helios Nanolab 650 (ThermoFisher Scientific, The Netherlands), equipped with X-Max 50 SDD EDX detector (Oxford, UK). First, as-deposited samples were covered with a protective 700-nm thick platinum layer via e-beam evaporation by introducing a metalorganic precursor. Subsequently, fine cross-sections were cut by progressively reducing the ion-beam current of the FIB from 2.5 nA to 0.4 nA at 30kV. Eventually, clean cross-sections were imaged via low kV SEM approach (2kV at 13 pA) at a tilt angle of 38 ° in respect to the samples surface normal. Cross sections images were analyzed via a home-made script in MATLAB® (The MathWorks, Massachusetts, USA) developed using only built-in functions and algorithms included in the Image Processing and Statistical Functions packages.

4.3 RESULTS

4.3.1 AFM CHARACTERIZATION

The extent of surface roughness has been analyzed via semi-contact atomic force microscopy. In **Figure 77**, the calculated round means square (R_{sq}) value of surface roughness for monolithic CrN and WN as well as nanolaminate (NL) coatings with

individual layer thickness from 100 nm/l to 10 nm/layer is reported. On the same graph, selected tridimensional 5-um square AFM topographies NL coatings with 100 nm/layer, 25 nm/layer and 10 nm/layer architecture are shown. All the surfaces are homogeneous with roughness values in the nanometer regime. Monolithic CrN expressed the highest roughness value among all coatings, while monolithic c-WN coatings comparatively showed a remarkably low roughness. The surface roughness of multilayer coatings is shown to decrease with decreasing individual layers thickness. This is in good agreement with the general assumption that the lower the deposition time for each constituent layer, i.e., its thickness, the lower the building up of structural defects such as porosities and piling up of coating material.

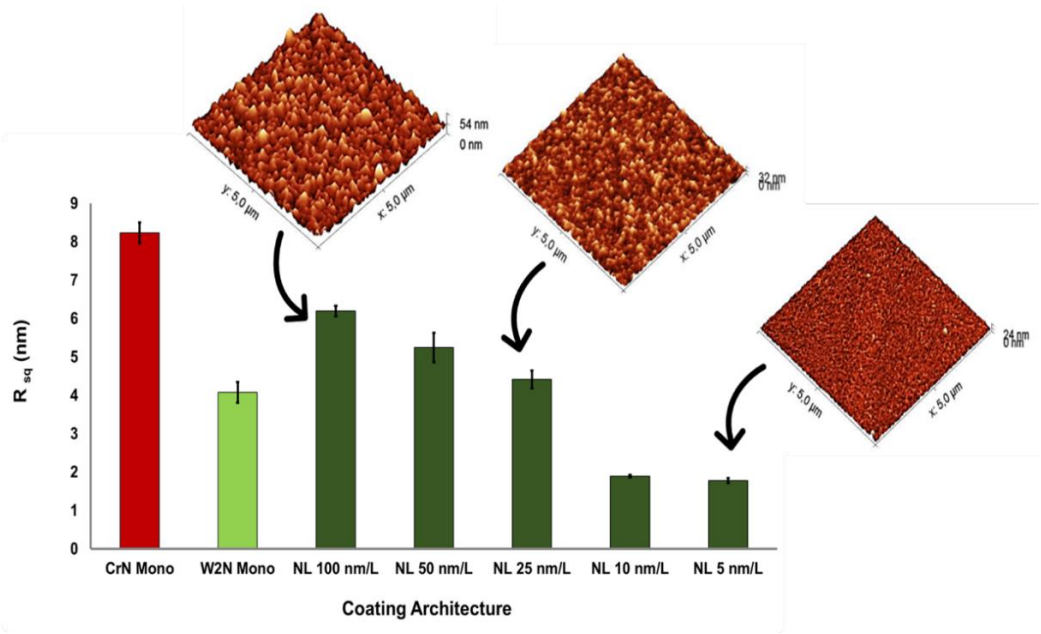

***Figure 77**: Surface roughness values for different CrN/WN multilayer coatings and a selection of representative 3-dimensional AFM topographies*

4.3.2 XRD CHARACTERIZATION

Depending on deposition parameters such as reactive gas mixture composition, substrate bias and substrate temperature, Tungsten and Chromium nitrides can be deposited in cubic phases, hexagonal phases or a mixture of the two [425], [434] . By comparing the diffraction experimental data with the Powder Diffraction File (PDF) database, both CrN

and WN are found to be deposited in their cubic phases, with a dominating (200) orientation (see **Figure 78-A**). Concerning CrN, <111> and <200> peaks occur respectively at 2θ values of 37.4 and 43.6 degrees, whilst for cubic WN, the same peaks occur at 37.1 and 42.8 degrees. In nanolaminate systems the cubic phases of the constituent materials are retained. Peaks-maxima positions and intensities vary in respect to the monolithic references and to a different extent depending on the multilayer architecture. Due to the larger cross-section for the interaction of W over Cr, the corresponding peak intensities of the WN components are more intense than those of CrN, which in turn are only visible for individual layer thicknesses of 100 nm-per-layer.

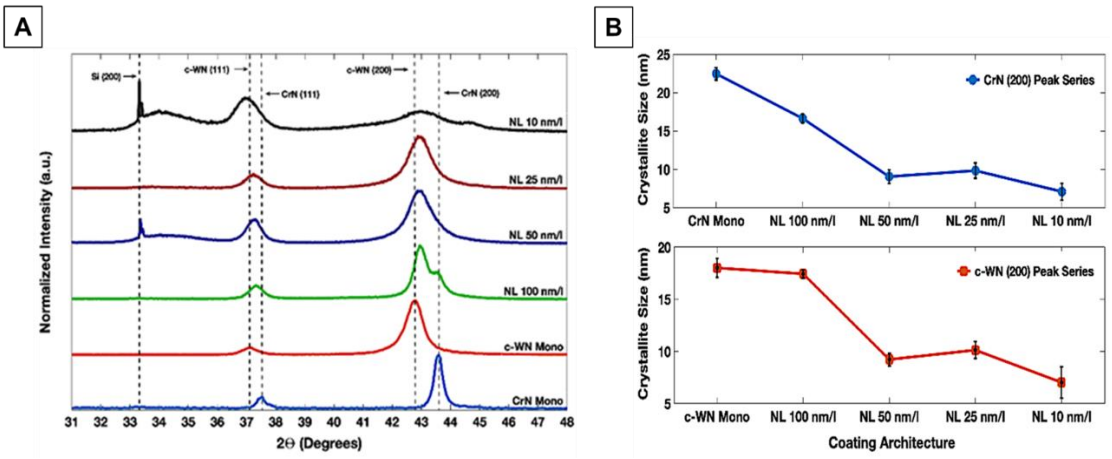

***Figure 78**: A) XRD diffractograms of nanolaminate systems with different individual layer thicknesses (reported next to each profile) and B) apparent crystallite sizes calculated by using the Scherrer formula on deconvoluted <200> peaks contributions for the two constituent materials.*

The apparent crystallite sizes are determined by fitting the <200> peak signals with Voigt curves to extract the full width at half maximum (FWHM) for each peak and then using its value in the Scherrer equation [190]:

$$D_{hkl} = K * \frac{\lambda}{FWHM_{hkl} * \cos\theta_{hkl}}$$

Where D is the crystallite size, λ is the x-ray wavelength (0.15414 nm for Cu Kα radiation), θ is the Bragg angle corresponding to the peak maximum position, *hkl* are the Miller indices for the analyzed peak and K is the Scherrer shape-factor coefficient, set equal to 0.9 by convention, detailed crystallites shape information being missing [188], [190]. For the fitting procedure, initial guess of peak centers positions is provided based

on the values of the monolithic coatings. From the calculated apparent grain sizes reported in **Figure 78-B**, all the coatings are nanocrystalline with crystallite size decreasing by progressively thinning the thickness of the individual coatings, which act as an upper bound for crystal growth.

4.3.3 ANALYTICAL PROTOCOL

The procedure proposed allows the determination of the interface roughness between each couple of adjacent layers in multilayer samples. Images are treated by MATLAB as numerical matrices with each pixel consisting of a brightness value ranging from 0 (black) to 255 (white). The tool exploits the Z-contrast in SEM micrographs of CrN and WN samples due to the large difference in atomic number between Chromium (Z=24) and Tungsten (Z=74) to determine point of maximum brightness difference, corresponding to the interface between CrN and WN layers.

4.3.3.1 DETERMINATION OF INTERFACE PROFILES

First, a region of interest (ROI) is interactively defined on the image to exclude image portions non including the multilayer structure. For each column of the matrix generated from the ROI, an array containing the column-wise pixels values is recorded and a column-wise intensity profile is obtained (**Figure 79-A**). This intensity profile is then differentiated to determine the points of maximum intensity, i.e., brightness, variation (**Figure 79-B**). The points of maximum variation in the Differential Brightness Curve (DBC) correspond to the interfaces between dark low-Z (i.e., CrN) and bright high-Z (i.e., WN) layers. The MATLAB defined peak-identification parameters of *peak prominence* and *minimum peak distance* between consecutive peaks are adjusted. This is pursued by a trial-and-error procedure on a single column of the image and serves to identify the peaks corresponding to interfaces while avoid recording local extrema in the DBC which do not correspond to interfaces as well as missing out actual peaks from the DBC. Each maximum and minimum point in the curves correspond to the punctual transition from a dark CrN to a bright WN material image. Once the parameters are optimized, the procedure of peak identification is looped to process the whole image within the ROI, and all the interface locations within the ROI are stored as individual arrays with values

following interfacial profiles. Such profiles are then superimposed on the cross-section image with a fixed color code, red for WN upper interfaces and green for CrN upper interfaces **(Figure 80**).

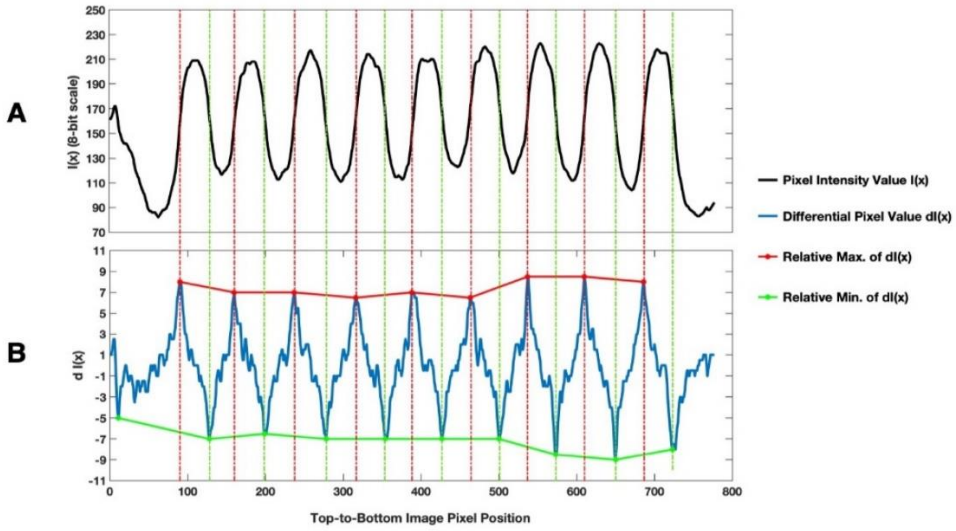

***Figure 79**: (A) Example of pixel intensity value profile along one cross-section image column in the direction orthogonal to the sample surface and (B) the corresponding differential profile. Red and green dotted lines show the correspondence of dI(x) peaks with the inversion points in the original data I(x), corresponding to the interface between dark and bright layers in the image.*

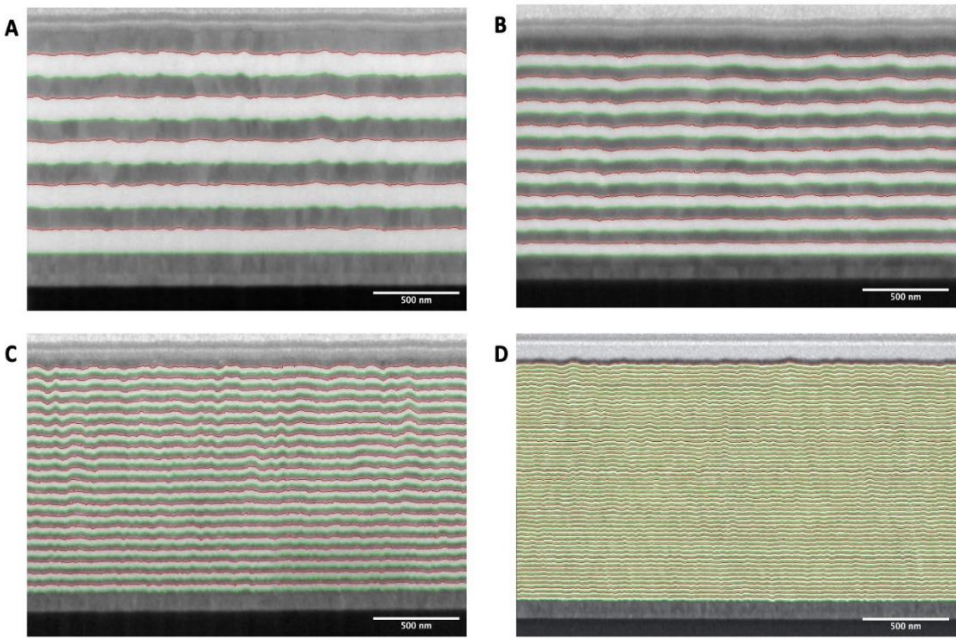

***Figure 80**: SEM cross-section images of nanolaminate coatings with (A) 100 nm per layer, (B), 50 nm per layer, (C)25 nm per layer and (D) 10 nm per layer. Interfacial profiles are also reported. Red and green line profiles represent the CrN-on-WN and WN-on-CrN interfaces respectively. The last interface between the platinum pad and the topmost coating layer as well as the interface between the first CrN and the underlying Cr interlayer are not included in the analysis.*

4.3.3.2 INTERFACE ROUGHNESS ANALYSIS

The second part of the interface roughness analysis starts with the calculation the standard deviation *Std* of the interfacial profiles. The Std value is representative for the deviation of each interfacial profile from perfect linearity representative of a perfectly smooth interface. In **Figure 81,** the average Std values are plotted versus the corresponding interface position across the multilayer thickness for each multilayer system. At this point, the relative increment $r_{1/2}$ of the Std value of each layer in respect to the Std value of the underlying one is calculated as:

$$r_{1/2} = \frac{Std\ {}_1^{\,i} - Std\ {}_2^{\,i-1}}{Std\ {}_2^{\,i-1}} * 100$$

Here, subscripts 1 and 2 refer respectively to the topmost and underlying interfaces in each pair and *i* is the interface position index.

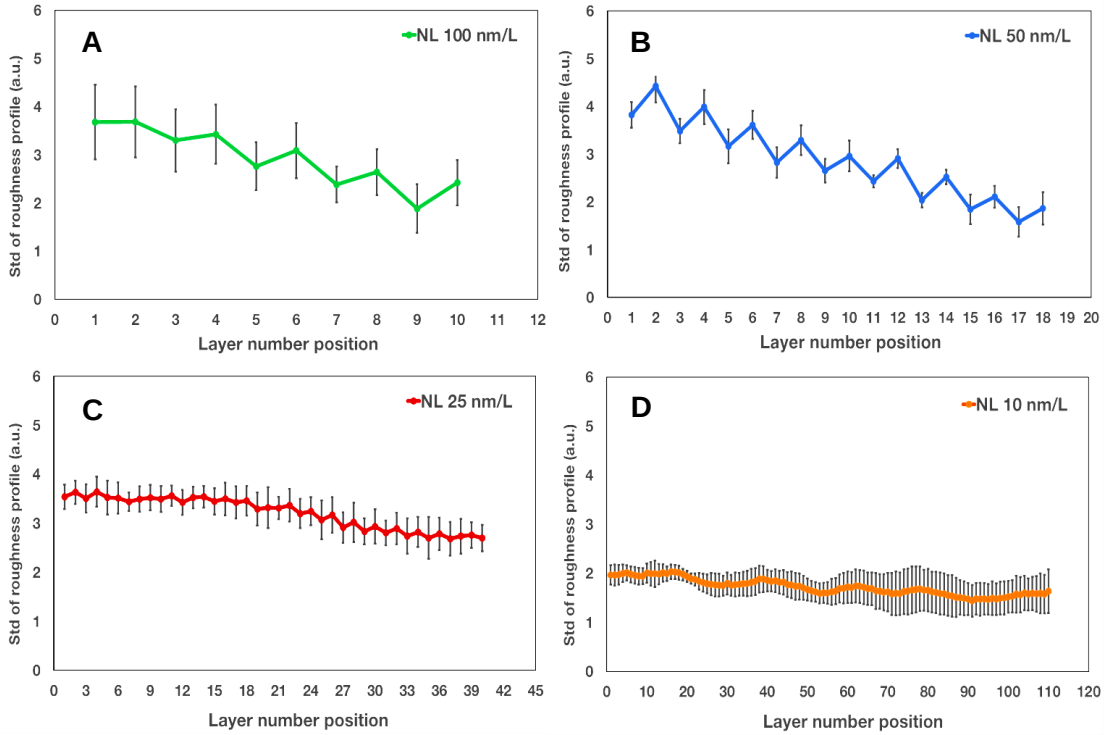

Figure 81*: Line standard deviation (Std) values at each layer position for the (A) 100 nm/l, (B) 50 nm/l, (C) 25 nm/l and (D) 10 nm/L coatings architectures. Error bars represent the standard deviation of calculated Std values at the same position (i.e., for corresponding layers) on different cross-section images. Layer position numbers grow from the surface to the substrate.*

The $r_{1/2}$ values were calculated for all the interface pairs from the coating's surface towards the Cr interlayer. Then, the whole set of $r_{1/2}$ values was separated into distinct CrN-on-WN and WN-on-CrN series, with the $r_{1/2}$ values constituting each series defined as $r_{1/2}^{CrN/WN}$ and $r_{1/2}^{WN/CrN}$ respectively. The corresponding mean values $< r_{1/2}^{CrN/WN} >$ and $< r_{1/2}^{WN/CrN} >$ were then calculated for each cross-section image by averaging the $r_{1/2}^{CrN/WN}$ and $r_{1/2}^{WN/CrN}$ series separately (see **Figure 82**). At least three cross-sections per multilayer architecture were processed according to the procedure descripted above, each providing one $< r_{1/2}^{CrN/WN} >$ and one $< r_{1/2}^{WN/CrN} >$ values. These were eventually used to calculate the architecture-average values $< R_{1/2}^{CrN/WN} >$ and $< R_{1/2}^{WN/CrN} >$ for each coating architecture (**Table 15)**.

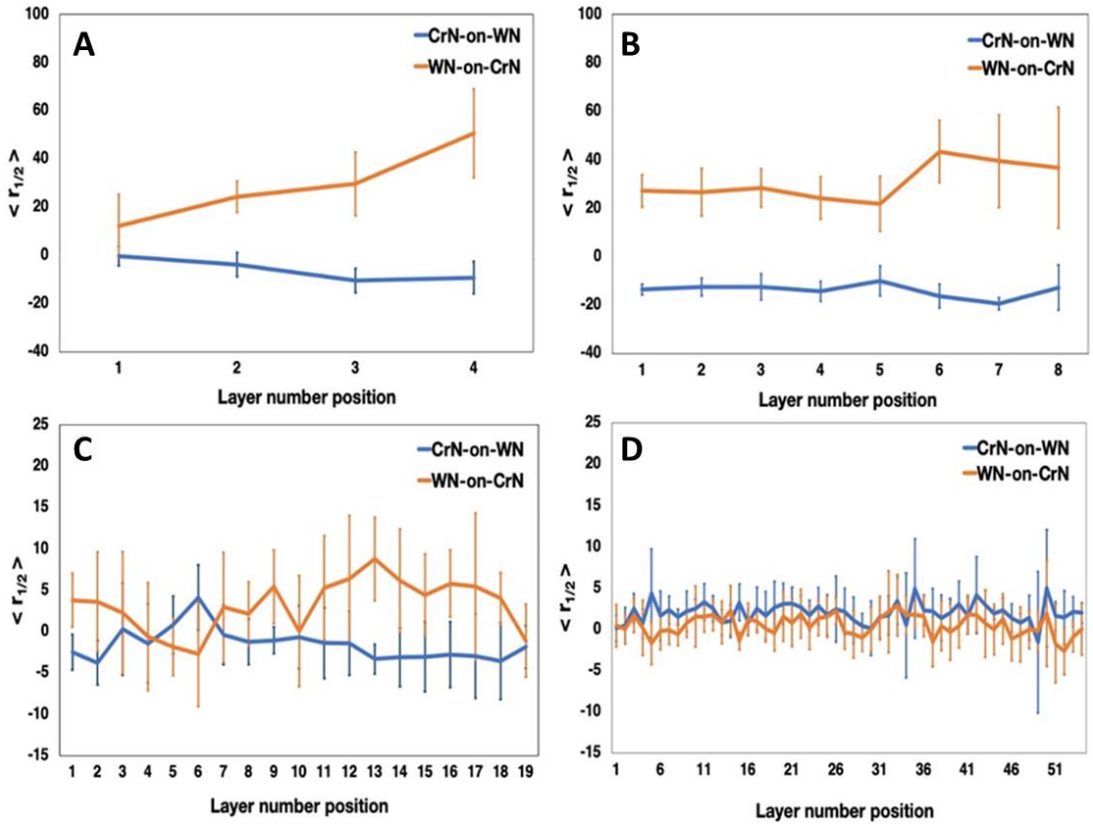

Figure 82*: Average relative roughness variations values < r1/2 > for the two series CrN-on-WN (blue curves) and WN-on-CrN (orange curves) referred to the CrN/WN nanolaminate systems with (A) 100, (B) 50, (C) 25 and (D) 10 nm-per-layer architecture. Error bars are standard deviations calculated from at least three values per point. Layer number position grows in the direction from the sample surface to the substrate*

Table 15: Average relative contributions and corresponding errors for the CrN/WN multilayer coatings.

Coating Architecture	$< R_{1/2}^{CrN/WN} >$	CrN-to-WN Std. Dev.	$< R_{1/2}^{WN/CrN} >$	WN_on_CrN Std. Dev.
100 nm/L	-4,68	11,32	33,06	20,05
50 nm/L	-12,09	10,02	20,47	16,77
25 nm/L	-0,88	7,06	4,89	10,10
10 nm/L	0,48	2,39	1,24	2,29

Eventually, the architecture-average $< R_{1/2}^{CrN/WN} >$ and $< R_{1/2}^{WN/CrN} >$ values are available and plotted in **Figure 83**. It can be observed that the two materials behave differently. The roughness increment of WN layers is positive all nanolaminate systems, while the effect of CrN layers showed a more complex behavior. For both series, the corresponding effect is larger when relatively thick layers are deposited and decreases with the individual layers thickness.

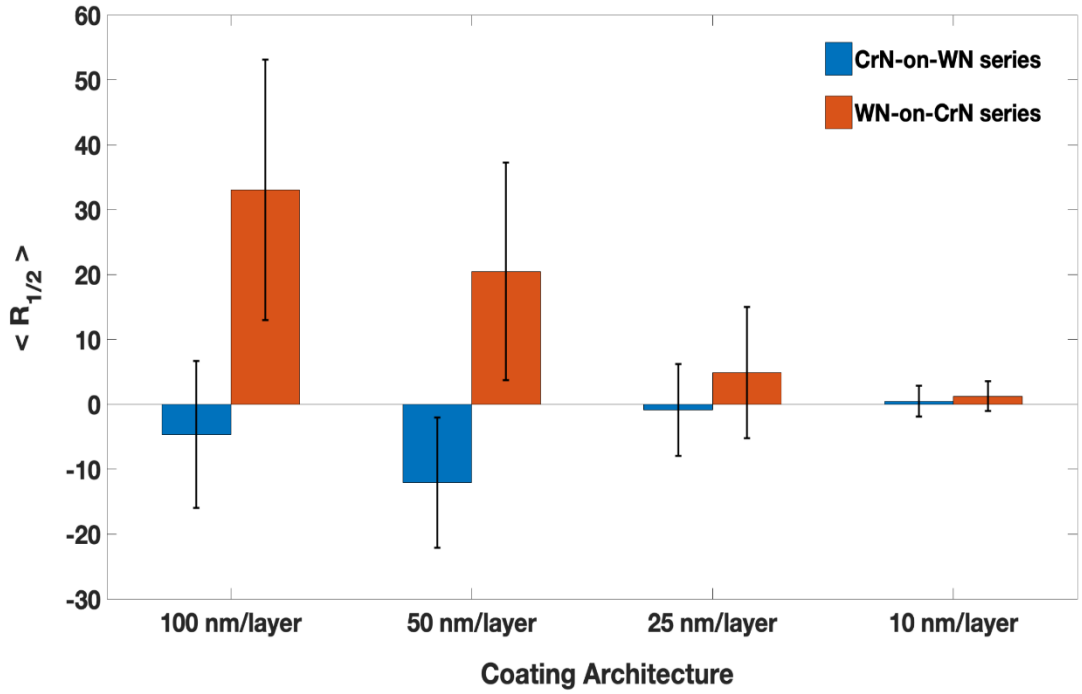

***Figure 83**: Comparison of the architecture-averaged <$R_{1/2}^{CrN/WN}$> and <$R_{1/2}^{WN/CrN}$> values for all the coatings architectures considered, with the corresponding standard deviations*

4.4 DISCUSSION

Magnetron sputtered nanolaminate coatings based on alternate deposition of CrN and c-WN on Si <100> substrates showed a decreasing surface roughness with progressively thinner constituent layers, with each material contributing differently to the progressive build-up of interfacial roughness. As shown in **Figure 83,** the magnitude of the two materials' contribution evolves differently as a function of the individual layers thickness. The magnitude of $< R_{1/2}^{WN/CrN} >$ decreases monotonically with the individual layers thickness, and such behavior can be rationalized by considering a size-confinement effect [430]; on the contrary, the evolution of $< R_{1/2}^{CrN/WN} >$ shows a different trend, requiring a more insightful description. Monolithic CrN seems to revert the increment of roughness with respect to the underlying WN layer. This apparent behavior can be interpreted by considering the energy transfer contributions to the growing surface during WN and CrN deposition steps [157], [159]–[161], [166], [167], [463]. In sputtering processes with a negatively biased substrate, the energy delivered to the growing surface is largely constituted by the kinetic energy of impinging positive ions accelerated through the substrate sheath [159] and the flux of reflected neutrals [159], [160] and only marginally on the input target power [161]. The sputtering yield depends on the relative atomic weight of target atoms and gas ions [159], [160], [167]. Hence, due to the larger target-to-argon atomic weight ratio, the sputtering yield of Tungsten in argon plasma is less than that of Chromium. This means that when sputtering Tungsten fewer but more energetic metallic ions and atoms are ejected from the target than when using a Chromium target [167]. Also, the larger target-to-mass ratio enhances the backscattering efficiency of neutralized Argon atoms at the target surface towards the growing film [167]. Besides, the higher Ar fraction (65% vs 33%) and the lower target power densities (2.75 vs 1.65 $W*cm^{-2}$) used during the deposition of WN layers further increase the density of backscattered Ar atoms [157], [464]. Therefore, more energetic particles and more neutralized Ar atoms impinge on the growing surface during the deposition of WN layers. Both these contributions can explain the levelling of the underlying CrN layers during WN deposition steps as well as the absence of the same effect when depositing CrN on the previous WN layers. Hence, it can be assumed that when the individual layer thickness is still relatively high, as in the case of samples with 100 nm/l architecture, the surface-

levelling effect described earlier is opposed by the intrinsic roughness development behavior. When the individual layer thickness is brought down to 50 nm/l and thinner, the second contribution is constrained, allowing a more pronounced roughness reduction effect. As the constituent layers thickness is further reduced to 25 nm per layer, the two opposing trends of CrN and c-WN are still retained, but with a much lower magnitude. Eventually, as the individual layer thickness is restricted to 10 nm per layer, both contributions substantially approach zero owning to the very thin constituent layers. As a matter of facts, a slight trend inversion seems to occur. This fact might be explained by considering the relative nature of the roughness variations. In fact, by reducing the thickness of the individual layers, the positive roughness variation carried by c-WN layers is almost annihilated, and the relative negative contribution carried by CrN might then look reversed.

4.5 CONCLUSIONS

The main results of this analysis consist in part in the development of an analytical tool to investigate the development of interfacial properties along the coating thickness, and partly in the use of such tool to discriminate the individual contributions and behaviors of the constituent materials. This permits a higher degree of rationalization with respect to the analysis of surface roughness values of the coatings. A recent update of the script also permits to calculate the average thickness of each constituent and the development of each layer thickness during film growth. This has been implemented by calculating the average distance between two consecutive interface profiles and by inserting a pixel-to-distance calibration tool using image objects of known length such as image scale-bars, for instance. It is worth to highlight that the validity of the proposed method can be of use not only in tribological coatings but in any deposition route of multilayer materials where surface roughness control is important, for instance for barrier coatings and reflective mirrors.

5 MULTILAYERS ANALYSIS PART II: STRUCTURAL, MECHANICAL AND ELECTROCHEMICAL CHARACTERIZATION OF MULTILAYER COATINGS ON TOOL AND STAIN-LESS STEEL SUBSTRATES

5.1 INTRODUCTION

The second part of the research work on multilayer systems regards the characterization of CrN/WN and CrN/MoN multilayers coatings deposited onto D2 tool steel substrates. The main characterization approaches involve:

- A structural investigation via XRD, by standard Θ-2Θ scan.
- The measurement of stiffness and microhardness by means of Vickers nanoindentation and a qualitative estimation of coatings adhesion via the Daimler-Benz test using a Rockwell-C indentation route.
- The valuation of the corrosion protection characteristics through linear Potentiodynamic Polarization (PP) and qualitative Electrochemical Impedance Spectroscopy (EIS)

The main results of the characterizations are also supported by additional information. XRD-based residual stress analysis and texture analysis were performed on monolithic CrN, MoN and WN to help explain the mechanical and electromechanical measured properties of the multilayer systems. Also, the crystallite size in multilayer systems was calculated for coatings with varying thickness of the constituent layers. Semi-contact AFM topographies were acquired to calculate the surface roughness of the coatings. This was primarily needed to determine the conditions for the nanoindentation tests. FIB-cut cross-sections were imaged with SEM to check the conformity of the multilayer systems and studying the compliance of the different coatings to localized defects, which were also investigated with respect to heir source.

5.2 MATERIALS AND METHODS

5.2.1 SUBSTRATE PREPARATION

D2 (1.5 %wt C, 0.3%wt Si, 12.0%wt Cr, 0.8%wt Mo, 0.9%Wt. V, Fe to completion) and AISI 304 (0.07%wt. C, 1%wt. Si, 18%wt. Cr, 9%wt. Nickel, 2%wt. Mn, 0.05% P,S and 0.1%wt. N, Fe to completion) steel substrates were pre-cleaned from the storage oil by a ultrasound bath in ethanol for 10 minutes, then rinsed in distilled water and isopropanol and dry-blown by means of a Nitrogen gun. Si (100) substrates were cleaned in a two-step process by an Ultrasound bath in ethanol (96% pure) for 5 minutes and RCA-1 solution (H_2O:H_2O_2: NH_4OH at a 3:1:1 ratio in volume) for 10 minutes at 80°C, rinsed in deionized water and blow-dried with a Nitrogen gun. Pre-cleaned, substrates were placed on the sample holder 8 cm beneath the target surface. When a base pressure of 3E-05 mbar was reached, substrates were further treated by a two-step plasma etching route. The first step consisted of 5 minutes of 100W (90 V) RF plasma in an Ar: O2 atmosphere (flux ratio Ar:O2 = 4:1) total pressure of 5 E-03 mbar. The second step consisted of 10 minutes of 200W (130 V) RF plasma in Ar atmosphere, to a total pressure of 4E-03 mbar. Then, substrates were preheated to an actual substrate temperature of about 230 °C and left thermalize for 45 minutes after the set-point was reached. In the meantime, the two targets in use were pre-sputtered at a TPD of 2.65 W cm^{-2} for 10 minutes to remove any surface compound formed during the exposure to ambient pressure.

5.2.2 COATINGS DEPOSITION

All coatings were deposited via DC magnetron sputtering using 6-inch circular targets of Cr (99.995% purity), Mo (99.95% purity) and W (99.95% purity) in a N2/Ar reactive gas mixture made up with N2 fractions of 66%, 50% and 40% respectively. The working pressure was 3E-03 mbar. The substrate was pre-heated at 230°C and left thermalize for 45 minutes after the set-point temperature was reached. A substrate bias of -40V was kept during all the deposition steps. At the end of the temperature equilibration time, a 90 ± 10 nm layer of Cr was deposited prior than the first nitride layer to promote adhesion of the multilayer stack onto the steel substrate. In all the samples, the first and last nitride

layer consist of CrN. A total number of 21, 41, 101, 201 and 401 layers were deposited for the 100, 50, 25, 10 and 5 nm-per-layer architecture respectively, for a total thickness of 2.20±0.05 μm measured by SEM imaging on FIB-milled cross-sections. Deposition times varied consistently for the different coatings, ranging from about 45 minutes for the monolayer coatings, to nearly 10 hours for the 5-nm-per-layer architecture coatings, owning to parts moving times for target selection and substrate positioning between each deposition step

5.2.3 XRD CHARACTERIZATION

The structural properties of multilayer coatings consisting of repetitions of the structural unit CrN/WN (i.e., the CrWN system) and CrN/MoN (i.e., the CrMoN system) have been investigated via XRD in standard Bragg-Brentano configuration, using an Advanced X-ray diffractometer SmartLab machine (Rigaku Corporation, Akishima-shi, Tokyo, Japan), mounting a monochromatized 2.2 KW Cu anode source (Cu Kα = 1.5406 Å) and a 1D semiconductor detector D/teX Ultra 250. Monolayer coatings of CrN, MoN and WN were deposited for comparison and to provide reference position of diffraction peaks. The substrate were D2 tool steel samples with one-side mirror finish, a diameter of 1.5±0.2 cm and thickness of 4±1 mm. Prior to each measurement, the sample surface was cleaned with acetone and isopropanol and air dried. The sample height was adjusted each time to make the samples surface coincide with the focusing circle defined by the Source-Sample-Detector system. In all cases the angular range was 30-90 degrees, the angular 2Θ step resolution was 0.03 degrees and a scan time of 0.5 s/point was used. For pole figure measurements, the SmartLab Studio II Texture Plugin was used. An angular step of 5 degrees were adopted for both α (tilt) and β (in-plane sample rotation) angles. Residual stress measurements were performed using the $\sin^2\psi$ method permitted by the SmartLab Studio II Stress Plugin. The analysis was performed on the most intense peaks observed, corresponding to the <200> planes for each single-layer coating. Despite for the $\sin^2\psi$ the analysis of high-angle peak is recommended, the textured growth of the coatings did not allow it. Hence, the most intense medium angle <200> peak was chosen. In each case, seven ψ angle values were probed, corresponding to 0°, 17°, 25°, 30°, 35°, 40° and 45°. For each ψ angle, the sample was in-plane rotated with an angular resolution

of 5°C and an acquisition time of 30 seconds per angle. All measurements were performed two duplicates per sample type.

5.2.4 AFM IMAGING

AFM measurements were performed in semi-contact mode on an Asylum Research MFP3D AFM probe (Oxford Instruments, Abingdon, England) using diamond-like carbon (DLC) non-contact NSG01 tips with a nominal tip radius of 2-4 nm (NT-MDT®, NT-MDT LLC, Moscow - Zelenograd, Russia). For each sample, three 5-μm-square surface areas were imaged, from which average and standard deviation surface roughness R_{sq} data were calculated through Gwydion™ software.

5.2.5 INDENTATION TESTS

Indentation tests were performed using a Fischerscope H100C Nanoindenter (Helmut Fischer, Sindelfingen-Maichingen, Germany), with an effective loading range of 0.4 mN–1 N (40 mg–100 g). The instrument s property of the Thin Film and Surfaces department at the Jozef Stefan Institute, Ljubljana (Slovenia). A Vickers diamond tip (4-sided pyramid) which was approached to the sample by an electromagnetically driven coil. Upon contact, a steel cylinder was pressed around the indentation area to keep the sample still on the supporting stage during the measurement. All specimens were loaded with a peak force of 10 mN linearly ramped for a total loading time of 20 s, followed by 5 seconds of peak-load retention before unloading.

5.2.6 CORROSION TESTS

Potentiodynamic polarization (PP) and Electrochemical Impedance Spectroscopy (EIS) tests were performed in a NaCl aqueous solution at a salt concentration of 3.5%wt. No thermostat was used, but ambient temperature was monitored and only varied between 24 and 27 °C. The measurements were run using a PalmSens4 potentiostat equipped with an impedance analyzer (PalmSens BV Randhoeve 221, 3995 GA Houten, The Netherlands). A custom-made three-electrodes cell was used, employing a Pt counter electrode and a Ag/AgCl reference electrode (the latter filled with a 3M KCl solution, the same used for

storing). For corrosion tests, specimens consist in single and multilayer coatings deposited onto stainless steel of type AISI 304 using the same protocol described in section 5.2.1. Samples for corrosion tests required a further preparation, which is herewith described in detail. First, samples were sputter coated on the backside with a first, 100-nm-thick Cr coating and a top 200 nm Ag. The Cr coating serves as an adhesion layer between Ag and the Steel substrate. The role of Ag layer is to provide a compatible material for the following brazing of a copper lamina using an indium alloy paste. The lamina serves to provide electrical contact with the potentiostat during the measurements. After the Cu lamina was attached, an insulating sheath was spray-coated to cover all the specimens' surface but a front-area of 1.0 ±0.1 cm^2, which served as active site for the corrosion tests. The insulating polymeric sheath was left air-dry for 8 hours, then the spray-coating was repeated and left drying overnight. This way, all the specimen surface but the active region is shielded from the electrolytic solution. The specimens were dipped inside the electrolytic solution until all the active site was immersed, while keeping the electrical contact well above the water surface. PP and EIS tests were run after the system was left equilibrate for 1 hour, or until the Open Circuit Potential (OCP) was stabilized within 0.01 mV. Then, for PP tests, a DC potential was linearly ramped in the range between -0.7 and 0.4 V against the Ag/AgCl reference electrode potential, at steps of 10 mV with a scan rate of 5 mV/s. For EIS measurements, an AC potential with 20 mV peak-to-peak amplitude was superimposed to the OCP. EIS tests were run in the spectral range 100 kHz to 10 milli-Hz, but irregularities below 50 milli-Hz made this low-frequency regime unreliable and were therefore discarded. With these settings, PP and EIS tests lasted for about 35 and 45 minutes per sample, respectively.

5.3 RESULTS

5.3.1 FIB-SEM IMAGING OF MULTILAYER SYSTEMS

FIB cross-sectioning was carried out by milling an 8µm*4µm rectangular shape using a Ga beam accelerated at 30keV with a milling current of 100 pA for 10 minutes, with samples tilted at 45°C to place the surface perpendicular to the FIB beam direction. Imaging was performed using a low voltage SEM imaging (2-3 keV) minimizing the

electron-specimen interaction volume for improved spatial resolution. Tilt correction was applied to compensate for the 45°C inclination of the specimen holder.

Examples of cross-sections of a set of multilayer coatings with individual layer thickness ranging from 100 to 10 nm per layer are shown in **Figure 84** and **Figure 85** for CrN/WN and CrN/MoN, respectively. In all cases, the coatings are conformal with only localized defects occurring across the sample. Examples of typical defects encountered in the coatings are reported in **Figure 87**. SEM cross-section images of multilayer coatings with 5 nm-per-layer architectures are not shown because the multilayer stack is not visible due to resolution limits.

In the multilayer system, the alternated structure is visible thanks to the high Z-contrast between Chromium nitride (Z_{Cr} = 24), Molybdenum nitride (Z_{Mo} = 42) and Tungsten Nitride (Z_W= 74). Successive layers are uniformly deposited following the surface profile of the underlying material, with only minor asperities building up across the coating thickness (see inserts in **Figure 84** and **Figure 85**).

From the FIB-cut cross-sections, it is possible to notice that all multilayer coatings are finely structured. On the contrary, monolithic coatings grown at low temperature PVD processes tend to a fine columnar growth [465]–[467]. To visually compare the microstructure of monolithic and multilayer coatings, a FIB-cut cross-section of a single layer WN coating is shown in in **Figure 86-A**, while a cross-section of a CrN/WN multilayer coatings with a 10-nm-per-layer architecture is reported in **Figure 86-B**. The different microstructure is probably due to the periodic interruption of the deposition process of the multilayer system, which prevents coherent crystal growth. This also results in a finer surface granularity. As will be discussed in later sections of this chapter, the different microstructure can play a fundamental role in determining many important coatings properties.

Finally, despite the generally good coatings morphology and conformity, some localized defects were also encountered, and their presence needs to be addressed.

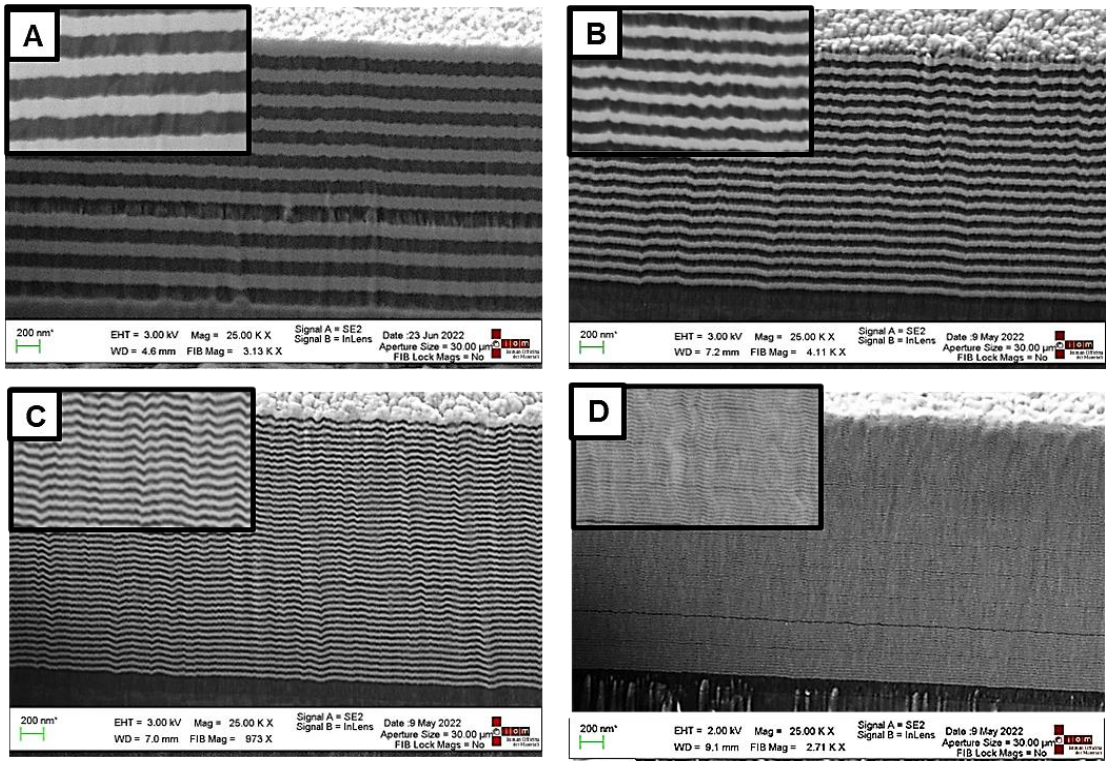

***Figure 84**: SEM micrographs of FIB-cut cross-sections in multilayer CrN/WN coatings with (A) 100 (B) 50, (C) 25 and (D) 10 nm-per-layer architectures. Insert show a 4x magnification the same section's detail.*

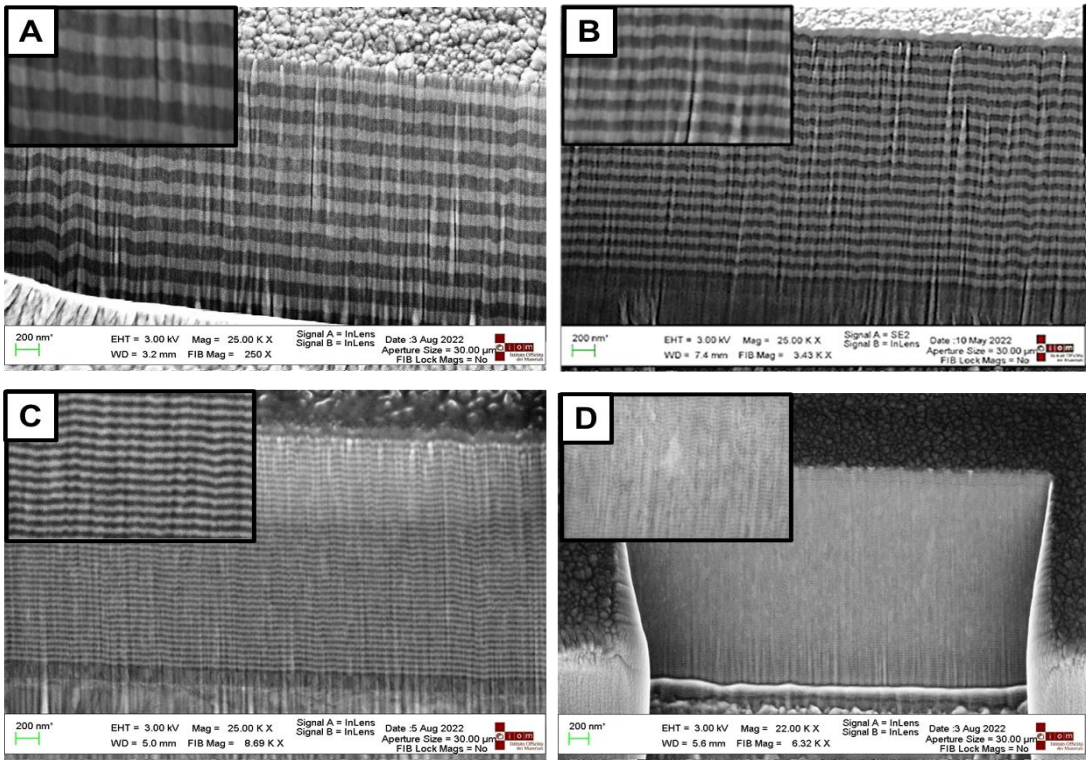

***Figure 85**: SEM micrographs of FIB-cut cross-sections in multilayer CrN/MoN coatings with (A) 100 (B) 50, (C) 25 and (D) 10 nm-per-layer architectures. Insert show a 4x magnification the same section's detail.*

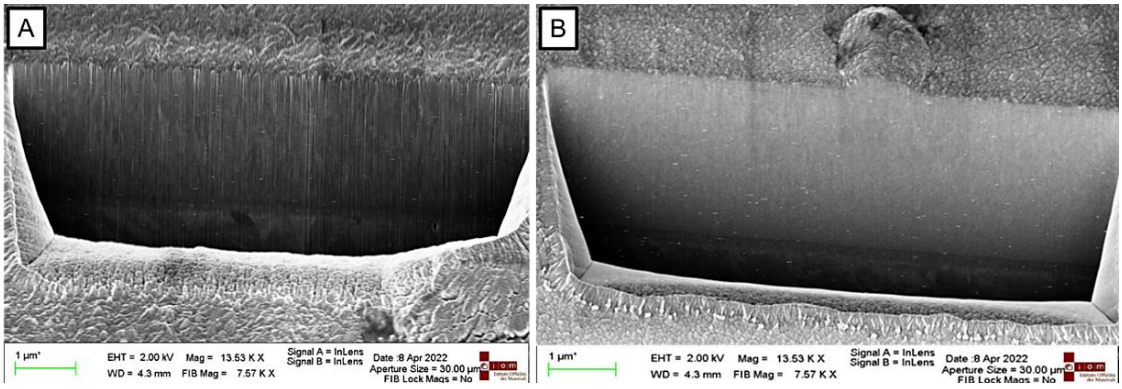

Figure 86: Comparison of the microstructure of (A) a monolithic Single layer coating of WN and (B) a multilayer CrN/WN coating with 10 nm-per-layer architecture.

5.3.1.1 STRUCTURAL DEFECTS

The most frequently encountered defects are due to foreign particles deposited during the sputtering process or left on the substrate even after the wet and plasma etching cleaning steps. The presence of these particles can severely compromise the conformal deposition of the coatings and generate cracks and porosities within the coating. Cracks extending from the surface towards the substrate and hence exposing the substrate to the external environment are particularly troublesome with respect to the penetration of oxidant or corrosive species and their interaction with the substrate itself [112], [360]–[362]. Galvanic corrosion can occur in the electrochemical cell constituted by the coating material, the electrolyte and the steel [398], [468]. This accelerates the dissolution rate, promotes the detachment of the coating, and ultimately ruin the structural integrity of the piece. The presence of closed porosities is usually not relevant with respect to corrosive wear, as the substrate does not get in contact with the corrosive species, Nonetheless, porosities reduce the mechanical sustain of the coating, facilitating its failure under external mechanical loads. On the contrary, the multilayer architecture show the capability of confining the cracks propagation (see for example **Figure 87-A** and **Figure 87-C**), unless very severe defects are introduced by, for instance, disproportionally large foreign particles, as in **Figure 87-B**. Notably, the occurrence of longitudinal cracks, i.e., cracks extending from the coating's surface towards the substrate, was mostly limited to monolithic coatings, while in nanolaminates it resulted in the formation of nodular defects emerging from the coating's surface, as shown in **Figure 87-B-C-F**. This can be understood by considering the different microstructure of monolithic and multilayer

coatings. Columnar microstructure favors the propagation of cracks through the low-density grain boundary regions which extend orthogonally to the sample surface, in the direction of film growth. It must be highlighted that despite the density of defects can be reduced by optimizing the substrate cleaning procedures and the operative conditions of the deposition process, it is practically impossible to completely remove them [459]. The mechanical and even more the electrochemical characterization of PVD coatings are therefore inevitably affected by a certain degree of variability, which must be considered in the evaluation of coatings properties.

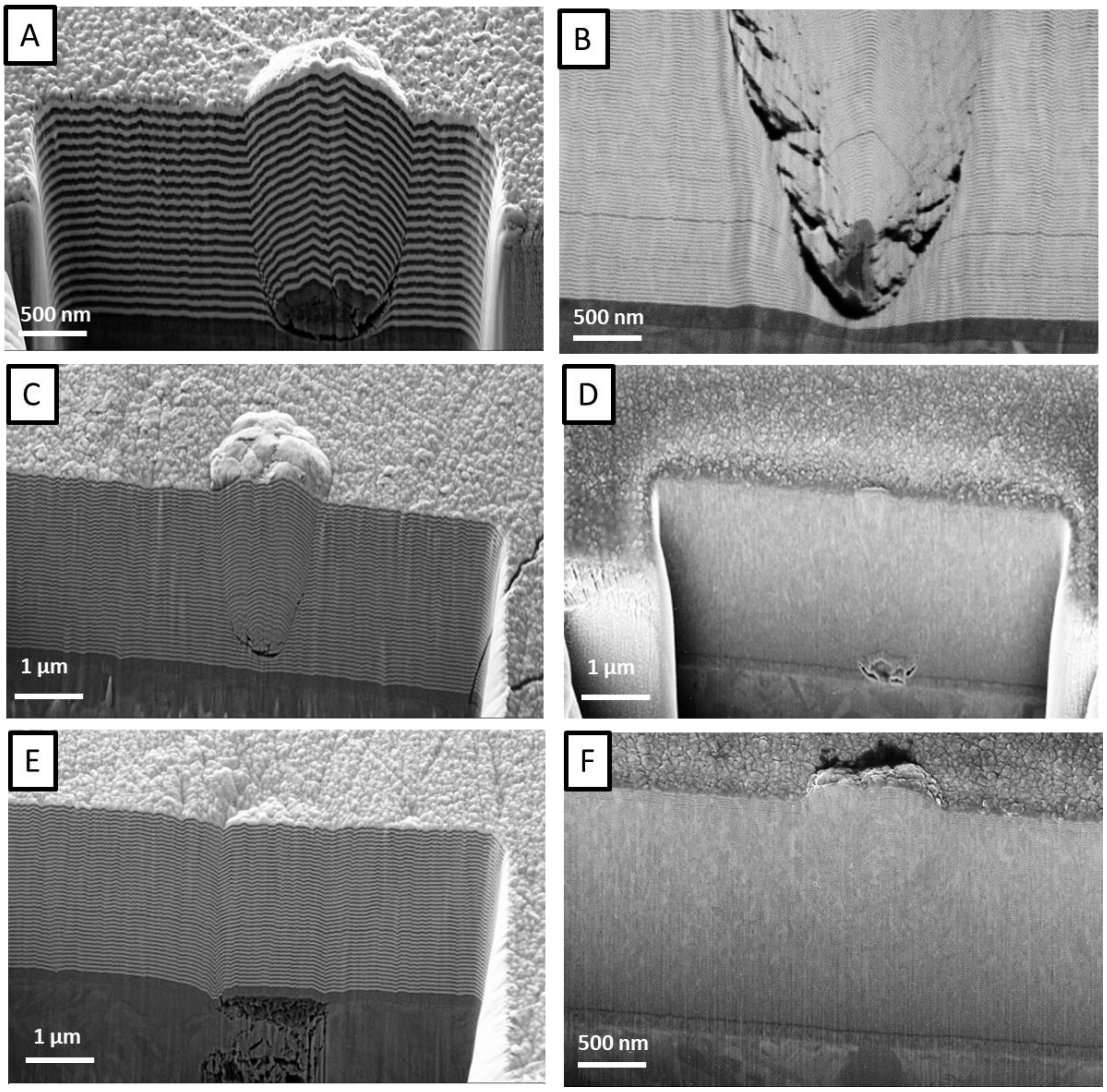

Figure 87: FIB-cut cross sections exposing structural defects within the coatings. Severe vertical cracks like the one shown in panel A extending from the surface towards the substrate were mainly visible in monolithic coatings, due to the columnar microstructure. Nodular defects and collateral structural defects are shown in panels B-F, demonstrating variable severity depending on the seeding defect, such as foreign deposited particles (B, C), residual particles on the coating (D), surface depressions on the substrate surface (E) and slightly protruding carbide grains from the steel substrate (F).

5.3.2 STRUCTURAL INVESTIGATION

Normalized XRD data for the CrWN and CrMoN system are reported in **Figure 88** and **Figure 89**, respectively, along with the miller indexes of the of the signals originated from the coating. Peak indexing was performed by comparing the experimental peak positions of constituent monolayer coatings with reference data in the PDF database. Although the unique possible identification of the crystallographic phase of CrN coating, CrN Peak positions of CrN differ substantially from the reference values. For instance, the <200> peak lies at 43,02 °, against the predicted 43.64 degrees (PDF# 11-65) corresponding to interplanar distances of the <200> planes of 0,210 nm against the predicted 0,207, an increment of just 1.5%. A similar variation is also observed for the <111> peak, lying at 37,11 ° instead of the predicted 37.56 ° corresponding to a variation for the <111> interplanar distance of 1.2%. This slight lattice enlargement can be due to an increase concentration of interstitial N_2 or to lattice adjustments on the steel substrate. Notably, this effect was not observed in the CrN coatings deposited onto Si substrate. Hence, a substrate-mediated effect seems to be responsible for such enlargement. Interestingly, such significant variation in XRD peak position was not observed for WN and MoN coatings, for which a better correspondence with reference peaks positions was observed.

As mentioned, XRD data for the CrWN and CrMoN multilayers in **Figure 88** and **Figure 89** are normalized. This is because the intensities of the signals from MoN and WN were much higher than those of CrN. This can be attributed to two factors. First, texture analysis of the three nitride coatings revealed that CrN, MoN and WN grow in very dissimilar ways, as shown by the pole figures in **Figure 90**. In pole figures, the distance between the center and the edge represent defines the tilt angle α with respect to the normal direction of the sample surface, while the angular position on the circumference defines the rotation angle β around the specimen vertical axis [469], [470].

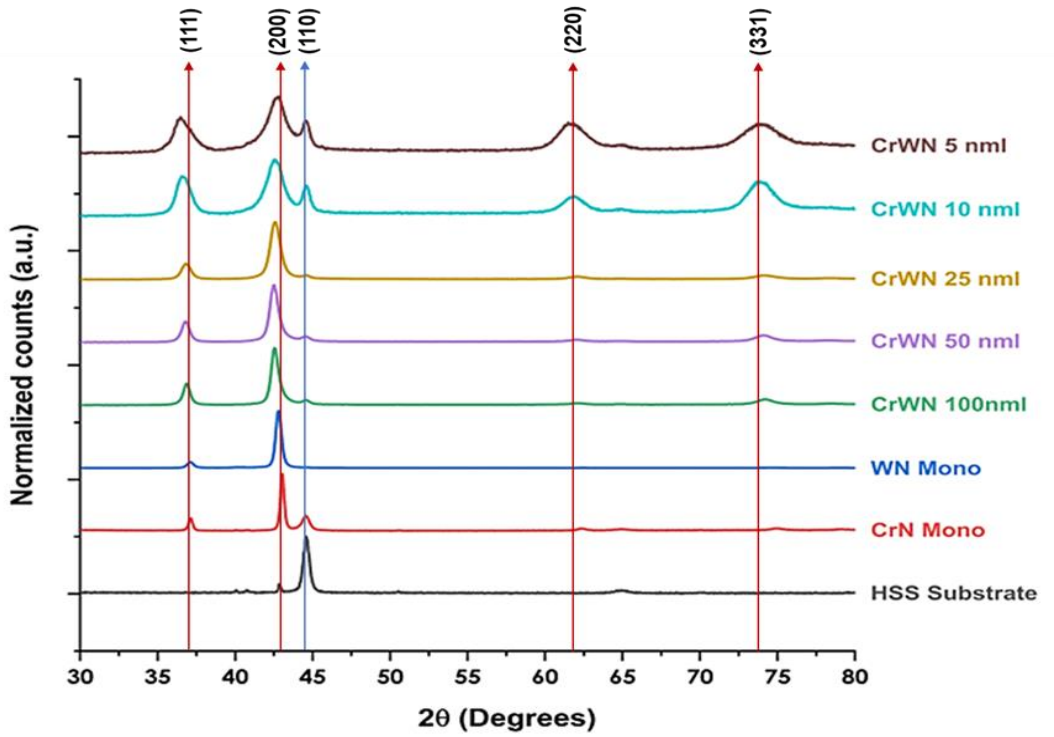

***Figure 88**: Normalized XRD profiles of the CrN/WN system for the monolithic and multilayer coatings.*

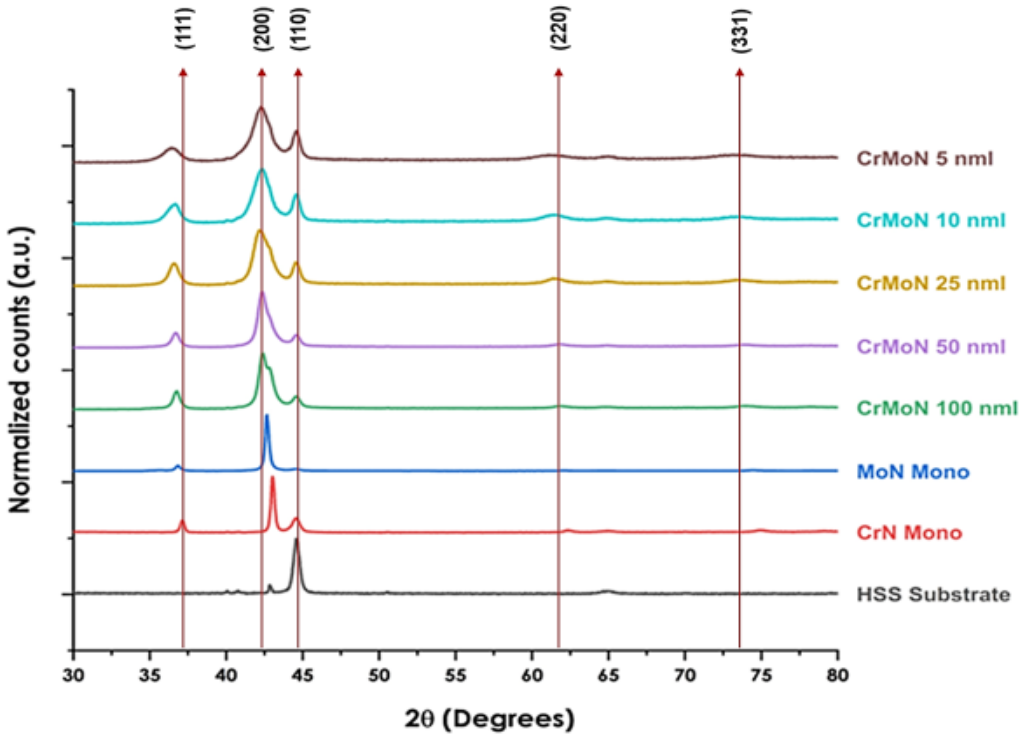

***Figure 89**: Normalized XRD profiles of the CrN/MoN system for the monolithic and multilayer coatings*

Comparing **Figure 90-B** for the CrN, **Figure 90-D** for MoN and **Figure 90-F** for WN coatings, it can be seen that CrN is poorly textured towards the surface normal, while it has a stronger <200> signal for a tilt angle of 90°C and with a preferential lateral orientation (the confined red area at the external edge in Figure 90-B. On the contrary, MoN and WN <200> planes are very textured towards tilt angle α=0, i.e., the direction parallel to the specimen surface normal. In Bragg Brentano measurements, only the crystallographic planes parallel to the specimen surface contribute to the diffraction pattern. Hence, in the case of strongly textured MoN and WN coatings, the <200> contribution overwhelms the <200> peak of the poorly textured CrN, for which only a reduced fraction of the <200> planes effectively contribute to the diffraction pattern.

A second reason could be linked to X-Ray diffraction being a coherent scattering process involving an ordered array of scattering centers via constructive interference processes [471]. The intensity of X-Ray scattering from a crystal depends on its structure factor, which is a function of the electron density, through the atomic form factor, and the crystal cell structure [472].

Physically, X-Ray scattering occurs through the interaction of the radiation with the electrons of the interacting atom. In cubic CrN, MoN and WN, the crystallographic cells are all the same NaCl type, with 4 metallic cations per cell. Hence, the structure-contribution to the x-ray scattering is expected to be invariant in the three cases of interest. From the interplanar distance of the <200> planes, the lattice parameters of the three materials can be calculated by multiplying the <200> interplanar distance by a factor 2, giving values of about 0.414, 0.418 and 0.422 nm for CrN, MoN and WN, respectively. Hence, the electronic density in each material can be approximated by the number of electrons within the cell, which is (neglecting Nitrogen contributions) 96, 168 and 296 respectively. Hence a larger diffraction intensity is expected for higher-Z elements.

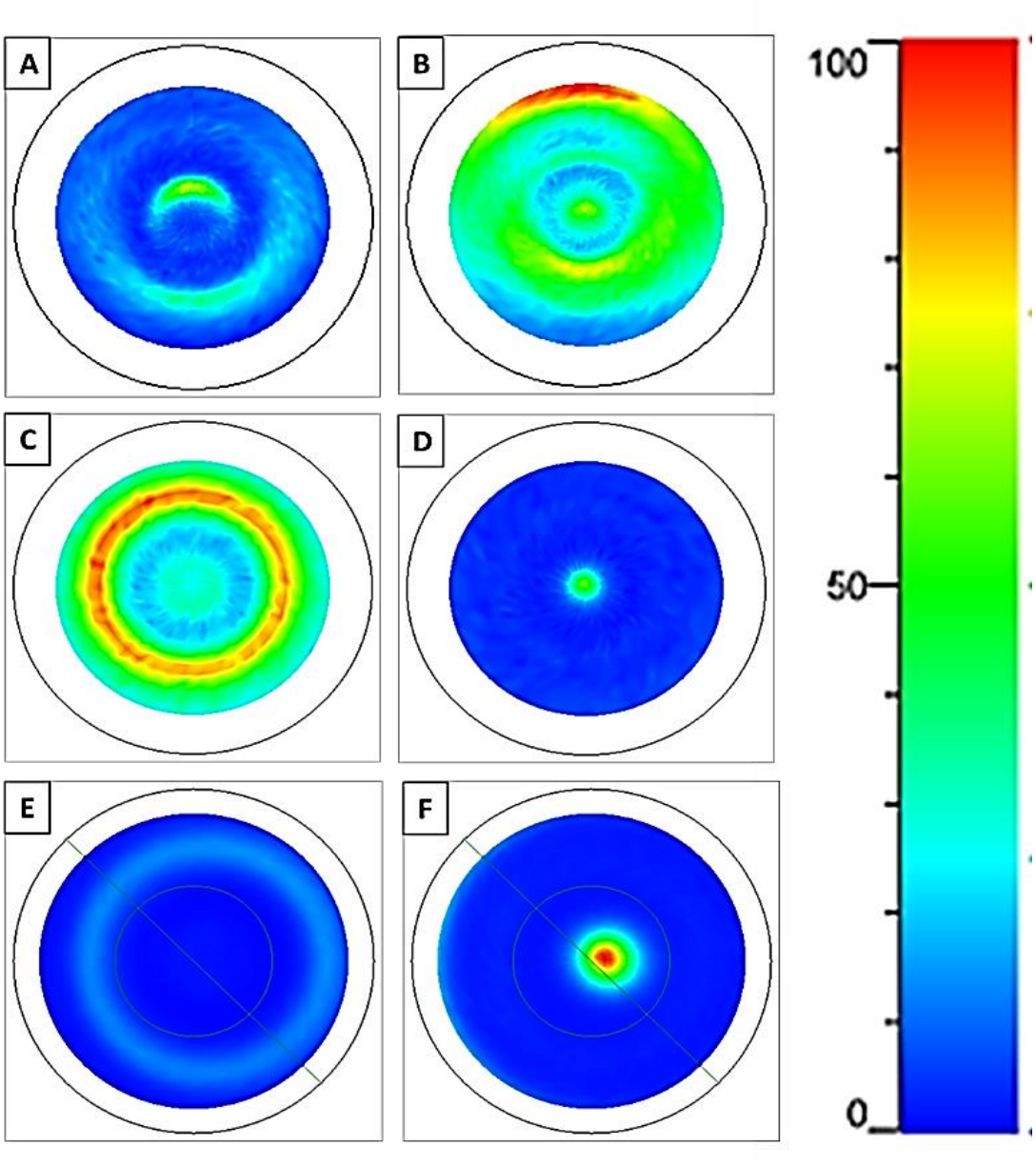

***Figure 90**: Pole figures for (A) WN <111>, (B) WN <200>, (C) CrN <111> and (D) CrN <200>. The normalized color scale goes from blue (low signal), to red (high signal, indicating the intensity distribution of the peak. The surface coverage is indicative of the 3D distribution of the corresponding crystallographic orientation in the specimen.*

5.3.2.1 CRYSTALLITE SIZE AND STRAIN RELAXATION

The calculation of crystallite size as a function of the individual layer thickness was accomplished by means of Scherrer analysis using **Equation (2-4),** with the purpose of identifying a relation between the individual-layer thickness and crystallite size. Despite all coatings showed a preferential orientation towards the <200> direction, the <200> peak features were difficult to determine in multilayer coatings, because of the overlap of

the <200> contributions from CrN with those, much more intense, generated from the coupling WN or MoN. Hence, in the case of CrN in the CrWN system the analysis is performed on the <220> peak at around 63°C. This has been attributed to CrN because in the single-layer coatings it was the only coating showing a peak at that angular position. Within the CrMoN system, instead, peak deconvolution was performed on the multilayer <200> peak positions. In the analysis, instrumental broadening was not subtracted, therefore the measured crystallite size provides a lower bound of the actual crystallite size in the sample. The results of Scherrer analysis are represented in **Figure 91** for the CrWN and the CrMoN systems. All coatings are nanocrystalline, with apparent crystallite size diminishing with thinner constituent layer thickness. This is predictable, as the alternated structure determines the upper bound for crystal growth.

Also, in **Figure 92-A** it is shown that by progressively reducing the thickness of the constituent layers, a shift of the peak positions towards lower angles was observed for CrN and MoN. This might be due to a reduction of the compressive stress imposed by the periodically interrupted ion flux and to the larger fraction of low-density grain boundaries determined by the finer grains size noticed from the Scherrer analysis.

On the contrary, the slightly opposite trend for WN visible in **Figure 92-B** suggests a higher compression. The reason for this trend is somewhat uncertain. It is possible that given the tendency of WN to grow in a textured manner, the expansion of the adjacent CrN layers imposes a compression on the WN grains. In the case of MoN, the texturing was less pronounced, as suggested by the different intensity of the pole figure. It is then possible that in this case, a larger compliance of MoN grains compensates for the expansion of adjacent CrN crystallites.

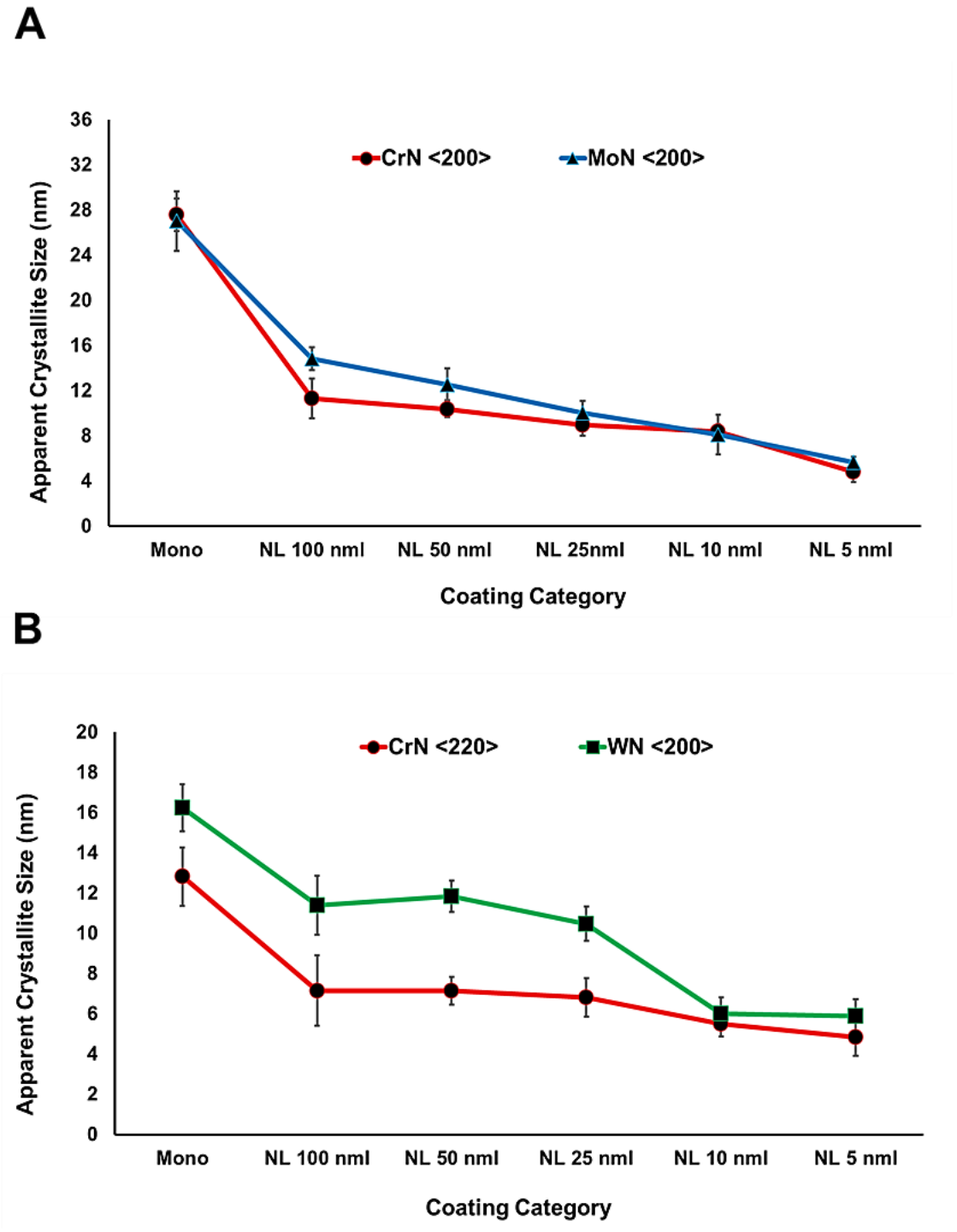

***Figure 91**: Calculated apparent grain size from (A) the MoN (200) and the CrN (220) peak contributions in the CrMoN system and (B) the WN <200> CrN <220> peaks contributions in the CrWN system*

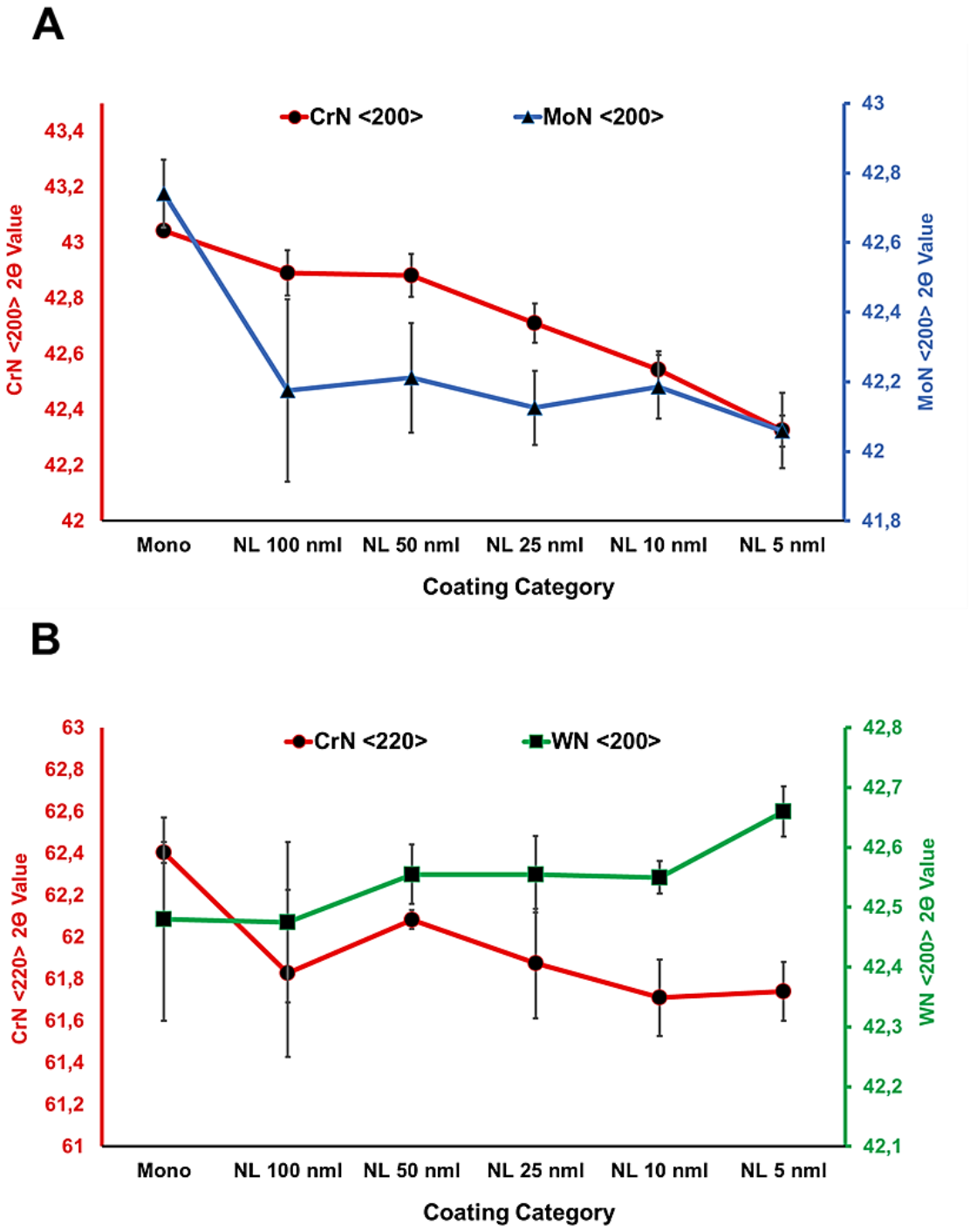

***Figure 92**: 2Θ values corresponding to the peak-maximum positions in (A) the CrMoN and (B) the CrWN system for the diffraction peaks indicated in the legend.*

5.3.2.2 RESIDUAL STRESS MEASUREMENTS

Residual stress measurements were performed on single layer coatings deposited on D2 steel. As mentioned in **Section 5.2.3**, stress analysis execution on multilayer coatings was not possible due to the relatively strong texturing of the coatings, to the rapid drop in peak intensity for multilayer systems with thinner individual layers, and to the strong overlap of the most prominent peaks of constituent materials. Nonetheless, stress analysis on single-layer coatings can provide valuable indications on the relative stress contribution apported by each material to the multilayer coating systems.

The 2Θ position of the <200> peak used for the analysis was found to decrease by increasing the tilt angle ψ. More importantly, the relation between the d-spacing, and hence the 2Θ values according to the Bragg law (see **Equation (2-3)**), and the $\sin^2\psi$ was found to be approximately linear (**Figure 93**), which confirms the assumptions of biaxial residual stress values, and the applicability of the method for stress evaluation.

The residual stress can be calculated from the slope of the linear curve used to fit the data, once the elastic modulus, and the Poisson coefficient of each material are known. The Poisson coefficients for the three materials were set to 0.3, based on literature common values [147], [473]. As for the elastic modulus was calculated by its definition using the reduced young modulus calculated by the nanoindentation tests shown later in this chapter and using tabulated values for the stiffness and Poisson coefficient of the diamond tip used for the indentations. Results of the calculation are shown in **Figure 94**.

All three materials have negative residual stresses, which means they are in a compressive state. Besides residual stress absolute value increases with heavier atoms. This suggests the strong influence of the particles impact energy delivered during the sputtering process to the growing film, which increases when sputtering heavier materials at lower TPD. Such considerations permit to explain in a reasonable manner both larger stresses of MoN and WN with respect to CrN and the larger stress of WN with respect to MoN.

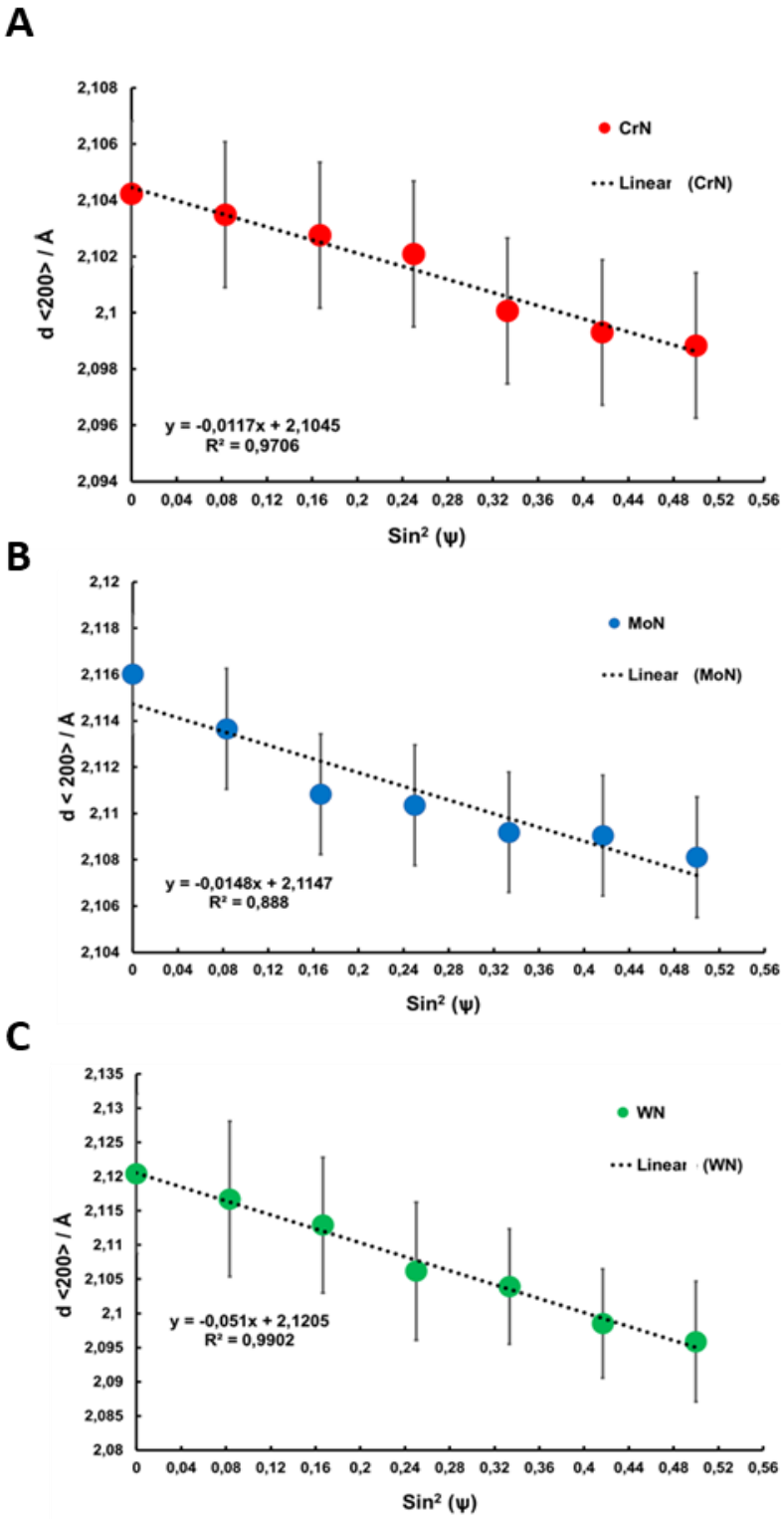

Figure 93: Dependance of the d-spacing of <200> planes with the tilt angle ψ for A) CrN, B) MoN and C) WN single layer coatings deposited on D2 steel substrates by DC magnetron sputtering. All samples are 2.2 microns-thick

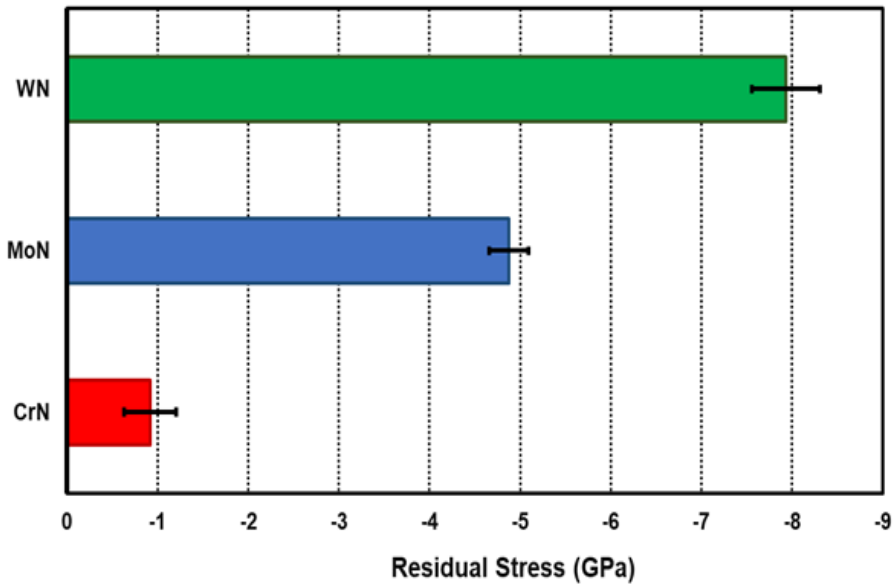

***Figure 94**: Residual stresses calculated for the three monolithic CrN, MoN and WN coatings. All coatings are in a compressive state (negative residual stress), with very large stresses found within the WN and MoN coatings*

5.3.3 MECHANICAL CHARACTERIZATION

5.3.3.1 VICKERS NANOINDENTATION

Nanoindentation tests were performed to measure the reduced young modulus and microhardness of test coatings. The purpose of this analysis was to correlate these mechanical properties to the design architecture of the coatings. As discussed in the Experimental Methods chapter, nanoindentation tests should respect a set of operative rules to yield reliable results. The 10% rule, also known as Bückel rule, states that the penetration depth at peak load should not exceed 10% of the coating, to be unaffected by the softer substrate. Then, the 5% rule states that the surface roughness of the sample should not exceed the 5% of the penetration depth at peak load, to minimize the scattering of experimental data. Therefore, a preliminary test was made to estimate the penetration depth as a function of the applied maximum load, to determine which peak load was suitable to respect both the operative rules. To this aim, a sacrificial CrN coating was tested by indenting with a series of increasing maximum loads ranging from 1 N down to 5 mN (**Figure 95**).

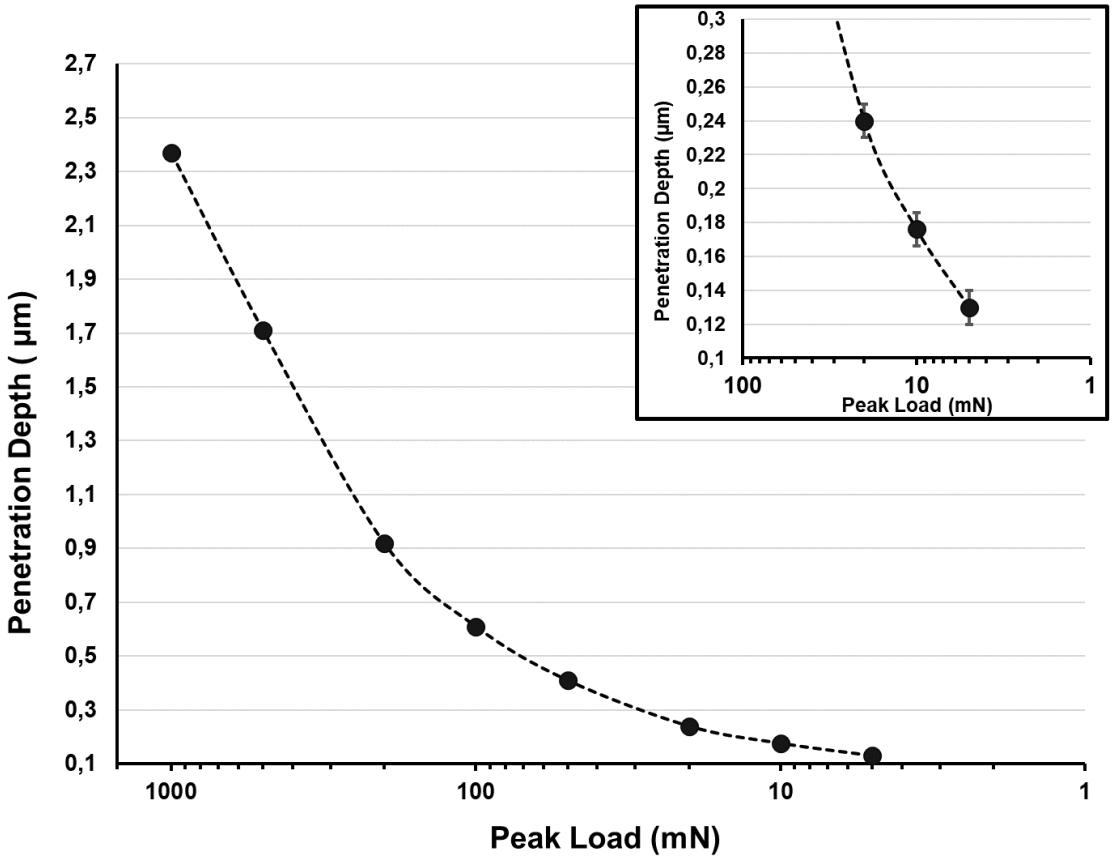

Figure 95*: Penetration depth as a function of peak normal load. Peak load scale is logarithmic. The insert shows a magnification in the low-load regime.*

It was found that the "10% rule" was respected only for peak loads lower than 10 mN. For 5 mN, the penetration was less than 100 nm and hence the 5% rule relating the penetration depth to the surface roughness was not respected. For this reason, it was decided to use a peak load of 10 mN to determine the microhardness of all the coatings. A summary of the coating's relevant properties and the compliance with the operative rule of indentation is reported in **Table 16**. Selected AFM topographies of single layer as well as multilayer coatings with 100 and 5 nm-per-layer architectures are also reported in **Figure 96**. As in the case of coatings deposited on Si substrates, the CrN monolithic coating shows the higher surface roughness with spiked asperities. All the coatings deposited onto the steel substrates have rougher surfaces than the equivalent coatings deposited on Si substrates. This is due to the higher surface roughness of the polished steel substrate (R_{sq} < 5 nm) compared to the finely polished single-crystal silicon wafer (R_{sq} < 0.9 nm).

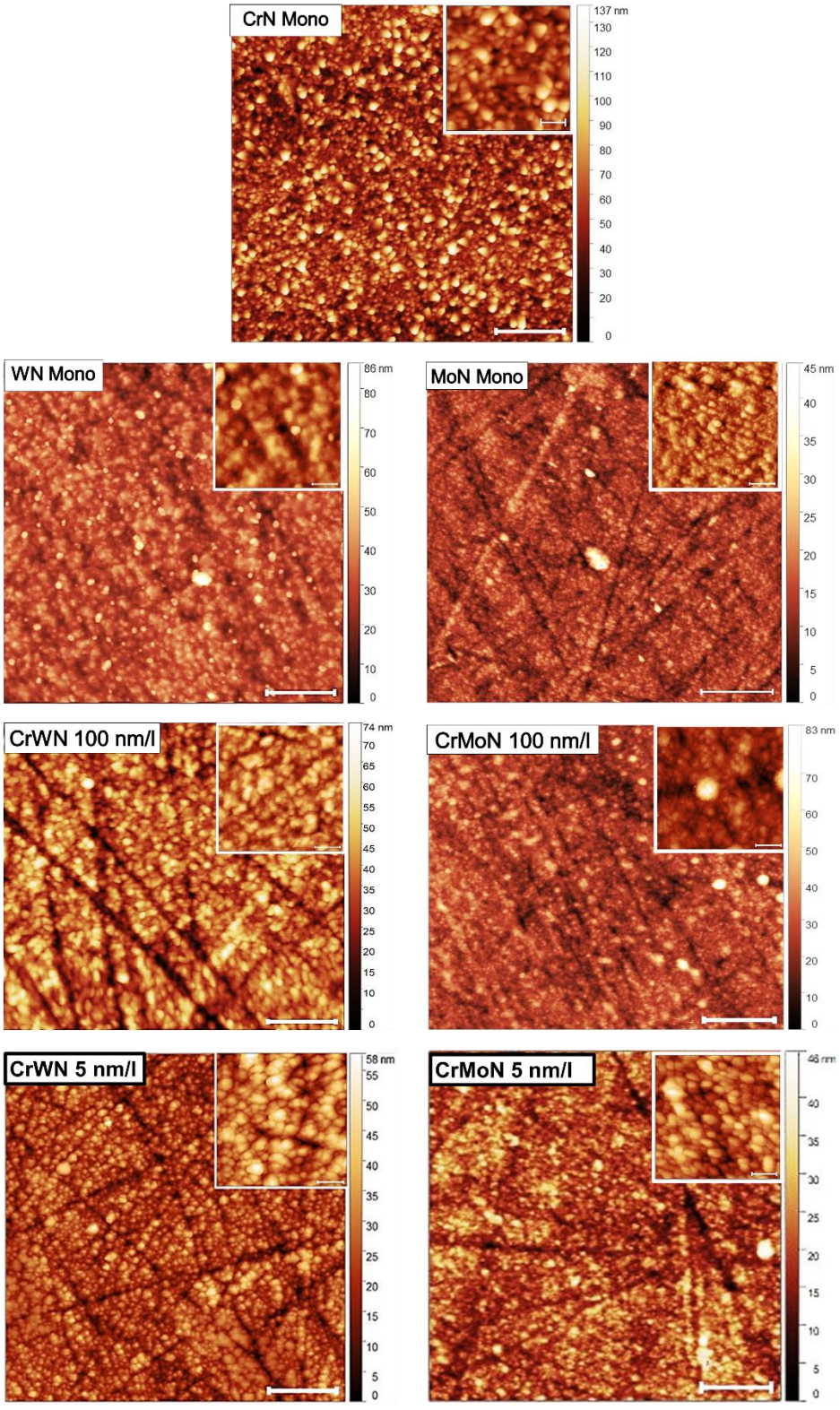

***Figure 96**: AFM topographies of single and multilayer coatings deposited onto mechanically polished D2 steel. Inserts show higher magnification images of 1µm square areas. The scratches deriving from the mechanical polishing of the substrate are clearly visible in nearly all samples. A slight decrease in roughness is observed with thinner constituent layers. Scale bars are 1 µm and 0.2 µm in large and insert images, respectively.*

***Table 16**: Samples parameters, indentation depth and the criteria for the 10% and 5% rules of indentation*

Sample	Thickness, T (nm), ± 50nm	Roughness R_q (nm), ± 0,2 nm	Max. Depth, D_{ind} (nm), ± 5 nm	D_{ind}/T (%)	R_q/D_{ind} (%)
CrN	2250	11,5	184	8	6
MoN	2300	4,3	179	8	2
WN	2270	9,2	160	7	6
CrWN 100 nm/l	2230	7,2	175	8	4
CrMoN 100 nm/l	2270	6,3	182	8	3
CrWN 50 nm/l	2290	5,8	181	8	3
CrMoN 50 nm/l	2320	6,1	179	8	3
CrWN 25 nm/l	2350	6,6	176	7	4
CrMoN 25 nm/l	2340	5,9	178	8	3
CrWN 10 nm/l	2320	6,3	171	7	4
CrMoN 10 nm/l	2280	6,9	176	8	4
CrWN 5 nm/l	2150	6,2	166	8	4
CrMoN 5 nm/l	2180	5,1	173	8	3

The measured values of microhardness *HV* and Reduced Young Modulus *E* from nanoindentation tests relative to the CrMoN and CrWN systems are reported in **Figure 97** and **Figure 98**, respectively. In both systems, the microhardness increases with a reduction of the individual layers thickness. The effect is more pronounced for multilayer coatings of the CrWN system than for those belonging to the CrMoN system. In CrWN coatings, an average microhardness of about 2200 HV (~22 GPa) is found for the multilayer systems with a 100 nm-per-layer architecture. Such values increase by approximately 50% with the 5 nm-per-layer architecture, reaching an average Vickers hardness exceeding 3100 HV (~31 GPa). Interestingly, this value is close to that of monolithic WN coatings, which is turn is in good agreement with typical values for this material, according to the literature.

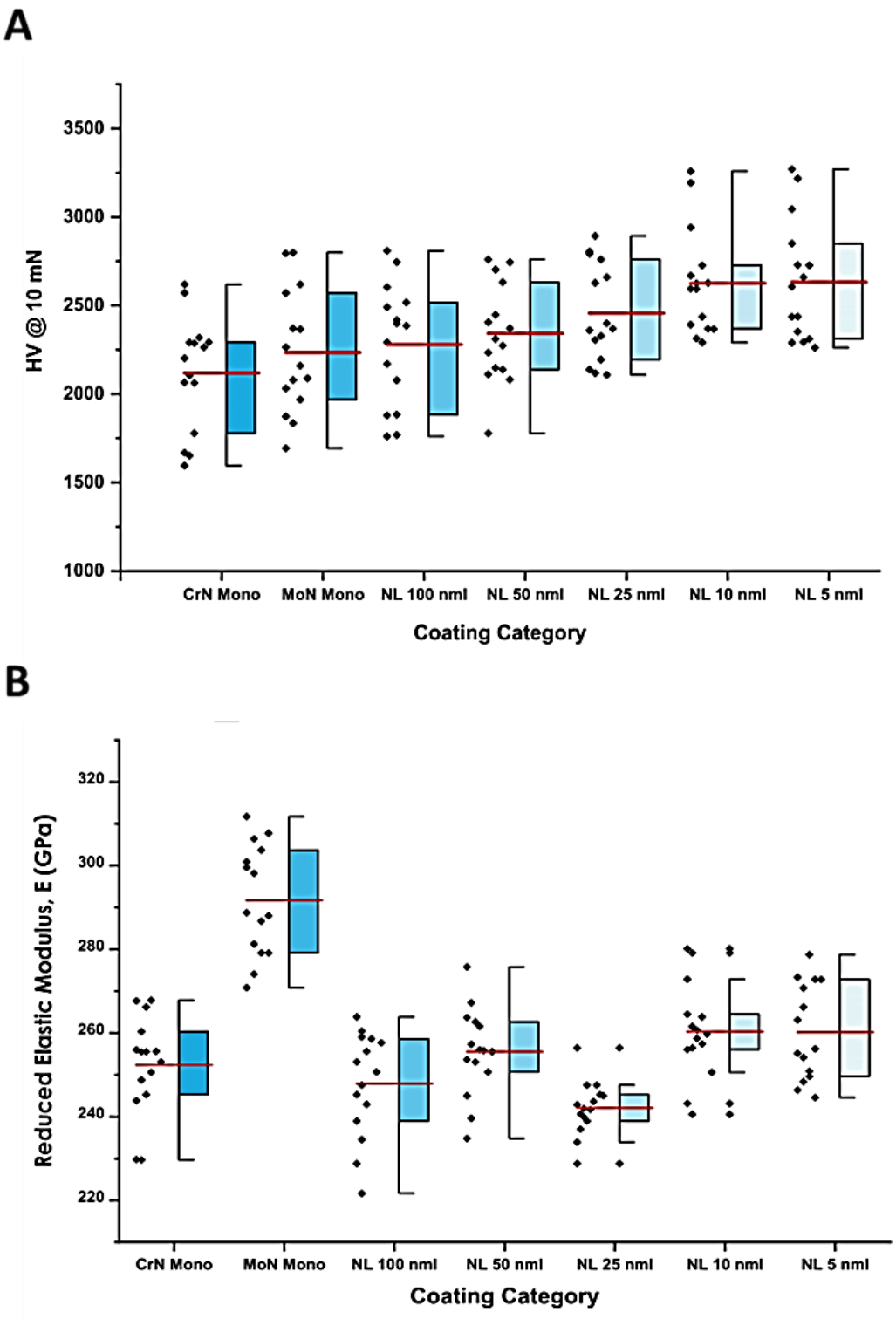

***Figure 97**: Boxplots showing the A) Vickers hardness and B) Reduced Elastic modulus values for nanolaminate coatings of the CrMoN system. For each sample, the data acquired from the whole dataset of 15 indentation are reported. Red horizontal lines correspond to mean values, while the whiskers length encloses all values within 1.5 times the interquartile range of the corresponding distribution, defined as the distance between the lower and upper limit of the specific boxplot.*

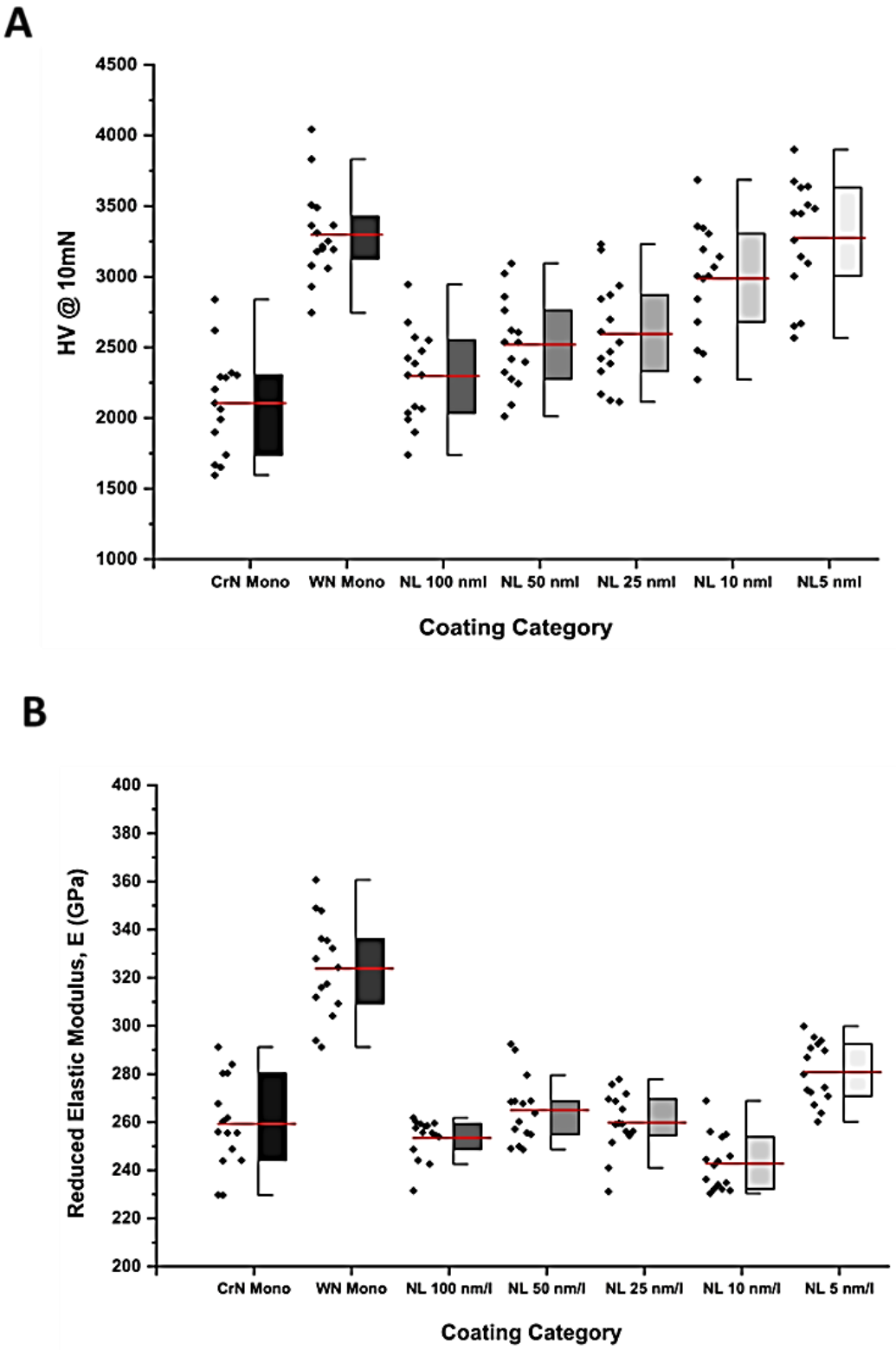

***Figure 98**: Boxplots showing the A) Vickers hardness and B) Reduced Elastic modulus values for nanolaminate coatings of the CrWN system. For each sample, the data acquired from the whole dataset of 15 indentation are reported. Red horizontal lines correspond to mean values, while the whiskers length encloses all values within 1.5 times the interquartile range of the corresponding distribution, defined as the distance between the lower and upper limit of the specific boxplot.*

The microhardness of the CrMoN coatings (**Figure 97-A**) reaches a maximum value of about 2700 HV (~27 GPa) for the 5-nm-per-layer architecture, approximately 10% less than for the equivalent coating in the CrWN system. The comparatively lower hardness of coatings the CrMoN system against the equivalent ones of the CrWN system is probably due to the lower hardness of the MoN constituent with respect to WN.

The reduced elastic modulus does not show a clear correlation with the coating's architecture. This is expected, as it mostly depends on the nature of the chemical bond among its constituent elements, which is not varying considerably among different coatings of the same system. Interestingly though, it seems that the elastic modulus of the coatings is considerably closer to the value of monolithic of CrN rather than being somewhere in between the value of CrN and the other constituent, be it MoN or WN. Hence, in both systems the coatings microhardness appears to be affected by both constituent materials contributions, while the stiffness is dominated by the softer constituent.

It must be highlighted that, despite both the 10% rule and the 5% rule were respected (**Table 16**), all measurements are affected by a large scattering of the experimental data. This is probably due to morphological inhomogeneities of the coatings on a large scale. Such inhomogeneity is not detected by AFM imaging as the scanned area was probably too narrow to be representative of the total surface topography of the coating. Another source of uncertainties could be environmental vibrations. The indentation tests were run in daytime with people occasionally passing-by the laboratory. Hence, it cannot be excluded that some apparently good acquisitions were affected by such disturbances. Another contribution may arise from slight surface tapering caused by a non-perfectly flattened substrate surfaces following the polishing procedure. This aspect was not directly investigated, and its contribution to the scattering of experimental data on low-scale indentations cannot be excluded with absolute certainty.

It is a well-established notion that hardness and stiffness alone do not constitute predictors of the wear behavior of coatings. Rather, composite quantities of Hardness (H) and Elasticity (E) offer a better proxy for the wear resistance of a coating [322]. This is particularly true for elastic materials which have low-to negligible plastic deformation mechanisms [474].

The quantity H/E and H^3/E^2 are often related to the fracture toughness resistance and plastic deformation resistance, respectively [322], [475]. The distribution of the H/E and H^3/E^2 values for the CrMoN and CrWN system is reported in **Figure 99** and **Figure 100,** respectively.

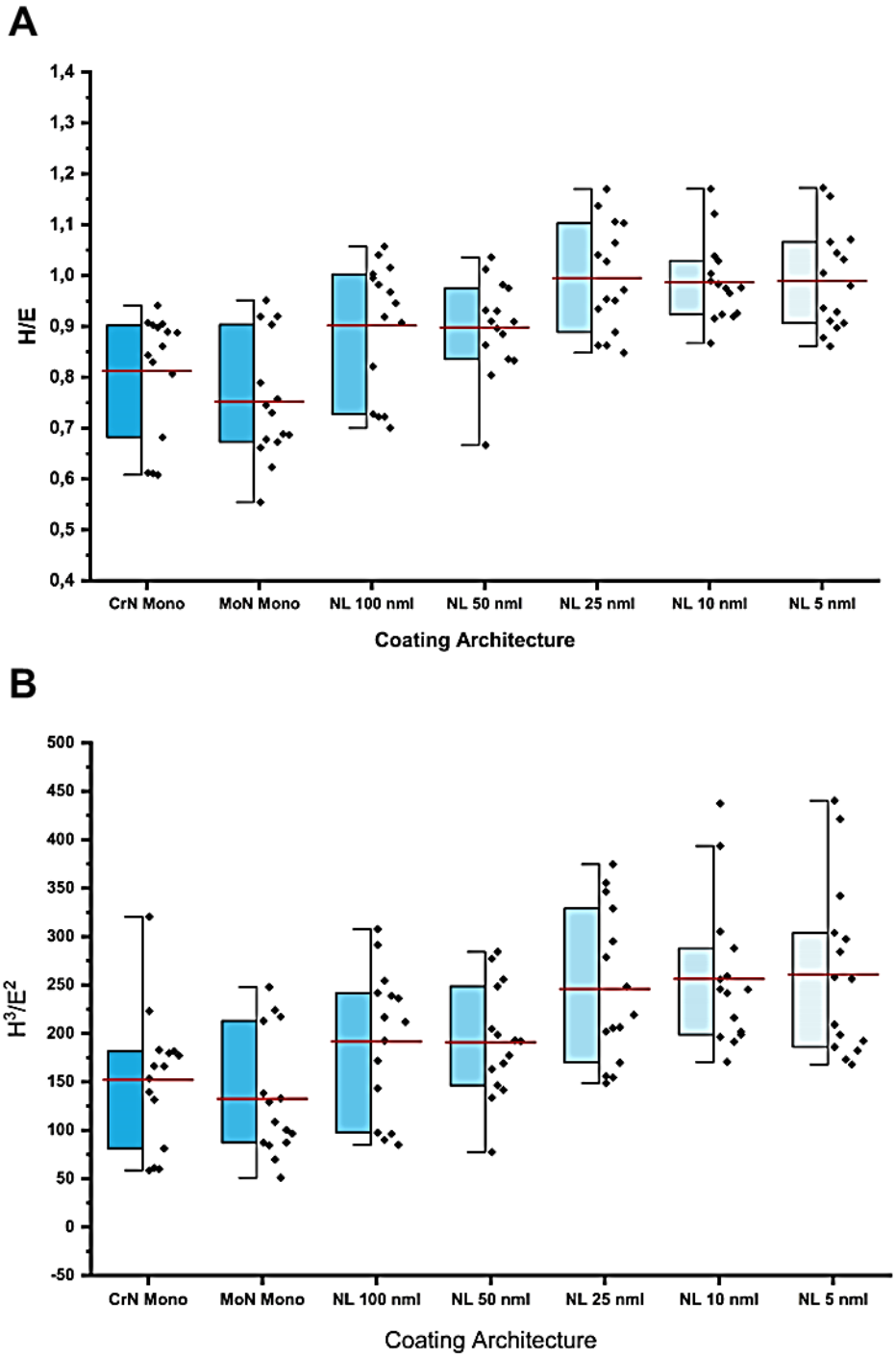

***Figure 99**: The (A) H/E and (B) H^3/E^2 ratios for the coatings in the CrMoN system. Both parameters increase for coatings with thinner layers. In the calculation, HV values have been converted to GPa.*

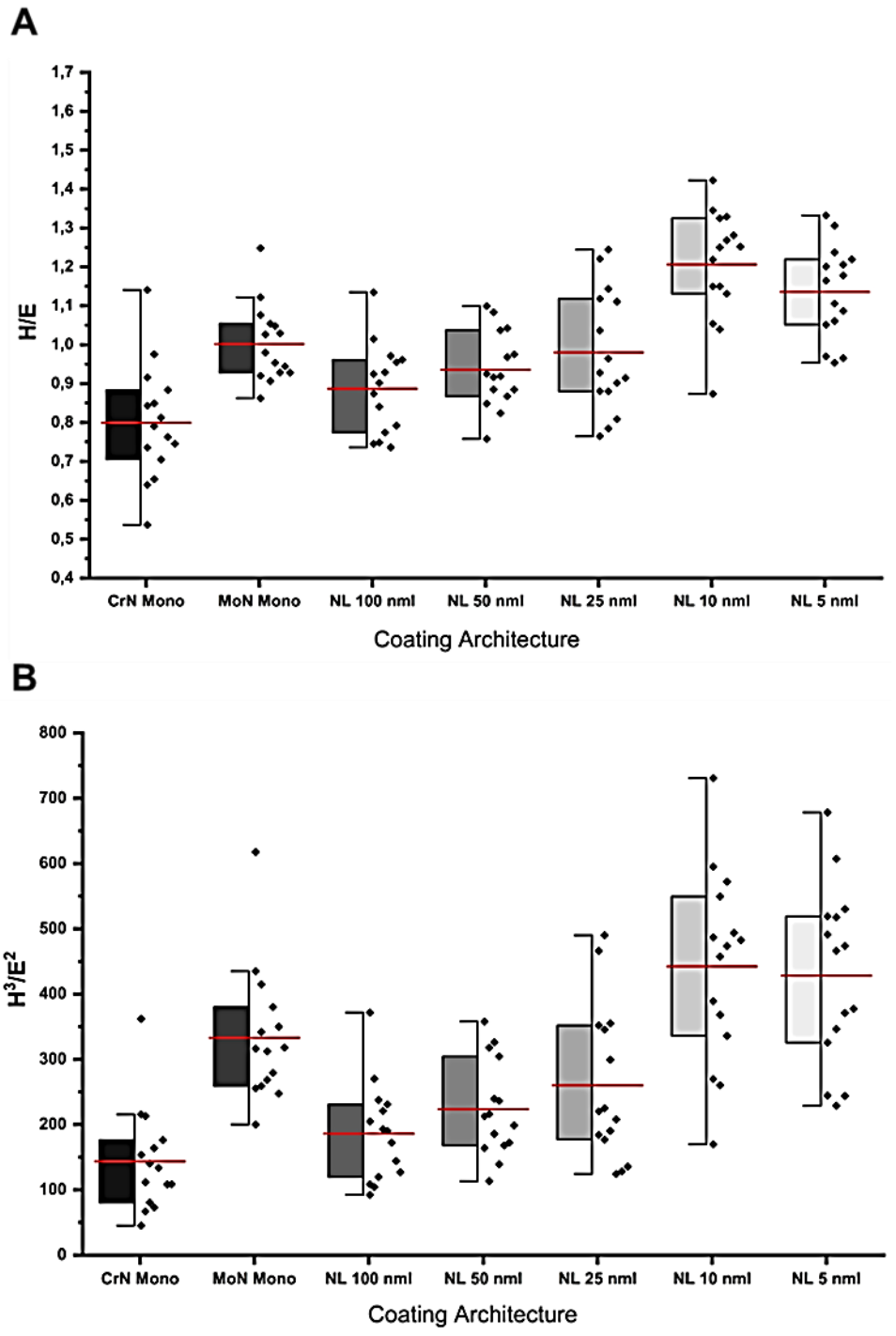

***Figure 100**: the (A) H/E and (H^3/E^2 ratios for the coatings in the CrWN system. Larger values are found for coatings with thinner constituent layers. In the calculation, HV values have been converted to GPa.*

The scattering of the H/E and H^3/E^2 values descends from the scattering of the HV and E values. In CrWN and CrMoN systems, both parameters increase for thinner constituent

layers. For the CrMoN system (**Figure 99**), the maximum average H/E and H^3/E^2 values of 0.99 and 261 GPa are found for the 5 nm-per-layer architecture. Instead, for the CrWN system (**Figure 100**) the maximum values are found for the 10 nm-per-layer architecture, giving average values of 1.2 and 442 GPa for the H/E and H^3/E^2 ratios, respectively. In the CrMoN system, both the H/E and H^3/E^2 ratios increase progressively whilst reducing the constituent layers thickness, while in the CrWN system an apparent abrupt change is found between the 25 and 10 nm-per-layer architecture. The abrupt increase for the 10 nm-per-layer architecture is mainly due to a simultaneous increase in the microhardness and a drop in elasticity as shown in **Figure 98 A-B**.

Comprehensively, these results suggest that with a reduction of the individual layer thickness, a larger resistance to wear could be expected thanks to both an increase in the fracture toughness resistance (H/E) and a resistance to plastic deformation (H^3/E^2).

5.3.3.2 ROCKWELL INDENTATION

Besides hardness and stiffness, adhesion is a paramount property of a coating system, which plays a strong impact on the wear resistance. Adhesive failure of a coating implies the detachment of the coated material from the substrate. This is usually mediated by shear stresses acting on the coating. For qualitative and comparative purposes, Rockwell-C indentation provides a useful means to evaluate the adhesive strength of coatings. Light-microscopy images of Rockwell C indentations are shown in **Figure 101** and **Figure 102** for the CrMoN and CrWN systems, respectively.

All the coatings were found to be affected by a poor adhesion to the substrate. A SEM investigation on the crack-borders evidenced that the delamination of the coating started right form the Cr adhesion layer (**Figure 103**). This was evident because the tool steel surface was clearly identifiable by the presence of darker and lighter pseudo-circular shapes which correspond to different forms of Tungsten carbides embedded in the steel matrix [476]–[478] .

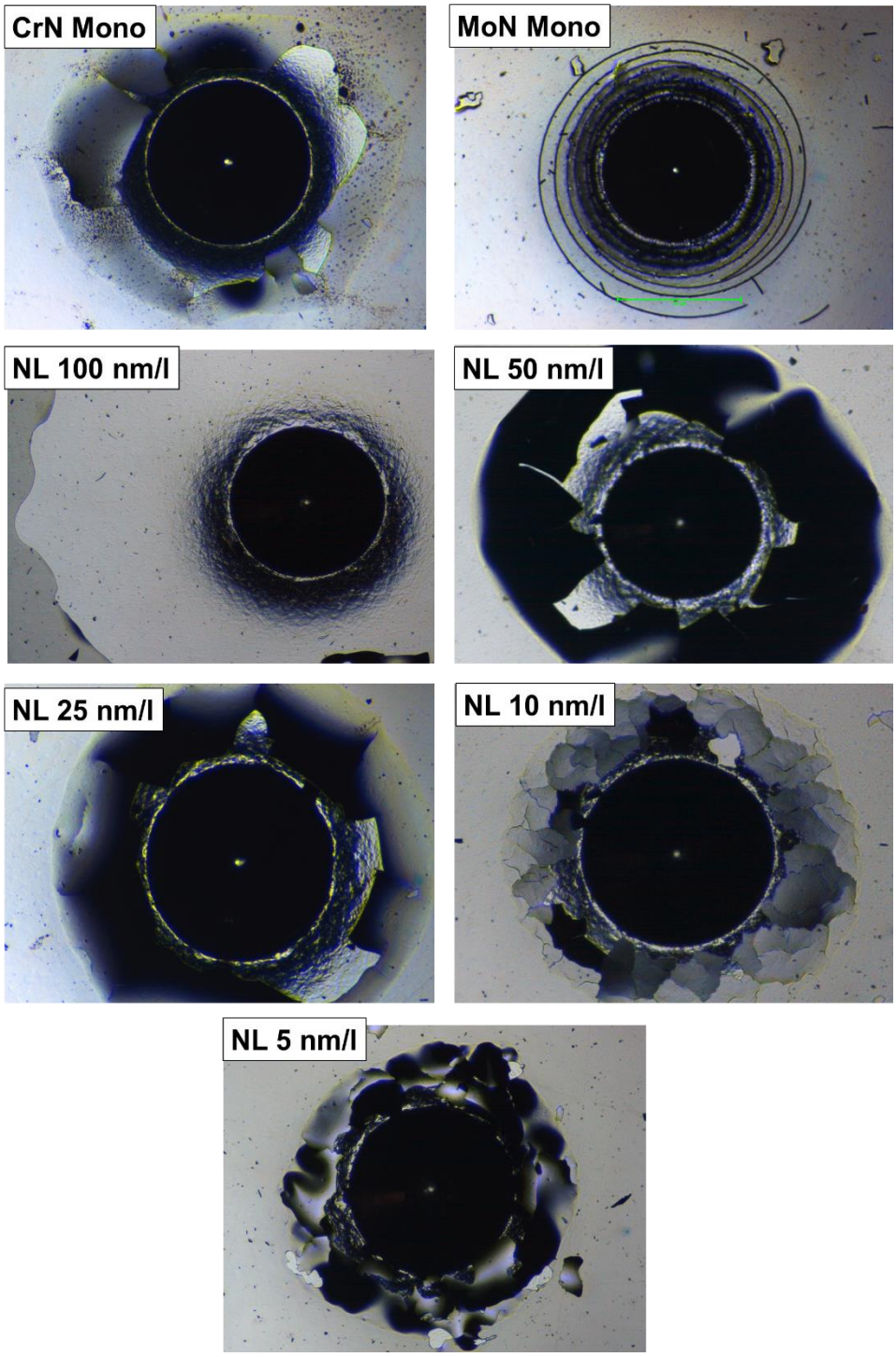

***Figure 101**: Rockwell-C indentation marks of coatings belonging to the CrMoN system. The diameter of the indentation mark is 1 mm in all the coatings*

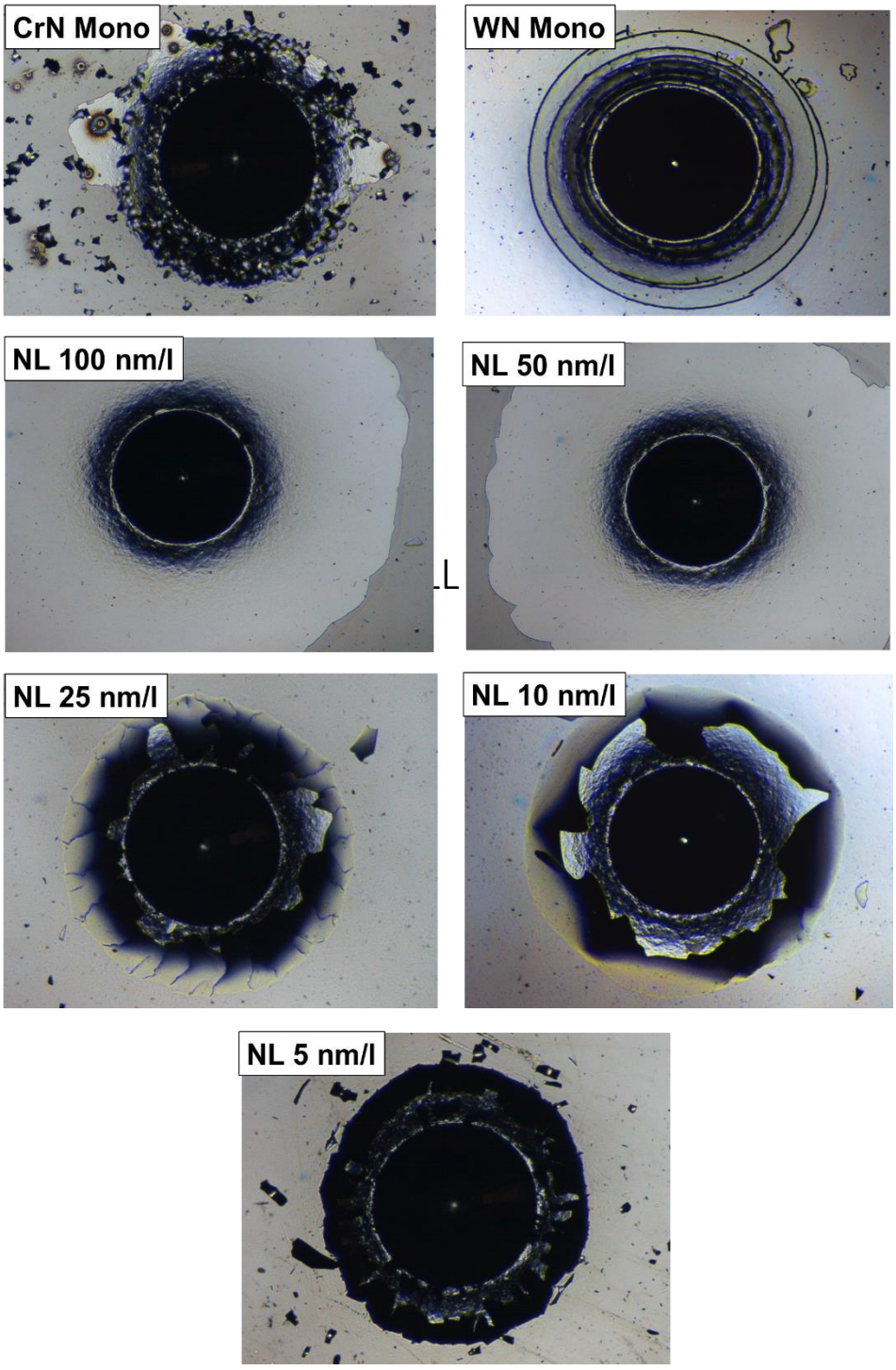

***Figure 102**: Rockwell-C indentation marks of coatings belonging to the CrWN system. The diameter of the indentation mark is 1 mm in all the coatings*

All coatings showed a relatively poor adhesion to the substrate, with the worst being the nanolaminate systems with a 100 and 50 nm-per-layer architectures. Starting from individual layer thickness of 25 nm, a better adhesion is evidenced. In fact, the

delamination in more nanostructured coatings is incomplete and involves a smaller area. The appearance of the indentation mark changes with a certain degree of continuity for coatings in the CrMoN system, as can be seen in **Figure 101**. This is in good agreement with the evolution of the H/E and H^3/E^2 values shown in **Figure 99**. On the contrary, the transition is more abrupt for the CrWN system between 50 and 25 -nm-per-layer coating samples. This too is in good accordance with the trend of the H/E and H^3/E^2 rations shown in **Figure 100**.

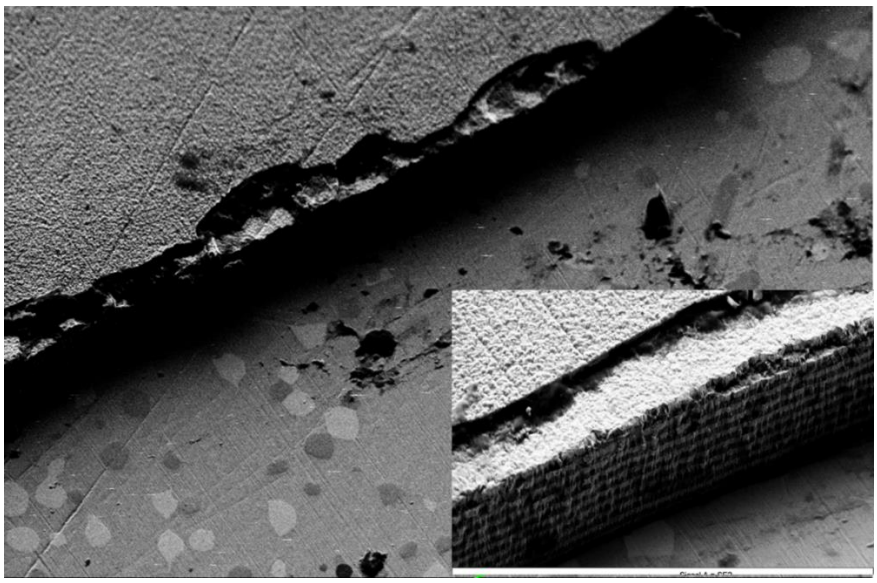

***Figure 103**: SEM micrograph of the delamination edge on a 100 nm-per-layer coating made up with CrN and WN layers. The presence of carbides was confirmed by comparison with the literature.*

5.3.4 ELECTROCHEMICAL CHARACTERIZATION

5.3.4.1 POTENTYODYNAMIC CHARACTERIZATION

The simplest way to estimate the anti-corrosion property of a coating is to test its current response to an applied DC potential sweep from reductive to oxidizing regime. This is commonly done by means of linear polarization, also known as Potentiodynamic Polarization (PP) tests. From these curves two main information can be directly drawn: the magnitude of the corrosion potential and the current in the anodic branch (oxidative behavior). A comfortable way to graphically represent PP curves is to plot the absolute value of the logarithm of the current density, *log(J)*, versus the applied DC potential. Exemplificative sets of PP curves for the CrMoN and CrWN systems are reported in **Figure 104**. Here, the current density corresponds to the absolute current as an area of 1

cm^2 was used as the electrochemically active site. The potential value where the anodic and cathodic branch asymptotically converge defines the corrosion potential. The corrosion current is then derived by fitting the Tafel equation (**Equation (2-19)**) to the anodic and cathodic branches at 50-100 mV from the corrosion potential.

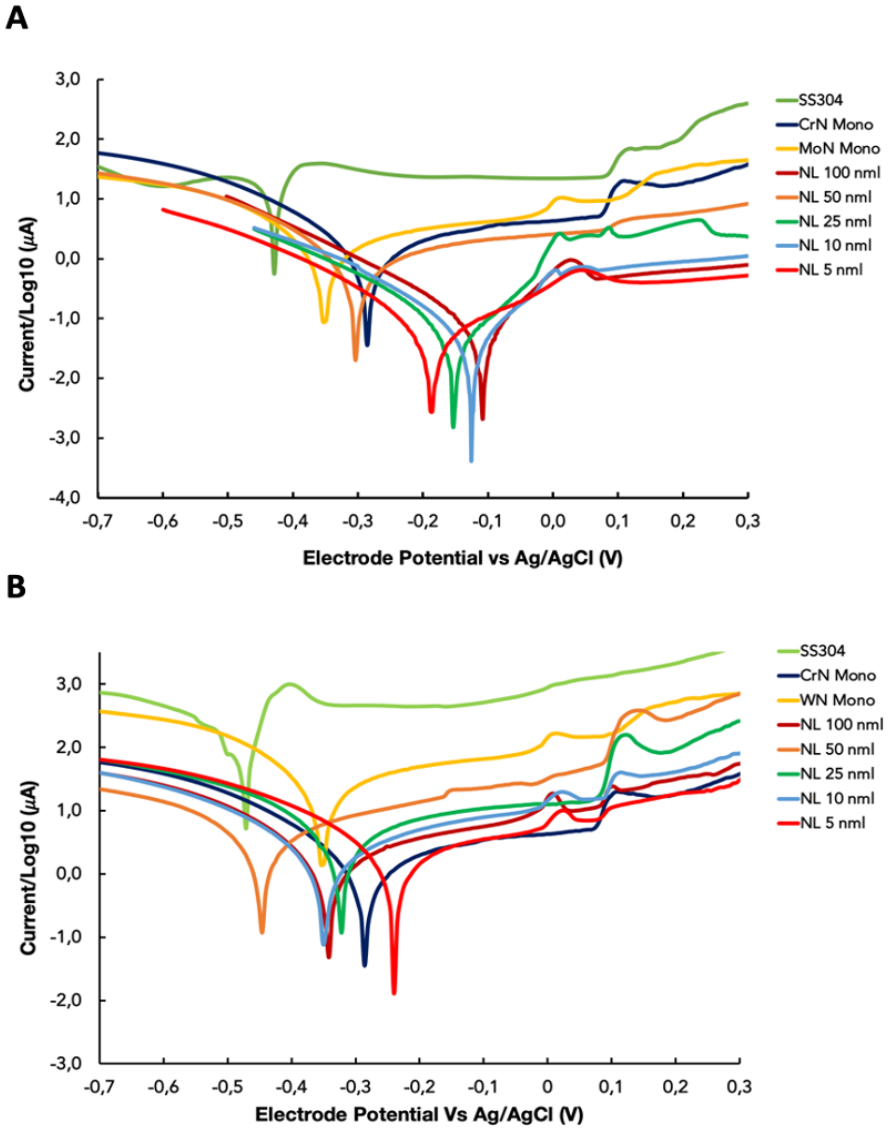

***Figure 104**:Comparative Potentiodynamic polarization plots for (A) the CrMoN system and (B) the CrWN system.*

The corrosion current has been calculated from the slope of the Tafel fit and imposing the condition of dynamic equilibrium of the anodic and cathodic current at the corrosion potential. Results for all the nanolaminate (NL) coatings are reported in **Figure 105**, along with reference corrosion current values calculated from PP tests performed on bare

substrates and single-layer (SL) coatings. Note that the current densities are reported in logarithmic scale.

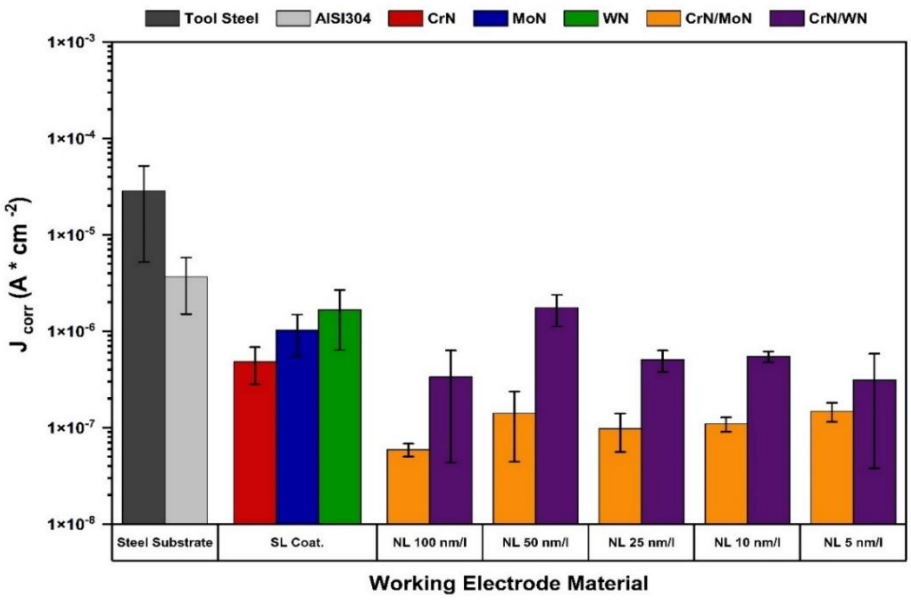

***Figure 105**: Corrosion current density calculated by means of the Tafel approximation on Potentiodynamic polarization curves for all the nanolaminate (NL) coatings in the CrMoN and CrWN systems. Corrosion currents of steel substrates and single-layer (SL) coatings are also reported for comparison. For each coating type at least 4 samples were analyzed. In all cases the active area was 1.0 ± 0.1 cm^2.*

All coatings yield lower corrosion currents than the bare substrates. Among single-layer coatings, CrN showed the lowest corrosion current of $5\pm2*10^{-7}$ A*cm^{-2} (red bar in **Figure 105)** , followed by MoN with $1\pm1*10^{-6}$ A*cm^{-2} (blue bar in **Figure 105)** and ultimately by WN with $2\pm1*10^{-6}$ A*cm^{-2} (green bar in **Figure 105)**. This trend is also reflected in the behavior of the two nanolaminate systems. Due to the lower corrosion resistance of WN, coatings in the CrWN system (purple bars in **Figure 105)** show corrosion current values between $3\pm1*10^{-7}$ and $2\pm1*10^{-6}$ A*cm^{-2}, between the individual values of the two constituent materials. This suggests that no additional benefit is provided by multilayering CrN with the non-protective WN. The corrosion behavior is mostly dictated by the protective action of CrN, in which the low-temperature favored formation of passivating Cr oxide instead of chlorinated Chromium compounds hinders the further dissolution of Cr ions into solution [479]. On the contrary, nanolaminate coatings within the CrMoN system (orange bars in **Figure 105**) show corrosion currents between $6\pm1*10^{-8}$ and $2\pm1*10^{-7}$ A*cm^{-2}, well below that recorded for CrN and MoN. This improved behavior was also suggested by the higher values of the corrosion potentials for the CrMoN system

with respect to the CrWN system (see **Figure 104**). In both systems, though, no clear trend is visible among coatings of the same multilayer system. This might suggest that the individual layer thickness does not play a fundamental role in determining the dissolution rates. Another possible explanation is the presence of defects within the coatings. These, depending on their severity can increase the effective active area of the electrode or, worse, provide channels for the electrolyte to the substrate. In both cases, the direct effect is an enhancement of the ionic exchange between the coating and the electrolyte and hence of the corrosion current. Ultimately, this effect can impair the corrosion protection of the coatings in such way to hide or moderate its dependency on coatings' architecture. Despite all coatings did not show any naked-eye visible damage caused by the electrochemical tests, SEM investigations revealed many micrometric and nanometric surface defects induced by the electrochemical attack, some of which are shown in **Figure 106**. Such defects include increased surface roughness, crack-openings, coating recession, formation and deposition of corrosion products and inclusion of salt microparticles within the coating's asperities.

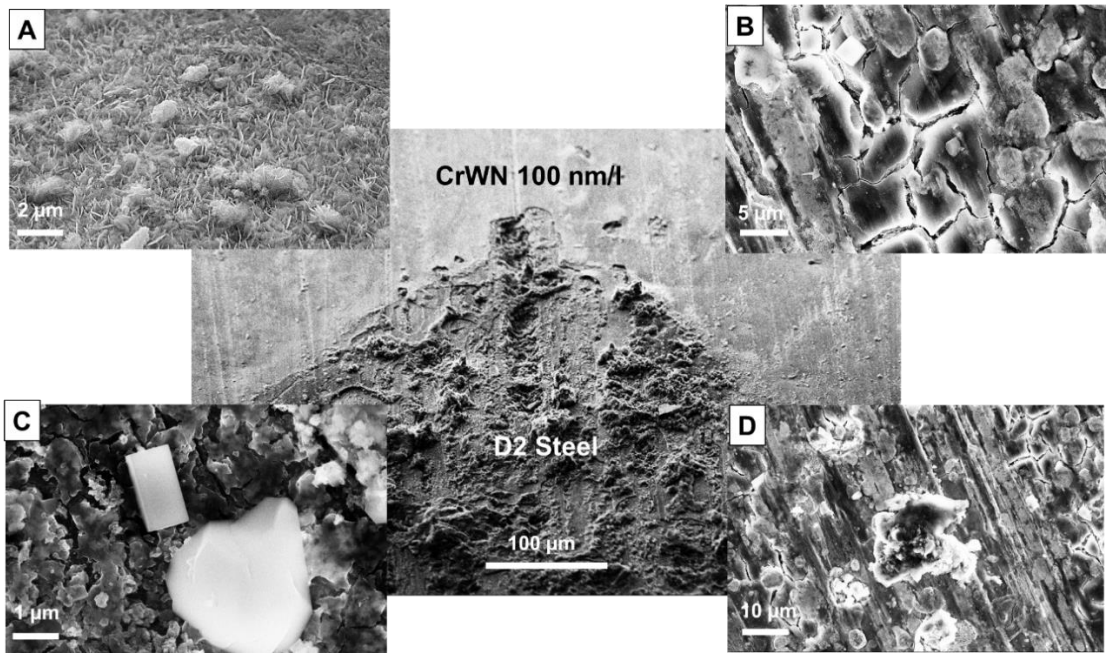

***Figure 106**: A SEM micrograph of the interface between a corroded area of a CrWN coated D2 steel substrate. Inserts A, B, C and D show typical corrosion-related features found on the surface of the corroded species. Insert A show the formation of small platelets on the corroded surface, along with corrosion debris; insert B shows a portion of the coating which is tore by corrosion-initiated cracks; insert (C) shows the occurrence of NaCl crystals embedded within corroded niches; insert (D) shows large corrosion debris along with surface cracks. Each insert reports its own scale-bar for size comparison.*

Nonetheless, in both systems the worst results were observed for the 50 nm-per-layer architecture. It could be argued that this layer thickness coincides with some sort of threshold thickness. In 100 nm-per-layer architectures, the first layer of CrN is thick enough to provide good resistance to ions diffusion through the outer portion of the coating towards the inner layers. When the thickness of the CrN layer is reduced to 50 nm, ion exchange through the first CrN layer could be enhanced, and a higher dissolution current is then recorded due to the dissolution of the less inert MoN and WN layers below. By further reducing the thickness to 25-nm-per-layers and less, the corrosion current drops once again. This can be due to a reduction of the channeling of ions through the more nanocrystalline layers (check **Figure 91-A** and **Figure 91-B**). On the other hand, this anti-channeling effect can be counterbalanced by the higher percentage of grain boundaries, which constitute areas more susceptible to chemical attack than the inner crystalline portions, due to the lower degree of atomic coordination of atoms at grain boundaries [480], [481]. These balancing effects might explain the absence of any clear dependance for the most nanostructured coatings, despite some opposite claims of increasing corrosion resistance with grain refinement in passivating do exist (see [481] and references therein) .

5.3.4.2 ELECTROCHEMICAL IMPEDANCE SPECTROSCOPY

Electrochemical Impedance Spectroscopy (EIS) can provide additional information on the corrosion resistance of sputtered nitride coatings. The main difference between PP and EIS is that in the former the DC potential is swept across a large range, causing the irreversible change of the material's surface, while the latter exploits small DC oscillations around the OCP, thus never stressing the material with high oxidative or reducing currents, while probing the capacitive and resistive response of the coating. Given the previous mechanical and PP results, EIS tests were conducted on a limited but representative set of samples, consisting of monolithic coatings of CrN, MoN and WN, and multilayer coatings consisting of nanolaminates with 100, 25 and 10 nm-per-layer architectures. For both systems, the Nyquist plots of the imaginary versus the real part of the impedance are reported in **Figure 107**, while Impedance Bode plots and Phase Bode Plots are reported in **Figure 108**. The Nyquist plots of both coatings system reveal relatively high impedance values, in line with those reported in the literature for nitride-

based hard coatings systems [379], [395], [396], [468], [482]–[484]. The radius of the semicircular-shaped curve in the Nyquist plot is directly correlated to the total impedance of the coating (i.e., the radius corresponds to the impedance modulus). In the CrMoN coatings system, the lowest impedance is provided by the monolithic MoN coating, followed by the monolithic CrN coating. The highest impedance is provided by the nanolaminates with increasingly thinner individual layer thickness. This trend is in good agreement with the results of the PP tests (see **Figure 104-A** and **Figure 105**).

Concerning the CrWN system, due to the low corrosion protection of WN coatings, only the 10-nm-per-layer coating provides an impedance exceeding that of CrN, with the other nanolaminate coatings lying in between the values of monolithic CrN and WN. This trend also is well supported by the reported results from the PP tests (see **Figure 104-B** and **Figure 105**). In any case, a positive influence of the nanostructured architecture is clearly visible in EIS measurements, contrarily to what previously observed in the case of PP tests, where nanolaminate coatings of the same system revealed no appreciable differences in anti-corrosion properties.

The bode plots reveal some further differences in the behavior of the tested coatings. Coatings in the CrMoN system follow very similar trends (**Figure 108 A-C**), suggesting similar electrochemical mechanisms. From the phase shift in **Figure 108-C**, it is possible to argue that the double-layer capacitive effect is determining the ion-exchange process even at low frequencies, given the still relatively high phase shift value of 60-70°C. On the contrary, the phase-shift of CrWN coatings at low frequencies (**Figure 108-D)**, tends to lower values, indicating a larger resistive behavior and hence a larger loss of the double-layer ability to drive the ion exchange [381], [386]–[388], [392]. This is particularly evident for the WN coating (green curve), which shows a major drop to less than 20 °C at the lowest frequency regime. Besides, by comparing the impedance values of the CrWN and CrN coatings (**Figure 108-B),** it can be seen that only the 10-nm-per-layer CrWN coating can match the monolithic CrN.

The hypothesis of a lower efficacy of the double layer established with CrWN coatings is also supported by the higher texture of WN layers against MoN, as shown in **Figure 90** in Section 5.3.2. In fact, a higher texture can ease the ions channeling through the coating, reducing the insulating effect of the double layer.

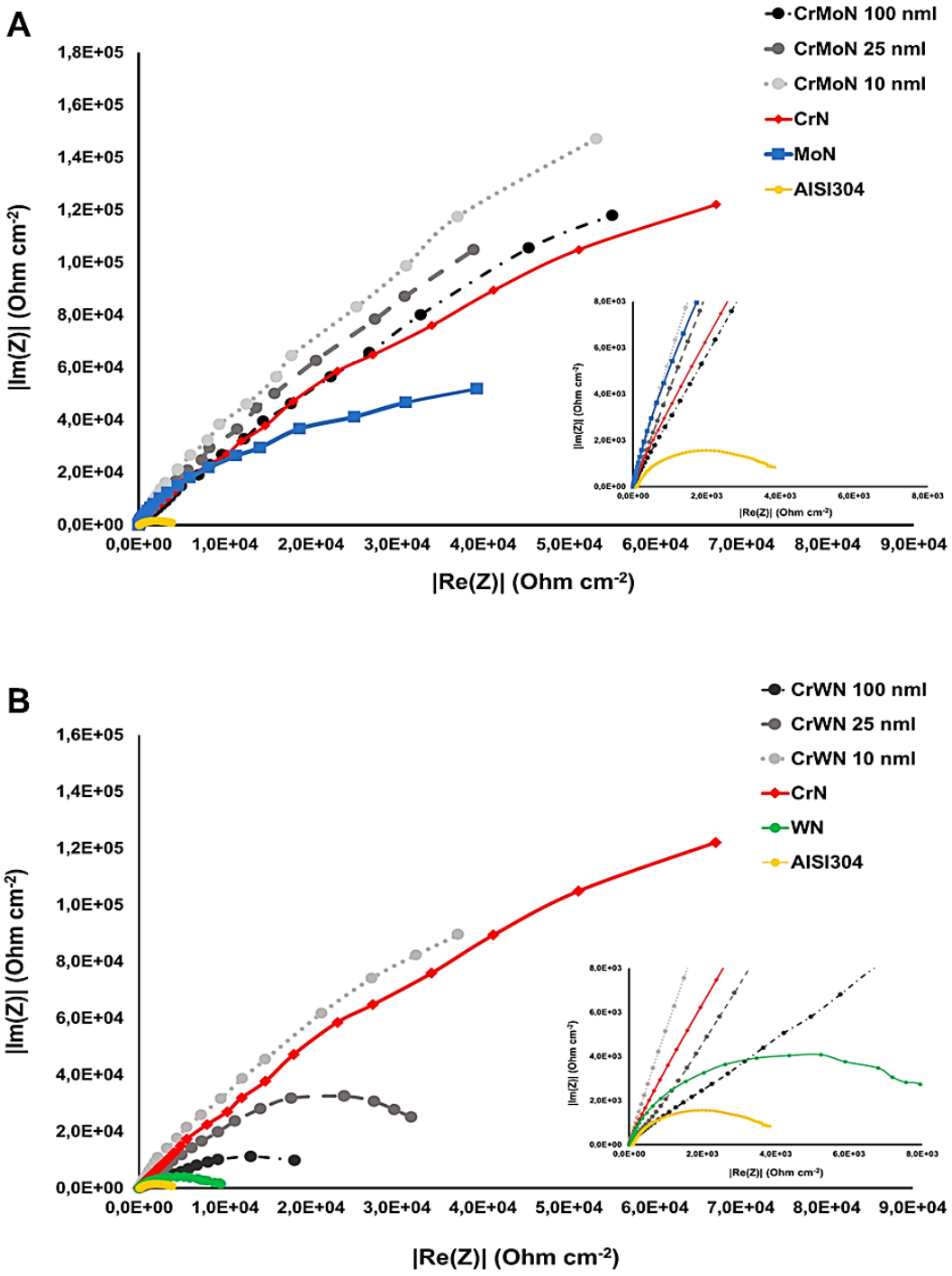

***Figure 107**: Nyquist plots for (A) the CrMoN and (B) the CrWN coatings system. Inserts focus on the low impedance region of the parent plot to highlight the curve of the AISI304 substrate.*

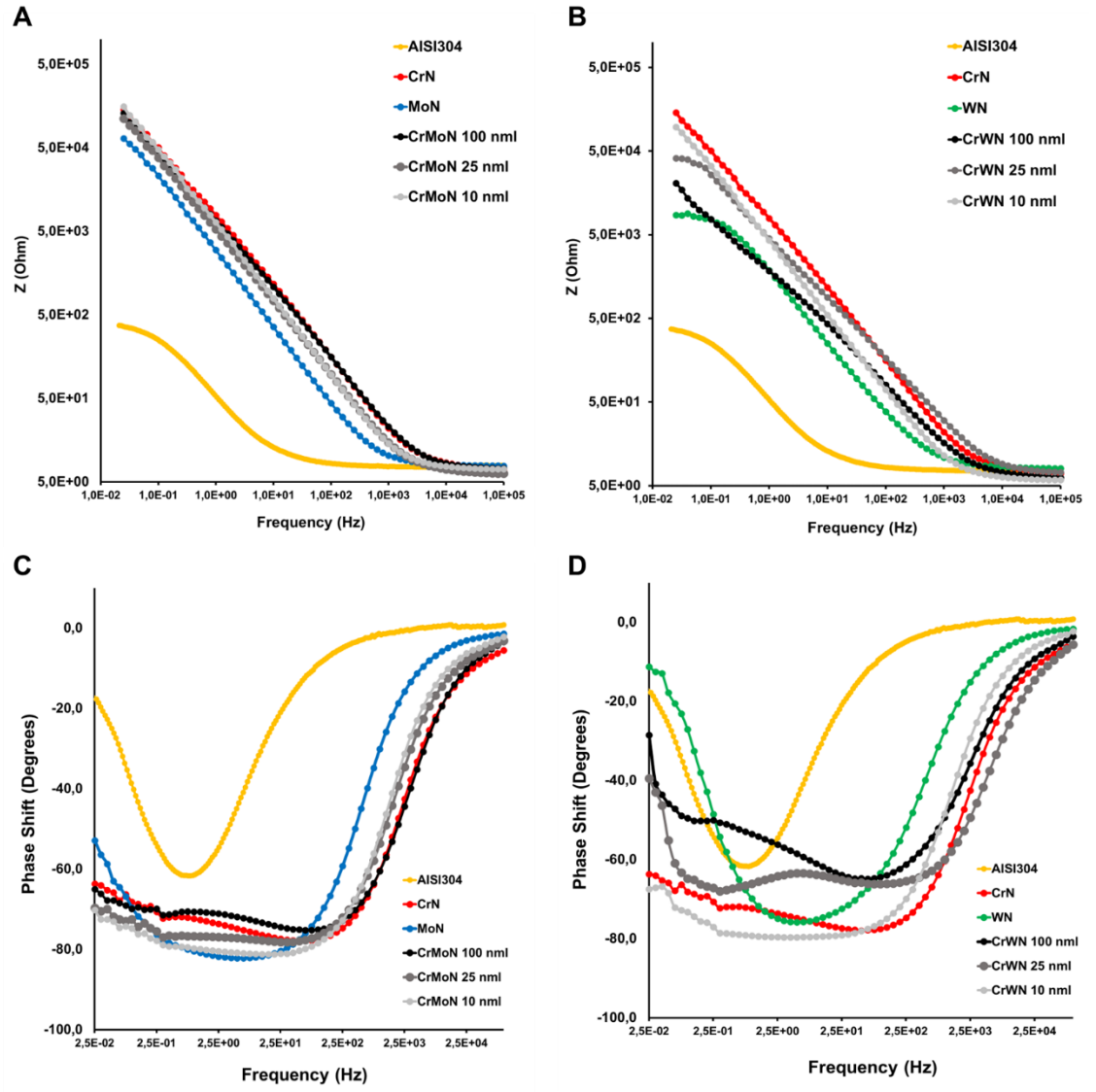

***Figure 108**: (A) and (B), Bode plots of the impedance versus input frequency for CrMoN and CrWN coatings respectively; (C) and (D) Bode plots of the phase shift between input AC potential and output AC current for CrMoN and CrWN coatings, respectively.*

5.4 DISCUSSION

The characterization of CrMoN and CrWN multilayer coating systems was carried out by investigating the mechanical and electrochemical properties of the coatings by means of nano and macro indentation tests as well as Potentiodynamic and Impedance Spectroscopy tests, respectively. In both systems, the impact of increasing the nanostructured character of the multilayer architecture on the resulting properties of interest was targeted and correlated to the grain refinement and structural characteristics.

The coatings with the higher microhardness and stiffness values belong to the CrWN system. This is attributed to the strong compressive residual stressed of the highly textured WN constituents (see **Figure 90** for the texture analysis result and **Figure 94** for the residual stress measurements). The increase in hardness with thinner constituent layers can be attributed to either a reduction of structural defects or to the deformation mechanisms between monolithic and multilayered coatings [69], [97], [485], [486]. In fact, an energetic obstacle to the vertical propagation of cracks and dislocations is provided by the varying stress fields at each interface. Rather than propagating through the coatings' thickness, dislocation and cracks are deflected at the interfaces, retarding the mechanical failure of the coating [79], [107], [333].

Nanoindentation tests showed that microhardness increases for more nanostructured architectures, i.e., for nanolaminate systems with progressively thinner constituent layers. A maximum hardness of about 3200 HV (32 GPa) was observed for CrWN coatings with 10 and 5 nm-per-layer architectures. These values are very close to that of monolithic WN, and in good agreement with previously reported values [412], [414], [431]. A qualitatively similar albeit less pronounced trend is observed also for the CrMoN system. Such more moderate improvement is probably due to the lower compressive residual stress of the MoN constituent with respect to WN (see **Figure 94**). A maximum hardness of about 2700 HV (27 GPa) was observed for the 5-nm-per-layer architecture. This value is relatively high and in accordance to previous studies [433] but much lower than what reported by other groups [96], [110]. In such works, high values exceeding 40 GPa are reported, but the different deposition technique (Arc-Discharge instead of Magnetron Sputtering) can have a strong impact on the final mechanical properties. Coatings belonging to both the CrMoN and CrWN systems showed good H/E and H^3/E^2 values. H/E values of about 1 and 1.2 were calculated for the 10- and 5-nm-per-layer architecture coatings of the CrMoN (**Figure 99-A**) and CrWN system (**Figure 100-A**), respectively. Such values correspond to an increase of about 25% and 33% against those obtained for monolithic CrN. Also, the H^3/E^2 ratio showed remarkable improvements for the more nanostructured coatings with respect to monolithic coatings and less-nanostructured architectures. Maximum H^3/E^2 values of about 250 and 450 GPa have been calculated for the 10- and 5-nm-per-layer architectures of CrMoN (**Figure 99-B**) and CrWN (**Figure 100-B)** nanolaminates, respectively, corresponding to an increase of about 67% and

200% against the 150 GPa calculated for the monolithic CrN. Such improvements can be due to the grain refinement observed for nanolayered systems with progressively thinner individual layers (see **Figure 91**). The thickness of the constituent layers poses an upper bound for crystal growth. A very finely grained structure can help increase the mechanical resistance by impeding the motions of dislocations under mechanical load. Dislocations generated within each grain accumulate at grain boundaries and create a stress field which impedes further material displacement, a phenomenon known as the Hall-Petch effect [485], [487], [488]. Incidentally, it should be noticed that in neither system an inverse Hall-Petch effect was observed [489]. The inverse Hall-Petch effect predicts a reduction in mechanical resistance to deformation for extremely fine-grained materials, due to the transition of the deformation mechanisms from dislocation generation and motion to grain boundaries sliding. The absence of this effect might be due to the additional deformation constraints imposed by the nanolayered architectures, which hinders the intergranular sliding across the interfaces. Regarding the coatings' adhesion, it was also observed (**Figure 101** and **Figure 102)** that the nanolayered structures remarkably help increase the adhesion of the coatings, as shown by the Rockwell-C indentation tests (i.e., the Daimler-Benz test). Nonetheless, these experiments revealed a comprehensively low adhesion of the coatings to the substrates. The SEM investigation on the delamination mark revealed that the weak point was the interface between the steel substrate and the Chromium interlayer (**Figure 103**). The low adhesion of the Cr layer could be due to the low deposition temperature (about 230 °C) or to an insufficient Ar etching pre-treatment. Despite this, the nanostructured coatings themselves showed good cohesion, with a limited concentration of cracks and limited inter-layer delamination.

The increased corrosion resistance of nanolayered coatings against the monolithic counterparts is usually motivated by the chemical inhomogeneity of the nanolaminate architecture with intermittent formation of passivating Cr-based compounds which pose an obstacle to the ion exchange between the coating and the electrolyte. Potentiodynamic polarization tests showed that for coatings within the CrWN system, the corrosion current is fundamentally determined by the CrN constituent, with WN being much more susceptible to chemical dissolution in NaCl solution. This can be due to the lack of formation of passivating oxides from Tungsten, as well as on the facile interdiffusion of

ions by channeling through the highly textured columnar WN grains (**Figure 90**). On the contrary, despite single-layer MoN coatings showed relatively high corrosion currents (see **Figure 104-A** and **Figure 105**), nanolaminate coatings of the CrMoN system showed corrosion currents significantly lower than MoN and even CrN. These improvements were also confirmed by the Impedance Spectroscopy tests, while for the CrWN system only the 5-nm-per-layer architecture showed a higher electrochemical impedance than monolithic CrN (**Figure 107**). Contrarily to what evidenced for the CrWN system, multilayering CrN with MoN yields significant improvements to the overall corrosion protection of the coating. The slight difference in corrosion current between monolithic MoN and WN (**Figure 105)** cannot alone explain the major difference in corrosion currents among the coatings of the CrMoN and the CrWN systems. Rather, it is possible that a better interface is established between CrN and MoN than between CrN and WN, yielding a more compact coating with improved capability of blocking the penetration of the electrolyte. In Section 2.3.5 it was observed that WN layers were characterized by a higher residual compressive stress than MoN and CrN (**Figure 94**), which made them more susceptible to cracking, especially when external bias was applied (**Figure 76**). This could constitute a major source of structural defects such as microcracks, which in turn might provide a further explanation for the lower corrosion resistance of coatings belonging to the CrWN system versus those of the CrMoN system. Another contribution can originate from the different behaviour of Mo and W in aqueous solution. Metal dissolution in aqueous solutions occurs through the formation of soluble chlorinated compounds [490]. In aqueous media, Molybdenum is capable of spontaneously forming stable passivating oxides [491], while Tungsten is usually poorly oxidized and hence a passivation layer is not easily formed without strong oxidants [492]. This could make Tungsten more prone to chlorination-induced dissolution in Cl-rich media than Molybdenum, helping explain the improved anticorrosion properties of the CrMoN system against CrWN. The contribution of grain size on corrosion properties is not well clarified. In fact, the higher fraction of chemically more active grain boundaries in nanolayered materials could contribute to enhance the reactivity towards the electrolyte. Nonetheless, if passivating compounds are formed, this could contribute to increase the corrosion resistance of the coating.

6 CONCLUDING REMARKS

Despite the results of the proposed doctoral thesis are satisfying and generally positive, some evident areas of improvements emerged. First, the adhesion of the coatings seems to be a critical point and must be improved. It must be admitted that coating mirrored, and flat surfaces does not consider the problem of coating complex geometries such as those of real cutting tools such as drills and milling tools. The sharp features of the cutting edges can impart additional stresses to the coating. Hence, the real-field properties of the coating are expectably lower than those observed on research samples. Besides the adhesion, also wear behavior should be investigated. Despite the mechanical predictors such as the H/E ratio provide useful information, the complex nature of wear phenomena should be directly investigated with appropriate test routines, such as pin-on-disc and ball-on-disc tests. Finally, the thermal behavior of the coatings must be investigated. Temperatures of a few hundred degrees are reached during machining wood-based materials. It is known that heating can soften the tool material, promote chemical reactions with oxidizing species, ultimately changing the performances of the coatings with respect to low temperature tests. Once all these tests are performed and the mentioned weaknesses of the proposed coatings resolved, then real wood-cutting tests could be performed, these providing the real potential application in the wood-industry.

7 ACKNOWLEDGMENTS

The project was entirely funded by the Interreg ITA-SLO NANOREGION project.

The author wishes to thank all the people collaborating to the development of the research activities. First of all, Dr. Simone Dal Zilio from CNR-IOM for providing important contributions in the training activities, work organization and conceptualization; Dr. Marco Lazzarino (CNR-IOM) and Prof. Orfeo Sbaizero for providing invaluable directions and mentoring in both technical and attitudinal aspects of my PhD journey.

Special thanks to all the people involved in the Nanoregion framework and in particular all the people I had the opportunity and pleasure to work with: Dr. Federica Rigoni and Dr. Davide Cristofori from the Department of Molecular Sciences and Nanosystems of the University of Venice, Prof. Mattia Fanetti and Dr. Andraž Mavrič from the Materials Research Laboratory at the University of Nova Gorica, Prof. Barbara Ressel from the Quantum Optics Laboratory at the University of Nova Gorica, Dr. Gregor Kapun from the Centre of Excellence in Nanoscience and Nanotechnology in Ljubljana, Dr. Catalin Ciubotaru from CNR-IOM.

Special thanks to Prof. Miha Čekada, from the Thin Film and Surface Department of the Józef Stefan Institute of Ljubljana, whose kindness and support were fundamental for the achievement of important results in this research.

BIBLIOGRAPHY

[1] J. L. Katz, P. Spencer, Y. Wang, A. Misra, O. Marangos, and L. Friis, "On the anisotropic elastic properties of woods," *J. Mater. Sci.*, vol. 43, no. 1, pp. 139–145, 2008, doi: 10.1007/s10853-007-2121-9.

[2] G. Blugan *et al.*, "Performance of lightweight coated oxide ceramic composites for industrial high speed wood cutting tools: A step closer to market," *Ceram. Int.*, vol. 43, no. 12, pp. 8735–8742, 2017, doi: 10.1016/j.ceramint.2017.04.005.

[3] W. Darmawan, "The Importance of Extractives and Abrasives in wood materials in the wear of cutting tools," vol. 7, pp. 4715–4729, 2012.

[4] D. Kazlauskas, V. Jankauskas, and S. Tuckute, "Research on tribological characteristics of hard metal WC-Co tools with TiAlN and CrN PVD coatings for processing solid oak wood," *Coatings*, vol. 10, no. 7, 2020, doi: 10.3390/coatings10070632.

[5] V. Jivkov, "State And Trends In the Development of the World, European and Bulgarian Furniture Trends," *Innov. Woodwork. Ind. Eng. Dsign*, vol. 15, no. January, pp. 7–16, 2020.

[6] V. Jivkov, "KEYNOTE ADDRESS IX INTERNATIONAL SCIENTIFIC AND TECHNICAL CONFERENCE INNOVATIONS IN FOREST INDUSTRY AND ENGINEERING DESIGN -INNO 2018 STATE AND TRENDS IN THE DEVELOPMENT OF THE WOR ...," no. January, 2020.

[7] R. Komanduri, "Cutting-tool Materials," *Encycl. Mater. Sci. Technol.*, no. Komanduri, pp. 1–13, 2001, doi: 10.1016/b0-08-043152-6/00353-3.

[8] A. Hosseini and H. A. Kishawy, "Cutting Tool Materials and Tool Wear," pp. 31–56, 2014, doi: 10.1007/978-3-662-43902-9_2.

[9] X. T. Duong, J. R. R. Mayer, and M. Balazinski, "Initial tool wear behavior during machining of titanium metal matrix composite (TiMMCs)," *Int. J. Refract. Met. Hard Mater.*, vol. 60, pp. 169–176, 2016, doi: 10.1016/j.ijrmhm.2016.07.021.

[10] K. Venkatesan, J. K. Patel, G. V. Raval, and H. V. Shah, "A Comparative study of tool wears in dry turning of Inconel X-750 and Waspaloy," *Mater. Today Proc.*, vol. 5, no. 5, pp. 13429–13437, 2018, doi: 10.1016/j.matpr.2018.02.337.

[11] C. Lahiff, S. Gordon, and P. Phelan, "PCBN tool wear modes and mechanisms in finish hard turning," *Robot. Comput. Integr. Manuf.*, vol. 23, no. 6, pp. 638–644, 2007, doi: 10.1016/j.rcim.2007.02.008.

[12] Y. Ayed, G. Germain, A. Ammar, and B. Furet, "Degradation modes and tool wear mechanisms in finish and rough machining of Ti17 Titanium alloy under high-pressure water jet assistance," *Wear*, vol. 305, no. 1–2, pp. 228–237, 2013, doi: 10.1016/j.wear.2013.06.018.

[13] A. T. Abbas, S. Anwar, H. Hegab, F. Benyahia, H. Ali, and A. Elkaseer, "Comparative evaluation of surface quality, tool wear, and specific cutting energy for wiper and conventional carbide inserts in hard turning of aisi 4340 alloy steel," *Materials (Basel).*, vol. 13, no. 22, pp. 1–16, 2020, doi: 10.3390/ma13225233.

[14] R. Bendikiene and G. Keturakis, "The influence of technical characteristics of wood milling tools on its wear performance," *J. Wood Sci.*, vol. 63, no. 6, pp. 606–614, 2017, doi: 10.1007/s10086-017-1656-x.

[15] B. Porankiewicz, P. Iskra, J. Sandak, C. Tanaka, and K. Jóźwiak, "High-speed steel tool wear during wood cutting in the presence of high-temperature corrosion and mineral contamination," *Wood Sci. Technol.*, vol. 40, no. 8, pp. 673–682, 2006, doi: 10.1007/s00226-006-0084-7.

[16] H. Aknouche, A. Outahyon, C. Nouveau, R. Marchal, A. Zerizer, and J. C. Butaud, "Tool wear effect on cutting forces: In routing process of Aleppo pine wood," *J. Mater. Process. Technol.*, vol. 209, no. 6, pp. 2918–2922, 2009, doi: 10.1016/j.jmatprotec.2008.06.062.

[17] J. Y. Sheikh-Ahmad and T. Morita, "Tool coatings for wood machining: Problems and prospects," *For. Prod. J.*, vol. 52, no. 10, pp. 43–51, 2002.

[18] V. Nasir and J. Cool, "A review on wood machining: characterization, optimization, and monitoring of the sawing process," *Wood Mater. Sci. Eng.*, vol. 15, no. 1, pp. 1–16, 2020, doi: 10.1080/17480272.2018.1465465.

[19] J. Karandikar, T. McLeay, S. Turner, and T. Schmitz, "Tool wear monitoring using naïve Bayes classifiers," *Int. J. Adv. Manuf. Technol.*, vol. 77, no. 9–12, pp. 1613–1626, 2015, doi: 10.1007/s00170-014-6560-6.

[20] A. Rizzo *et al.*, "The critical raw materials in cutting tools for machining applications: A review," *Materials (Basel).*, vol. 13, no. 6, pp. 1–49, 2020, doi: 10.3390/ma13061377.

[21] V. F. C. Sousa and F. J. G. Silva, "Recent advances on coated milling tool technology-a comprehensive review," *Coatings*, vol. 10, no. 3, 2020, doi: 10.3390/coatings10030235.

[22] S. N. Grigoriev, S. V. Fedorov, and K. Hamdy, "Materials, properties, manufacturing methods and cutting performance of innovative ceramic cutting tools - A review," *Manuf. Rev.*, vol. 6, 2019, doi: 10.1051/mfreview/2019016.

[23] B. Mills, "Recent developments in cutting tool materials," *J. Mater. Process. Technol.*, vol. 56, no. 1–4, pp. 16–23, 1996, doi: 10.1016/0924-0136(95)01816-6.

[24] A. M. Bayer, B. A. Becherer, and T. Vasco, "Bulletin: High Speed Tool Steels," *ASM Handb.*, vol. 16, pp. 51–59, 1989.

[25] K. Tsuda, "History of development of cemented carbides and cermet," *SEI Tech. Rev.*, no. 82, pp. 16–20, 2016.

[26] J. García, V. Collado Ciprés, A. Blomqvist, and B. Kaplan, "Cemented carbide microstructures: a review,"

Int. J. Refract. Met. Hard Mater., vol. 80, no. August 2018, pp. 40–68, 2019, doi: 10.1016/j.ijrmhm.2018.12.004.
[27] S. H. Chang and S. L. Chen, "Characterization and properties of sintered WC-Co and WC-Ni-Fe hard metal alloys," *J. Alloys Compd.*, vol. 585, pp. 407–413, 2014, doi: 10.1016/j.jallcom.2013.09.188.
[28] P. Gogolewski, J. Klimke, A. Krell, and P. Beer, "Al2O3 tools towards effective machining of wood-based materials," *J. Mater. Process. Technol.*, vol. 209, no. 5, pp. 2231–2236, 2009, doi: 10.1016/j.jmatprotec.2008.06.016.
[29] K. Broniszewski, J. Wozniak, M. Kostecki, K. Czechowski, L. Jaworska, and A. Olszyna, "Al2O3–V cutting tools for machining hardened stainless steel," *Ceram. Int.*, vol. 41, no. 10, pp. 14190–14196, 2015, doi: 10.1016/j.ceramint.2015.07.044.
[30] A. A. Vereschaka, A. D. Batako, A. A. Krapostin, N. N. Sitnikov, and G. V. Oganyan, "Improvement in Reliability of Ceramic Cutting Tool using a Damping System and Nano-structured Multi-layered Composite Coatings," *Procedia CIRP*, vol. 63, no. 2212, pp. 563–568, 2017, doi: 10.1016/j.procir.2017.03.145.
[31] J. V. C. Souza, O. M. De Macedo Silva, M. Do Carmo Andrade Nono, J. P. B. Machado, M. Pimenta, and M. V. Ribeiro, "Si 3N 4 ceramic cutting tool sintered with CeO 2 and Al 2O 3 additives with AlCrN coating," *Mater. Res.*, vol. 14, no. 4, pp. 514–518, 2011, doi: 10.1590/S1516-14392011005000077.
[32] W. Grzesik, "Cutting Tool Materials," *Adv. Mach. Process. Met. Mater.*, pp. 35–63, 2017, doi: 10.1016/b978-0-444-63711-6.00004-1.
[33] W. M. J. Garrison, "Steels : Classifications," in *Encyclopedia of Materials Science and Technology*, 2001, pp. 1–4.
[34] Y. W. Luo, H. J. Guo, X. L. Sun, J. Guo, and F. Wang, "Influence of Tempering Time on the Microstructure and Mechanical Properties of AISI M42 High-Speed Steel," *Metall. Mater. Trans. A Phys. Metall. Mater. Sci.*, vol. 49, no. 12, pp. 5976–5986, 2018, doi: 10.1007/s11661-018-4924-5.
[35] Y. W. Luo, H. J. Guo, X. L. Sun, and J. Guo, "Influence of the Nitrogen Content on the Carbide Transformation of AISI M42 High-Speed Steels during Annealing," *Sci. Rep.*, vol. 8, no. 1, pp. 1–10, 2018, doi: 10.1038/s41598-018-22461-z.
[36] S. Šolić, Z. Schauperl, M. Godec, and V. Tropša, "Microstructural Changes in Heat Treatment of Pm High-Speed Steels," *Tech. J.*, vol. 11, no. April, pp. 166–170, 2017, [Online]. Available: https://www.researchgate.net/publication/340871321
[37] S. Šolić, Z. Schauperl, M. Godec, and V. Tropša, "Microstructural Changes in Heat Treatment of Pm High-Speed Steels," *Tech. J.*, vol. 11, no. April, pp. 166–170, 2017.
[38] A. S. Chaus, "On the wear resistance of high-speed steels," *J. Fricț. Wear*, vol. 29, no. 1, pp. 24–34, 2008, doi: 10.3103/s1068366608010054.
[39] K. Bobzin, "High-performance coatings for cutting tools," *CIRP J. Manuf. Sci. Technol.*, vol. 18, no. 2017, pp. 1–9, 2017, doi: 10.1016/j.cirpj.2016.11.004.
[40] Y. W. Luo, H. J. Guo, X. L. Sun, J. Guo, and F. Wang, "Influence of Tempering Time on the Microstructure and Mechanical Properties of AISI M42 High-Speed Steel," *Metall. Mater. Trans. A Phys. Metall. Mater. Sci.*, vol. 49, no. 12, pp. 5976–5986, 2018, doi: 10.1007/s11661-018-4924-5.
[41] A. M. F. Rocha *et al.*, "Corrosion behaviour of WC hardmetals with nickel-based binders," *Corros. Sci.*, vol. 147, no. November 2018, pp. 384–393, 2019, doi: 10.1016/j.corsci.2018.11.015.
[42] E. O. Correa, J. N. Santos, and A. N. Klein, "Microstructure and mechanical properties of WC Ni-Si based cemented carbides developed by powder metallurgy," *Int. J. Refract. Met. Hard Mater.*, vol. 28, no. 5, pp. 572–575, 2010, doi: 10.1016/j.ijrmhm.2010.04.003.
[43] Z. Roulon, J. M. Missiaen, and S. Lay, "Carbide grain growth in cemented carbides sintered with alternative binders," *Int. J. Refract. Met. Hard Mater.*, vol. 86, 2020, doi: 10.1016/j.ijrmhm.2019.105088.
[44] P. K. Katiyar and N. S. Randhawa, "Corrosion behavior of WC-Co tool bits in simulated (concrete, soil, and mine) solutions with and without chloride additions," *Int. J. Refract. Met. Hard Mater.*, vol. 85, no. August, p. 105062, 2019, doi: 10.1016/j.ijrmhm.2019.105062.
[45] S. H. Chang and S. L. Chen, "Characterization and properties of sintered WC-Co and WC-Ni-Fe hard metal alloys," *J. Alloys Compd.*, vol. 585, pp. 407–413, 2014, doi: 10.1016/j.jallcom.2013.09.188.
[46] E. O. Correa, J. N. Santos, and A. N. Klein, "Microstructure and mechanical properties of WC Ni-Si based cemented carbides developed by powder metallurgy," *Int. J. Refract. Met. Hard Mater.*, vol. 28, no. 5, pp. 572–575, 2010, doi: 10.1016/j.ijrmhm.2010.04.003.
[47] D. Johansson *et al.*, "Assessment of metal cutting tools using cost performance ratio and tool life analyses," *Procedia Manuf.*, vol. 38, no. Faim 2019, pp. 816–823, 2019, doi: 10.1016/j.promfg.2020.01.114.
[48] M. Parlinska-Wojtan *et al.*, "Influence of intergranular phases on edge integrity of Si3N4/SiC wood cutting tools," *J. Eur. Ceram. Soc.*, vol. 31, no. 14, pp. 2711–2719, 2011, doi: 10.1016/j.jeurceramsoc.2011.01.021.
[49] Y. Guo, P. X. Cao, H. N. Liu, Y. Teng, H. Wang, and X. L. Guo, "Tribological Properties of Ceramics Tool Materials in Contact with Wood-Based Materials," *Adv. Mater. Res.*, vol. 764, pp. 65–69, 2013, doi: 10.4028/www.scientific.net/amr.764.65.
[50] W. Liu *et al.*, "PVD-CrAlN and TiAlN coated Si3N4 ceramic cutting tools —1. Microstructure, turning performance and wear mechanism," *Ceram. Int.*, vol. 43, no. 12, pp. 8999–9004, 2017, doi: 10.1016/j.ceramint.2017.04.041.
[51] M. Woydt, A. Skopp, I. Dörfel, and K. Witke, "Wear engineering oxides/antiwear oxides©," *Tribol. Trans.*,

vol. 42, no. 1, pp. 21–31, 1999, doi: 10.1080/10402009908982185.
[52] P. Beer, P. Gogolewski, J. Klimke, and A. Krell, “Tribological behaviour of sub-micron cutting-ceramics in contact with wood-based materials,” *Tribol. Lett.*, vol. 27, no. 2, pp. 155–158, 2007, doi: 10.1007/s11249-007-9212-2.
[53] S. R. Banik *et al.*, “State of the art on zirconia toughened alumina cutting tools,” *Mater. Today Proc.*, vol. 18, pp. 2632–2641, 2019, doi: 10.1016/j.matpr.2019.07.123.
[54] D. Galusek and D. Galusková, “Alumina matrix composites with non-oxide nanoparticle addition and enhanced functionalities,” *Nanomaterials*, vol. 5, no. 1, pp. 115–143, 2014, doi: 10.3390/nano5010115.
[55] M. Szutkowska, S. Cygan, M. Podsiadło, J. Laszkiewicz-łukasik, J. Cyboroń, and A. Kalinka, “Properties of TiC and TiN reinforced alumina–zirconia composites sintered with spark plasma technique,” *Metals (Basel).*, vol. 9, no. 11, 2019, doi: 10.3390/met9111220.
[56] J. J. Swab, A. A. Wereszczak, J. Tice, R. Caspe, R. H. Kraft, and J. W. Adams, “Mechanical and Thermal Properties of Advanced Ceramics for Gun Barrel Applications,” *Mater. Res.*, no. February, 2005.
[57] K. Bobzin, “High-performance coatings for cutting tools,” *CIRP J. Manuf. Sci. Technol.*, vol. 18, no. 2017, pp. 1–9, 2017, doi: 10.1016/j.cirpj.2016.11.004.
[58] E. Benedicto, D. Carou, and E. M. Rubio, “Technical, Economic and Environmental Review of the Lubrication/Cooling Systems Used in Machining Processes,” *Procedia Eng.*, vol. 184, pp. 99–116, 2017, doi: 10.1016/j.proeng.2017.04.075.
[59] K. Smyrnova *et al.*, “Microstructure, Mechanical and Tribological Properties of Advanced Layered WN/MeN (Me = Zr, Cr, Mo, Nb) Nanocomposite Coatings,” *Nanomaterials*, vol. 12, no. 3, 2022, doi: 10.3390/nano12030395.
[60] N. R. Dhar, M. Kamruzzaman, and M. Ahmed, “Effect of minimum quantity lubrication (MQL) on tool wear and surface roughness in turning AISI-4340 steel,” *J. Mater. Process. Technol.*, vol. 172, no. 2, pp. 299–304, 2006, doi: 10.1016/j.jmatprotec.2005.09.022.
[61] H. Caliskan, P. Panjan, and C. Kurbanoglu, *Hard Coatings on Cutting Tools and Surface Finish*, vol. 3–3, no. January 2017. Elsevier Ltd., 2017. doi: 10.1016/B978-0-12-803581-8.09178-5.
[62] L. A. Dobrzański and D. Pakuła, “Comparison of the structure and properties of the PVD and CVD coatings deposited on nitride tool ceramics,” *J. Mater. Process. Technol.*, vol. 164–165, pp. 832–842, 2005, doi: 10.1016/j.jmatprotec.2005.02.094.
[63] D. T. Quinto, “Twenty-Five Years of Pvd Coatings At the Cutting Edge,” *News Bull. A Publ. Vac. Coat. Ind.*, vol. 5, no. 20, pp. 17–22, 2007.
[64] D. G. Bhat, “Chemical vapor deposition,” *Coatings Technol. Fundam. Testing, Process. Tech.*, pp. 36-1-36–11, 2006.
[65] I. Y. Konyashin, “PVD/CVD technology for coating cemented carbides,” *Surf. Coatings Technol.*, vol. 71, no. 3, pp. 277–283, 1995, doi: 10.1016/0257-8972(94)02325-K.
[66] B. Warcholinski and A. Gilewicz, “Tribological properties of CrN x coatings,” vol. 37, no. 2, pp. 498–504, 2009.
[67] A. Lippitz, T. Hübert, and T. Hu, “XPS investigations of chromium nitride thin films,” *Surf. Coatings Technol.*, vol. 200, no. 1-4 SPEC. ISS., pp. 250–253, 2005, doi: 10.1016/j.surfcoat.2005.02.091.
[68] S. Grasser, R. Daniel, and C. Mitterer, “Microstructure modifications of CrN coatings by pulsed bias sputtering,” *Surf. Coatings Technol.*, vol. 206, no. 22, pp. 4666–4671, 2012, doi: 10.1016/j.surfcoat.2012.05.043.
[69] M. Wen *et al.*, “Nanoindentation of coatings,” *Surf. Coatings Technol.*, vol. 7, no. 2, pp. 204–213, 2017, doi: 10.1149/1.2192734.
[70] K. Bouzid *et al.*, “Wear and Corrosion Resistance of CrN-based Coatings Deposited by R . F Magnetron Sputtering To cite this version : HAL Id : hal-01202851 Science Arts & Métiers (SAM),” 2017.
[71] W. Münz, “Titanium aluminum nitride films: A new alternative to TiN coatings,” *J. Vac. Sci. Technol. A Vacuum, Surfaces, Film.*, vol. 4, no. 6, pp. 2717–2725, 1986, doi: 10.1116/1.573713.
[72] Y. P. Feng, L. Zhang, R. X. Ke, Q. L. Wan, Z. Wang, and Z. H. Lu, “Thermal stability and oxidation behavior of AlTiN, AlCrN and AlCrSiWN coatings,” *Int. J. Refract. Met. Hard Mater.*, vol. 43, pp. 241–249, 2014, doi: 10.1016/j.ijrmhm.2013.11.018.
[73] G. S. Fox-Rabinovich *et al.*, “Design and performance of AlTiN and TiAlCrN PVD coatings for machining of hard to cut materials,” *Surf. Coatings Technol.*, vol. 204, no. 4, pp. 489–496, 2009, doi: 10.1016/j.surfcoat.2009.08.021.
[74] Q. X. Fan *et al.*, “Microstructure and corrosion resistance of the AlTiN coating deposited by arc ion plating,” *Acta Metall. Sin. (English Lett.*, vol. 29, no. 12, pp. 1119–1126, 2016, doi: 10.1007/s40195-016-0497-8.
[75] Y. H. Chen *et al.*, “Effects of decomposition route and microstructure on h-AlN formation rate in TiCrAlN alloys,” *J. Alloys Compd.*, vol. 691, pp. 1024–1032, 2017, doi: 10.1016/j.jallcom.2016.08.299.
[76] L. Chen and Y. X. Xu, “Influence of interfacial structure on the mechanical and thermal properties of CrAlN/ZrN multilayer coatings,” *Mater. Des.*, vol. 106, pp. 1–5, 2016, doi: 10.1016/j.matdes.2016.05.082.
[77] A. Liu, J. Deng, H. Cui, Y. Chen, and J. Zhao, “Friction and wear properties of TiN, TiAlN, AlTiN and CrAlN PVD nitride coatings,” *Int. J. Refract. Met. Hard Mater.*, vol. 31, pp. 82–88, 2012, doi: 10.1016/j.ijrmhm.2011.09.010.
[78] H. C. Barshilia, N. Selvakumar, B. Deepthi, and K. S. Rajam, “A comparative study of reactive direct

current magnetron sputtered CrAlN and CrN coatings," *Surf. Coatings Technol.*, vol. 201, no. 6, pp. 2193–2201, 2006, doi: 10.1016/j.surfcoat.2006.03.037.
[79] A. Krella, "Resistance of PVD coatings to erosive and wear processes: A review," *Coatings*, vol. 10, no. 10, 2020, doi: 10.3390/COATINGS10100921.
[80] S. J. Bull, D. G. Bhat, and M. H. Staia, "Properties and performance of commercial TiCN coatings. Part 2: Tribological performance," *Surf. Coatings Technol.*, vol. 163–164, pp. 507–514, 2003, doi: 10.1016/S0257-8972(02)00651-5.
[81] M. Gassner, N. Schalk, M. Tkadletz, M. Pohler, C. Czettl, and C. Mitterer, "Influence of cutting speed and workpiece material on the wear mechanisms of CVD TiCN/A-Al2O3 coated cutting inserts during turning," *Wear*, vol. 398–399, no. June 2017, pp. 90–98, 2018, doi: 10.1016/j.wear.2017.11.019.
[82] D. Stiens, T. ; Manns, and S. Ruppi, "Coated cutting tool insert with MT-CVD TiCN on TiAI(C,N)," 2016
[83] X. Meng-Burany and A. T. Alpas, "FIB and TEM studies of damage mechanisms in DLC coatings sliding against aluminum," *Thin Solid Films*, vol. 516, no. 2, pp. 325–335, 2007, doi: https://doi.org/10.1016/j.tsf.2007.06.038.
[84] V. F. C. Sousa, J. Castanheira, F. J. G. Silva, J. S. Fecheira, G. Pinto, and A. Baptista, "Wear behavior of uncoated and coated tools in milling operations of ampco (Cu-be) alloy," *Appl. Sci.*, vol. 11, no. 16, 2021, doi: 10.3390/app11167762.
[85] L. Ward, F. Junge, A. Lampka, M. Dobbertin, C. Mewes, and M. Wienecke, "The effect of bias voltage and gas pressure on the structure, adhesion and wear behavior of diamond like carbon (DLC) Coatings with Si interlayers," *Coatings*, vol. 4, no. 2, pp. 214–230, 2014, doi: 10.3390/coatings4020214.
[86] J. V. C. Souza, M. C. A. Nono, J. P. B. Machado, O. M. M. Silva, F. C. L. Melo, and M. V. Ribeiro, "Cutting performance of diamond coated Si3N4 tool during turning," *Mater. Sci. Forum*, vol. 660–661, no. April 2014, pp. 106–111, 2010, doi: 10.4028/www.scientific.net/MSF.660-661.106.
[87] R. P. Martinho, F. J. G. Silva, and A. P. M. Baptista, "Cutting forces and wear analysis of Si3N4 diamond coated tools in high speed machining," *Vacuum*, vol. 82, no. 12, pp. 1415–1420, 2008, doi: 10.1016/j.vacuum.2008.03.065.
[88] N. Shulumba *et al.*, "Temperature-dependent elastic properties of Ti1-xAlxN alloys," *Appl. Phys. Lett.*, vol. 107, no. 23, 2015, doi: 10.1063/1.4936896.
[89] K. M. Calamba *et al.*, "Enhanced thermal stability and mechanical properties of nitrogen deficient titanium aluminum nitride (Ti0.54Al0.46Ny) thin films by tuning the applied negative bias voltage," *J. Appl. Phys.*, vol. 122, no. 6, pp. 0–10, 2017, doi: 10.1063/1.4986350.
[90] H. Lind *et al.*, "Improving thermal stability of hard coating films via a concept of multicomponent alloying," *Appl. Phys. Lett.*, vol. 99, no. 9, pp. 2011–2014, 2011, doi: 10.1063/1.3631672.
[91] Y. C. Chim, X. Z. Ding, X. T. Zeng, and S. Zhang, "Oxidation resistance of TiN, CrN, TiAlN and CrAlN coatings deposited by lateral rotating cathode arc," *Thin Solid Films*, vol. 517, no. 17, pp. 4845–4849, 2009, doi: 10.1016/j.tsf.2009.03.038.
[92] A. A. Vereschaka, S. N. Grigoriev, A. S. Vereschaka, A. Y. Popov, and A. D. Batako, "Nano-scale multilayered composite coatings for cutting tools operating under heavy cutting conditions," *Procedia CIRP*, vol. 14, pp. 239–244, 2014, doi: 10.1016/j.procir.2014.03.070.
[93] V. P. Tabakov, A. S. Vereschaka, and A. A. Vereschaka, "Multilayer composition coatings for cutting tools: formation and performance properties," *Mech. Ind.*, vol. 18, no. 7, p. 706, 2018, doi: 10.1051/meca/2017063.
[94] A. A. Vereschaka *et al.*, "Nano-scale multi-layered coatings for improved efficiency of ceramic cutting tools," *Int. J. Adv. Manuf. Technol.*, vol. 90, no. 1–4, pp. 27–43, 2017, doi: 10.1007/s00170-016-9353-2.
[95] O. V. Maksakova *et al.*, "Nanoscale architecture of (CrN/ZrN)/(Cr/Zr) nanocomposite coatings: Microstructure, composition, mechanical properties and first-principles calculations," *J. Alloys Compd.*, vol. 831, 2020, doi: 10.1016/j.jallcom.2020.154808.
[96] B. O. Postolnyi *et al.*, "Multilayer design of CrN / MoN protective coatings for enhanced hardness and toughness," *J. Alloys Compd.*, vol. 725, pp. 1188–1198, 2017, doi: 10.1016/j.jallcom.2017.07.010.
[97] A. Pogrebnjak, K. Smyrnova, and O. Bondar, "Nanocomposite multilayer binary nitride coatings based on transition and refractory metals: Structure and properties," *Coatings*, vol. 9, no. 3, 2019, doi: 10.3390/coatings9030155.
[98] R. Hahn, M. Bartosik, R. Soler, C. Kirchlechner, G. Dehm, and P. H. Mayrhofer, "Superlattice effect for enhanced fracture toughness of hard coatings," *Scr. Mater.*, vol. 124, pp. 67–70, 2016, doi: 10.1016/j.scriptamat.2016.06.030.
[99] A. Azizpour, R. Hahn, F. edo. F. F. Klimashin, T. T. omas. Wojcik, E. Poursaeidi, and P. H. Mayrhofer, "Deformation and Cracking Mechanism in CrN/TiN Multilayer Coatings," *Coatings*, vol. 9, no. 363, pp. 1–17, 2019, doi: doi:10.3390/coatings9060363.
[100] E. J. Herrera-Jimenez, A. Raveh, T. Schmitt, E. Bousser, J. E. Klemberg-Sapieha, and L. Martinu, "Solid solution hardening in nanolaminate ZrN-TiN coatings with enhanced wear resistance," *Thin Solid Films*, vol. 688, no. April, p. 137431, 2019, doi: 10.1016/j.tsf.2019.137431.
[101] C. Shi, C.M.; Wang, T.G.; Pei, Z.L.; Gong, J., Sun, "Microstructure, Interface, and Properties of Multilayered CrN/Cr2O3 Coatings Prepared by Arc Ion Plating," *J. Mater. Sci. Technol.*, vol. 30, no. 12, pp. 1193–1201, 2014.
[102] P. E. Hovsepian and A. P. Ehiasarian, "Six strategies to produce application tailored nanoscale multilayer

structured PVD coatings by conventional and High Power Impulse Magnetron Sputtering (HIPIMS)," *Thin Solid Films*, vol. 688, no. April, 2019, doi: 10.1016/j.tsf.2019.137409.
[103] M. Khadem, O. V. Penkov, H. K. Yang, and D. E. Kim, "Tribology of multilayer coatings for wear reduction: A review," *Friction*, vol. 5, no. 3, pp. 248–262, 2017, doi: 10.1007/s40544-017-0181-7.
[104] D. Pinheiro, M. T. Vieira, and M. A. Djouadi, "Advantages of depositing multilayer coatings for cutting wood-based products," *Surf. Coatings Technol.*, vol. 203, no. 20–21, pp. 3197–3205, 2009, doi: 10.1016/j.surfcoat.2009.03.052.
[105] E. Contreras Romero, J. Cortínez Osorio, R. Talamantes Soto, A. Hurtado Macías, and M. Gómez Botero, "Microstructure, mechanical and tribological performance of nanostructured TiAlTaN-(TiAlN/TaN)n coatings: Understanding the effect of quaternary/multilayer volume fraction," *Surf. Coatings Technol.*, vol. 377, no. April, p. 124875, 2019, doi: 10.1016/j.surfcoat.2019.07.086.
[106] D. Kovar, M. D. Thouless, and J. W. Halloran, "Crack Deflection and Propagation in Layered Silicon Nitride/Boron Nitride Ceramics," *J. Am. Ceram. Soc.*, vol. 81, no. 4, pp. 1004–1112, 2005, doi: 10.1111/j.1151-2916.1998.tb02438.x.
[107] A. Vereschaka *et al.*, "Development of a model of crack propagation in multilayer hard coatings under conditions of stochastic force impact," *Materials (Basel).*, vol. 14, no. 2, pp. 1–20, 2021, doi: 10.3390/ma14020260.
[108] J. Lin, J. J. Moore, B. Mishra, M. Pinkas, and W. D. Sproul, "Nano-structured CrN/AlN multilayer coatings synthesized by pulsed closed field unbalanced magnetron sputtering," *Surf. Coatings Technol.*, vol. 204, no. 6–7, pp. 936–940, 2009, doi: 10.1016/j.surfcoat.2009.04.013.
[109] D. D. Kumar, N. Kumar, S. Kalaiselvam, S. Dash, and R. Jayavel, "Wear resistant super-hard multilayer transition metal-nitride coatings," *Surfaces and Interfaces*, vol. 7, no. March, pp. 74–82, 2017, doi: 10.1016/j.surfin.2017.03.001.
[110] A. D. Pogrebnjak *et al.*, "Superhard CrN/MoN coatings with multilayer architecture," *Mater. Des.*, vol. 153, no. 2017, pp. 47–59, 2018, doi: 10.1016/j.matdes.2018.05.001.
[111] S. Zhang, L. Wang, Q. Wang, and M. Li, "A superhard CrAlSiN superlattice coating deposited by a multi-arc ion plating: II. Thermal stability and oxidation resistance," *Surf. Coatings Technol.*, vol. 214, pp. 160–167, 2013, doi: 10.1016/j.surfcoat.2012.05.144.
[112] M. Fenker, M. Balzer, and H. Kappl, "Corrosion protection with hard coatings on steel: Past approaches and current research efforts," *Surf. Coatings Technol.*, vol. 257, pp. 182–205, 2014, doi: 10.1016/j.surfcoat.2014.08.069.
[113] M. Danek, F. Fernandes, A. Cavaleiro, and T. Polcar, "Influence of Cr additions on the structure and oxidation resistance of multilayered TiAlCrN films," *Surf. Coatings Technol.*, vol. 313, pp. 158–167, 2017, doi: 10.1016/j.surfcoat.2017.01.053.
[114] H. Olia, R. Ebrahimi-Kahrizsangi, F. Ashrafizadeh, and I. Ebrahimzadeh, "Corrosion study of TiN, TiAlN and CrN multilayer coatings deposit on martensitic stainless steel by arc cathodic physical vapour deposition," *Mater. Res. Express*, vol. 6, no. 4, p. 2022, 2019, doi: 10.1088/2053-1591/aaff11.
[115] C. Gaona-Tiburcio *et al.*, "Corrosion resistance of multilayer coatings deposited by PVD on Inconel 718 using electrochemical impedance spectroscopy technique," *Coatings*, vol. 10, no. 6, pp. 1–11, 2020, doi: 10.3390/COATINGS10060521.
[116] E. Lotfi-khojasteh, M. Sahebazamani, H. Elmkhah, M. Nouri, O. Imantalab, and A. Fattah-alhosseini, "A study of the electrochemical and tribological properties of TiN/CrN nano-layer coating deposited on carburized-H13 hot-work steel by Arc-PVD technique," *J. Asian Ceram. Soc.*, vol. 9, no. 1, pp. 247–259, 2021, doi: 10.1080/21870764.2020.1863577.
[117] P. M. Samim, A. Fattah-alhosseini, H. Elmkhah, O. Imantalab, and M. Nouri, "A study on comparing surface characterization and electrochemical properties of single-layer CrN coating with nanostructured multilayer ZrN/CrN coating in 3.5 wt.% NaCl solution," *Surfaces and Interfaces*, vol. 21, no. September, 2020, doi: 10.1016/j.surfin.2020.100721.
[118] W. Darmawan, H. Usuki, I. S. Rahayu, C. Gottlober, and R. Marchal, "Wear characteristics of multilayer-coated cutting tools when milling particleboard," *For. Prod. J.*, vol. 60, no. 7–8, pp. 615–621, 2010, doi: 10.13073/0015-7473-60.7.615.
[119] H. Winkelmann, E. Badisch, M. Roy, and H. Danninger, "Corrosion mechanisms in the wood industry, especially caused by tannins," *Mater. Corros.*, vol. 60, no. 1, pp. 40–48, 2009, doi: 10.1002/maco.200805016.
[120] J. Chladil, J. Sedlák, E. R. Šebelov, M. Kučera, and M. Dado, "Cutting conditions and tool wear when machining wood-based materials," *BioResources*, vol. 14, no. 2, pp. 3495–3505, 2019, doi: 10.15376/biores.14.2.3495-3505.
[121] J. Keckes *et al.*, "Cell-wall recovery after irreversible deformation of wood," *Nat. Mater.*, vol. 2, no. 12, pp. 810–814, 2003, doi: 10.1038/nmat1019.
[122] D. Kretschmann, "Velcro mechanics in wood," *Nat. Mater.*, vol. 2, no. 12, pp. 775–776, 2003, doi: 10.1038/nmat1025.
[123] B. Thibaut *et al.*, "Wood machining with a focus on French research in the last 50 years," *Ann. For. Sci.*, vol. 73, no. 1, pp. 163–184, 2016, doi: 10.1007/s13595-015-0460-2.
[124] B. Warcholinski, A. Gilewicz, and J. Ratajski, "Cr2N/CrN multilayer coatings for wood machining tools,"

Tribol. Int., vol. 44, no. 9, pp. 1076–1082, 2011, doi: 10.1016/j.triboint.2011.05.004.
[125] B. P. Nedic´ and M. D. Eric´, "Cutting temperature measurement and material machinability," *Therm. Sci.*, vol. 18, no. March 2016, pp. S259–S268, 2014, doi: 10.2298/TSCI120719003N.
[126] M. Merhar, "Influence of Temperature Distribution on Circular Saw Blade Natural Frequencies during Cutting," *BioResources*, vol. 16, no. 1, pp. 1076–1090, 2021, doi: 10.15376/biores.16.1.1076-1090.
[127] M. Gauvent, E. Rocca, P. J. Meausoone, and P. Brenot, "Corrosion of materials used as cutting tools of wood," *Wear*, vol. 261, no. 9, pp. 1051–1055, 2006, doi: 10.1016/j.wear.2006.03.036.
[128] W. Wei *et al.*, "The research progress of machining mechanisms in milling wood-based materials," *BioResources*, vol. 13, no. 1, pp. 2139–2149, 2018, doi: 10.15376/biores.13.1.Wei.
[129] X. Li, S. Wang, G. Du, Z. Wu, and Y. Gong, "Manufacturing particleboard using hemp shiv and wood particles with low free formaldehyde emission urea-formaldehyde resin," *For. Prod. J.*, vol. 64, no. 5–6, pp. 187–191, 2014, doi: 10.13073/FPJ-D-13-00073.
[130] D. Kazlauskas, V. Jankauskas, R. Kreivaitis, and S. Tučkutė, "Wear behaviour of PVD coating strengthened WC-Co cutters during milling of oak-wood," *Wear*, vol. 498–499, no. March, 2022, doi: 10.1016/j.wear.2022.204336.
[131] P. K. Katiyar, "A comprehensive review on synergy effect between corrosion and wear of cemented tungsten carbide tool bits: A mechanistic approach," *Int. J. Refract. Met. Hard Mater.*, vol. 92, no. May, p. 105315, 2020, doi: 10.1016/j.ijrmhm.2020.105315.
[132] P. K. Katiyar and N. S. Randhawa, "Corrosion behavior of WC-Co tool bits in simulated (concrete, soil, and mine) solutions with and without chloride additions," *Int. J. Refract. Met. Hard Mater.*, vol. 85, no. August, p. 105062, 2019, doi: 10.1016/j.ijrmhm.2019.105062.
[133] A. M. F. Rocha *et al.*, "Corrosion behaviour of WC hardmetals with nickel-based binders," *Corros. Sci.*, vol. 147, no. November 2018, pp. 384–393, 2019, doi: 10.1016/j.corsci.2018.11.015.
[134] J. P. . Costes and P. . Larricq, "Towards high cutting speed in wood-milling," *Ann. For. Sci.*, vol. 59, pp. 857–865, 2002, doi: 10.1051/forest.
[135] J. Ratajski *et al.*, "Hard coatings for woodworking tools - a review," *J. Achievments Mater. Manuf. Eng.*, vol. 37, no. 2, pp. 668–674, 2009.
[136] G. Keturakis and V. Lisauskas, "Influence of the sharpness angle on the initial wear of the wood milling knives," *Medziagotyra*, vol. 16, no. 3, pp. 205–209, 2010.
[137] J. Y. Sheikh-Ahmad, "High-temperature wear of cemented tungsten carbide tools while machining particleboard and fiberboard," *J. Wood Sci.*, vol. 45, no. 6, pp. 445–455, 1999, doi: 10.1007/BF00538952.
[138] A. Gilewicz, B. Warcholinski, P. Myslinski, and W. Szymanski, "Anti-wear multilayer coatings based on chromium nitride for wood machining tools," *Wear*, vol. 270, no. 1–2, pp. 32–38, 2010, doi: 10.1016/j.wear.2010.09.002.
[139] A. Gilewicz and B. Warcholinski, "Tribological properties of CrCN/CrN multilayer coatings," *Tribol. Int.*, vol. 80, pp. 34–40, 2014, doi: 10.1016/j.triboint.2014.06.012.
[140] O. Y. Piskunova *et al.*, "Protective Woodcutting Tool Coatings," *Acta Univ. Agric. Silvic. Mendelianae Brun.*, vol. 64, no. 3, pp. 835–839, 2016, doi: 10.11118/actaun201664030835.
[141] M. A. . Djouadi, C. Nouveau, P. . Beer, and M. Lambertin, "CrxNy hard coatings deposited with PVD method on tools for wood machining," *Surf. Coatings Technol.*, vol. 133–134, pp. 478–483, 2000, doi: 10.1016/S0257-8972(00)00980-4.
[142] K. Nadolny *et al.*, "Moving towards sustainable manufacturing by extending the tool life of the pine wood planing process using the AlCrBN coating," *Sustain. Mater. Technol.*, vol. 28, 2021, doi: 10.1016/j.susmat.2021.e00259.
[143] P. Czarniak, K. Szymanowski, P. Panjan, and J. Górski, "Initial Study of the Effect of Some PVD Coatings ('TiN/AlTiN' and 'TiAlN/a-C:N') on the Wear Resistance of Wood Drilling Tools," *Forests*, vol. 13, no. 2, 2022, doi: 10.3390/f13020286.
[144] J. A. . Thornton, "Magnetron Sputtering: basic physics and application to cylindrical magnetrons," *J. Vac. Sci. Technol.*, vol. 15, no. 2, pp. 171–177, 1978.
[145] F. H. W. . Löffler, "Formation of non-equilibrium phases in PVD process," *Vacuum*, vol. 43, no. 5–7, pp. 397–402, 1992.
[146] M. J. Mehl, D. Finkenstadt, C. Dane, G. L. W. Hart, and S. Curtarolo, "Finding the stable structures of N1-xWx with an ab initio high-throughput approach," *Phys. Rev. B - Condens. Matter Mater. Phys.*, vol. 91, no. 18, pp. 1–19, 2015, doi: 10.1103/PhysRevB.91.184110.
[147] K. Balasubramanian, L. Huang, and D. Gall, "Phase stability and mechanical properties of Mo1-xNx with 0 ≤ × ≤ 1," *J. Appl. Phys.*, vol. 122, no. 19, pp. 1–12, 2017, doi: 10.1063/1.4998686.
[148] P. J. Kelly and R. D. Arnell, "Magnetron sputtering: A review of recent developments and applications," *Vacuum*, vol. 56, no. 3, pp. 159–172, 2000, doi: 10.1016/S0042-207X(99)00189-X.
[149] J. A. Thornton, "Influence Of Substrate Temperature And Deposition Rate On Structure Of Thick Souttered Cu Coatings.," *J Vac Sci Technol*, vol. 12, no. 4, pp. 830–835, 1975, doi: 10.1116/1.568682.
[150] J. E. Greene, "Review Article: Tracing the recorded history of thin-film sputter deposition: From the 1800s to 2017," *J. Vac. Sci. Technol. A Vacuum, Surfaces, Film.*, vol. 35, no. 5, p. 05C204, 2017, doi: 10.1116/1.4998940.
[151] A. Anders, "Physics of arcing, and implications to sputter deposition," *Thin Solid Films*, vol. 502, no. 1–2,

pp. 22–28, 2006, doi: 10.1016/j.tsf.2005.07.228.
[152] W. D. Sproul, D. J. Christie, and D. C. Carter, “Control of reactive sputtering processes,” *Thin Solid Films*, vol. 491, no. 1–2, pp. 1–17, 2005, doi: 10.1016/j.tsf.2005.05.022.
[153] K. Sarakinos, J. Alami, and S. Konstantinidis, “High power pulsed magnetron sputtering: A review on scientific and engineering state of the art,” *Surf. Coatings Technol.*, vol. 204, no. 11, pp. 1661–1684, 2010, doi: 10.1016/j.surfcoat.2009.11.013.
[154] V. Kouznetsov, K. MacÁk, J. M. Schneider, U. Helmersson, and I. Petrov, “A novel pulsed magnetron sputter technique utilizing very high target power densities,” *Surf. Coatings Technol.*, vol. 122, no. 2–3, pp. 290–293, 1999, doi: 10.1016/S0257-8972(99)00292-3.
[155] A. Anders, “A review comparing cathodic arcs and high power impulse magnetron sputtering (HiPIMS),” *Surf. Coatings Technol.*, vol. 257, pp. 308–325, 2014, doi: 10.1016/j.surfcoat.2014.08.043.
[156] A. Nyaiesh and L. Holland, “The dependence of deposition rate on power input for dc and rf magnetron sputtering,” *Vacuum*, vol. 31, no. 7, pp. 315–317, 1981, doi: 10.1016/S0042-207X(81)80503-9.
[157] T. P. Drüsedau, T. Bock, T.-M. John, F. Klabunde, and W. Eckstein, “Energy transfer into the growing film during sputter deposition: An investigation by calorimetric measurements and Monte Carlo simulations,” *J. Vac. Sci. Technol. A Vacuum, Surfaces, Film.*, vol. 17, no. 5, pp. 2896–2905, 1999, doi: 10.1116/1.581957.
[158] C. Priestland and S. D. Hersee, “The effects of pressure on the deposition rate in rf sputtering processes,” *Vacuum*, vol. 22, no. 3, pp. 103–106, 1972, doi: 10.1016/0042-207X(72)90468-X.
[159] H. Kersten, H. Deutsch, H. Steffen, G. M. W. Kroesen, and R. Hippler, “The energy balance at substrate surfaces during plasma processing,” *Vacuum*, vol. 63, no. 3, pp. 385–431, 2001, doi: 10.1016/S0042-207X(01)00350-5.
[160] S. Gauter, F. Haase, and H. Kersten, “Experimentally unraveling the energy flux originating from a DC magnetron sputtering source,” *Thin Solid Films*, vol. 669, no. May 2018, pp. 8–18, 2019, doi: 10.1016/j.tsf.2018.10.021.
[161] J. R. Woodworth, M. E. Riley, D. C. Meister, B. P. Aragon, M. S. Le, and H. H. Sawin, “Ion energy and angular distributions in inductively coupled radio frequency discharges in argon,” *J. Appl. Phys.*, vol. 80, no. 3, pp. 1304–1311, 1996, doi: 10.1063/1.362977.
[162] J. Pelleg, L. Z. Zevin, and S. Lungo, “Reactive-sputter-deposited TiN films on glass substrates,” *Thin Solid Films*, vol. 197, pp. 117–128, 1991.
[163] J. Lin, W. D. Sproul, J. J. Moore, Z. L. Wu, and S. L. Lee, “Effect of negative substrate bias voltage on the structure and properties of CrN films deposited by modulated pulsed power (MPP) magnetron sputtering,” *J. Phys. D. Appl. Phys.*, vol. 44, no. 42, 2011, doi: 10.1088/0022-3727/44/42/425305.
[164] F. Cai, Y. Gao, W. Fang, T. Mao, S. Zhang, and Q. Wang, “Improved adhesion and cutting performance of AlTiSiN coatings by tuning substrate bias voltage combined with Ar ion cleaning pre-treatment,” *Ceram. Int.*, vol. 44, no. 15, pp. 18894–18902, 2018, doi: 10.1016/j.ceramint.2018.07.125.
[165] Q. Kong *et al.*, “Influence of substrate bias voltage on the microstructure and residual stress of CrN films deposited by medium frequency magnetron sputtering,” *Mater. Sci. Eng. B Solid-State Mater. Adv. Technol.*, vol. 176, no. 11, pp. 850–854, 2011, doi: 10.1016/j.mseb.2011.04.015.
[166] J. A. Thornton, “Substrate heating in cylindrical magnetron sputtering,” *Thin Solid Films*, vol. 54, no. 1, pp. 23–31, 1978.
[167] J. L. Thornton, John A.; Lamb, “Substrate heating rate for planar and cylindrical-post magnetron sputtering sources,” *Thin Solid Films*, vol. 119, pp. 87–95, 1984.
[168] S. C. Liang *et al.*, “Effects of substrate temperature on the structure and mechanical properties of (TiVCrZrHf)N coatings,” *Appl. Surf. Sci.*, vol. 257, no. 17, pp. 7709–7713, 2011, doi: 10.1016/j.apsusc.2011.04.014.
[169] E. S. Ameh, “A review of basic crystallography and x-ray diffraction applications,” *Int. J. Adv. Manuf. Technol.*, vol. 105, no. 7–8, pp. 3289–3302, 2019, doi: 10.1007/s00170-019-04508-1.
[170] M. Etter and R. E. Dinnebier, “A century of powder diffraction: A brief history,” *Zeitschrift fur Anorg. und Allg. Chemie*, vol. 640, no. 15, pp. 3015–3028, 2014, doi: 10.1002/zaac.201400526.
[171] J. M. Thomas, “The birth of X-ray crystallography,” *Nature*, vol. 491, pp. 186–187, 2012.
[172] R. E. Dinnebier, K. Friese, and M. Solid, “Modern X-Ray Methods in Mineralogy,” *Stress Int. J. Biol. Stress*, pp. 1–57, 2000.
[173] B. D. . Cullity, *Elements of X-RAY Diffraction*, Second. Addison-Wesley, 1978.
[174] A. Chauhan, “Powder XRD Technique and its Applications in Science and Technology,” *J. Anal. Bioanal. Tech.*, vol. 5, no. 6, 2014, doi: 10.4172/2155-9872.1000212.
[175] R. Delhez, T. H. De Keijse, and E. J. Mittemeijer, “Role of x-ray diffraction analysis in surface engineering: Investigation of microstructure of nitrided iron and steels,” *Surf. Eng.*, vol. 3, no. 4, pp. 331–342, 1987, doi: 10.1179/sur.1987.3.4.331.
[176] L. Velterop, R. Delhez, T. H. De Keijser, E. J. Mittemeijer, and D. Reefman, “X-ray diffraction analysis of stacking and twin faults in f.c.c. metals: A revision and allowance for texture and non-uniform fault probabilities,” *J. Appl. Crystallogr.*, vol. 33, no. 2, pp. 296–306, 2000, doi: 10.1107/S0021889800000133.
[177] R. A. Butera and D. H. Waldeck, “X-ray diffraction investigation of alloys,” *J. Chem. Educ.*, vol. 74, no. 1, pp. 115–119, 1997, doi: 10.1021/ed074p115.
[178] P. Gogola, Z. Gabalcová, H. Suchánek, M. Babinec, M. Bonek, and M. Kusý, “Quantitative X-ray

diffraction analysis of Zn-Al based alloys," *Arch. Metall. Mater.*, vol. 65, no. 2, pp. 959–966, 2020, doi: 10.24425/amm.2020.132844.
[179] H. H. W. Stanjek, "Basics of X-Ray Diffraction," *Hyperfine Interact.*, vol. 154, pp. 107–119, 2004.
[180] J.-P. Zhang, P.-Q. Liao, H.-L. Zhou, R.-B. Lin, and X.-M. Chen, "Single-crystal X-ray diffraction studies on structural transformations of porous coordination polymers," *Chem. Soc. Rev.*, vol. 43, no. 16, pp. 5789–5914, 2014, doi: 10.1039/x0xx00000x.
[181] M. Spiliopoulou *et al.*, "Applications of X-ray Powder Diffraction in Protein Crystallography and Drug Screening," *Crystals*, vol. 10, no. 2, 2020, doi: 10.3390/cryst10020054.
[182] B. Lavina, P. Dera, and R. T. Downs, "Modern X-ray diffraction methods in mineralogy and geosciences," *Spectrosc. Methods Mineral. Mater. Sci.*, vol. 78, pp. 1–31, 2014, doi: 10.2138/rmg.2014.78.1.
[183] A. A. Bunaciu, E. gabriela Udriştioiu, and H. Y. Aboul-Enein, "X-Ray Diffraction: Instrumentation and Applications," *Crit. Rev. Anal. Chem.*, vol. 45, no. 4, pp. 289–299, 2015, doi: 10.1080/10408347.2014.949616.
[184] L. B. Mccusker, R. B. Von Dreele, D. E. Cox, D. Louër, and P. Scardi, "Rietveld refinement guidelines," *J. Appl. Crystallogr.*, vol. 32, no. 1, pp. 36–50, 1999, doi: 10.1107/S0021889898009856.
[185] J. S. O. Evans and I. R. Evans, "Structure Analysis from Powder Diffraction Data: Rietveld Refinement in Excel," *J. Chem. Educ.*, vol. 98, no. 2, pp. 495–505, 2021, doi: 10.1021/acs.jchemed.0c01016.
[186] H. M. Rietveld, "Line profiles of neutron powder-diffraction peaks for structure refinement," *Acta Crystallogr.*, vol. 22, no. 1, pp. 151–152, 1967, doi: 10.1107/s0365110x67000234.
[187] A. L. . Patterson, "The Scherrer Formula for X-Ray Particle Size Determination," *Phys. Rev.*, vol. 56, pp. 978–982, 1939.
[188] J. I. Langford and A. J. C. Wilson, "Scherrer after sixty years: A survey and some new results in the determination of crystallite size," *J. Appl. Crystallogr.*, vol. 11, no. 2, pp. 102–113, 1978, doi: 10.1107/s0021889878012844.
[189] V. Uvarov and I. . Popov, "Metrological Characterization of X- ray Diffraction Methods for Nanocrystallite Size Determination Related papers," *Mater. Charact.*, vol. 58, pp. 883–891, 2007.
[190] U. Holzwarth and N. Gibson, "The Scherrer equation versus the 'Debye-Scherrer equation'," *Nat. Publ. Gr.*, vol. 6, no. 9, p. 534, 2011, [Online]. Available: http://www.nature.com/doifinder/10.1038/nnano.2011.145%5Cnpapers2://publication/doi/10.1038/nnano.2011.145
[191] A. Monshi, M. R. Foroughi, and M. R. Monshi, "Modified Scherrer Equation to Estimate More Accurately Nano-Crystallite Size Using XRD," *World J. Nano Sci. Eng.*, vol. 02, no. 03, pp. 154–160, 2012, doi: 10.4236/wjnse.2012.23020.
[192] Y. W. Lin, J. H. Huang, W. J. Cheng, and G. P. Yu, "Effect of Ti interlayer on mechanical properties of TiZrN coatings on D2 steel," *Surf. Coatings Technol.*, vol. 350, no. April, pp. 745–754, 2018, doi: 10.1016/j.surfcoat.2018.04.077.
[193] M. Nespolo, M. I. Aroyo, and B. Souvignier, "Crystallographic shelves: Space-group hierarchy explained," *J. Appl. Crystallogr.*, vol. 51, no. 5, pp. 1481–1491, 2018, doi: 10.1107/S1600576718012724.
[194] C. Méndez, J. M. Podestá, S. Toro, A. E. Huespe, and J. Oliver, "Making use of symmetries in the three-dimensional elastic inverse homogenization problem," *Int. J. Multiscale Comput. Eng.*, vol. 17, no. 3, pp. 261–280, 2019, doi: 10.1615/IntJMultCompEng.2019029111.
[195] J. S. Tse, "A chemical perspective on high pressure crystal structures and properties," *Natl. Sci. Rev.*, vol. 7, no. 1, pp. 149–169, 2020, doi: 10.1093/nsr/nwz144.
[196] D. Gentili, M. Gazzano, M. Melucci, D. Jones, and M. Cavallini, "Polymorphism as an additional functionality of materials for technological applications at surfaces and interfaces," *Chem. Soc. Rev.*, vol. 48, no. 9, pp. 2502–2517, 2019, doi: 10.1039/c8cs00283e.
[197] M. Giulietti, M. M. Seckler, S. Derenzo, M. I. Ré, and E. Cekinski, "Industrial crystallization and precipitation from solutions: State of the technique," *Brazilian J. Chem. Eng.*, vol. 18, no. 4, pp. 423–440, 2001, doi: 10.1590/S0104-66322001000400007.
[198] D. Nguyen-Trong, K. Pham-Huu, and P. Nguyen-Tri, "Simulation on the Factors Affecting the Crystallization Process of FeNi Alloy by Molecular Dynamics," *ACS Omega*, vol. 4, no. 11, pp. 14605–14612, 2019, doi: 10.1021/acsomega.9b02050.
[199] T. Ando, X. Li, S. Nakao, T. Kasai, M. Shikida, and K. Sato, "Effect of crystal orientation on fracture strength and fracture toughness of single crystal silicon," *Proc. IEEE Int. Conf. Micro Electro Mech. Syst.*, pp. 177–180, 2004, doi: 10.1109/MEMSYS.2003.1189715.
[200] E. Merson, R. Brydson, and A. Brown, "The effect of crystallographic orientation on the mechanical properties of titanium," *J. Phys. Conf. Ser.*, vol. 126, 2008, doi: 10.1088/1742-6596/126/1/012020.
[201] N. Waeselmann, "Structural Transformations in Complex Perovskite-Type Relaxor and Relaxor-Based Ferroelectrics at High Pressures and Temperatures," Universität Hamburg, 2012.
[202] D. Kriegner, Z. Matěj, R. Kužel, and V. Holý, "Powder diffraction in bragg-brentano geometry with straight linear detectors," *J. Appl. Crystallogr.*, vol. 48, no. 2005, pp. 613–618, 2015, doi: 10.1107/S1600576715003465.
[203] G. V. Fetisov, "X-ray diffraction methods for structural diagnostics of materials: progress and achievements," *Uspekhi Fiz. Nauk*, vol. 190, no. 01, pp. 2–36, 2020, doi: 10.3367/ufnr.2018.10.038435.

[204] C. F. Holder and R. E. Schaak, “Tutorial on Powder X-ray Diffraction for Characterizing Nanoscale Materials,” *ACS Nano*, vol. 13, no. 7, pp. 7359–7365, 2019, doi: 10.1021/acsnano.9b05157.
[205] W. Hume-Rothery, “On the bond lengths and interatomic distances in certain molecules and crystals,” *Proc. R. Soc. London. Ser. A. Math. Phys. Sci.*, vol. 197, no. 1048, pp. 17–27, 1949, doi: 10.1098/rspa.1949.0048.
[206] B. Nasiri-Tabrizi, “Thermal treatment effect on structural features of mechano-synthesized fluorapatite-titania nanocomposite: A comparative study,” *J. Adv. Ceram.*, vol. 3, no. 1, pp. 31–42, 2014, doi: 10.1007/s40145-014-0090-4.
[207] H. J. Bunge, “Influence of Texture on Powder Diffraction,” *Textures Microstruct.*, vol. 29, no. 1–2, pp. 1–26, 1997, doi: 10.1155/tsm.29.1.
[208] F. T. L. Muniz, M. A. R. Miranda, C. Morilla Dos Santos, and J. M. Sasaki, “The Scherrer equation and the dynamical theory of X-ray diffraction,” *Acta Crystallogr. Sect. A Found. Adv.*, vol. 72, no. 3, pp. 385–390, 2016, doi: 10.1107/S205327331600365X.
[209] I. C. . Noyan and J. B. . Cohen, *Residual Stress Measurement by Diffraction and Interpretation*, First. Springer-Verlag New York Inc., 1987.
[210] N. S. . S. Rossini, M. . Dassisti, K. Y. . Y. Benyounis, and A. G. . G. Olabi, “Methods of measuring residual stresses in components,” *Mater. Des.*, vol. 35, pp. 572–588, 2012, doi: 10.1016/j.matdes.2011.08.022.
[211] F. A. Kandil, J. D. Lord, A. T. Fry, and P. V Grant, “A Review of Residual Stress measurements methods - A guide to technique selection,” Teddington, MiddIsex, UK, 2001.
[212] P. S. Prevey, “X-Ray diffraction residual stress techniques,” 1986. doi: 10.31399/asm.hb.v10.a0001761.
[213] Q. Wang, F. Zhou, and J. Yan, “Evaluating mechanical properties and crack resistance of CrN, CrTiN, CrAlN and CrTiAlN coatings by nanoindentation and scratch tests,” *Surf. Coatings Technol.*, vol. 285, pp. 203–213, 2016, doi: 10.1016/j.surfcoat.2015.11.040.
[214] M. E. ; Fitzpatrick, A. T. . Fry, P. Holdway, J. . Shackleton, F. A. . Kandil, and L. . Suominen, “Determination of Residual Stresses by X-ray Diffraction,” 2005. doi: 10.1063/1.3525214.
[215] D. Delbergue *et al.*, “Comparison of Two X-Ray Residual Stress Measurement Methods : Sin2 ψ and Cos α , Through the Determination of a Martensitic Steel X-Ray Elastic Constant To cite this version : HAL Id : hal-01823988 Comparison of Two X-Ray Residual Stress Measurement Metho,” *Mater. Res.*, vol. 2, pp. 55–60, 2016.
[216] M. R. Ardigo, M. Ahmed, and A. Besnard, “Stoney formula: Investigation of curvature measurements by optical profilometer,” *Adv. Mater. Res.*, vol. 996, pp. 361–366, 2014, doi: 10.4028/www.scientific.net/AMR.996.361.
[217] K. T. Chen, J. H. Chang, and J. Y. Wu, “Modified Stoney’s Equation for Evaluation of Residual Stresses on Thin Film,” *Appl. Mech. Mater.*, vol. 789–790, pp. 25–32, 2015, doi: 10.4028/www.scientific.net/amm.789-790.25.
[218] J. Guo, H. Fu, B. Pan, and R. Kang, “Recent progress of residual stress measurement methods: A review,” *Chinese J. Aeronaut.*, vol. 34, no. 2, pp. 54–78, 2021, doi: 10.1016/j.cja.2019.10.010.
[219] A. M. Korsunsky, M. Sebastiani, and E. Bemporad, “Residual stress evaluation at the micrometer scale: Analysis of thin coatings by FIB milling and digital image correlation,” *Surf. Coatings Technol.*, vol. 205, no. 7, pp. 2393–2403, 2010, doi: 10.1016/j.surfcoat.2010.09.033.
[220] M. Sebastiani, C. Eberl, E. Bemporad, and G. M. Pharr, “Depth-resolved residual stress analysis of thin coatings by a new FIB-DIC method,” *Mater. Sci. Eng. A*, vol. 528, no. 27, pp. 7901–7908, 2011, doi: 10.1016/j.msea.2011.07.001.
[221] M. Sebastiani *et al.*, “Nano-scale residual stress profiling in thin multilayer films with non-equibiaxial stress state,” *Nanomaterials*, vol. 10, no. 5, 2020, doi: 10.3390/nano10050853.
[222] A. J. G. Lunt and A. M. Korsunsky, “A review of micro-scale focused ion beam milling and digital image correlation analysis for residual stress evaluation and error estimation,” *Surf. Coatings Technol.*, vol. 283, pp. 373–388, 2015, doi: 10.1016/j.surfcoat.2015.10.049.
[223] Q. Luo and A. H. Jones, “High-precision determination of residual stress of polycrystalline coatings using optimised XRD-sin2ψ technique,” *Surf. Coatings Technol.*, vol. 205, no. 5, pp. 1403–1408, 2010, doi: 10.1016/j.surfcoat.2010.07.108.
[224] I. G. McDonald, W. M. Moehlenkamp, D. Arola, and J. Wang, “Residual Stresses in Cu/Ni Multilayer Thin Films Measured Using the Sin2ψ Method,” *Exp. Mech.*, vol. 59, no. 1, pp. 111–120, 2019, doi: 10.1007/s11340-018-00447-2.
[225] E. Bemporad *et al.*, “A critical comparison between XRD and FIB residual stress measurement techniques in thin films,” *Thin Solid Films*, vol. 572, pp. 224–231, 2014, doi: 10.1016/j.tsf.2014.09.053.
[226] A. F. Jankowski and T. O. Wilford, “Grain Size Variation in Coatings,” *J. Met.*, no. June, pp. 28–30, 1987.
[227] M. Hans *et al.*, “Crystallite size-dependent metastable phase formation of TiAlN coatings,” *Sci. Rep.*, vol. 7, no. 1, pp. 1–7, 2017, doi: 10.1038/s41598-017-16567-z.
[228] A. Haase, M. Klatt, A. Schafmeister, R. Stabenow, and B. Ortner, “The generalized sin2 ψ method: An advanced solution for X-ray stress analysis in textured materials,” *Powder Diffr.*, vol. 29, no. 2, pp. 133–136, 2014, doi: 10.1017/S088571561400030X.
[229] J. Musil and J. Vlček, “Magnetron sputtering of films with controlled texture and grain size,” *Mater. Chem. Phys.*, vol. 54, no. 1–3, pp. 116–122, 1998, doi: 10.1016/S0254-0584(98)00020-0.
[230] O. V. Sobol *et al.*, “A computer simulation of radiation-induced structural changes and properties of

multiperiod ZrNx/MoNx system," *J. Nano- Electron. Phys.*, vol. 9, no. 2, pp. 1–5, 2017, doi: 10.21272/jnep.9(2).02031.
[231] L. A. Dobrzański, K. Lukaszkowicz, and K. Labisz, "Structure, texture and chemical composition of coatings deposited by PVD techniques," *Arch. Mater. Sci. Eng.*, vol. 37, no. 1, pp. 45–52, 2009.
[232] A. Bogner, P. H. Jouneau, G. Thollet, D. Basset, and C. Gauthier, "A history of scanning electron microscopy developments: Towards 'wet-STEM' imaging," *Micron*, vol. 38, no. 4, pp. 390–401, 2007, doi: 10.1016/j.micron.2006.06.008.
[233] F. . Haguenau, P. W. . Hawkes, J. L. . Hutchinson, B. . Satiat-Jeunemaitre, G. T. . Simon, and D. B. . Williams, "Key events in the history of electron microscopy (multiple letters)," *Microsc. Microanal.*, vol. 9, no. 4, pp. 96–138, 2003, doi: 10.1017/s1431927603030538.
[234] M. Reza, E. Kontturi, A. S. Jääskeläinen, T. Vuorinen, and J. Ruokolainen, "Transmission electron microscopy for wood and fiber analysis-A review," *BioResources*, vol. 10, no. 3, pp. 6230–6261, 2015, doi: 10.15376/biores.10.3.reza.
[235] R. Borrajo Pelaez and P. Hedström, "Recent Developments of Crystallographic Analysis Methods in the Scanning Electron Microscope for Applications in Metallurgy," *Crit. Rev. Solid State Mater. Sci.*, vol. 43, no. 6, pp. 455–474, 2018, doi: 10.1080/10408436.2017.1370576.
[236] R. Wouters and L. Froyen, "Scanning electron microscope fractography in failure analysis of steels," *Mater. Charact.*, vol. 36, no. 4–5, pp. 357–364, 1996, doi: 10.1016/s1044-5803(96)00070-8.
[237] B. A. Ishaque, H. Stürz, and E. Basad, "Fatigue Fracture of a Short Stem Hip Replacement: A Failure Analysis With Electron Microscopy and Review of the Literature," *J. Arthroplasty*, vol. 26, no. 4, pp. 665.e17-665.e20, 2011, doi: 10.1016/j.arth.2010.05.021.
[238] M. . Carl, C. A. . Smith, and M. L. . Young, "Dual-Beam Scanning Electron Microscope (SEM) and Focused Ion Beam (FIB): A Practical Method for Characterization of Small Cultural Heritage Objects Matthew," *Mater. Res. Soc. Symp. - Proc.*, vol. 1656, 2014, doi: 10.1557/opl.2014.
[239] J. S. Becker and R. G. Gordon, "Diffusion barrier properties of tungsten nitride films grown by atomic layer deposition from bis(tert-butylimido)bis(dimethylamido)tungsten and ammonia," *Appl. Phys. Lett.*, vol. 82, no. 14, pp. 2239–2241, 2003, doi: 10.1063/1.1565699.
[240] L. E. Franken, K. Grünewald, E. J. Boekema, and M. C. A. Stuart, "A Technical Introduction to Transmission Electron Microscopy for Soft-Matter: Imaging, Possibilities, Choices, and Technical Developments," *Small*, vol. 16, no. 14, 2020, doi: 10.1002/smll.201906198.
[241] L. F. Kourkoutis, J. M. Plitzko, and W. Baumeister, "Electron microscopy of biological materials at the nanometer scale," *Annu. Rev. Mater. Res.*, vol. 42, pp. 33–58, 2012, doi: 10.1146/annurev-matsci-070511-155004.
[242] A. V. Crewe, J. Wall, and L. M. Welter, "A high-resolution scanning transmission electron microscope," *J. Appl. Phys.*, vol. 39, no. 13, pp. 5861–5868, 1968, doi: 10.1063/1.1656079.
[243] J. Goldstein *et al.*, *Scanning Electron Microscopy and X-Ray Microanalysis*, Third Edit. New York: Springer Science+Business Media, 2007.
[244] H. H. Rose, "Optics of high-performance electron microscopes," *Sci. Technol. Adv. Mater.*, vol. 9, no. 1, 2008, doi: 10.1088/0031-8949/9/1/014107.
[245] D. J. Smith, "Ultimate resolution in the electron microscope?," *Mater. Today*, vol. 11, no. SUPPL., pp. 30–38, 2008, doi: 10.1016/S1369-7021(09)70005-7.
[246] J. I. Goldstein, D. E. Newbury, J. R. Michael, N. W. M. Ritchie, J. H. J. Scott, and D. C. Joy, *Scanning Electron Microscope (SEM) Instrumentation*, Fourth Edi. 2018. doi: 10.1007/978-1-4939-6676-9_5.
[247] D. B. Williams and C. B. Carter, *Transmission Electron Microscopy: Basics*, Second. New York: Springer Science+Business Media, 2009. doi: 10.1007/978-1-4757-2519-3_6.
[248] K. Kanaya and S. Okayama, "Penetration and energy-loss theory of electrons in solid targets," *J. Phys. D. Appl. Phys.*, vol. 5, no. 1, pp. 43–58, 1972, doi: 10.1088/0022-3727/5/1/308.
[249] B. Freitag, S. Kujawa, P. M. Mul, J. Ringnalda, and P. C. Tiemeijer, "Breaking the spherical and chromatic aberration barrier in transmission electron microscopy," *Ultramicroscopy*, vol. 102, no. 3, pp. 209–214, 2005, doi: 10.1016/j.ultramic.2004.09.013.
[250] H. Niedrig, "Physical Background of Electron Backscattering," *Scanning*, vol. 1, no. 1, pp. 17–34, 1978.
[251] T. Koshikawa and R. Shimizu, "A Monte Carlo calculation of low-energy secondary electron emission from metals," *J. Phys. D. Appl. Phys.*, vol. 7, no. 9, pp. 1303–1315, 1974, doi: 10.1088/0022-3727/7/9/318.
[252] K. Peters, "Generation, Collection and Properties of an SE-I Enriched Signal Suitable for High-Resolution SEM on Bulk Specimens," *Electron Beam Interact. With Solids Microsc. Microanal. Microlithogr.*, vol. 1982, no. 1, pp. 363–372, 1982.
[253] B. J. Griffin, "A comparison of conventional Everhart-Thornley style and in-lens secondary electron detectors-a further variable in scanning electron microscopy," *Scanning*, vol. 33, no. 3, pp. 162–173, 2011, doi: 10.1002/sca.20255.
[254] H. Seiler, "Secondary electron emission in the scanning electron microscope," *J. Appl. Phys.*, vol. 54, no. 11, 1983, doi: 10.1063/1.332840.
[255] K. Kumagai and T. Sekiguchi, "Sharing of secondary electrons by in-lens and out-lens detector in low-voltage scanning electron microscope equipped with immersion lens," *Ultramicroscopy*, vol. 109, no. 4, pp. 368–372, 2009, doi: 10.1016/j.ultramic.2009.01.005.

[256] V. N. E. Robinson, “Robinson_BSE imaging.pdf,” *Scanning*, vol. 3, pp. 15–26, 1980.
[257] E. I. Rau, V. Y. Karaulov, and S. V. Zaitsev, “Backscattered electron detector for 3D microstructure visualization in scanning electron microscopy,” *Rev. Sci. Instrum.*, vol. 90, no. 2, 2019, doi: 10.1063/1.5054746.
[258] M. Haider, S. Uhlemann, E. Schwan, G. Rose, B. Kabius, and K. Urban, “Electron microscopy image enhanced,” *Nature*, vol. 392, no. 6678, pp. 768–769, 1998, doi: 10.1038/33823.
[259] D. C. Joy, “The aberration corrected SEM - The ultimate accessory?,” *Microsc. Microanal.*, vol. 10, no. SUPPL. 2, pp. 952–953, 2004, doi: 10.1017/S1431927604880930.
[260] H. Rose and W. Wan, “Aberration correction in electron microscopy,” *Proc. IEEE Part. Accel. Conf.*, vol. 2005, pp. 44–48, 2005, doi: 10.1109/PAC.2005.1590354.
[261] P. E. . Batson, N. . Dellby, and O. L. . Krivanek, “Sub-Angstrom resolution using aberration corrected electron optics,” *Nature*, vol. 418, pp. 598–601, 2002, doi: 10.1093/oxfordjournals.jmicro.a050032.
[262] R. Shiloh *et al.*, “Spherical aberration correction in a scanning transmission electron microscope using a sculpted thin film,” *Ultramicroscopy*, vol. 189, pp. 46–53, 2018, doi: 10.1016/j.ultramic.2018.03.016.
[263] R. Klie, “Reaching a new resolution standard with electron microscopy,” *Physics (College. Park. Md).*, vol. 2, 2009, doi: 10.1103/physics.2.85.
[264] H. Wiedemann, “Particle Dynamics in Electro-Magnetic Fields,” in *Particle Accelerator Physics*, Fourth., Springer, Cham, 2015, pp. 99–124.
[265] P. Li *et al.*, “Recent advances in focused ion beam nanofabrication for nanostructures and devices: Fundamentals and applications,” *Nanoscale*, vol. 13, no. 3, pp. 1529–1565, 2021, doi: 10.1039/d0nr07539f.
[266] R. Minev, M. Ilieva, and J. Kettle, “FIB milling and characterization of CrC coatings on tool steel substrate,” *... Conf. Multi- ...*, no. April 2014, 2007, [Online]. Available: http://www.4m-net.org/files/papers/4M2007/367309/PID367309.pdf
[267] P. Panjan, A. Drnovšek, P. Gselman, M. Čekada, and M. Panjan, “Review of growth defects in thin films prepared by PVD techniques,” *Coatings*, vol. 10, no. 5, 2020, doi: 10.3390/COATINGS10050447.
[268] S. Drvarič Talian *et al.*, “Which Process Limits the Operation of a Li-S System?,” *Chem. Mater.*, 2019, doi: 10.1021/acs.chemmater.9b03255.
[269] A. A. Volinsky, L. Rice, W. Qin, and N. D. Theodore, “FIB failure analysis of memory arrays,” *Microelectron. Eng.*, vol. 75, no. 1, pp. 3–11, 2004, doi: 10.1016/j.mee.2004.03.088.
[270] Y. Chen and X. Zhang, “Focused ion beam technology and application in failure analysis,” in *2010 11th International Conference on Electronic Packaging Technology High Density Packaging*, 2010, pp. 957–960. doi: 10.1109/ICEPT.2010.5582645.
[271] L. A. Giannuzzi and F. A. Stevie, “A review of focused ion beam milling techniques for TEM specimen preparation,” *Micron*, vol. 30, pp. 197–204, 1999, [Online]. Available: http://zenobi.ethz.ch/content/dam/ethz/special-interest/chab/organic-chemistry/zenobi-group-dam/documents/Education/LecturesExercises/Analytical Strategy 2014/HS2015/Wepf Additional Material 1.pdf
[272] C. Kizilyaprak, A. G. Bittermann, J. Daraspe, and B. M. Humbel, “FIB-SEM tomography in biology,” *Methods Mol. Biol.*, vol. 1117, pp. 541–558, 2014, doi: 10.1007/978-1-62703-776-1_24.
[273] V. Lam and E. Villa, “Practical Approaches for Cryo-FIB Milling and Applications for Cellular Cryo-Electron Tomography,” *Methods Mol. Biol.*, vol. 2215, pp. 49–82, 2021, doi: 10.1007/978-1-0716-0966-8_3.
[274] D. Kiener, C. Motz, M. Rester, M. Jenko, and G. Dehm, “FIB damage of Cu and possible consequences for miniaturized mechanical tests,” *Mater. Sci. Eng. A*, vol. 459, no. 1–2, pp. 262–272, 2007, doi: 10.1016/j.msea.2007.01.046.
[275] A. Aitkaliyeva, J. W. Madden, B. D. Miller, and J. I. Cole, “Implementation of focused ion beam (FIB) system in characterization of nuclear fuels and materials,” *Micron*, vol. 67, no. April, pp. 65–73, 2014, doi: 10.1016/j.micron.2014.06.010.
[276] J. Liu, R. Niu, J. Gu, M. Cabral, M. Song, and X. Liao, “Effect of Ion Irradiation Introduced by Focused Ion-Beam Milling on the Mechanical Behaviour of Sub-Micron-Sized Samples,” *Sci. Rep.*, vol. 10, no. 1, pp. 1–8, 2020, doi: 10.1038/s41598-020-66564-y.
[277] J. J. McClelland, A. V. Steele, B. Knuffman, K. A. Twedt, A. Schwarzkopf, and T. M. Wilson, “Bright focused ion beam sources based on laser-cooled atoms,” *Appl. Phys. Rev.*, vol. 3, no. 1, 2016, doi: 10.1063/1.4944491.
[278] L. Bischoff, P. Mazarov, L. Bruchhaus, and J. Gierak, “Liquid metal alloy ion sources - An alternative for focussed ion beam technology,” *Appl. Phys. Rev.*, vol. 3, no. 2, 2016, doi: 10.1063/1.4947095.
[279] R. Jenkins, R. Manne, R. Robin, and C. Senemaud, “IUPAC—nomenclature system for x-ray spectroscopy,” *X-Ray Spectrom.*, vol. 20, no. 3, pp. 149–155, 1991, doi: 10.1002/xrs.1300200308.
[280] P. Van der Heide, *X-Ray Photoelectron Spectroscopy: An introduction to principle and practice*. Hoboke, New Jersey: John Wiley and Sons Inc., 2012.
[281] M. Niaz, S. Klassen, B. McMillan, and D. Metz, “Reconstruction of the history of the photoelectric effect and its implications for general physics textbooks,” *Sci. Educ.*, vol. 94, no. 5, pp. 903–931, 2010, doi: 10.1002/sce.20389.
[282] F. A. Stevie and C. L. Donley, “Introduction to x-ray photoelectron spectroscopy,” *J. Vac. Sci. Technol. A*, vol. 38, no. 6, p. 063204, 2020, doi: 10.1116/6.0000412.

[283] J. F. Moulder, “The impact of the scanning XPS microprobe on industrial applications of X-ray photoelectron spectroscopy,” *J. Electron Spectros. Relat. Phenomena*, vol. 231, no. 10, pp. 43–49, 2019, doi: 10.1016/j.elspec.2018.04.003.
[284] C. S. S. R. Kumar, *Surface science tools for nanomaterials characterization*. 2015. doi: 10.1007/978-3-662-44551-8.
[285] G. Greczynski and L. Hultman, “X-ray photoelectron spectroscopy: Towards reliable binding energy referencing,” *Prog. Mater. Sci.*, vol. 107, no. July 2019, p. 100591, 2020, doi: 10.1016/j.pmatsci.2019.100591.
[286] M. P. Seah, I. S. Gilmore, and S. J. Spencer, “Quantitative XPS: I. Analysis of X-ray photoelectron intensities from elemental data in a digital photoelectron database,” *J. Electron Spectros. Relat. Phenomena*, vol. 120, no. 1–3, pp. 93–111, 2001, doi: 10.1016/S0368-2048(01)00311-5.
[287] M. P. Seah, “The quantitative analysis of surfaces by XPS: A review,” *Surf. Interface Anal.*, vol. 2, no. 6, pp. 222–239, 1980, doi: 10.1002/sia.740020607.
[288] A. G. Shard, “Detection limits in XPS for more than 6000 binary systems using Al and Mg Kα X-rays,” *Surf. Interface Anal.*, vol. 46, no. 3, pp. 175–185, 2014, doi: 10.1002/sia.5406.
[289] S. Tougaard, “Energy loss in XPS: Fundamental processes and applications for quantification, non-destructive depth profiling and 3D imaging,” *J. Electron Spectros. Relat. Phenomena*, vol. 178–179, no. C, pp. 128–153, 2010, doi: 10.1016/j.elspec.2009.08.005.
[290] A. G. Shard, “Practical guides for x-ray photoelectron spectroscopy: Quantitative XPS,” *J. Vac. Sci. Technol. A*, vol. 38, no. 4, p. 041201, 2020, doi: 10.1116/1.5141395.
[291] I. Lindgren, “Chemical shifts in X-ray and photo-electron spectroscopy: A historical review,” *J. Electron Spectros. Relat. Phenomena*, vol. 137–140, no. SPEC. ISS., pp. 59–71, 2004, doi: 10.1016/j.elspec.2004.02.086.
[292] D. R. Baer *et al.*, “XPS guide: Charge neutralization and binding energy referencing for insulating samples,” *J. Vac. Sci. Technol. A*, vol. 38, no. 3, p. 031204, 2020, doi: 10.1116/6.0000057.
[293] P. Persson, S. Lunell, A. Szöke, B. Ziaja, and J. Hajdu, “Shake-up and shake-off excitations with associated electron losses in X-ray studies of proteins,” *Protein Sci.*, vol. 10, no. 12, pp. 2480–2484, 2001, doi: 10.1110/ps.ps.26201.
[294] H. Shinotsuka, S. Tanuma, C. J. Powell, and D. R. Penn, “Calculations of electron inelastic mean free paths. X. Data for 41 elemental solids over the 50eV to 200keV range with the relativistic full Penn algorithm,” *Surf. Interface Anal.*, vol. 47, no. 9, pp. 871–888, 2015, doi: 10.1002/sia.5789.
[295] H. Shinotsuka, S. Tanuma, C. J. Powell, and D. R. Penn, “Calculations of electron inelastic mean free paths. XII. Data for 42 inorganic compounds over the 50 eV to 200 keV range with the full Penn algorithm,” *Surf. Interface Anal.*, vol. 51, no. 4, pp. 427–457, 2019, doi: 10.1002/sia.6598.
[296] J. H. . Scofield, “Hhartree-Slater Subshell Photo-oxidation Cross-Sections,” *J. Electron Spectros. Relat. Phenomena*, vol. 8, pp. 129–137, 1976.
[297] M. A. Flores-Mancera, J. S. Villarrubia, and G. Massillon-Jl, “Electron Inelastic Mean Free Paths for LiF, CaF2, Al2O3, and Liquid Water from 433 keV down to the Energy Gap,” *ACS Omega*, vol. 5, no. 8, pp. 4139–4147, 2020, doi: 10.1021/acsomega.9b03872.
[298] W. S. M. Werner, “Questioning a Universal Law for Electron Attenuation,” *Physics (College. Park. Md).*, vol. 12, 2019, doi: 10.1103/physics.12.93.
[299] G. . Binning, C. F. . Quate, and C. . Gerber, “Atomic Force Microscope,” *Phys. Rev. Lett.*, vol. 56, no. 9, pp. 930–933, 1986, doi: 10.1201/9781420075250.
[300] G. . Binning, H. . Rohrer, C. . Gerber, and E. . Weibel, “Surface Studies by Scanning Tunneling Microscopy,” *Phys. Rev. Lett.*, vol. 49, no. 1, pp. 57–61, 1982, [Online]. Available: http://scholar.google.com/scholar?hl=en&btnG=Search&q=intitle:r+1982#0%5Cnhttp://scholar.google.com/scholar?hl=en&btnG=Search&q=intitle:R.(1982)%230
[301] G. . Binning, C. . Gerber, E. . Stoll, T. R. . Albrecht, and C. F. . Quate, “Atomic Resolution With Atomic Force Microscope,” *Surf. Sci.*, vol. 190, pp. 1–6, 1987.
[302] C. Hellenthal, R. Heimbuch, K. Sotthewes, E. S. Kooij, and H. J. W. Zandvliet, “Determining the local density of states in the constant current STM mode,” *Phys. Rev. B - Condens. Matter Mater. Phys.*, vol. 88, no. 3, pp. 1–6, 2013, doi: 10.1103/PhysRevB.88.035425.
[303] K. W. Shinato, F. Huang, and Y. Jin, “Principle and application of atomic force microscopy (AFM) for nanoscale investigation of metal corrosion,” *Corros. Rev.*, vol. 38, no. 5, pp. 423–432, 2020, doi: 10.1515/corrrev-2019-0113.
[304] F. Cellini, Y. Gao, and E. Riedo, “Å-Indentation for non-destructive elastic moduli measurements of supported ultra-hard ultra-thin films and nanostructures,” *Sci. Rep.*, vol. 9, no. 1, pp. 1–16, 2019, doi: 10.1038/s41598-019-40636-0.
[305] Y. A. Mota *et al.*, “Monoclinic phase transformation and mechanical durability of zirconia ceramic after fatigue and autoclave aging,” *J. Biomed. Mater. Res. - Part B Appl. Biomater.*, vol. 105, no. 7, pp. 1972–1977, 2017, doi: 10.1002/jbm.b.33720.
[306] M. Beltrami *et al.*, “Surface roughness control in nanolaminate coatings of chromium and tungsten nitrides,” *Micro Nano Eng.*, vol. 14, p. 100107, 2022, doi: https://doi.org/10.1016/j.mne.2022.100107.
[307] R. Garcia, “Nanomechanical mapping of soft materials with the atomic force microscope: Methods, theory

and applications," *Chem. Soc. Rev.*, vol. 49, no. 16, pp. 5850–5884, 2020, doi: 10.1039/d0cs00318b.
[308] N. Alharbi, S. Teerakanok, J. D. Satterthwaite, R. Giordano, and N. Silikas, "Quantitative nano-mechanical mapping AFM-based method for elastic modulus and surface roughness measurements of model polymer infiltrated ceramics," *Dent. Mater.*, vol. 38, no. 6, pp. 935–945, 2022, doi: 10.1016/j.dental.2022.03.002.
[309] Y. F. Dufrêne *et al.*, "Imaging modes of atomic force microscopy for application in molecular and cell biology," *Nat. Nanotechnol.*, vol. 12, no. 4, pp. 295–307, 2017, doi: 10.1038/nnano.2017.45.
[310] S. Liu and Y. Wang, "Application of AFM in microbiology: A review," *Scanning*, vol. 32, no. 2, pp. 61–73, 2010, doi: 10.1002/sca.20173.
[311] N. Goodman, Frank O.; Garcia, "Roles of the attractive and repulsive forces in atomic force microscopy," *Phys. Rev. B*, vol. 43, no. 6, pp. 4728–4731, 1991.
[312] G. Meyer and N. M. Amer, "Novel optical approach to atomic force microscopy," *Appl. Phys. Lett.*, vol. 53, no. 12, pp. 1045–1047, 1988, doi: 10.1063/1.100061.
[313] A. San Paulo and R. García, "High-resolution imaging of antibodies by tapping-mode atomic force microscopy: Attractive and repulsive tip-sample interaction regimes," *Biophys. J.*, vol. 78, no. 3, pp. 1599–1605, 2000, doi: 10.1016/S0006-3495(00)76712-9.
[314] Y. Martin, C. C. Williams, and H. K. Wickramasinghe, "Atomic force microscope-force mapping and profiling on a sub 100-Å scale," *J. Appl. Phys.*, vol. 61, no. 10, pp. 4723–4729, 1987, doi: 10.1063/1.338807.
[315] J. Shen, D. Zhang, F. H. Zhang, and Y. Gan, "AFM characterization of patterned sapphire substrate with dense cone arrays: Image artifacts and tip-cone convolution effect," *Appl. Surf. Sci.*, vol. 433, pp. 358–366, 2018, doi: 10.1016/j.apsusc.2017.10.077.
[316] F. J. Giessibl, "Advances in atomic force microscopy," *Rev. Mod. Phys.*, vol. 75, no. 3, pp. 949–983, 2003, doi: 10.1103/RevModPhys.75.949.
[317] F. Marques-Moros, A. Forment-Aliaga, E. Pinilla-Cienfuegos, and J. Canet-Ferrer, "Mirror effect in atomic force microscopy profiles enables tip reconstruction," *Sci. Rep.*, vol. 10, no. 1, pp. 1–8, 2020, doi: 10.1038/s41598-020-75785-0.
[318] J. Shen, D. Zhang, F. H. Zhang, and Y. Gan, "AFM tip-sample convolution effects for cylinder protrusions," *Appl. Surf. Sci.*, vol. 422, pp. 482–491, 2017, doi: 10.1016/j.apsusc.2017.06.053.
[319] D. R. Sahoo, P. Agarwal, and M. V. Salapaka, "Transient force atomic force microscopy: A new nano-interrogation method," *Proc. Am. Control Conf.*, pp. 2135–2140, 2007, doi: 10.1109/ACC.2007.4283047.
[320] A. Keyvani, M. S. Tamer, J. W. van Wingerden, J. F. L. Goosen, and F. van Keulen, "A comprehensive model for transient behavior of tapping mode atomic force microscope," *Nonlinear Dyn.*, vol. 97, no. 2, pp. 1601–1617, 2019, doi: 10.1007/s11071-019-05079-2.
[321] S. Magonov, "VISUALIZATION OF POLYMERS AT SURFACES AND INTERFACES WITH ATOMIC FORCE MICROSCOPY," in *Handbook of Surfaces and Interfaces of Materials*, First., vol. 2, H. S. Nalwa, Ed. Academic Press, 2001, pp. 393–430. doi: 10.1016/B978-0-12-513910-6.50029-3.
[322] A. Leyland and A. Matthews, "On the significance of the H/E ratio in wear control: A nanocomposite coating approach to optimised tribological behaviour," *Wear*, vol. 246, no. 1–2, pp. 1–11, 2000, doi: 10.1016/S0043-1648(00)00488-9.
[323] G. Pintaude, "Introduction of the Ratio of the Hardness to the Reduced Elastic Modulus for Abrasion," *Tribol. - Fundam. Adv.*, 2013, doi: 10.5772/55470.
[324] B. D. Beake, "The influence of the H/E ratio on wear resistance of coating systems – Insights from small-scale testing," *Surf. Coatings Technol.*, no. February, 2022, doi: 10.1016/j.surfcoat.2022.128272.
[325] E. Broitman, "Indentation Hardness Measurements at Macro-, Micro-, and Nanoscale: A Critical Overview," *Tribol. Lett.*, vol. 65, no. 1, pp. 1–18, 2017, doi: 10.1007/s11249-016-0805-5.
[326] S. M. Walley, "Historical origins of indentation hardness testing," *Mater. Sci. Technol. (United Kingdom)*, vol. 28, no. 9–10, pp. 1028–1044, 2012, doi: 10.1179/1743284711Y.0000000127.
[327] D. Tabor, "The hardness of solids," *Rev Phys Technol*, vol. 1, no. 3, pp. 145–179, 1970, doi: 10.1088/0034-6683/1/3/i01.
[328] N. K. Mukhopadhyay and P. Paufler, "Micro- and nanoindentation techniques for mechanical characterisation of materials," *Int. Mater. Rev.*, vol. 51, no. 4, pp. 209–245, 2006, doi: 10.1179/174328006X102475.
[329] W.Heinke, A.Leyland, A.Matthews, G.Berg, C.Friedrich, and E.Broszeit, "Evaluation of PVD nitride coatings,using impact,scratch and Rockwell-C adhesion tests," *Thin solid Film*, vol. 270, pp. 431–438, 1995.
[330] E. Broitman and L. Hultman, "Adhesion improvement of carbon-based coatings through a high ionization deposition technique," *J. Phys. Conf. Ser.*, vol. 370, no. 1, 2012, doi: 10.1088/1742-6596/370/1/012009.
[331] D. Hatic *et al.*, "Rockwell adhesion test – Approach to standard modernization," *Gap between Vis. Res. Vis. Softw.*, p. 1, 2020, [Online]. Available: https://weber.itn.liu.se/~marfa45/egev2020/posters/poster-sub6694.pdf
[332] M. S. Farhan, "A review on adhesion strength of single and multilayer coatings and the evaluation method," *Wasit J. Eng. Sci.*, vol. 4, no. 4, pp. 1–27, 2016.
[333] J. Chen and S. J. Bull, "Approaches to investigate delamination and interfacial toughness in coated systems: An overview," *J. Phys. D. Appl. Phys.*, vol. 44, no. 3, 2011, doi: 10.1088/0022-3727/44/3/034001.
[334] H. Buckel, "Progress in Micro-indentation hardness testing," *Metall. Rev.*, vol. 4, no. 13, pp. 49–100, 1959.

[335] Y. Li *et al.*, “Mapping the elastic properties of two-dimensional MoS2 via bimodal atomic force microscopy and finite element simulation,” *npj Comput. Mater.*, vol. 4, no. 1, 2018, doi: 10.1038/s41524-018-0105-8.
[336] G. Cao and H. Gao, “Mechanical properties characterization of two-dimensional materials via nanoindentation experiments,” *Prog. Mater. Sci.*, vol. 103, no. 35, pp. 558–595, 2019, doi: 10.1016/j.pmatsci.2019.03.002.
[337] K. K. Al-Quraishi, Q. He, W. Kauppila, M. Wang, and Y. Yang, “Mechanical testing of two-dimensional materials: a brief review,” *Int. J. Smart Nano Mater.*, vol. 11, no. 3, pp. 207–246, 2020, doi: 10.1080/19475411.2020.1791276.
[338] A. Caron, “Quantitative hardness measurement by instrumented AFM-indentation,” *J. Vis. Exp.*, vol. 2016, no. 117, pp. 1–9, 2016, doi: 10.3791/54706.
[339] N. A. Sakharova, J. V. Fernandes, J. M. Antunes, and M. C. Oliveira, “Comparison between Berkovich, Vickers and conical indentation tests: A three-dimensional numerical simulation study,” *Int. J. Solids Struct.*, vol. 46, no. 5, pp. 1095–1104, 2009, doi: 10.1016/j.ijsolstr.2008.10.032.
[340] G. M. Pharr and W. C. Oliver, “Measurement of Thin Film Mechanical Properties Using Nanoindentation,” *MRS Bull.*, vol. 17, no. 7, pp. 28–33, 1992, doi: 10.1557/S0883769400041634.
[341] J. Hay, P. Agee, and E. Herbert, “Continuous stiffness measurement during instrumented indentation testing,” *Exp. Tech.*, vol. 34, no. 3, pp. 86–94, 2010, doi: 10.1111/j.1747-1567.2010.00618.x.
[342] W. C. Oliver and G. M. Pharr, “Measurement of hardness and elastic modulus by instrumented indentation: Advances in understanding and refinements to methodology,” *J. Mater. Res.*, vol. 19, no. 1, pp. 3–20, 2004, doi: 10.1557/jmr.2004.19.1.3.
[343] W. C. Oliver and G. M. Pharr, “An improved technique for determining hardness and elastic modulus using load and displacement sensing indentation experiments,” *J. Mater. Res.*, vol. 7, no. 6, pp. 1564–1581, 1992.
[344] X. Li and B. Bhushan, “A review of nanoindentation continuous stiffness measurement technique and its applications,” *Mater. Charact.*, vol. 48, no. 1, pp. 11–36, 2002, doi: 10.1016/S1044-5803(02)00192-4.
[345] G. M. Pharr, J. H. Strader, and W. C. Oliver, “Critical issues in making small-depth mechanical property measurements by nanoindentation with continuous stiffness measurement,” *J. Mater. Res.*, vol. 24, no. 3, pp. 653–666, 2009, doi: 10.1557/jmr.2009.0096.
[346] A. C. Fischer-Cripps, P. Karvánková, and S. Vepřek, “On the measurement of hardness of super-hard coatings,” *Surf. Coatings Technol.*, vol. 200, no. 18–19, pp. 5645–5654, 2006, doi: 10.1016/j.surfcoat.2005.07.096.
[347] C. A. Schuh, “Nanoindentation studies of materials,” *Mater. Today*, vol. 9, no. 5, pp. 32–40, 2006, doi: 10.1016/S1369-7021(06)71495-X.
[348] Agilent Technologies, “Indentation Rules of Thumb - Applications and Limits,” 2010. [Online]. Available: https://www.semanticscholar.org/paper/Indentation-Rules-of-Thumb-—-Applications-and-Note/1f89c80f83b9cbac10fd8715ac381824abafd467
[349] G. Berg and P. Grau, “Influence of the Substrate Hardness on the Validity of Bückle’s Rule,” *Cryst. Res. Technol.*, vol. 28, no. 7, pp. 989–994, 1993, doi: 10.1002/crat.2170280722.
[350] L. Chen, A. Ahadi, J. Zhou, and J. E. Ståhl, “Modeling effect of surface roughness on nanoindentation tests,” *Procedia CIRP*, vol. 8, pp. 334–339, 2013, doi: 10.1016/j.procir.2013.06.112.
[351] Y. Xia, M. Bigerelle, J. Marteau, P. E. Mazeran, S. Bouvier, and A. Iost, “Effect of surface roughness in the determination of the mechanical properties of material using nanoindentation test,” *Scanning*, vol. 36, no. 1, pp. 134–149, 2014, doi: 10.1002/sca.21111.
[352] G. T. Burstein, “A hundred years of Tafel’s Equation: 1905-2005,” *Corros. Sci.*, vol. 47, no. 12, pp. 2858–2870, 2005, doi: 10.1016/j.corsci.2005.07.002.
[353] M. Stern and A. L. Geary, “Electrochemical Polarization: I . A Theoretical Analysis of the Shape of Polarization Curves,” *J. Electrochem. Soc.*, vol. 104, no. 1, p. 56, 1957.
[354] W. v. Baeckmann, “The History of Corrosion Protection,” *Handb. Cathodic Corros. Prot.*, pp. 1–26, 1997, doi: 10.1016/b978-088415056-5/50008-3.
[355] R. Ramachandran and M. Nosonovsky, “Coupling of surface energy with electric potential makes superhydrophobic surfaces corrosion-resistant,” *Phys. Chem. Chem. Phys.*, vol. 17, no. 38, pp. 24988–24997, 2015, doi: 10.1039/c5cp04462f.
[356] C. Zhang, K. Yamanaka, H. Bian, and A. Chiba, “Corrosion-resistant carbide-reinforced martensitic steel by Cu modification,” *npj Mater. Degrad.*, vol. 3, no. 1, 2019, doi: 10.1038/s41529-019-0092-3.
[357] M. Rodríguez Ripoll, N. Ojala, C. Katsich, V. Totolin, C. Tomastik, and K. Hradil, “The role of niobium in improving toughness and corrosion resistance of high speed steel laser hardfacings,” *Mater. Des.*, vol. 99, pp. 509–520, 2016, doi: 10.1016/j.matdes.2016.03.081.
[358] S. Vakili, A. Akbari, and R. Mohammadzadeh, “Corrosion resistance of plasma nitrided AISI M2 high speed steel,” *Prot. Met. Phys. Chem. Surfaces*, vol. 51, no. 4, pp. 630–636, 2015, doi: 10.1134/S2070205115040334.
[359] G. . Ramasamy and J. . Ratnasingam, “A Review of Cemented Tungsten Carbide Tool Wear during Wood Cutting Processes,” *J. Appl. Sci.*, vol. 10, no. 22, pp. 2799–2804, 2010.
[360] D. K. Merl, P. Panjan, M. Panjan, and M. Čekada, “The role of surface defects density on corrosion resistance of PVD hard coatings,” *Plasma Process. Polym.*, vol. 4, no. SUPPL.1, pp. 613–617, 2007, doi: 10.1002/ppap.200731416.

[361] P. Panjan *et al.*, “Influence of growth defects on the corrosion resistance of sputter-deposited tialn hard coatings,” *Coatings*, vol. 9, no. 511, pp. 1–16, 2019, doi: 10.3390/coatings11020123.
[362] A. Korhonen, “Corrosion of thin hard PVD coatings,” *Vacuum*, vol. 45, no. 10–11, pp. 1031–1034, 1994, doi: 10.1016/0042-207X(94)90015-9.
[363] W. S. Tait, “Electrochemical corrosion basics,” *Handb. Environ. Degrad. Mater. Third Ed.*, pp. 97–115, 2018, doi: 10.1016/B978-0-323-52472-8.00005-8.
[364] B. E. Wilde, “A relationship between steady-state corrosion potential and the anodic dissolution kinetics of the 300 series austenitic stainless steels,” *Corros. Sci.*, vol. 7, no. 6, pp. 315–324, 1967, doi: 10.1016/S0010-938X(67)80021-0.
[365] S. Laurens *et al.*, “Steady-state polarization response of chloride-induced macrocell corrosion systems in steel reinforced concrete - Numerical and experimental investigations,” *Cem. Concr. Res.*, vol. 79, pp. 272–290, 2016, doi: 10.1016/j.cemconres.2015.09.021.
[366] C. Andrade and C. Alonso, “Corrosion rate monitoring and on-site,” *Constr. Build. Mater.*, vol. 10, no. 5, pp. 315–328, 1996.
[367] E. J. F. Dickinson and A. J. Wain, “The Butler-Volmer equation in electrochemical theory: Origins, value, and practical application,” *J. Electroanal. Chem.*, vol. 872, 2020, doi: 10.1016/j.jelechem.2020.114145.
[368] A. J. . Bard and L. R. Faulkner, *Electrochemical Methods: Fundamentals and Applications*, 2nd ed. John Wiley and Sons, 2001. [Online]. Available: http://elib.tu-darmstadt.de/tocs/95069577.pdf
[369] R. Guidelli *et al.*, “Defining the transfer coefficient in electrochemistry: An assessment (IUPAC Technical Report),” *Pure Appl. Chem.*, vol. 86, no. 2, pp. 245–258, 2014, doi: 10.1515/pac-2014-5026.
[370] H. H. Bauer, “The electrochemical transfer - coefficient,” *Electroanal. Chem. Interfacial Electrochem.*, vol. 16, pp. 419–432, 1968.
[371] D. A. Noren and M. A. Hoffman, “Clarifying the Butler-Volmer equation and related approximations for calculating activation losses in solid oxide fuel cell models,” *J. Power Sources*, vol. 152, no. 1–2, pp. 175–181, 2005, doi: 10.1016/j.jpowsour.2005.03.174.
[372] D. B. Matthews, “The stern-geary and related methods for determining corrosion rates,” *Aust. J. Chem.*, vol. 28, no. 2, pp. 243–251, 1975, doi: 10.1071/CH9750243.
[373] P. Khadke, T. Tichter, T. Boettcher, F. Muench, W. Ensinger, and C. Roth, “A simple and effective method for the accurate extraction of kinetic parameters using differential Tafel plots,” *Sci. Rep.*, vol. 11, no. 1, p. 8974, 2021, doi: 10.1038/s41598-021-87951-z.
[374] M. Stern, “A method for obtain corrosion rates from polarization data.pdf,” *Corrosion*, vol. 14, pp. 60–64, 1958.
[375] G. Song, “Transpassivation of Fe – Cr – Ni stainless steels,” *Corros. Sci.*, no. 47, pp. 1953–1987, 2005.
[376] V. Encinas-Sánchez, M. T. de Miguel, M. I. Lasanta, G. García-Martín, and F. J. Pérez, “Electrochemical impedance spectroscopy (EIS): An efficient technique for monitoring corrosion processes in molten salt environments in CSP applications,” *Sol. Energy Mater. Sol. Cells*, vol. 191, no. August 2018, pp. 157–163, 2019, doi: 10.1016/j.solmat.2018.11.007.
[377] H. H. Hernández *et al.*, “Electrochemical Impedance Spectroscopy (EIS): A Review Study of Basic Aspects of the Corrosion Mechanism Applied to Steels,” in *Electrochemical Impedance Spectroscopy*, M. El-Azazy, M. ; Min, and P. ; Annus, Eds. London: Intech Open, 2019, pp. 1–33. [Online]. Available: doi: 10.5772/intechopen.94470
[378] K. Jüttner, “Electrohcemical Impedance Spectroscopy (EIS) of corrosion processes on inhomogeneous surfaces,” *Electrochim. Acta*, vol. 35, no. 10, pp. 1501–1508, 1990.
[379] C. Liu, Q. Bi, A. Leyland, and A. Matthews, “An electrochemical impedance spectroscopy study of the corrosion behavior of PVD coated steels in 0.5 N NaCl aqueous solution: Part II. EIS interpretation of corrossion behaviour,” *Corros. Sci.*, vol. 45, no. 6, pp. 1257–1273, 2003, doi: 10.1016/S0010-938X(02)00214-7.
[380] P. Feng, K. Wan, G. Cai, L. Yang, and Y. Li, “Synergistic protective effect of carboxymethyl chitosan and cathodic protection of X70 pipeline steel in seawater,” *RSC Adv.*, vol. 7, no. 6, pp. 3419–3427, 2017, doi: 10.1039/C6RA25310E.
[381] M. N. Idris, A. R. Daud, and N. K. Othman, “Electrochemical impedance spectroscopy study on corrosion inhibition of benzyltriethylammonium chloride,” *AIP Conf. Proc.*, vol. 1571, no. December 2013, pp. 23–28, 2013, doi: 10.1063/1.4858624.
[382] H. Cesiulis, N. Tsyntsaru, A. Ramanavicius, and G. Ragoisha, “The Study of Thin Films by Electrochemical Impedance Spectroscopy,” in *Nanostructures and Thin Films for Multifunctional Applications*, 1st ed., no. October 2017, V. Tiginyanu, Ion; Topala, Pavel; Ursaki, Ed. Springer, 2016, pp. 3–43. doi: 10.1007/978-3-319-30198-3.
[383] Q. Meyer, Y. Zeng, and C. Zhao, “Electrochemical impedance spectroscopy of catalyst and carbon degradations in proton exchange membrane fuel cells,” *J. Power Sources*, vol. 437, no. July, 2019, doi: 10.1016/j.jpowsour.2019.226922.
[384] P. Boillat, F. N. Büchi, L. Gubler, and T. J. Schmidt, “Use and Misuse of Electrochemical Impedance Spectroscopy ({EIS}) in Fuel Cell Research,” *{ECS} Meet. Abstr.*, vol. {MA}2019-0, no. 32, p. 1435, Sep. 2019, doi: 10.1149/ma2019-02/32/1435.
[385] Z. He and F. Mansfeld, “Exploring the use of electrochemical impedance spectroscopy (EIS) in microbial

fuel cell studies," *Energy Environ. Sci.*, vol. 2, no. 2, pp. 215–219, 2009, doi: 10.1039/b814914c.
[386] J. L. Gilbert and P. Khullar, "Analysis of Electrochemical Impedance Spectra Using Phase Angle Symmetry Across Log Frequency," *J. Electrochem. Soc.*, vol. 167, no. 2, p. 021505, 2020, doi: 10.1149/1945-7111/ab69f6.
[387] N. O. Laschuk, E. B. Easton, and O. V. Zenkina, "Reducing the resistance for the use of electrochemical impedance spectroscopy analysis in materials chemistry," *RSC Adv.*, vol. 11, no. 45, pp. 27925–27936, 2021, doi: 10.1039/d1ra03785d.
[388] S. Wang, J. Zhang, O. Gharbi, V. Vivier, M. Gao, and M. E. Orazem, "Electrochemical Impedance Spectroscopy," *Nat. Rev. Method Prim.*, vol. 1, no. 41, pp. 1–21, 2021, doi: 10.5189/revpolarography.65.87.
[389] F. Ciucci, "Modeling electrochemical impedance spectroscopy," *Curr. Opin. Electrochem.*, vol. 13, no. 4, pp. 132–139, 2019, [Online]. Available: https://doi.org/10.1016/j.coelec.2018.12.003
[390] S. J. Shin *et al.*, "On the importance of the electric double layer structure in aqueous electrocatalysis," *Nat. Commun.*, vol. 13, no. 1, 2022, doi: 10.1038/s41467-021-27909-x.
[391] S. Skale, V. Doleček, and M. Slemnik, "Substitution of the constant phase element by Warburg impedance for protective coatings," *Corros. Sci.*, vol. 49, no. 3, pp. 1045–1055, 2007, doi: https://doi.org/10.1016/j.corsci.2006.06.027.
[392] S. R. Taylor and E. Gileadi, "Physical interpretation of the Warburg impedance," *Corrosion*, vol. 51, no. 9, pp. 664–671, 1995, doi: 10.5006/1.3293628.
[393] S. M. Park and J. S. Yoo, "Electrochemical impedance spectroscopy for better electrochemical measurements," *Anal. Chem.*, vol. 75, no. 21, pp. 455–461, 2003.
[394] J. T. S. Irvine, D. C. Sinclair, and A. R. West, "Electroceramics: Characterization by Impedance Spectroscopy," *Adv. Mater.*, vol. 2, no. 3, pp. 132–138, 1990, doi: 10.1002/adma.19900020304.
[395] L. Zhang, Y. Chen, Y. P. Feng, S. Chen, Q. L. Wan, and J. F. Zhu, "Electrochemical characterization of AlTiN, AlCrN and AlCrSiWN coatings," *Int. J. Refract. Met. Hard Mater.*, vol. 53, pp. 68–73, 2015, doi: 10.1016/j.ijrmhm.2015.03.018.
[396] V. K. William Grips, H. C. Barshilia, V. E. Selvi, Kalavati, and K. S. Rajam, "Electrochemical behavior of single layer CrN, TiN, TiAlN coatings and nanolayered TiAlN/CrN multilayer coatings prepared by reactive direct current magnetron sputtering," *Thin Solid Films*, vol. 514, no. 1–2, pp. 204–211, 2006, doi: 10.1016/j.tsf.2006.03.008.
[397] X. Liu, J. Xiong, Y. Lv, and Y. Zuo, "Study on corrosion electrochemical behavior of several different coating systems by EIS," *Prog. Org. Coatings*, vol. 64, no. 4, pp. 497–503, 2009, doi: 10.1016/j.porgcoat.2008.08.012.
[398] C. Liu, Q. Bi, A. Leyland, and A. Matthews, "An Electrochemical Impedance Spectroscopy study of the corrosion behavior of PVD coated steels in 0.5 N NaCl aqueous solution: Part I: Establishment of Equivalent Circuits for EIS data modelling," *Corros. Sci.*, vol. 45, no. 6, pp. 1243–1256, 2003, doi: 10.1016/S0010-938X(02)00214-7.
[399] G. J. . Brug, A. L. G. . Van Den Eeden, M. . Sluyters-Rehbach, and J. Sluyters, "The analysis of electrode impedances complicated by the presence of a constant phase element," vol. 176, pp. 275–295, 1984.
[400] S. Holm, T. Holm, and Ø. G. Martinsen, "Simple circuit equivalents for the constant phase element," *PLoS One*, vol. 16, no. 3 March, pp. 1–12, 2021, doi: 10.1371/journal.pone.0248786.
[401] J. S. Yoo and S. M. Park, "An electrochemical impedance measurement technique employing fourier transform," *Anal. Chem.*, vol. 72, no. 9, pp. 2035–2041, 2000, doi: 10.1021/ac9907540.
[402] H. S. Lee, J. K. Singh, and J. H. Park, "Pore blocking characteristics of corrosion products formed on Aluminum coating produced by arc thermal metal spray process in 3.5 wt.% NaCl solution," *Constr. Build. Mater.*, vol. 113, pp. 905–916, 2016, doi: 10.1016/j.conbuildmat.2016.03.135.
[403] J. R. Xavier, "SECM and EIS Studies of Galvanic Corrosion of Copper/Iron Connected to Automotive Parts in Seawater," *Met. Mater. Int.*, vol. 26, no. 11, pp. 1679–1687, 2020, doi: 10.1007/s12540-019-00482-1.
[404] J. Huang, Z. Li, B. Y. Liaw, and J. Zhang, "Graphical analysis of electrochemical impedance spectroscopy data in Bode and Nyquist representations," *J. Power Sources*, vol. 309, pp. 82–98, 2016, doi: 10.1016/j.jpowsour.2016.01.073.
[405] A. Gilewicz and B. Warcholinski, "Deposition and characterisation of Mo2N/CrN multilayer coatings prepared by cathodic arc evaporation," *Surf. Coatings Technol.*, vol. 279, pp. 126–133, 2015, doi: 10.1016/j.surfcoat.2015.08.042.
[406] B. S. Lou, Y. C. Chang, and J. W. Lee, "High temperature oxidation behaviors of CrNx and Cr-Si-N thin films at 1000 °C," *Coatings*, vol. 9, no. 9, 2019, doi: 10.3390/coatings9090540.
[407] B. Navinšek, P. Panjan, and I. Milošev, "Industrial applications of CrN (PVD) coatings, deposited at high and low temperatures," *Surf. Coatings Technol.*, vol. 97, no. 1–3, pp. 182–191, 1997, doi: 10.1016/S0257-8972(97)00393-9.
[408] P. Panjan, B. Navinšek, A. Cvelbar, A. Zalar, and I. Milošev, "Oxidation of TiN, ZrN, TiZrN, CrN, TiCrN and TiN/CrN multilayer hard coatings reactively sputtered at low temperature," *Thin Solid Films*, vol. 281–282, no. 1–2, pp. 298–301, 1996, doi: 10.1016/0040-6090(96)08663-4.
[409] B. Navinšek, P. Panjan, and A. Cvelbar, "Characterization of low temperature CrN and TiN (PVD) hard coatings," *Surf. Coatings Technol.*, vol. 75, pp. 155–161, 1995.
[410] E. Y. Choi, M. C. Kang, D. H. Kwon, D. W. Shin, and K. H. Kim, "Comparative studies on microstructure

and mechanical properties of CrN, Cr-C-N and Cr-Mo-N coatings," *J. Mater. Process. Technol.*, vol. 187–188, pp. 566–570, 2007, doi: 10.1016/j.jmatprotec.2006.11.090.
[411] B. Warcholinski and A. Gilewicz, "Tribological Properties of CrNx Coatings," *J. Achievments Mater. Manuf. Eng.*, vol. 47, no. 2, pp. 498–504, 2009, doi: 10.1016/S0167-8922(08)70754-5.
[412] T. Polcar, N. M. G. Parreira, and A. Cavaleiro, "Tribological characterization of tungsten nitride coatings deposited by reactive magnetron sputtering," *Wear*, vol. 262, pp. 655–665, 2007, doi: 10.1016/j.wear.2006.07.010.
[413] T. Polcar, N. M. G. Parreira, and A. Cavaleiro, "Structural and tribological characterization of tungsten nitride coatings at elevated temperature," *Wear*, vol. 265, no. 3–4, pp. 319–326, 2008, doi: 10.1016/j.wear.2007.10.011.
[414] B. D. Ozsdolay, C. P. Mulligan, K. Balasubramanian, L. Huang, S. V. Khare, and D. Gall, "Cubic β-WNx layers: Growth and properties vs N-to-W ratio," *Surf. Coatings Technol.*, vol. 304, pp. 98–107, 2016, doi: 10.1016/j.surfcoat.2016.06.079.
[415] Y. Kong, X. Tian, C. Gong, and P. K. Chu, "Enhancement of toughness and wear resistance by CrN/CrCN multilayered coatings for wood processing," *Surf. Coatings Technol.*, vol. 344, no. October 2017, pp. 204–213, 2018, doi: 10.1016/j.surfcoat.2018.03.027.
[416] J. J. Roa *et al.*, "Contact damage and fracture micromechanisms of multilayered TiN/CrN coatings at micro- and nano-length scales," *Thin Solid Films*, vol. 571, no. P2, pp. 308–315, 2014, doi: 10.1016/j.tsf.2014.04.018.
[417] I. Jauberteau *et al.*, "Molybdenum nitride films: Crystal structures, synthesis, mechanical, electrical and some other properties," *Coatings*, vol. 5, no. 4, pp. 656–687, 2015, doi: 10.3390/coatings5040656.
[418] J. Wang, P. Munroe, Z. Zhou, and Z. Xie, "Nanostructured molybdenum nitride-based coatings: Effect of nitrogen concentration on microstructure and mechanical properties," *Thin Solid Films*, vol. 682, no. May, pp. 82–92, 2019, doi: 10.1016/j.tsf.2019.05.011.
[419] F. F. Klimashin, N. Koutná, H. Euchner, D. Holec, and P. H. Mayrhofer, "The impact of nitrogen content and vacancies on structure and mechanical properties of Mo-N thin films," *J. Appl. Phys.*, vol. 120, no. 18, 2016, doi: 10.1063/1.4966664.
[420] A. Fan, L. Qin, L. Tian, and B. Tang, "Corrosion resistance of Molybdenum Nitride modified Ti6Al4V alloy in HCl solution," *J. Wuhan Univ. Technol. Mater. Sci. Ed.*, vol. 23, no. 3, pp. 358–361, 2008, doi: 10.1007/s11595-007-3358-5.
[421] K. Balasubramanian, S. Khare, and D. Gall, "Vacancy-induced mechanical stabilization of cubic tungsten nitride," *Phys. Rev. B*, vol. 94, no. 17, pp. 36–38, 2016, doi: 10.1103/PhysRevB.94.174111.
[422] U. Plank, G. Meisl, U. von Toussaint, T. Höschen, and W. Jacob, "Study of the temperature-dependent nitrogen retention in tungsten surfaces using X-ray photoelectron spectroscopy," *Nucl. Mater. Energy*, vol. 17, no. September, pp. 48–55, 2018, doi: 10.1016/j.nme.2018.08.006.
[423] R. Mateus, M. C. Sequeira, C. Porosnicu, C. P. Lungu, A. Hakola, and E. Alves, "Thermal and chemical stability of the β-W2N nitride phase," *Nucl. Mater. Energy*, vol. 12, pp. 462–467, 2017, doi: 10.1016/j.nme.2017.03.040.
[424] P. Phadke, J. M. Sturm, R. W. E. van de Kruijs, and F. Bijkerk, "Sputtering and nitridation of transition metal surfaces under low energy, steady state nitrogen ion bombardment," *Appl. Surf. Sci.*, vol. 505, no. November 2019, p. 144529, 2020, doi: 10.1016/j.apsusc.2019.144529.
[425] P. Hones, N. Martin, M. Regula, and F. Lévy, "Structural and mechanical properties of chromium nitride, molybdenum nitride, and tungsten nitride thin films," *J. Phys. D. Appl. Phys.*, vol. 36, no. 8, pp. 1023–1029, 2003, doi: 10.1088/0022-3727/36/8/313.
[426] T. Polcar, N. M. G. Parreira, and A. Cavaleiro, "Tungsten oxide with different oxygen contents: Sliding properties," *Vacuum*, vol. 81, no. 11–12, pp. 1426–1429, 2007, doi: 10.1016/j.vacuum.2007.04.001.
[427] D. Wainstein and A. Kovalev, "Tribooxidation as a way to improve thewear resistance of cutting tools," *Coatings*, vol. 8, no. 6, pp. 1–9, 2018, doi: 10.3390/coatings8060223.
[428] G. Gassner, P. H. Mayrhofer, K. Kutschej, C. Mitterer, and M. Kathrein, "A new low friction concept for high temperatures: Lubricious oxide formation on sputtered VN coatings," *Tribol. Lett.*, vol. 17, no. 4, pp. 751–756, 2004, doi: 10.1007/s11249-004-8083-z.
[429] G. Gassner, P. H. Mayrhofer, K. Kutschej, C. Mitterer, and M. Kathrein, "Magnéli phase formation of PVD Mo-N and W-N coatings," *Surf. Coatings Technol.*, vol. 201, no. 6, pp. 3335–3341, 2006, doi: 10.1016/j.surfcoat.2006.07.067.
[430] F. B. Wu, S. K. Tien, and J. G. Duh, "Manufacture, microstructure and mechanical properties of CrWN and CrN/WN nanolayered coatings," *Surf. Coatings Technol.*, vol. 200, no. 5–6, pp. 1514–1518, 2005, doi: 10.1016/j.surfcoat.2005.08.039.
[431] W. Y. Wu *et al.*, "Microstructure, mechanical and tribological properties of CrWN films deposited by DC magnetron sputtering," *Vacuum*, vol. 87, pp. 209–212, 2013, doi: 10.1016/j.vacuum.2012.01.026.
[432] T. N. Lin, S. Han, K. W. Weng, and C. T. Lee, "Investigation on the structural and mechanical properties of anti-sticking sputtered tungsten chromium nitride films," *Thin Solid Films*, vol. 529, pp. 333–337, 2013, doi: 10.1016/j.tsf.2012.09.036.
[433] R. A. Koshy, M. E. Graham, and L. D. Marks, "Synthesis and characterization of CrN/Mo2N multilayers and phases of Molybdenum nitride," *Surf. Coatings Technol.*, vol. 202, no. 4–7, pp. 1123–1128, 2007, doi:

10.1016/j.surfcoat.2007.07.090.
[434] L. Shen and N. Wang, “Effect of nitrogen pressure on the structure of Cr-N, Ta-N, Mo-N, and W-N nanocrystals synthesized by arc discharge,” *J. Nanomater.*, vol. 2011, 2011, doi: 10.1155/2011/781935.
[435] A. Inspektor and P. A. Salvador, “Architecture of PVD coatings for metalcutting applications: A review,” *Surf. Coatings Technol.*, vol. 257, pp. 138–153, 2014, doi: 10.1016/j.surfcoat.2014.08.068.
[436] A. Baptista, F. Silva, J. Porteiro, J. Míguez, and G. Pinto, “Sputtering physical vapour deposition (PVD) coatings: A critical review on process improvement andmarket trend demands,” *Coatings*, vol. 8, no. 11, 2018, doi: 10.3390/COATINGS8110402.
[437] T. Göbel, S. Menzel, M. Hecker, W. Brückner, K. Wetzig, and C. Genzel, “Stress measurements in thermal loaded (Ti, Al) N hard coatings,” *Surf. Coatings Technol.*, vol. 142–144, pp. 861–867, 2001, doi: 10.1016/S0257-8972(01)01102-1.
[438] T. W. B. Riyadi, D. Setiadhi, A. D. Anggono, W. A. Siswanto, and H. H. Al-Kayiem, “Analysis of mechanical and thermal stresses due to TiN coating of Fe substrate by physical vapor deposition,” *Forces Mech.*, vol. 4, p. 100042, 2021, doi: 10.1016/j.finmec.2021.100042.
[439] A. L. Thomann *et al.*, “Energy transferred to the substrate surface during reactive magnetron sputtering of aluminum in Ar/O2 atmosphere,” *Thin Solid Films*, vol. 539, pp. 88–95, 2013, doi: 10.1016/j.tsf.2013.05.075.
[440] M. M. Waite and S. I. Shah, “Target poisoning during reactive sputtering of silicon with oxygen and nitrogen,” *Mater. Sci. Eng. B Solid-State Mater. Adv. Technol.*, vol. 140, no. 1–2, pp. 64–68, 2007, doi: 10.1016/j.mseb.2007.04.001.
[441] D. W. Hoffman and J. A. Thornton, “Compressive Sress And Inert Gas in Mo Films Sputtered From a Cylindrical-Post Magnetron with Ne, Ar, Kr, and Xe.,” *J. Vac. Sci. Technol.*, vol. 17, no. 1, pp. 380–383, 1979, doi: 10.1116/1.570394.
[442] M. Naveed, A. Obrosov, A. Zak, W. Dudzinski, A. A. Volinsky, and S. Weiß, “Sputtering power effects on growth and mechanical properties of Cr2AlC MAX phase coatings,” *Metals (Basel).*, vol. 6, no. 11, 2016, doi: 10.3390/met6110265.
[443] K. Schmid *et al.*, “Interaction of nitrogen plasmas with tungsten,” *Nucl. Fusion*, vol. 50, no. 2, 2010, doi: 10.1088/0029-5515/50/2/025006.
[444] D. W. Hoffman and J. A. Thornton, “COMPRESSIVE STRESS AND INERT GAS IN Mo FILMS SPUTTERED FROM A CYLINDRICAL-POST MAGNETRON WITH Ne, Ar, Kr, AND Xe.,” *J. Vac. Sci. Technol.*, vol. 17, no. 1, pp. 380–383, 1979, doi: 10.1116/1.570394.
[445] D. Tsai, E. Chen, Z. Chang, and F. Shieu, “Mechanical , and Electrical Properties of (CrHfNbTaTiVZr) N Coatings Deposited by Reactive Magnetron Sputtering,” 2022.
[446] W. Sun *et al.*, “Thermodynamic Routes to Novel Metastable Nitrogen-Rich Nitrides,” *Chem. Mater.*, vol. 29, no. 16, pp. 6936–6946, 2017, doi: 10.1021/acs.chemmater.7b02399.
[447] F. Capotondi *et al.*, “Effect of N2 partial pressure on the growth of chromium nitride coatings,” *Metall. Ital.*, vol. 99, no. 7–8, pp. 15–20, 2007.
[448] G. H. Major *et al.*, “Practical guide for curve fitting in x-ray photoelectron spectroscopy,” *J. Vac. Sci. Technol. A*, vol. 38, no. 6, p. 061203, 2020, doi: 10.1116/6.0000377.
[449] S. Wang *et al.*, “Synthesis, crystal structure, and elastic properties of novel tungsten nitrides,” *Chem. Mater.*, vol. 24, no. 15, pp. 3023–3028, 2012, doi: 10.1021/cm301516w.
[450] C. Steinbrüchel, B. J. Curtis, H. W. Lehmann, and R. Widmer, “Diagnostics of Low-Pressure Oxygen RF Plasmas and the Mechanism for Polymer Etching: A Comparison of Reactive Sputter Etching and Magnetron Sputter Etching,” *IEEE Trans. Plasma Sci.*, vol. 14, no. 2, pp. 137–144, 1986, doi: 10.1109/TPS.1986.4316516.
[451] E. Oks and A. Anders, “Evolution of the plasma composition of a high power impulse magnetron sputtering system studied with a time-of-flight spectrometer,” *J. Appl. Phys.*, vol. 105, no. 9, 2009, doi: 10.1063/1.3125443.
[452] W. Bauer, G. Betz, H. Bangert, A. Bergauer, and C. Eisenmenger-Sittner, “Intrinsic resputtering during film deposition investigated by Monte Carlo simulation,” *J. Vac. Sci. Technol. A Vacuum, Surfaces, Film.*, vol. 12, no. 6, pp. 3157–3164, 1994, doi: 10.1116/1.579231.
[453] C. L. Chang and C. S. Huang, “Effect of bias voltage on microstructure, mechanical and wear properties of Al-Si-N coatings deposited by cathodic arc evaporation,” *Thin Solid Films*, vol. 519, no. 15, pp. 4923–4927, 2011, doi: 10.1016/j.tsf.2011.01.054.
[454] Y. Liu, S. Yu, Q. Shi, X. Ge, and W. Wang, “Multilayer Coatings for Tribology: A Mini Review,” *Nanomaterials*, vol. 12, no. 9, 2022, doi: 10.3390/nano12091388.
[455] W. M. Seidl, M. Bartosik, S. Kolozsvári, H. Bolvardi, and P. H. Mayrhofer, “Influence of coating thickness and substrate on stresses and mechanical properties of (Ti,Al,Ta)N/(Al,Cr)N multilayers,” *Surf. Coatings Technol.*, vol. 347, no. April, pp. 92–98, 2018, doi: 10.1016/j.surfcoat.2018.04.060.
[456] A. M. Engwall, Z. Rao, and E. Chason, “Origins of residual stress in thin films: Interaction between microstructure and growth kinetics,” *Mater. Des.*, vol. 110, pp. 616–623, 2016, doi: 10.1016/j.matdes.2016.07.089.
[457] A. McGinnis, T. Watkins, and K. Jagannadham, “Residual stresses in a multilayer system of coatings,” *Int. Cent. Diffr. Data*, vol. 41, 1999.

[458] R. Daniel, K. J. Martinschitz, J. Keckes, and C. Mitterer, “The origin of stresses in magnetron-sputtered thin films with zone T structures,” *Acta Mater.*, vol. 58, no. 7, pp. 2621–2633, 2010, doi: 10.1016/j.actamat.2009.12.048.
[459] P. Panjan, M. Čekada, M. Panjan, and D. Kek-Merl, “Growth defects in PVD hard coatings,” *Vacuum*, vol. 84, no. 1, pp. 209–214, 2009, doi: 10.1016/j.vacuum.2009.05.018.
[460] D. M. Mattox, “Surface effects on the growth, adhesion and properties of reactively deposited hard coatings,” *Surf. Coatings Technol.*, vol. 81, no. 1, pp. 8–16, 1996, doi: 10.1016/0257-8972(95)02652-5.
[461] H. . Holleck, M. . Lahres, and P. . Woll, “Multilayer Coatings - Ingluence of Fabrication Parameters on Constitution and Properties,” *Surf. Coatings Technol.*, vol. 41, pp. 179–190, 1990.
[462] D. G. Stearns, P. . Mirkarimi, and E. Spiller, “Localized defects in multilayer coatings,” *Thin Solid Films*, vol. 446, pp. 37–49, 2004, doi: 10.1016/S0040-6090.
[463] A. Thomann *et al.*, “Energy flux measurements during magnetron sputter deposition processes,” *Surf. Coat. Technol.*, vol. 377, pp. 1–14, 2019.
[464] P. Cormier *et al.*, “Measuring the energy flux at the substrate position during magnetron sputter deposition processes,” *J. Appl. Phys.*, vol. 113, no. 013305, pp. 1–8, 2013, doi: 10.1063/1.4773103.
[465] R. Messier, A. P. Giri, and R. A. Roy, “Revised structure zone model for thin film physical structure,” *J. Vac. Sci. Technol. A Vacuum, Surfaces, Film.*, vol. 2, no. 2, pp. 500–503, 1984, doi: 10.1116/1.572604.
[466] J. A. . Thornton, “Structure Zone Models of Thin Films,” *Model. Optycal Thin Film.*, vol. 821, no. 2, pp. 95–103, 1987.
[467] E. Mirica, G. Kowach, and H. Du, “Modified Structure Zone Model to Describe the Morphological Evolution of ZnO Thin Films Deposited by Reactive Sputtering,” *Cryst. Growth Des.*, vol. 4, no. 1, pp. 157–159, 2004, doi: 10.1021/cg025596b.
[468] O. Lavigne, C. Alemany-Dumont, B. Normand, S. Berthon-Fabry, and R. Metkemeijer, “Thin chromium nitride PVD coatings on stainless steel for conductive component as bipolar plates of PEM fuel cells: Ex-situ and in-situ performances evaluation,” *Int. J. Hydrogen Energy*, vol. 37, no. 14, pp. 10789–10797, 2012, doi: 10.1016/j.ijhydene.2012.04.035.
[469] I. Katsuhiko and S. Kobayashi, “Various pole figure measurement techniques with SmartLab, assisting thin film characterization,” *Rigaku J.*, vol. 34, no. 2, pp. 10–16, 2018.
[470] K. Nagao and E. Kagami, “X-ray thin film measurement techniques: VII. Pole figure measurement,” *Rigaku J.*, vol. 27, no. 2, pp. 6–14, 2011.
[471] J. H. Hubbell, “Review and history of photon cross section calculations,” *Phys. Med. Biol.*, vol. 51, no. 13, pp. 245–262, 2006, doi: 10.1088/0031-9155/51/13/R15.
[472] J. C. Zheng, Y. Zhu, L. Wu, and J. W. Davenport, “On the sensitivity of electron and X-ray scattering factors to valence charge distributions,” *J. Appl. Crystallogr.*, vol. 38, no. 4, pp. 648–656, 2005, doi: 10.1107/S0021889805016109.
[473] P. Hones, R. Consiglio, N. Randall, and F. Leacutevy, “Mechanical properties of hard chromium tungsten nitride coatings,” *Surf. Coatings Technol.*, vol. 125, no. 1–3, pp. 179–184, 2000, doi: 10.1016/S0257-8972(99)00541-1.
[474] X. Chen, Y. Du, and Y. W. Chung, “Commentary on using H/E and H3/E2 as proxies for fracture toughness of hard coatings,” *Thin Solid Films*, vol. 688, no. April, p. 137265, 2019, doi: 10.1016/j.tsf.2019.04.040.
[475] X. Chen, Y. Du, and Y. W. Chung, “Commentary on using H/E and H3/E2 as proxies for fracture toughness of hard coatings,” *Thin Solid Films*, vol. 688, no. April, p. 137265, 2019, doi: 10.1016/j.tsf.2019.04.040.
[476] P. Bajaj, A. Hariharan, A. Kini, P. Kürnsteiner, D. Raabe, and E. A. Jägle, “Steels in additive manufacturing: A review of their microstructure and properties,” *Mater. Sci. Eng. A*, vol. 772, no. October 2019, 2020, doi: 10.1016/j.msea.2019.138633.
[477] A. M. El-Rakayby and B. Mills, “On the microstructure and mechanical properties of high-speed steels,” *J. Mater. Sci.*, vol. 23, no. 12, pp. 4340–4344, 1988, doi: 10.1007/BF00551928.
[478] Y. Liu, J. Li, W. Liang, J. Gao, Y. Qi, and C. Shang, “Precipitation behaviors of carbides in high speed steel during esr and heat treatment,” *Metals (Basel).*, vol. 11, no. 11, 2021, doi: 10.3390/met11111781.
[479] A. Zahs, M. Spiegel, and H. J. Grabke, “Chloridation and oxidation of iron, chromium, nickel and their alloys in chloridizing and oxidizing atmospheres at 400-700°C,” *Corros. Sci.*, vol. 42, no. 6, pp. 1093–1122, 2000, doi: 10.1016/S0010-938X(99)00142-0.
[480] M. Soleimani, H. Mirzadeh, and C. Dehghanian, “Effect of grain size on the corrosion resistance of low carbon steel,” *Mater. Res. Express*, vol. 7, no. 1, 2019, doi: 10.1088/2053-1591/ab62fa.
[481] K. D. Ralston and N. Birbilis, “Effect of grain size on corrosion: A review,” *Corrosion*, vol. 66, no. 7, pp. 0750051–07500513, 2010, doi: 10.5006/1.3462912.
[482] N. S. Mansoor, A. Fattah-alhosseini, H. Elmkhah, and A. Shishehian, “Electrochemical behavior of TiN, CrN and TiN/CrN nanostructured coatings on the nickel-chromium alloy used in dental fixed prosthesis,” *J. Asian Ceram. Soc.*, vol. 8, no. 3, pp. 694–710, 2020, doi: 10.1080/21870764.2020.1776915.
[483] Z. A. Fazel, H. Elmkhah, A. Fattah-Alhosseini, K. Babaei, and M. Meghdari, “Comparing electrochemical behavior of applied CrN/TiN nanoscale multilayer and TiN single-layer coatings deposited by CAE-PVD method,” *J. Asian Ceram. Soc.*, vol. 8, no. 2, pp. 510–518, 2020, doi: 10.1080/21870764.2020.1756065.
[484] D. Yang, C. Liu, X. Liu, M. Qi, and G. Lin, “EIS diagnosis on the corrosion behavior of TiN coated NiTi surgical alloy,” *Curr. Appl. Phys.*, vol. 5, no. 5, pp. 417–421, 2005, doi: 10.1016/j.cap.2004.11.002.

[485] P. Barai and G. J. Weng, “Mechanics of very fine-grained nanocrystalline materials with contributions from grain interior, GB zone, and grain-boundary sliding,” *Int. J. Plast.*, vol. 25, no. 12, pp. 2410–2434, 2009, doi: 10.1016/j.ijplas.2009.04.001.
[486] S. J. Bull, “Nanoindentation of coatings,” *J. Phys. D. Appl. Phys.*, vol. 38, no. 24, 2005, doi: 10.1088/0022-3727/38/24/R01.
[487] P. M. Anderson and C. Li, “Hall-Petch relations for multilayered materials,” *Nanostructured Mater.*, vol. 5, no. 3, pp. 349–362, 1995, doi: 10.1016/0965-9773(95)00250-I.
[488] N. Hansen, “Hall-petch relation and boundary strengthening,” *Scr. Mater.*, vol. 51, no. 8 SPEC. ISS., pp. 801–806, 2004, doi: 10.1016/j.scriptamat.2004.06.002.
[489] Z. B. Qi, P. Sun, F. P. Zhu, Z. C. Wang, D. L. Peng, and C. H. Wu, “The inverse Hall-Petch effect in nanocrystalline ZrN coatings,” *Surf. Coatings Technol.*, vol. 205, no. 12, pp. 3692–3697, 2011, doi: 10.1016/j.surfcoat.2011.01.021.
[490] N. F. Drobot, E. N. Trifonova, V. A. Krenev, and D. V. Drobot, “Oxidative dissolution of refractory metals by chlorination in aqueous organic media,” *Koord. Khimiya*, vol. 31, no. 4, pp. 262–265, 2005.
[491] W. A. Badawy and F. M. Al-Kharafi, “Corrosion and passivation behaviors of molybdenum in aqueous solutions of different pH,” *Electrochim. Acta*, vol. 44, no. 4, pp. 693–702, 1998, doi: 10.1016/S0013-4686(98)00180-7.
[492] D. Tamboli, S. Seal, V. Desai, and A. Maury, “Studies on passivation behavior of tungsten in application to chemical mechanical polishing,” *J. Vac. Sci. Technol. A Vacuum, Surfaces, Film.*, vol. 17, no. 4, pp. 1168–1173, 1999, doi: 10.1116/1.581790.

"Every little piece in your life
will add up to one
Every little piece in your life will
mean something to someone"

The Editors